The *in-situ* structural characterization of layered double hydroxide materials in catalytic and biological applications

By

Christopher Hobbs

Supervisor: Valeria Nicolosi

A thesis in fulfilment of the requirements of the degree of

Doctor in Philosophy

in the

School of Physics

Trinity College Dublin

March 2019

Declaration

I declare that this thesis has not been submitted as an exercise for a degree at this or any other university and it is entirely my own work, except for unpublished collaborative work and assistance acknowledged herein.

I agree to deposit this thesis in the University's open access institutional repository or allow the Library to do so on my behalf, subject to Irish Copyright Legislation and Trinity College Library conditions of use and acknowledgement.

_____

Christopher Hobbs, March 2019

Acknowledgements

First and foremost, I would like to sincerely thank my supervisor, **Prof. Valeria Nicolosi**, for giving me the opportunity to pursue my PhD research studies in the CPAM research group for the last 4 years. The guidance, motivation and support imparted by Prof. Nicolosi is greatly appreciated.

Along with that, I would like to thank both current and past members of the Nicolosi **CPAM research group.** The helpful, hard-working and enthusiastic approach to our group's scientific work has made much of my studies possible. It has been a great pleasure to work with every member of the Nicolosi group. A particular mention to **Dr. Sonia Jaskaniec,** who I have had the pleasure of working with throughout the four years. From teaching me how to boil water in the laboratory to designing and implementing full scientific projects, much of my PhD research is credited to the synthesis work of Dr. Jaskaniec.

On that note, my sincere gratitude goes to **Mr. Dermot Daly**, **Mr. Clive Downing** and **Dr. Eoin K. McCarthy** for the SEM and TEM instrumentation training as well as their advice and knowledge involving numerous experiments over the last four years. Their support and teachings are owed a massive credit to my development as an electron microscopist. I also acknowledge current and past **Advanced Microscopy Laboratory** residents that have made for an enjoyable environment to work in every day during my time here.

As part of my PhD project, I have been lucky enough to be involved in a diverse range of national and international interdisciplinary collaborations throughout my journey in the CPAM research group. In this regard, I would like to thank **Prof. Fergal O'Brien** (RCSI & AMBER) and the **Tissue Engineering Research Group (TERG)**, **RCSI Dublin**. I am grateful of the opportunities they have provided me to learn about the research areas of tissue engineering through their research. In addition, I would like to thank the TERG members for the several samples they have provided to me for my own electron microscopy studies throughout the last four years. I would also like to

acknowledge **Prof. Adriele Prina-Mello** and **Dr. Dania Movia** (Trinity Translational Medicine Institute, TCD & AMBER) for their helpful knowledge and provision of many samples that have been hugely beneficial to my work. My thanks also to **Dr. Maurice C.D Mourad** and **Dr. Karl Mandel** for their insightful knowledge and assistance relating to the layered double hydroxide material studies.

Last, and by no means least, my sincerest gratitude goes to my family. I cannot thank them enough for their support and guidance not only for my PhD studies, but for providing me with the best opportunities throughout my education to pursue my career as a scientist. I hope I have done you proud.

List of Publications

Gilroy, D. A., **Hobbs, C**., Nicolosi, V., Buckley, C. T., O'Brien, F. J., & Kearney, C. J. (2017). Development of magnetically active scaffolds as intrinsically-deformable bioreactors. *MRS Communications*, *7*(3), 367–374. https://doi.org/10.1557/mrc.2017.41

Gonzalez-fernandez, T., Sathy, B. N., **Hobbs, C.,** Cunniffe, G. M., Mccarthy, H. O., Dunne, N. J., … Kelly, D. J. (2017). Mesenchymal stem cell fate following non-viral gene transfection strongly depends on the choice of delivery vector. *Acta Biomaterialia*, *55*, 226–238. https://doi.org/10.1016/j.actbio.2017.03.044

Jaskaniec, S., **Hobbs, C.,** Seral-Ascaso, A., Coelho, J., Browne, M. P., Tyndall, D., … Nicolosi, V. (2018). Low-temperature synthesis of high quality Ni-Fe layered double hydroxides hexagonal platelets. *Scientific Reports*, *8*, 4–11. https://doi.org/10.1038/s41598-018-22630-0

Hobbs, C., Jaskaniec, S., Mccarthy, E. K., Downing, C., Opelt, K., Güth, K., Shmeliov, A., Mourad, M.C.D., Mandel, K., Nicolosi, V. (2018). Structural transformation of layered double hydroxides: an in situ TEM analysis. *Npj 2D Materials and Applications*, *2*(4). https://doi.org/10.1038/s41699-018-0048-4

Mahon, O. R., O'Hanlon, S., Cunningham, C. C., McCarthy, G. M., **Hobbs, C.,** Nicolosi, V., Kelly, D.J., Dunne, A. (2018). Orthopaedic implant materials drive M1 macrophage polarization in a spleen tyrosine kinase- and mitogen-activated protein kinase-dependent manner. Acta Biomaterialia, 65, 426–435. https://doi.org/10.1016/j.actbio.2017.10.041

Stauch, C., **Hobbs, C**., Shmeliov, A., Nicolosi, V., Ballweg, T., Luxenhofer, R., & Mandel, K. (2018). Colloidal Core–Satellite Supraparticles via Preprogramed Burst of Nanostructured Micro-Raspberry Particles. *Particle and Particle Systems Characterization*, *35*(7), 1–9. https://doi.org/10.1002/ppsc.201800096

Ryan, E. J., Ryan, A.J., Gonzalez-Vazquez, A., Philippart, A., Ciraldo, F.E., **Hobbs, C.,** Nicolosi, V., Boccaccini, A.R., Kearney, C.J., O'Brien, F.J. (2019). Collagen scaffolds functionalised with copper-eluting bioactive glass reduce infection and enhance osteogenesis and angiogenesis both in vitro and in vivo. *Biomaterials* **197,** 405–416.

Gonzalez-fernandez, T, et. al. 4D bioprinting using pore-forming bioinks to enable spatio-temporally defined gene delivery to stem cells (2018), submitted to Nature Biomedical Engineering.

Awards

Best Student Oral Presentation in the Physical Sciences, Microscopy Society of Ireland Annual Symposium, Dublin, 2016.

M&M Student Scholar Award, Microscopy and Microanalysis 2018, Baltimore, MD, USA, 2018.

New Researcher Award in Physical Sciences, 19th International Microscopy Congress, Sydney, Australia, 2018.

Abbreviations

- 2-D: Two-dimensional
- 3-D: Three-dimensional
- AES: Atomic emission spectroscopy
- CCD: Charge couple display
- EDX: Energy dispersive x-ray spectroscopy
- EELS: Electron energy loss spectroscopy
- EFTEM: Energy filtered transmission electron microscopy
- EM: Electron microscopy
- FEG: Field emission gun
- FTIR: Fourier Transform Infrared Spectroscopy
- GFP: Green Fluorescent Protein
- HIM: Helium Ion microscopy
- LDH: Layered double hydroxide
- MSC: Mesenchymal stem cell
- MMO: Mixed metal oxide
- pDNA: plasmid DNA
- SAED: Selected area electron diffraction
- SEM: Scanning electron microscopy
- STEM: Scanning transmission electron microscopy
- TEM: Transmission electron microscopy
- XRD: X-ray diffraction

Abstract

The overall aim of this PhD research is to understand the physical behaviours of layered double hydroxide (LDH) nanomaterials in applied environments. Two aspects of LDH-based applications were studied. Firstly, the thermal evolution of LDH nanomaterials were investigated using high-end (scanning) transmission electron microscopy ((S)TEM). The LDH nanomaterials underwent morphological, crystallographic and spectroscopic changes during thermal decomposition. The Ni-Fe LDHs were observed to evolve into an array of mixed metal oxides and spinel phases, shown by high resolution TEM (HRTEM), energy filtered TEM (EFTEM) and electron energy loss spectroscopy (EELS). In particular, in-situ TEM revealed the real-time processes of thermal decompositions where a nucleation and growth of an array of Nickel-based particles was observed. This NiO array was found to be embedded throughout a $NiFe_2O_4$ matrix. Similar behaviours were also seen ex-situ where STEM-EELS highlighted a segregation of Ni and Fe species upon ex-situ thermal decompositions of Ni-Fe LDH nanomaterials.

Secondly, Mg-Al LDH properties were examined as they interacted with DNA based biomolecules and transfected by biological cells. It was found that the Mg-Al LDHs were successfully up-taken by mesenchymal stem cells and A549 cells. After 72 hours, the particles were observed to reside in the cytoplasm regions. Electron diffraction related studies indicated that the LDH particles retained their crystallographic nature. This was corroborated by EFTEM and STEM-EELS studies of the oxygen K edge, whilst maintaining their structural integrity.

The associated findings have vital influences on the future LDH applications in the areas of catalysis, flame retardants and drug delivery. Notwithstanding these research areas, our results impact future applications as a whole, where the versatile LDH nanomaterials should be considered as prime candidates across nanotechnology.

Thesis Summary

This PhD thesis begins with the introduction to the world of nanotechnology and more precisely, two-dimensional (2-D) nanomaterials. We explore the areas of research where
2-D materials have been the subject of much scientific interest in recent times. We then focus our attention to layered double hydroxides (LDH). These versatile 2-D nanomaterials are shown to have several applications across nanotechnology such as pharmaceutics, energy storage, nanomedicine and adsorbents. In particular, we discuss in detail the recent progressions LDHs have had in catalysis and drug delivery. We address what is missing from the field from a characterization perspective. There is a clearly a need to fully understand our materials to determine structure-property relationships and to evaluate the roles of LDHs in their applications.

Perhaps one of the leading characterization tools in materials science, transmission electron microscopy was our choice to characterize such materials. The instrument and associated analytical techniques that can be performed in the microscope are discussed in Chapter 2. We explain how TEM can reveal both structural and chemical information at high spatial resolutions, right down to the atomic level.

The experimental results of this PhD work is presented in three experimental chapters. The first of which is entails a comprehensive TEM characterization of two types of LDHs, namely Mg-Al LDH and Ni-Fe LDH. We identify and compare the morphological and crystallographic features using TEM and electron diffraction. Moreover, the chemical information and electronic structure features of these materials are probed using energy dispersive x-ray spectroscopy and electron energy loss spectroscopy. The aging evolutions of both LDH compositions are also investigated by characterizing them at interval stages of the synthesis procedures. The high energy electron beam was observed to affect the observed LDH features. In light of this, we studied the influence electron beam exposures and imaging parameters have on the morphological (TEM), crystallographic (electron diffraction) and chemical structure

(EELS) of the Ni-Fe LDH material. These studies provide a platform to build on as we evaluate the LDH properties in applied environments in the following chapters.

Chapter 4 brings the LDHs to life at the nanoscale with in-situ TEM. These characterization methods elucidate the thermal decompositions of both Mg-Al LDH and Ni-Fe LDHs. We further show how certain structures nucleate and develop during these thermal decompositions by combining in-situ heating and energy filtered TEM methods. The thermally treated structures were then characterized themselves as an independent material. EFTEM and STEM-EELS highlight the distribution of the Ni and Fe localisations after thermal decomposition studies. High resolution TEM (HRTEM) was performed to identify the crystallographic features at high spatial resolution such as at interfacial regions. The thermal evolution in-situ study was also extended to EELS edge features. The Ni-Fe LDH was subjected to elevated temperatures and the evolution of the O K edge, Ni $L_{2,3}$ edge and Fe $L_{2,3}$ edge was investigated. Samples using ex-situ heat treatments were also characterized and compared to that of the in-situ experimentations.

We change our tune slightly as we turn to Chapter 5. In this chapter we exemplify the versatility of the LDH materials. The behaviour of Mg-Al LDHs as potential drug delivery vectors to biological cells are studied. Firstly, we investigate how Mg-Al LDHs interact with biomedical therapeutics. The nanoscale structural and chemical properties of the composites are assessed and provide important information in relation to their suitability as gene delivery vectors. Furthermore, the up-take processes and intracellular properties of the Mg-Al LDHs involved in mesenchymal stem cells and A549 lung adenocarcinoma epithelial cells are characterized using advanced TEM methods. In particular, an EFTEM and EELS study of the Oxygen K edge revealed information about the fate of the LDH particles in the A549 cells. In parallel to this, we conducted a time dependent study of the LDH exposures. Cell culture samples were fixed at various timepoints up to 72 hours and subsequently characterized using similar TEM approaches.

We conclude our experimental results and discuss impacts on the field in Chapter 6. This also includes a discussion on how the experimentations and results from this

thesis can be used as a springboard from which further strands of study could be taken. Preliminary results of in-situ liquid TEM characterizes the Ni-Fe LDHs in aqueous environments. In parallel to Chapter 3, the effect of the electron beam on the LDH structures in water is observed.

In addition, the interaction of LDHs with other structures is briefly studied in both a materials science and biological science related experiments. In the case of the former, we present the formation of LDHs with other layered materials to form nanocomposites. This area has been a hot topic of research in very recent times. We demonstrate how Ni-Fe LDHs can be combined with layered MXenes. The thermal evolution of this composite is preliminarily investigated using our previous in-situ heating protocols. A particular attention is paid to the effect MXenes have, if any, on the Ni-Fe LDHs decompositions, previously studied in Chapter 4.

A further nanocomposite with biomedical applications is the construction of collagen-LDH scaffolds. These could provide novel methods of effective gene/drug delivery as well as promoting favourable cell growth for tissue engineering applications. We study the extent of interaction of the Mg-Al LDHs with individual collagen fibrils, highlighted through the application of TEM spectroscopic methods.

Table of Contents

Chapter 1: Introduction

Looking back at humanity's scientific thoughts over the last century, one clear concept has been on the minds of many scientists, 'small things are perplexing'. Indeed, we do not need to travel far back in history to see this obsession:

A lecture series entitled 'What is Life?' was given by Erwin Schrodinger at our very own Trinity College Dublin in 1944. As part of his introductory lecture, he asked 'Why are atoms so small?', albeit a description of his own naivety to understanding living organisms. Nevertheless, a true interest at such scales was at heart. Moving forward to 1959, Richard Feynman delivered a talk entitled 'There's plenty of room at the Bottom' at the American Physical Society at the California Institute of Technology. He stated, 'enormous amounts of information can be carried in an extremely small space'. The outlook of making things smaller is also found throughout the industry world. Moore's law states that the number of transistors doubles every year, halving the costs. This empirical law describes the evolution of the ever-famous transistor reaching small scales, an objective of all modern-day computers and smart phones. At the turn of the new millennium, rock band
Blink-182 released their hit single 'All the Small Things', which peaked at number two in the UK singles charts. Granted, the influences of punk rock may not extend to science, but these scientific envisages of the nanoscale is shared amongst many researchers today. Several technologies have incorporated materials synthesized at these scales, so-called nanomaterials, have been incorporated into a wide range of technologies today, such as batteries, biomedical devices and even golf balls.[1–3] These technologies are made possible by the processing and characterization of materials. Moreover, the associated methods allow us to expand our knowledge, develop new technologies and are truly owed great credit for the world we live in today. One fascinating and applicable aspect of the materials science world are two-dimensional (2-D) materials.

1.1 2-D Nanomaterials: A Journey to Flatland

Two-dimensional nanomaterials are materials with very high aspect ratios in two dimensions with respect to the third. This is caused by the strong in-plane bonds but have weak out of plane bonds i.e. Van der Waals forces, giving them a 'flat' nature. Examples of these 2-D nanomaterials include graphene, boron nitrides, transition metal dichalcogenides, layered oxides and clays.[4] They have been in the spotlight of nanomaterials research due to their excessive interesting and useful properties such as accessible surface areas, favourable interactions with other materials.[4] These properties have been utilised in a variety of applications such as energy storage, nanomedicine and catalysis.[5,6]

2-D materials are prepared in a variety of different ways. Firstly, 2-D nanosheets have been found to be directly synthesized using chemical methods in a 'bottom-up' approach style. This is done by techniques such as co-precipitation to generate high-quality dispersions of thin nanosheets. This will be the basis of the materials synthesized throughout this thesis and has been thoroughly investigated by previous PhD research of our group, conducted by Dr. Sonia Jaskaniec.

It is more often the case that 2-D materials are made by a 'top-down' style approach by mechanical exfoliation or liquid phase exfoliation. The former involves 'ripping' the layers from precursor bulk materials.[7] This is found to produce high quality monolayer and multilayer samples but at the sacrifice of low yields. Thus, it is obvious why this is not an ideal case for high volume demands, most typically required for industrial applications. Pioneered work by our own group and fellow colleagues in the CRANN (TCD) developed methods and samples. This resulted in large scale productions whilst maintaining high quality stable 2-D material dispersions.[8,9] Originally starting with graphite crystals, this liquid phase exfoliation method involved placing the material in a suitable solvent and providing energy in the form of ultrasound. This energy was sufficient to break the Van der Waals bonds between the layers resulting in stable colloidal dispersions of graphene.[8,10]

A breakthrough study led by our own Prof. Nicolosi discovered that this liquid phase exfoliation method could also be extended to a large number of other layered crystals.

This flourished the field of 2-D nanomaterials, with the generation of a wide variety of layered materials of interesting physical and chemical properties. This novel idea is today the core concept of our group's research. The effective processing, characterization and implementation of these layered materials has led to a number of insightful and impactful scientific publications.[11–15]

1.2 Electron microscopy: Seeing the Nanoscale

Certainly, one of the primary objectives of any scientific method is to critically assess the physical and chemical properties of our materials. Many of these procedures rely on our characterizations to effectively 'observe' the sample to assess such properties. For example, light microscopy techniques are capable of studying cellular behaviours, high-speed cameras are used to observe animal behaviours and even high-powered telescopes provide ways of analysing the motion of galaxies.[16–18] Indeed at any length scale, a major concern is what resolution can we see with our lens system. This is no different at the nanoscale. Optical microscopy techniques simply do not suffice when we wish to characterize materials at smaller length scales. Furthermore, the design, functionality and processing of materials now requires information at high spatial resolutions to determine correct structure-property relationships as well as an optimization of related processes. This resolution gap can be overcome using electrons. A mathematical description of these benefits is described in the next subsection. The concepts and equations of the next section are based from the textbook, 'Transmission Electron Microscopy: A Textbook for Materials Science' by D.B Williams and C.B Carter.[19]

1.2.1 Electrons: Our eyepiece to the nanoscale

The use of visible light microscopy, i.e. photons, presents challenges when our desired material feature we wish to characterize are beyond the diffraction limit. This is due to the wavelength of light and the attainable resolution δ is governed by the Rayleigh criterion,

$$\delta = \frac{0.61\lambda}{\mu \sin(\beta)} \tag{1}$$

Where λ is the wavelength and $\mu \sin(\beta)$ is known as the numerical aperture of the lens and it close to unity for a visible light microscope. So in the in case of visible light, i.e. photons ($\lambda \approx 550$ nm for green light), the resolution is evaluated as $\delta \approx 300$ nm.

To 'see' beyond this limit, we need to make use of particles with a significantly smaller wavelength, i.e. electrons. Electron microscopy is a technique using high-energy electrons to characterise materials. The DeBroglie equation relates the wavelength of the electron to its momentum, and hence its mass m_0,

$$\lambda = \frac{h}{p} = \frac{h}{m_0 v} \tag{2}$$

$$eV = \frac{m_0 v^2}{2} \tag{3}$$

By comparing to the energy relationship of the electron, the wavelength λ of the electron can be related to its accelerating voltage V including a relativistic correction by the equation,

$$\lambda = \frac{\mathrm{h}}{\sqrt{2\mathrm{m}_0 \mathrm{eV}\left(1 + \frac{\mathrm{eV}}{2\mathrm{m}_0 \mathrm{c}^2}\right)}} \tag{4}$$

In the transmission electron microscope (an instrument which we will discuss in great detail at a later stage), the ideal convergence angle β is determined by aperture radius r and focal length L as $\beta = \frac{r}{L}$. In a typical FEI Titan with an aperture diameter of 50 μm and a focal length of 2 mm, β is evaluated as 12.5 mrad. This can be extended to incorporation of spherical aberrations Cs (another topic which will be addressed in a

later section) where the optimum convergence angle can be evaluated as $\beta = (\frac{4\lambda}{C_S})^{0.25} \approx 10$ mrad. We note that for an electron microscope, $\mu \approx 1$ for a vacuum and $\sin(\beta) \approx \beta$ using small angles approximations. The wavelength of the electron can be determined by the acceleration voltage of our electron source. When a routine voltage of 300 kV is applied, the electron has a wavelength value of approximately 2pm. This results in a diffraction limit δ of 0.1 nm.

As the electron interacts with matter, it is subjected to scattering events by the nucleus or other electrons of the atom. This is a very important property for us to 'see' the nanoscale. For simplicity, we refine our discussion to the case where the electron interacts with the nucleus of the atom. A visual representation is shown in Figure 1.1.

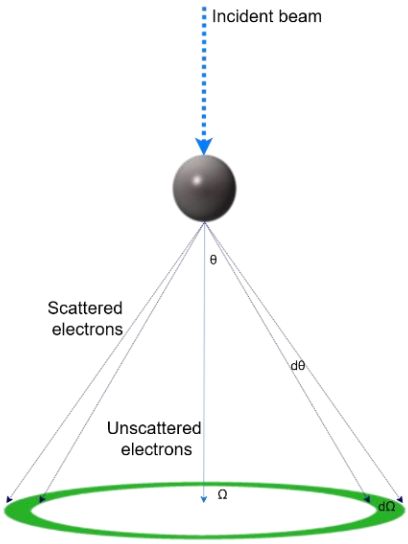

Figure 1.1 Electron scattering from single atom site. The electron is scattered through angle θ into solid angle Ω. Figure is adapted from Williams and Carter.[19]

The differential cross section describes the angular distribution of scattering from an atom. This is mathematically defined as,

$$\frac{d\sigma}{d\Omega} = \frac{1}{2\pi\sin(\theta)} \cdot \frac{d\sigma}{d\theta} \tag{5}$$

The case of high angle electron-nucleus scattering is described by the total Rutherford cross section as,

$$\sigma_R(\theta) = \frac{e^4 Z^2}{16(4\pi\varepsilon_0 E_0)^2} \cdot \frac{\mathrm{d}\Omega}{\sin^4\left(\frac{\theta}{2}\right)} \tag{6}$$

Where Z is the atomic number of the atomic scattering site, E_0 is the incident energy of the electrons and θ is the scattering angle. This cross section gives us an idea of how the electron will scatter from an atom in a material. We can increase the cross section and hence likelihood of scattering by looking at heavier elements or using an electron beam of lower energy. For example, when imaging 'heavier' high Z number atoms, say Carbon vs. Gold, the cross section increases by a factor on the order of 100. Similarly, using electrons of lower energy also has the same effect of increasing the cross section.

A complimentary approach, incorporating the electrons wave nature, can also be used to depict how scattering from an atom occurs. We introduce the atomic-scattering factor $f(\theta)$, which is a measure of the amplitude of an electron wave as it is scattered from an atom,

$$|f(\theta)|^2 = \frac{\mathrm{d}\sigma(\theta)}{\mathrm{d}\Omega} \tag{7}$$

$$f(\theta) = \frac{\left(1 + \frac{E_0}{m_0 c^2}\right)}{8\pi^2 a_0} \cdot \left(\frac{\lambda}{\sin\left(\frac{\theta}{2}\right)}\right)^2 (Z - f_X) \tag{8}$$

where f_X is the atomic scattering factor for X-rays, a_0 is the Bohr radius of the scattering atom and the other terms are defined as before.

We can extend the elastic scattering from a single atomic site to a more realistic situation. This atomic structure factor F is a measure of the amplitude scattered from a

unit cell in a crystal. It is related to the atomic scattering amplitude by the relationship.[19]

$$F(\theta) = \sum_{i}^{\infty} f_i 2e^{2\pi i(hx_i+ky_i+lz_i)} \tag{9}$$

This amplitude of scattering is hence dependent of the type of atom, positions of the atomic sites (x,y,z) and atomic planes (hkl).

Beyond the spatial resolutions provided by electrons, there is a generation of further distinguishable signals upon interaction with matter. Figure 1.2 displays the available signals of this interaction. In addition to using diffraction and scattered signals to create contrast, TEM methods capitalise on X-rays and energy loss electrons to reveal rich chemical information about the specimen. The collection and interpretation of associated data will be discussed in the subsequent chapter.

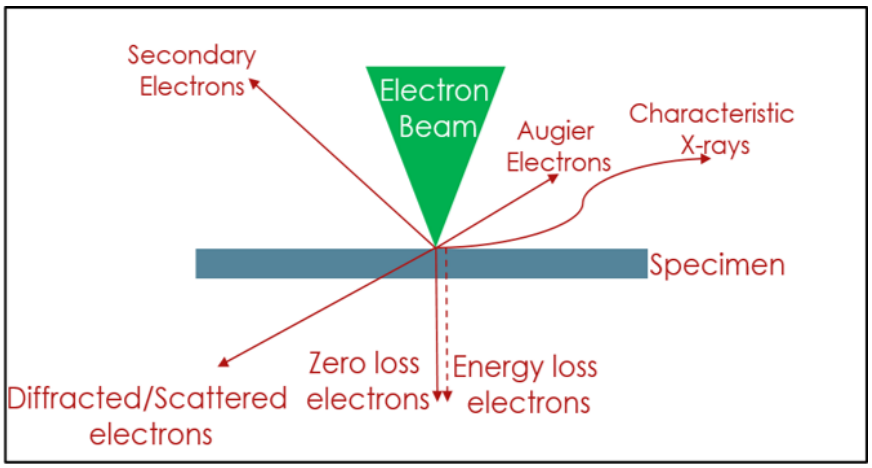

Figure 1.2: Schematic representation of the available signals upon electron-matter interaction. This figure was adapted from Williams & Carter.[19]

It is noted that even though there are many interesting signals from such interactions, there can also be undesirable effects induced by the incident electrons in the form of specimen modifications and even damages. The next section discusses the potential detrimental effects caused by the beam.

1.2.2 Electron beam damage

As the electron beam interacts with a specimen, detrimental effects can be introduced. This can result in structural and chemical changes to the sample.[1] The damage induced by the beam can be temporary or permanent to the specimen, but in most cases is unwanted.[20] In relation to biological samples, this beam-induced damage can cause unwanted modifications of the specimen structure, morphology and composition.

Radiolysis: Chemical bonds in samples such as polymers can be broken due to the inelastic scattering. This electron-electron interaction can cause polymer chains to break as well as forming free radicals, hence a change in structure may be induced.[1] In particular, it is the covalent and Van Der Waals bonds are strongly affected by radiolytic damage. The inelastic scattering induces an excitation and a resulting de-excitation of electrons within these molecules, causing a potential change in electronic states. This is viewed via the changing of molecular and chemical arrangements, and a loss of crystallinity in certain cases.[20] In addition, this electronic structure change can result in mass loss due to bond breakages and also can have an effect on spectroscopic techniques such as electron energy loss spectroscopy. Polymer specimens can also lose crystalline features as a result of this radiation damage.[1]

Knock-On/Atomic Displacement: As the electron beam penetrates close to the nucleus, energy is transferred from the incident electrons to the atomic nuclei (mass number A). This causes a dislodgment of the atoms and results in lattice defects.[1] The energy transferred (E) is related to the incident electron energy (E_0), deflection angle (θ) due to scattering and mass number A such that,[20]

$$E = E_{max}\sin^2\left(\frac{\theta}{2}\right) \tag{10}$$

$$E_{max} = \frac{E_0}{465.7A}\left(1.02 + \frac{E_0}{10^6}\right) \tag{11}$$

While the energy transfer for small θ angles is negligible, it is not the case for backscattering ($\theta > 90°$) or high values of incident energy E_0.[20] If the transferred energy exceeds that of the specimen's displacement energy E_d, it can displace the atomic nuclei. As a result, properties of the material are prone to damage such as the displacement of nuclei which leads to a degradation of crystalline structures.[20] For example, Aluminium has an E_d value of 17 eV, with a corresponding incident energy E_0 of 180 keV.[21] In particular, modern day TEMs are capable of attaining such E_0 values, and hence 'knock-on' damage is a concern for specimens, particularly those with low atomic numbers. This damage mechanism can be reduced by lowering the incident energy E_0 i.e. lowering the accelerating voltage of the TEM.

A further concern of high-angle electron scattering is sputtering. This occurs when the electron beam interacts with an atom at the surface. These surface atoms are free to exit the specimen due to the lack of interstitial sites available within the material.[20] The sublimation energy, E_s, is the minimum energy required to emit the surface atom from the material. If the incident energy E_0 is greater than that of E_s, electron sputtering will occur. Egerton *et. al* presents the sublimation energy's dependence on atomic number Z. It is evident that the lower-Z atoms sputter at an energy less than 200 keV. This study analyses many low-Z atomic materials and as such electron sputtering must be considered as a damaging mechanism during TEM studies.[20]

Electrostatic Charging: Charging of an insulating specimen is due to elastic (backscattering coefficient) and inelastic (secondary electrons) scattering. This charging occurs when the rate of incoming electrons onto the TEM specimen exceeds the rate of outgoing electrons. The current balance is presented by Egerton *et. al* as,

$$I - I_t + \frac{V_S}{R_S} = I\eta(t) + I\delta(V_S) \tag{12}$$

Where I is the incident current, I_t is the transmitted electron current, V_S is the developed surface potential due to the beam, R_S represents the effective resistance between irradiated area and surrounding regions, η(t) is the backscattering coefficient

and $\delta(V_S)$ is an effective secondary electron yield at $+V_S$..[20] As I approaches I_t, as is the case with the absorbed electrons in a TEM thin specimen, V_S becomes positive and thus positive charging occurs. Under these conditions, the charge balance is achieved by increasing V_S.[20] This can lead to an electric field that can cause electrical breakdown and migration of ions. In addition, a mechanical force capable of tearing films within the TEM sample is also possible due to charging.[20]

Heating: Phonons (collective oscillations of the atoms in the sample) heat the specimen resulting in damage to biological tissues and polymers.[1] Heating of the specimen due to the electron beam interaction is pronounced at high current densities, however low current densities may also induce energy transfers and appreciable heating effects to samples such as organic materials and low-Z atoms, which is the case presented by the current study. Under standard TEM conditions, this heating is negligible for good conductors i.e. a high thermal conductivity.[1] Conversely, insulators can be subject to substantial heating effects due to their low thermal conductivity.[1] For example, when the electron probe is decreased in diameter from 1 μm to 1 nm and the current density increases by a factor of 10^6, the change in temperature ΔT is only approximately 1 K.[20]

Reducing beam damage: Ionization and heating damage can be reduced by introducing a cooling mechanism to the sample,[35] for example, in-situ cooling of the TEM specimen to liquid nitrogen temperatures. By lowering the temperature, the material sensitivity and atomic mobility is reduced, rather than an alteration to the inelastic cross section. Coating of a TEM sample in a carbon/metal reduces the mass loss damage. This preventative mechanism reduces temperature variations and charging effects of the specimen[30]. Moreover, radiation beam damage can be attenuated by using a low electron dose. This reduces the number of electron-electron interactions. However, this technique has its drawbacks as it often results in low signal to noise ratios on the CCD cameras in TEM and annular detectors in STEM, which can be corrected for through the use of signal averaging.[1] For example, bases of nucleic acids degrade completely at an electron dosage with an order of magnitude of 10^{-2} C cm^{-2} at an incident beam energy of less than 100 keV.[36]

1.3 The Cell: Uncharted territory for Electron microscopy

Electron microscopy unites the worlds of biology and the nanoscale. The resolutions provided by EM methods allow for the observation and characterization of cellular ultrastructure features.[22,23] Although the focus of this thesis is in electron microscopy, we briefly introduce the ultrastructural features and uptake pathways of biological cells. This will greatly assist the reader with essential background information when interpreting future aspects of this thesis.

1.3.1 Eukaryotic cellular ultrastructure

Much like atoms make-up materials, cells are the basic building blocks of all living organisms. They too themselves have their own intricate nature. Eukaryotic cells are composed of organelles i.e. small cellular structures of specific function in cells. We list and illustrate the main organelles of these cells. Further details of these structures can be found in the textbook, 'Essential Cell Biology: Fourth Edition' by Alberts *et. al*.[24]
A schematic of cellular ultrastructures is presented below, courtesy of Encyclopaedia Britannica 2008 ©.

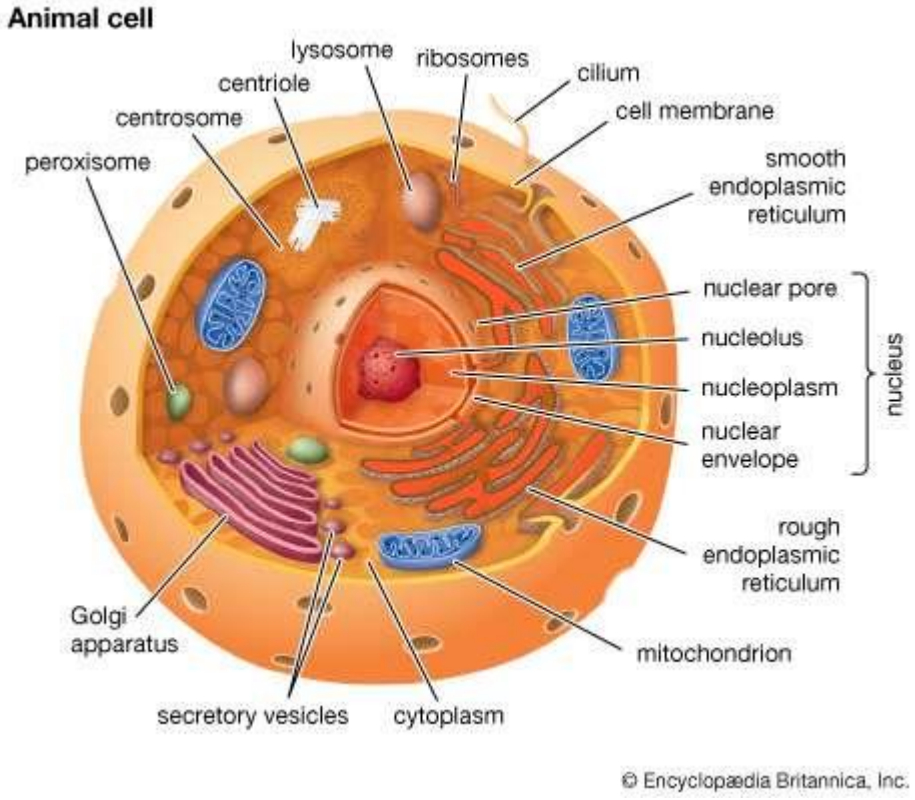

Figure 1.3 Schematic of eukaryotic cell ultrastructure.
© Encyclopaedia Britannica Inc.

Firstly, the *nucleus* is arguably the most vital organelle of eukaryotic cells. A nuclear envelope, composed of two concentric membranes, encapsulates the genetic information encoded giant chain molecules, known to us as DNA.

The *cell cytoplasm* is the liquid enclosed by the cell membrane, containing water, salts and proteins.

In amongst the cytoplasmic regions lies *mitochondria*. These organelles are responsible for making chemical energy in the cell. This is done by consuming oxygen and releasing carbon dioxide i.e. cellular respirators.

The *endoplasmic reticulum* makes cell membrane-components and materials that are to be exited from the cell. The *golgi apparatus* acts as a storage mechanism for materials that will undergo cell excretion or transport to another cell region.

Lysosomes are small irregular organelles that digest intracellular materials to release nutrients or breakdown unwanted materials.

Within the cell itself, there are many features of the cell that are on the micro and nano scales and hence not observable by optical light.

The *plasma membrane* creates a barrier between the cytosol organelles from the outside media environments. The structure of the plasma membrane consists of protein-containing lipid bi-layer of about 5nm in thickness. Although it has a primary role of protecting and restricting escape of the organelles, it can also affect the cell growth, movement and morphology. Moreover, it also plays a key role in the importation and exportation of molecules to and from the cell. The flexible lipid bi-layer generates small vesicles that transport cargoes around the cell cytoplasm. The processes occur in a variety of pathways and are briefly described below. This information will be important for future interpretations of results which will be discussed in following chapters.

1.3.2 Mechanisms of endocytosis

Clathrin-mediated endocytosis dominates most of the molecular uptake of eukaryotic cells. This uptake process is initiated from the clustering of endocytic coated clathrin proteins inside the cell cytoplasm. This aggregation forms to the plasma membrane region forming 'clathrin coated pits'. Scission then occurs in the protein-rich regions and a clathrin coated membrane is created by the assistance of actin proteins. Finally, the vesicle undergoes an uncoating of the clathrin and sent further into the cell.[25]

Caveolin mediated endocytosis is the formation of cave-like invaginations in the plasma membrane which themselves become internalized by the cell.

Larger particles are typically up-taken by *phagocytosis*. This involves the progressive formation of invaginations surrounding the material and then internalized within the cell.[26]

Macropinocytosis is a clathrin independent endocytic pathway. It entails actin mediated ruffling of the plasma membrane,[27] creating macropinocytic vesicles with no coating and are considerably larger (>200nm) than clathrin-mediated vesicles.

It is also noted that passive uptake processes can occur across the plasma membrane. Molecules may transmit through the lipid by-layer into the cell due to concentration balances i.e. osmosis/diffusion.

1.3.3 Cell types

The work of this PhD thesis involves two types of cells.

Mesenchymal stem cells (MSCs): MSCs are found in adult tissues including murine and humans. These multipotent cells have the ability to differentiate into a range of cell lines such as osteoblasts, chondrocytes and adipocytes. In addition, these cells are self-renewable, easily accessible and can be culturally expanded in vitro.[28,29] Thus, this makes them primary candidates for experiments in areas such as regenerative medicine and tissue engineering. Practically speaking, there has been many successful works from our collaborators in the Tissue Engineering Research Group (RCSI, Dublin) involving mesenchymal stem cells.[30–32] The familiarity with these cells lines was also a reason why we elected to use them for our LDH based experiments of this thesis.

A549 cells: Scientists are still currently searching safe and efficient targeted treatments of cancer cells in the body. One example are A549 cells, which are human lung adenocarcinoma cells. They are of obvious interest in the area of therapeutic studies as lung cancer remains one of the most common types worldwide.[33] The A549 cell line is often used in targeted drug delivery testing as it is based on pulmonary deliveries, with instantaneous absorption into the blood stream.[34] The A549 cell line is also well studied and characterized in a variety of targeted therapy applications, making it an ideal cell line to study from our perspective.[35–38] Again from a practical outlook, our collaborators in the Trinity Translational Medical Institute (TCD, Dublin) have had extensive experience with A549 epithelial cells involving nanoparticle uptake.[39,40] This made for a natural progression to use them for our own LDH-based exposures in cultured in vitro experiments.

1.4 Layered Double Hydroxides

Reverting our attention back to the world of material science and 2-D nanomaterials, we now discuss, in detail, the flagship material studied in this thesis. Layered double hydroxides (LDH) are a fascinating material of the 2-D nanomaterial family. The literature has shown that these LDH materials are relatively new to the field of mineralogy and materials science, having only been first described by Allman and Taylor in separate studies in 1968 and 1969 respectively.[41,42] Having said that, the material ancestors of LDHs have been used for centuries. Talc, a similar material in the form of white magnesium powders was used for medical purposed in the 19th century, having beneficial aspects in cosmetics, pharmaceuticals and plastics in the modern era. Similarly, $Mg(OH)_2$ i.e. brucite, was a mineral first described by mineralogist Archibauld Bruce (1777-1818, USA).[43] LDHs, also known as anionic clays or hydrotalcite-like materials, attain a lamellar structure in nature, similar to that of other 2-D materials such as boron nitride and graphite.

1.4.1 General structure of LDHs

The general formula of the LDH structure is given by

$$[M_{1-x}{}^{2+}M^{3+}{}_x(OH)_2]^{x+}[A^{n-}]_{x/n} \cdot \ mH_2O \qquad (13)$$

Where M^{2+}, M^{3+} represent the divalent/trivalent cations in the layers, A^{n-} depicts the charge compensating anion and x, where an LDH crystal phase is obtained when $0.2 \leq x \leq 0.33$. The layers themselves are similar to that of brucite, $Mg(OH)_2$.[44] In the case of the LDH structure the is a substitution of trivalent M^{3+} metals, gives rise to a positive surface charge in the cationic layers. Each metal site is coordinated in the centre of edge-sharing octahedrals with OH^- groups at their vertices forming infinite sheets. The O-H bonding lies along the three fold axis (i.e. the basal plane) and are directed towards the vacant tetrahedral sites in adjacent layers.[45] These ions lie perpendicularly to the plane of the layers and their stacking gives a three-dimensional

structure. Charge compensation is achieved in between the metallic layers by intercalation of negatively charged anions. In general, the positive charge is balanced by the presence of water and anionic species in the interlayers. Hence, the layers are held together by electrostatic interactions and hydrogen bonding with the intercalated species giving the LDHs their overall 'anionic clay' structure. The LDH material typically adopts a 3R rhombohedral or 2H hexagonal symmetry.[46] Figure 1.4 displays a schematic representation of the LDH structure with viewing directions normal to the basal plane (001).

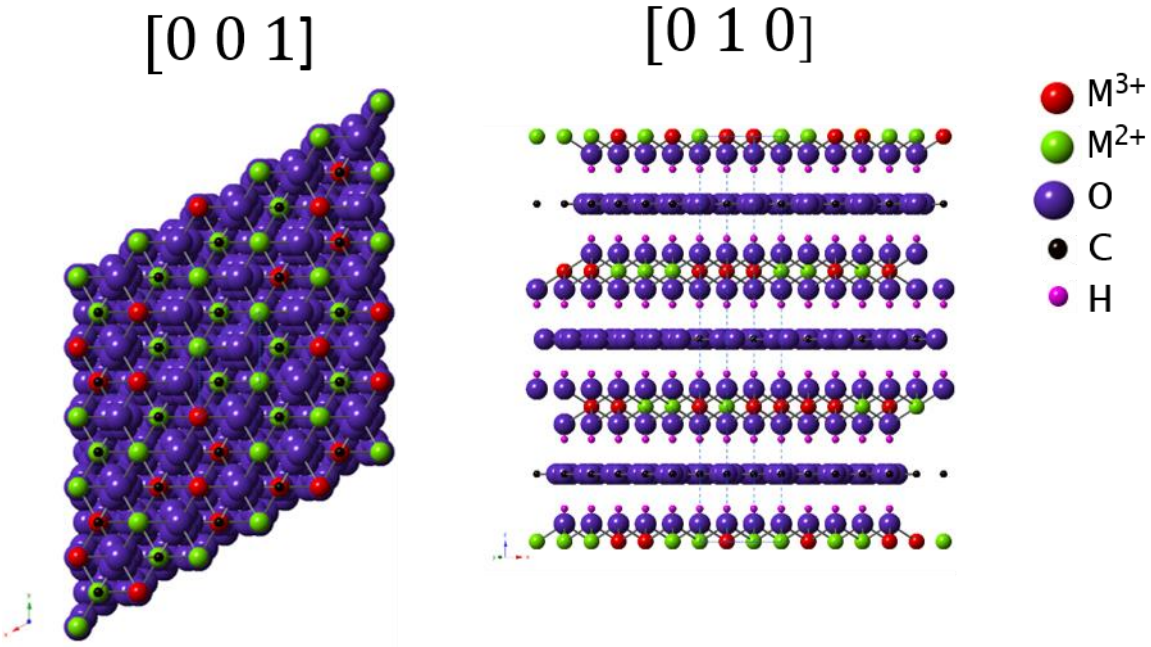

Figure 1.4 Crystal schematic of typical LDH structure viewed along the [001] and [010] directions. Schematics were visualised using CrystalMaker™. Cationic layers composed of M2+ and M3+ metals are octahedrally surrounded by OH groups. The layers are charge compensated by anionic interlayer moieties such as carbonate (CO_2^{3-}), nitride (NO^{3-}) and water (H_2O).

There is a wide variety of possible metal combinations within the layers such as Co, Cu, Mg, Mn, Ni, and Zn for the M^{2+} and similarly Al, Fe and Ga as examples of M^{3+} sites.[47] This tuning of the material composition also extends to M^{2+}/M^{3+} charge ratios of the cationic sites giving many possible compositions and stoichiometry. The range of LDH structures is also extended by the nature of the anions in the LDH interlayers. In fact, there is are large numbers of compounds that can occupy these regions. Along

with water molecules, interlayer inorganic anions such as Br^-, Cl^-. NO^{3-}. SO_4^{2-} and CO_3^{2-} can be occupied within the interlayers. Furthermore, a fascinating feature of LDH materials is their ability to 'anion exchange' the interlayer guests, expanding the range of anionic compound that can be intercalated. In this process, LDHs can substitute their interlayer species for alternative anionic compounds.[48] The literature shows a vast number of studies investigating the intercalation and subsequent release of both simple and complex anions. For example, organic chains including carboxylates and biomolecules such as amino acids have been seen to be effectively intercalated.[49,50] Moreover, there is a wide range of drugs that have been shown to be successfully intercalated, as reviewed by Rives *et. al*.[46] Previous findings have also highlighted the intercalation of coordination compounds and polyoxometalates.[51]

The interaction occurs as a weak bond between the host layers and guest species. This allows for the varied orientation of the interlayer molecules with their amount being dependent on the positive surface charge availabilities in the host layers.[52] Another interesting property in this context is the ability of the LDHs to alter their basal spacing to accommodate a range of interlayer species for exfoliation[53] or drug intercalation.[54] This expansion of basal spacing were verified using x-ray diffraction and high resolution TEM approaches. More so when it comes to applications, LDH materials span a wide scope of applications across nanotechnology. This is largely due to the tunability of the potential LDH structures.

1.4.2 Synthesis procedures of LDHs

A variety of different routes have been developed to prepare materials of this type. The main synthesis procedures are briefly described as follows:

Co-precipitation methods: This is the slow addition of a metal containing solution to another solution engulfing the anionic species. This is accompanied by a slow increment in pH by the addition of a base or urea hydrolysis which leads to LDH precipitation.[46] Controlled synthesis parameters permits the intercalation of specific anions in the interlayer. This is achieved by as well as conducting the synthesis is carbon-free environments to prevent carbonate contamination in the host galleries.[47]

Reconstruction: Another unique property is the 'memory-effect' of LDHs. After calcination procedures, the dehydrated and mixed oxide phases of LDHs can reform their original structures upon contact with water or suitable anionic species.[55] This is often exploited to create LDH based structures.

Anion Exchange: As previously mentioned, the ability of anion exchange can be utilised as a synthesis method to create. In this process, precipitated LDHs are mixed in solution with an excess of the intended anion to be intercalated.[46,56] An initial anionic species is that of nitride as it is easiest to remove using these methods.

1.4.3 Applications of LDHs

LDHs can be considered in a class of their own relative to other 2-D nanomaterials. This is credited to the large variety of advantageous properties of LDH nanomaterials, leading to significant interest in nanotechnology. Some of these properties include: low cost of production, simplistic fabrication methods, tunable characteristics, large number of accessible bonding sites, positively charged layers, anion exchange abilities and biocompatibility.[57] The versatility of the LDH nanomaterials is shown through many different applications of LDH-based materials in research sectors such as adsorbents,[58] energy storage,[59] flame retardants,[60,61] magnetics,[62] medicine, polymer composites,[63] sensors,[64] and transistors.[65]

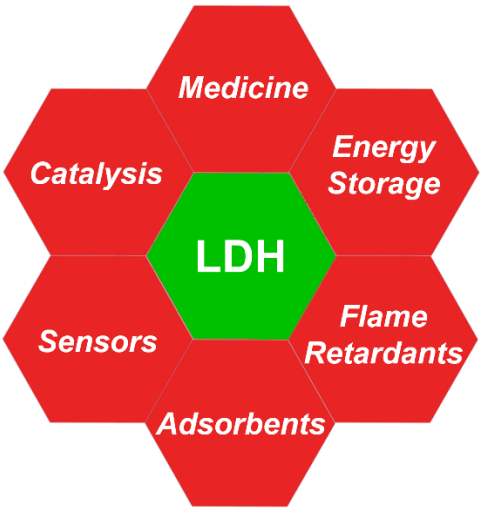

Figure 1.5 Various applications of LDHs.

Without doubt, the properties have led to LDHs establishing themselves as powerhouses in the area of 2-D materials and nanotechnology. In context of this thesis work, we will divulge our interest in two fields in which LDHs are applied: catalysis and gene/drug delivery.

1.4.4 LDHs in catalysis

Generally speaking, catalysis is heavily involved across a large proportion of the manufacturing and scientific industry. The attention it has received is truly deserved and is undoubtedly important from an environmental, economic and social perspective.[66–68] Particular topical energy and chemical industries rely on the design and production of effective heterogeneous catalysts. The activity, selectivity and ultimate performance of such catalysts is due to specific properties of the LDH structures. Firstly, the intrinsic 2-D nature of the nanosheets makes for a large number of highly accessible basic sites used in solid based catalysts. This is accompanied with an even distribution of cations within the layers which results in better catalytic performance. Moreover, the modulation of the size, composition and morphology of the LDHs make them attractive candidates for catalyst based studies. The flexibility of the synthesis can also lead to high catalytic activity, selectivity and stabililty.[69–71] These unique LDH properties have resulted in a wide variety of applications within catalysis itself such as electrocatalysis,[72] photocatalysis,[73] and nanocomposite catalysis.[70] Additionally, there are alternative treatments that have been used to enhance the LDH catalytic performance:

Exfoliation has proven to increase the number of reactive catalytic sites, enhancing electrocatalytic performance. Wang *et. al* used a nitrogen and argon plasmas to exfoliate Co-Fe LDHs. They found that these exfoliation processes generated high surface areas, surplus edge and corner sites which contributed to excellent overpotentials.[74,75] Similarly, Song *et. al* exfoliated similar Ni-Co LDH nanomaterials exhibiting favourable OER performances.[76]

Novel approaches have devised LDH compositions that contribute to the field of electrocatalysis. Ni-V LDHs have been reported to show high catalytic activity for water oxidation compared to the benchmark Ni-Fe LDH composition.[77] Recently, the

development of ternary metallic LDHs have exhibited by substitution of a third metal cation into the metallic layers has led to enhanced photocatalytic activities.[78–82]

The catalytic behaviour of LDHs has also been enhanced by their suitable interaction with other nanostructures such as carbon nanotubes, [83] Yttrium particles,[84] graphene,[85] palladium[86] and quantum dots.[87–89] The construction of the LDHs to form nanocomposites for enhanced catalytic activities further extends to the favourable interaction with substrates such as Nickel foams and carbon supports.[90,91]

The thermal decomposition of LDHs results in mixed metal oxide (MMO) fabrications for electrocatalytic applications. The resulting generation of MMO phases has provided further routes of enhancing catalytic behaviour. The thermal treatment of the LDH precursors results in homogenous stable dispersions of MMOs. These hold similar attributes for catalytic studies such as basic site availability of crystal facets, good thermal stability and synergistic interactions.[69,70] Strikingly, the calcination of LDH materials has also been a central interest in the catalytic field in the recent literature. Puscasu *et. al* utilised zinc based LDHs to generate Zn-based oxides which exhibited greater phenol degradations in photocatalysis.[92] Yuan *et. al* reported the use of similar Zn-Al LDHs to fabricate mixed metal oxides for Cr(VI) reduction.[93] In addition, Tang *et. al* synthesized Ni-Fe alloys from Ni-Fe LDH catalysts for CO methanation.[94]

A fall-back of many of these catalysis studies is the lack of high-end characterization of the associated LDH materials. Much of this literature utilises bulk techniques such as UV-Vis spectroscopy, x-ray photoelectron spectroscopy (XPS) and x-ray diffraction (XRD) as characterization methods. Electron microscopy has been applied in some cases but is restricted to basic imaging whilst related crystallographic and spectroscopic studies are limited. The single particle chemical composition is overlooked. These studies would be improved by incorporating TEM spectroscopic characterizations. For example, the study of the distribution of metals such as vanadium or tertiary substitutions like Ce, Co and Cu would be of interest from a materials science point of view.

Electron microscopy methodologies can be important to determine correct structure-property relationships of LDHs in the fields of catalysis. The high spatial resolutions will help to understand catalytic mechanisms such as the behaviour of catalytic sites, the synergetic relationships and topotactic transformations as a result of catalytic activity. As well as this, EM could impact future designs and optimizations of catalytic materials with an outlook of a greener more efficient world.

1.4.5 LDH as a gene/drug delivery vector

Without question, all aspects of healthcare are of central interest in modern society. The effective treatment of diseases and infections as well as the development of diagnostics are continuous areas of concern worldwide today. Interestingly, the roles and responsibilities of materials science in this world has intensified over the last few years from scientific and medical interests. Research today is making great strides in amalgamating the worlds of materials science, nanoscience and biology. This is owed to the ground-breaking developments in techniques and technologies from all aspects of these fields. Perhaps one of the most influential progressions that was recognised was the technique of cryogenic transmission electron microscopy with the awarding of the Nobel Prize for Chemistry in 2017, 'for developing cryo-electron microscopy for the high-resolution structure determination of biomolecules in solution'. On top of this, there are also advancements that have contributed to the growth of this body of research. One interesting spoke is the application of nanoparticles to biological cells involved in tissue engineering, cancer therapy and antimicrobial treatments. Recent studies have utilised a vast range of nanoparticles such as nanotubes,[95] graphene,[96] iron oxide nanoparticles,[97] quantum dots and minerals across a diverse range of intended purposes in biological applications.[98] The fields of nanobiotechnology and nanomedicine are considered as young flourishing research fields, with the potential to produce the next generation of medical solutions.

The effective delivery of genes, drugs and other therapeutics to biological cells is of central importance in the fields of regenerative medicine and tissue engineering. Recent advances in non-viral drug delivery revolve around the interaction of nanomaterials and biomaterials, presenting an increased efficiency in the successful

delivery of the therapeutic. In addition, the use of nanoparticles as delivery vectors allow them to be imposed as targeted drug delivery vehicles in relation to diagnostic and therapeutic applications.

These layered structures provide promising properties in relation to non-viral drug delivery. LDH materials are biocompatible and as such are suitable to be used in cellular environments without a risk of cytotoxic effects. Furthermore, the large accessible positively charged surface areas is a striking feature in relation to cellular transfection. This is favourable in terms of drug delivery as the LDHs are attracted to the negatively charged cell membranes. But perhaps one of the main reasons they have attracted such interest in medical applications is the ability of the LDHs to exchange their anionic interlayer i.e. anion exchange. This process has applications in toxin removal, transition metal intercalation, drug delivery and exfoliation methods.[39]

The intercalation of drugs and genes has led to many successful applications of LDH materials in the medical and pharmaceutical sectors. For example, the successful intercalation of LDHs with amino acids,[99] antiobiotics,[100] cancer therapeutics,[101,102] and vitamins[103] has been previously seen. The intercalation of gene/drugs is illustrated in Figure 1.6. In the majority of these cases, the LDHs are designed to increase the stability and provide protection of the intercalated drugs as they are intended for delivery applications. Moreover, this properties of the LDHs could potentially be used in the treatment of diseases and illness.

In relation to drug delivery, the negatively charged anions, e.g. NO_3^- or Cl^-, can be replaced with biological molecules such as negatively charged plasmid DNA (pDNA). This pDNA-LDH complex can store and protect the biomolecules within the cationic layers.[104] This intercalation is a very efficient process, where its high efficacy is attributed to the electrostatic and hydrophobic interactions between drug molecules and hydroxide layers, as reviewed by Xu and Lu.[104] A further beneficial feature is the increased likelihood of cellular transfection due to its positive surface charge. Also, the chemical instability in the acidic environment of the cell can be considered as a constructive feature of the material, as this biodegradation assists in the delivery of therapeutics to biological cells.[105] Furthermore, the morphology of the LDH platelets

play an important role in relation to cellular uptake and bio-distribution. Recent studies have shown that smaller particles (≈50nm) tend to have a higher gene capacity than larger particles (≈100nm).[106]

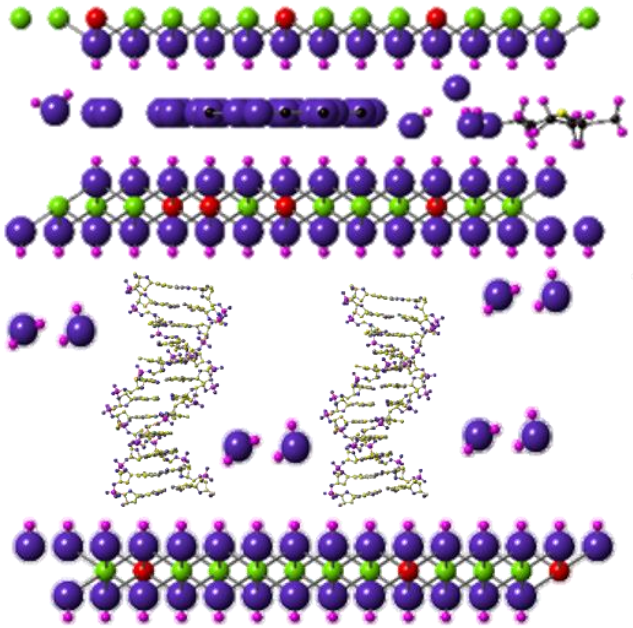

Figure 1.6: Schematic representation of DNA intercalation within the interlayer of LDH particles. Note that this schematic is not to scale.

Various studies have investigated the uptake of DNA/protein related structures into the LDH interlayers. The studies of Choy,[107] Gu,[108] Masarudin,[109] Nakayama[110] and Wong[111] portray and compare X-ray diffraction (XRD) patterns before and after the intercalation of LDHs with associated DNA structures.

Wong *et. al* presents both XRD and TEM evidence of DNA structure intercalation. However, this work only analyses this layer expansion based on a single case. Furthermore, it is difficult to interpret the *d* spacing of LDH particles in TEM imaging mode as the orientation of the platelets play a vital role in such calculations. As such, this study looks to analyse the complexes using a spectroscopic electron microscopy approach. Similarly, Gu *et. al* presents XRD and TEM studies however in contrast to Wong, where the argument claims a morphological variance before and after intercalation synthesis is presented. Whilst these studies conclude a successful

intercalation via XRD pattern interpretations, Ladewig presents an indistinguishable comparison between X-ray diffractograms before and after intercalation.[112] Instead the studies of Ladewig suggest a 'wrapping' of the plasmid DNA structures around the positively charged LDH layers, observed by TEM studies. This interaction mechanism is also postulated by Wong *et. al*.[111]

The morphological variation arguments presented by Ladewig *et. al* and Wong *et. al* lack corresponding spectroscopic data of their DNA-LDH complexes. In contrast, the work of Xu *et al* presents the interaction of plasmid DNA with LDH particles using spectroscopic data.[113] The STEM-EDX point analysis conducted by Xu highlight a Mg, Al and P peak. The P peak, as suggested, is a result of a plasmid DNA interaction. However, the presence of this peak is open to debate, as it is not significantly above the background counts. Also, the XRD studies[13-17] are typically conducted on a bulk scale and as such key nanoscale features of the biofunctionalization processes are overlooked.[107–110] This study will investigate how a pDNA structure interacts with the LDH platelets from an EM perspective. In particular, the morphological and spectroscopic characterizations will determine the structures, compositions and assess the capabilities of the nanobiocomposites to be employed as gene delivery vectors. This information is vital in understanding how the structures of the vectors play a role in their cellular uptake and delivery of their therapeutic cargo.

It is also a critical feature of non-viral gene delivery vectors to transfect cells i.e. delivery of nucleic acids. It is an utmost requirement that the vectors cross the cell membrane as otherwise the vectors would not be capable of delivering the proposed DNA or therapeutic in question. Chen *et al*. conclude that smaller LDH particles are more efficient with this delivery. However, the findings presented by these studies were evaluated using light microscopy, flow cytometry and gene expression experiments, whilst an electron microscopy approach was not considered.[106]
These findings are mirrored in the studies of Chung et al., where the cellular uptake of LDH particles is also investigated.[114] By imposing fluorescent tagging on the LDH particles, the cellular uptake can be analysed using confocal microscopy. Chung et al. found sufficient uptake of 50nm and 100nm LDHs with the former producing higher

uptake efficiencies. In addition, the work of Oh et al.[115] analysed the size dependence of LDHs to be accepted by the cells. The findings indicated that LDH particles of 50nm – 200nm were uptaken by cells. Also, the use of blocking specific endocytic pathways led to the finding that smaller LDH particles are uptaken via clathrin mediated endocytosis.

A subsequent vital requirement for the delivery of therapeutics or genes to cells is their successful transport to the cellular nucleus. The intracellular fate of the LDH and DNA particles play a key role in relation to this condition. Factors that influence the LDH intracellular fate are the degradation of the particles, the release of the loaded therapeutic and the successful delivery to the nucleus via endocytic mechanisms. Xu *et al*. presents the successful delivery of LDH (rod) nanoparticles to the cellular nucleus. This was confirmed by confocal microscopy where a strong green signal is accumulated in the nucleus due to the tagged LDHs with fluorescein isothiocyanate.[116] Ladewig *et al*. also indicates the intracellular behaviour of siRNA when combined with an LDH vector.[117] Confocal microscopy confirmed the endosomal escape of the fluorescently tagged siRNA. Moreover, this study establishes that the LDH particles 'protect' the intercalated nucleic acids and act as a carrier to the perinuclear regions of the cell.[117] In contrast, Tyner *et. al* [118] and Masarudin *et al*. investigate the delivery of green fluorescent proteins (GFP) utilising LDH particles as a gene delivery vector.[109] A similar mechanism of uptake is presented where these proteins are intercalated into LDH layers, investigated using XRD analysis, where a variation in *d* spacing was reported.[109] The LDH particles themselves were evaluated using TEM. Although a platelet structure was found, a sharp hexagonal shape was not portrayed. The advantage of using this protein is that it provides evidence of a full effective delivery to the cellular nucleus, as the green fluorescence is the result of successful gene expression in the nucleus due to the encoded green fluorescent protein in the attached therapeutic. These present the fluorescence using optical microscopy and in the case of Tyner *et al*., successful delivery after 24-48 hours was observed with transfection efficiencies of up to 90% in some cell lines.[118] Masarudin *et al*. suggest a variety of approaches to explain the release of the biomolecule from the LDH host particles.[109] It is postulated that the plasmid DNA is released via reverse ion exchange where the

plasmid DNA is exchanged with another molecule within the cellular bodies. A further postulate is the layer dissolution of the LDHs due to the acidic environment of the cell, thus releasing the therapeutic. These studies rely on the analysis of LDH uptake via optical microscopy with associated fluorescent tagging techniques. This is only suitable however for analysing larger data sets and is primarily a bulk technique. Moreover, optical microscopy is stunted by the diffraction limit and as such cannot resolve the interaction of individual LDHs with cellular membranes. This study aims to utilise EM analysis to investigate how the cells uptake the LDH nanomaterial with a particular emphasis on analysing the interaction of individual nanoparticles as they interact with cellular membranes and their structure once internalized in the cells. Furthermore, the application of EDX and EELS will enhance the characterization and detection of the LDHs in the cellular environment. This allows for the direct analysis of the size dependency of the LDH uptake and also eliminates the use of fluorescent tags, a requirement for optical microscopy.

There is an evident gap in the literature in relation to the intracellular behaviour of the LDH gene delivery vector. This is again due to the resolution limits of optical microscopy methods. Thus, EM characterizations can answer many postulates associated with the fate of the LDH material once internalized by the cell. An aspect of this study is to investigate the intracellular localisation of the LDH material. This is of critical importance as it verifies the LDHs capacity to effectively deliver the intended therapeutic. This was reviewed by Kakuthi et. al[20] where particles of smaller size are more efficient in relation to cellular acceptance and particles within 200 nm were uptaken via clathrin mediated endocytosis. Moreover, this review also presents an effect of the particle size on the intracellular localizations. Smaller particles (20nm) localize near the cellular nucleus in contrast to larger particles (180nm) which stay in the cytoplasmic regions[20]. Furthermore, Chen *et al.* and Ladewig *et al.* present the effective delivery of siRNA to cells using LDHs as a delivery vector.[106,117] However, the techniques presented were limited by optical microscopy and fluorescent tagging. Thus, the local cellular environments involving the LDH material could not be characterized.

More interestingly, this study seeks to investigate the stability of the LDH material as it transfects the cell. There are numerous questions to be addressed in this area of study. Firstly, how the LDH maintains its structure as it enters the cellular environment is a primary concern. A breakdown of the crystalline features or platelet structures of the LDH material may occur in the delivery process. Also, the lifetime of the LDH structures throughout the drug delivery process is of certain concern, particularly in relation to cytotoxic effects. It is yet to be evidenced what happens to the LDH materials once the therapeutic is delivered. Moreover, the cellular processes involved with the LDH material, should they exist in the cell, can be accurately characterized using EM methods. The techniques of TEM along with its complimentary spectroscopic techniques of EELS will provide methods to probe these queries related to non-viral drug delivery.

The analysis of afore mentioned systems using advanced EM methods presents its own technical challenges. The structural characterizations of layered materials require specific contrast mechanisms to highlight certain features of the materials such as diffraction contrast and Z contrast which will discussed in later chapters. This is also applicable to the related biomaterials of the current study as due to the low Z number and amorphous natures, effective mechanisms must be exploited to provide contrast. The characterizations and analytical methods, particularly those of EDX and EELS, also introduce a detrimental effect in the form of radiation damage.

1.5 Outline of Thesis

This thesis aims to contribute to these growing areas of research by exploring how state-of-the-art high spatial resolution characterizations can be used to understand the properties of layered double hydroxide nanomaterials. The primary characterization technique used throughout this thesis is transmission electron microscopy. This engulfs advanced techniques within this such as in-situ TEM, energy dispersive x-ray spectroscopy and electron energy loss spectroscopy.

There are several important areas where this thesis makes an original contribution to the field. This is addressed in three related research aims. Firstly, we will provide a complete TEM characterization of LDH nanomaterials, which were synthesized from scratch in our own research laboratories. The structural and chemical information is of interest from a materials science perspective but our findings also provide a reference for subsequent aims of this thesis. We next aim to unravel the mechanisms by which LDHs are used as catalytic precursors. The thermal evolutions of the LDH materials take a central focus of our characterizations in this regard. Our final objective is to elucidate behaviour of LDHs in a different application scheme. We are interested in how LDH nanomaterials employed as biomedical agents. In particular, we aim to investigate how LDHs interact with associated biomolecules intended for drug and gene delivery applications. We further seek to understand how LDHs behave in cellular environments, such as how they enter biological cells as well as their intracellular fate as a material.

Overall, this thesis is comprised of 6 chapters, including this Introduction chapter. The following chapters of this thesis present experimental techniques and findings of the research carried out during this PhD. Chapter 2 describes the experimental details of the characterization techniques used during the duration of the PhD study.

The experimental results and discussions are presented in Chapters 3, 4, and 5. Firstly, Chapter 3 concerns the EM characterization of two types of layered double hydroxide nanomaterials. The role of the electron beam on the associated findings is assessed in this chapter. This is followed by the experimental results from thermal decompositions of the studied LDH materials in Chapter 4. In-situ transmission electron microscopy

was used to characterize the associated decomposition behaviour. Chapter 5 describes the experimental results related to the features of LDH nanomaterials employed as biomedical gene delivery vectors. The uptake processes and intracellular fate of the LDH materials is the main focus of this chapter.

Finally, Chapter 6 draws conclusions from the results of Chapters 3, 4 and 5. An appendix of additional data is also included. Potential avenues of future work extending from this thesis work is also proposed.

1.6 Bibliography

1. Jiang, C., Hosono, E. & Zhou, H. Nanomaterials for lithium ion batteries. *Nano Today* **1,** 28–33 (2006).

2. Chavan, V. & Bartels, D. M. Graphene Core for a Golf Ball. (2017).

3. McNamara, K. & Tofail, S. A. M. Nanoparticles in biomedical applications. *Adv. Phys. X* **2,** 54–88 (2017).

4. Nicolosi, V., Chhowalla, M., Kanatzidis, M. G., Strano, M. S. & Coleman, J. N. Liquid Exfoliation of Layered Materials. *Science (80-.).* **340,** (2013).

5. Yin, F. *et al.* Functionalized 2D nanomaterials for gene delivery applications. *Coord. Chem. Rev.* **347,** 77–97 (2017).

6. Zhu, Y. *et al.* Structural Engineering of 2D Nanomaterials for Energy Storage and Catalysis. *Adv. Mater.* **30,** 1–19 (2018).

7. Li, H., Wu, J., Yin, Z. & Zhang, H. Preparation and applications of mechanically exfoliated single-layer and multilayer MoS2 and WSe2 nanosheets. *Acc. Chem. Res.* **47,** 1067–1075 (2014).

8. Coleman, J. N. *et al.* Two-Dimensional Nanosheets Produced by Liquid Exfoliation of Layered Materials. *Science (80-.).* **331,** 568–571 (2011).

9. Lotya, M. *et al.* Liquid Phase Production of Graphene by Exfoliation of Graphite in Surfactant / Water Solutions Liquid Phase Production of Graphene by Exfoliation of Graphite in Surfactant / Water Solutions. *J. Am. Chem. Soc.* **131,** 3611–3620 (2009).

10. Hernandez, Y. *et al.* High-yield production of graphene by liquid-phase exfoliation of graphite. *Nat. Nanotechnol.* **3,** 563–568 (2008).

11. Seral-Ascaso, A. *et al.* Synthesis of layered platelets by self-assembly of rhenium-based clusters directed by long-chain amines. *npj 2D Mater. Appl.* **1,** 11 (2017).

12. Zhang, C. J. *et al.* Transparent, Flexible, and Conductive 2D Titanium Carbide (MXene) Films with High Volumetric Capacitance. *Adv. Mater.* **29,** 1–9 (2017).

13. Nerl, H. C. *et al.* Probing the local nature of excitons and plasmons in few-layer MoS2. *npj 2D Mater. Appl.* **1,** 2 (2017).

14. Long, E. *et al.* An in situ and ex situ TEM study into the oxidation of titanium (IV) sulphide. *npj 2D Mater. Appl.* **1,** 22 (2017).

15. Mendoza-Sánchez, B., Coelho, J., Pokle, A. & Nicolosi, V. A 2D graphene-manganese oxide nanosheet hybrid synthesized by a single step liquid-phase co-exfoliation method for supercapacitor applications. *Electrochim. Acta* **174,** 696–705 (2015).

16. Dalcanton, J. J. 18 Years of science with the Hubble Space Telescope. *Nature* **457,** 41–50 (2009).

17. Weissbrod, A. *et al.* Automated long-term tracking and social behavioural phenotyping of animal colonies within a semi-natural environment. *Nat. Commun.* **4,** 1–10 (2013).

18. Meyer, P. & Dworkin, J. Applications of fluorescence microscopy to single bacterial cells. *Res. Microbiol.* **158,** 187–194 (2007).

19. Williams, D. B. & Carter, C. B. *Transmission Electron Microscopy: A Textbook for Materials Science*. (Springer).

20. Egerton, R. F., Li, P. & Malac, M. Radiation damage in the TEM and SEM. *Micron* **35,** 399–409 (2004).

21. Hobbs, L. . Radiation effects in analysis by TEM. *Introd. to Anal. Electron Microsc.* Plenum Pre**,** 399–445 (1987).

22. Zheng, Z. *et al.* A Complete Electron Microscopy Volume of the Brain of Adult Drosophila melanogaster. *Cell* **174,** 730–743.e22 (2018).

23. Lackovic, V. *et al.* Morphofunctional characteristics of endothelial cells in coronary atherosclerosis. *Arch. Biol. Sci.* **63,** 921–932 (2011).

24. Alberts, B. *et al. Essential Cell Biology: Fourth Edition*. (Garland Sciences).

25. Kaksonen, M. & Roux, A. Mechanisms of clathrin-mediated endocytosis. *Nat. Rev. Mol. Cell Biol.* **19,** 313–326 (2018).

26. Mulcahy, L. A., Pink, R. C. & Carter, D. R. F. Routes and mechanisms of extracellular vesicle uptake. *J. Extracell. Vesicles* **3,** 1–14 (2014).

27. Lim, J. P. & Gleeson, P. A. Macropinocytosis: An endocytic pathway for internalising large gulps. *Immunol. Cell Biol.* **89,** 836–843 (2011).

28. Horwitz, E. M. *et al.* Clarification of the nomenclature for MSC: The International Society for Cellular Therapy position statement. *Cytotherapy* **7,** 393–395 (2005).

29. Ullah, I., Subbarao, R. B. & Rho, G. J. Human mesenchymal stem cells - current trends and future prospective. *Biosci. Rep.* **35,** 1–18 (2015).

30. Menciá Castanõ, I., Curtin, C. M., Duffy, G. P. & O'Brien, F. J. Next generation bone tissue engineering: Non-viral miR-133a inhibition using collagen-nanohydroxyapatite scaffolds rapidly enhances osteogenesis. *Sci. Rep.* **6,** 1–10 (2016).

31. Walsh, D. P., Heise, A., Brien, F. J. O. & Cryan, S. An efficient , non-viral dendritic vector for gene delivery in tissue engineering. *Nat. Gene Ther.* **24,** 681–691 (2017).

32. Curtin, C. M. *et al.* Innovative collagen nano-hydroxyapatite scaffolds offer a highly efficient non-viral gene delivery platform for stem cell-mediated bone formation. *Adv. Mater.* **24,** 749–754 (2012).

33. Jaramillo, M. L. *et al.* Differential sensitivity of A549 non small lung carcinoma cell responses to epidermal growth factor receptor pathway inhibitors. *Cancer Biol. Ther.* **7,** 557–568 (2008).

34. Foster, K. A., Oster, C. G., Mayer, M. M., Avery, M. L. & Audus, K. L. Characterization of the A549 cell line as a type II pulmonary epithelial cell model for drug metabolism. *Exp. Cell Res.* **243,** 359–366 (1998).

35. Chittasupho, C., Lirdprapamongkol, K., Kewsuwan, P. & Sarisuta, N. Targeted delivery of doxorubicin to A549 lung cancer cells by CXCR4 antagonist conjugated PLGA nanoparticles. *Eur. J. Pharm. Biopharm.* **88,** 529–538 (2014).

36. Mu, Q. *et al.* Mechanism of cellular uptake of genotoxic silica nanoparticles. *Part. Fibre Toxicol.* **9,** 29 (2012).

37. Kim, J. S. *et al.* Cellular uptake of magnetic nanoparticle is mediated through energy-dependent endocytosis in A549 cells. *J. Vet. Sci.* **7,** 321–326 (2006).

38. Jiang, J. *et al.* Development of drug-loaded chitosan hollow nanoparticles for delivery of paclitaxel to human lung cancer A549 cells. *Drug Dev. Ind. Pharm.* **43,** 1304–1313 (2017).

39. Movia, D. *et al.* A safe-by-design approach to the development of gold nanoboxes as carriers for internalization into cancer cells. *Biomaterials* **35,** 2543–2557 (2014).

40. Singh, M., Movia, D., Mahfoud, O. K., Volkov, Y. & Prina-Mello, A. Silver nanowires as prospective carriers for drug delivery in cancer treatment: An in vitro biocompatibility study on lung adenocarcinoma cells and fibroblasts. *Eur. J. Nanomedicine* **5,** 195–204 (2013).

41. Taylor, H. F. W. Segregation and cation-ordering in sjogrenite and pyroaurite. *Mineral. Mag.* **37,** 338–342 (1969).

42. Allmann, R. The crystal structure of pyroaurite. *Acta Crystallogr. Sect. B Struct. Crystallogr. Cryst. Chem.* **24,** 972–977 (1968).

43. Bruce, A. On native magnesia from New Jersey. *Am. Mineral. J.* **1,** 26–30 (1814).

44. Sajid, M. & Basheer, C. Layered double hydroxides: Emerging sorbent materials for analytical extractions. *TrAC - Trends Anal. Chem.* **75,** 174–182 (2016).

45. Duan, X. & Evans, D. . *Layered Double Hydroxides*. (Springer, 2006). doi:10.1007/b100426

46. Rives, V., del Arco, M. & Martín, C. Intercalation of drugs in layered double hydroxides and their controlled release: A review. *Appl. Clay Sci.* **88–89,** 239–269 (2014).

47. Rives, V. *Layered Double Hydroxides present and future*. *Nova Science Publishers: New York* (2001). doi:10.1177/1090820X10380861

48. Mishra, G., Dash, B. & Pandey, S. Layered double hydroxides: A brief review from fundamentals to application as evolving biomaterials. *Appl. Clay Sci.* **153,** 172–186 (2018).

49. Tran, H. N., Lin, C. C. & Chao, H. P. Amino acids-intercalated Mg/Al layered double hydroxides as dual-electronic adsorbent for effective removal of cationic and oxyanionic metal ions. *Sep. Purif. Technol.* **192,** 36–45 (2018).

50. Benito, P., Labajos, F. M., Mafra, L., Rocha, J. & Rives, V. Carboxylate-intercalated layered double hydroxides aged under microwave-hydrothermal treatment. *J. Solid State Chem.* **182,** 18–26 (2009).

51. Yun, S. K. & Pinnavaia, T. J. Layered Double Hydroxides Intercalated by Polyoxometalate Anions with Keggin (α-$H_2W_{12}O_{40}^{6-}$), Dawson (α-$P_2W_{18}O_{62}^{6-}$), and Finke (Co. *Inorg. Chem.* **35,** 6853–6860 (1996).

52. Aisawa, S. *et al.* Intercalation behavior of amino acids into Zn-Al-layered double hydroxide by calcination-rehydration reaction. *J. Solid State Chem.* **177,** 3987–3994 (2004).

53. Ma, R., Liu, Z., Li, L., Iyi, N. & Sasaki, T. Exfoliating layered double hydroxides in formamide : a method to obtain positively charged nanosheets. 3809–3813 (2006). doi:10.1039/b605422f

54. Xia, S. J., Ni, Z. M., Xu, Q., Hu, B. X. & Hu, J. Layered double hydroxides as supports for intercalation and sustained release of antihypertensive drugs. *J. Solid State Chem.* **181,** 2610–2619 (2008).

55. Wong, F. & Buchheit, R. G. Utilizing the structural memory effect of layered double hydroxides for sensing water uptake in organic coatings. *Prog. Org. Coatings* **51,** 91–102 (2004).

56. Kooli, F., Jones, W. & Rives, V. An alternative route to polyoxometalate-exchanged layered double hydroxides: the use of ultrasound. *J. Mater. Sci. Lett.* **16,** 27–29 (1997).

57. Baig, N. & Sajid, M. Applications of layered double hydroxides based electrochemical sensors for determination of environmental pollutants: A review. *Trends Environ. Anal. Chem.* **16,** 1–15 (2017).

58. Ling, F. *et al.* A novel CoFe layered double hydroxides adsorbent: High adsorption amount for methyl orange dye and fast removal of Cr(VI). *Microporous Mesoporous Mater.* **234,** 230–238 (2016).

59. Flegler, A., Müssig, S., Prieschl, J., Mandel, K. & Sextl, G. Towards core-shell bifunctional catalyst particles for aqueous metal-air batteries : NiFe-layered double hydroxide nanoparticle coatings on g -MnO 2 microparticles. *Electrochim. Acta* **231,** 216–222 (2017).

60. Gao, Y., Wu, J., Wang, Q., Wilkie, A. & Hare, D. O. Flame retardant polymer / layered double hydroxide nanocomposites. *J. Mater.* **2,** 10996–11016 (2014).

61. Shan, X., Song, L., Xing, W., Hu, Y. & Lo, S. Effect of Nickel-Containing Layered Double Hydroxides and Cyclophosphazene Compound on the Thermal Stability and Flame Retardancy of Poly(lactic acid). *Ind. Eng. Chem. Res.* **51,** 13037–13045 (2012).

62. Abellán, G., Marti-Gastaldo, C., Ribera, A. & Coronado, E. Hybrid Materials Based on Magnetic Layered Double Hydroxides: A Molecular Perspective. *ACS Accounts Chem. Res.* **48,** 1601–1611 (2015).

63. Yan, D. *et al.* A combined study based on experiment and molecular dynamics : perylene tetracarboxylate intercalated in a layered double hydroxide matrix. *Phys. Chem. Chem. Phys.* **11,** 9200–9209 (2009).

64. Lu, Y. *et al.* Highly Sensitive Nonenzymatic Glucose Sensor Based on 3D Ultrathin NiFe Layered Double Hydroxide Nanosheets. *Electroanalysis* **29,** 1755–1761 (2017).

65. Zhao, Y., Hu, H., Yang, X., Yan, D. & Dai, Q. Tunable Electronic Transport Properties of 2D Layered Double Hydroxide Crystalline Microsheets with Varied Chemical Compositions. *Small* **12,** 4471–4476 (2016).

66. Catlow, C. R., Davidson, M., Hardacre, C. & Hutchings, G. J. Catalysis making the world a better place Subject Areas : *Phil. Trans. R. Soc. A* **374,** 20150089–20150090 (2016).

67. Thomas, J. M. Summarizing comments on the discussion and a prospectus for urgent future action. *Philos. Trans. R. Soc. A Math. Phys. Eng. Sci.* **374,** (2016).

68. Zaera, F. Nanostructured materials for applications in heterogeneous catalysis. *Chem. Soc. Rev.* **42,** 2746–2762 (2013).

69. Xu, M. & Wei, M. Layered Double Hydroxide-Based Catalysts: Recent Advances in Preparation, Structure, and Applications. *Adv. Funct. Mater.* **1802943,** 1802943 (2018).

70. Fan, G., Li, F., Evans, D. G. & Duan, X. Catalytic applications of layered double hydroxides : recent advances and perspectives. *Chem. Soc. Rev.* **43,** 7040–7066 (2014).

71. Anantharaj, S., Karthick, K. & Kundu, S. Evolution of layered double hydroxides (LDH) as high performance water oxidation electrocatalysts: A review with insights on structure, activity and mechanism. *Mater. Today Energy* **6,** 1–26 (2017).

72. Feng, J., He, Y., Liu, Y., Du, Y. & Li, D. Supported catalysts based on layered double hydroxides for catalytic oxidation and hydrogenation: general functionality and promising application prospects. *Chem. Soc. Rev.* **44,** 5291–5319 (2015).

73. Mohapatra, L. & Parida, K. A review on the recent progress , challenges and perspective of layered double hydroxides as promising photocatalysts. *J. Mater. Chem. A* **4,** 10744–10766 (2016).

74. Wang, Y. *et al.* In Situ Exfoliated, N-Doped, and Edge-Rich Ultrathin Layered Double Hydroxides Nanosheets for Oxygen Evolution Reaction. *Adv. Funct. Mater.* **28,** 1–6 (2018).

75. Wang, Y. *et al.* Layered Double Hydroxide Nanosheets with Multiple Vacancies Obtained by Dry Exfoliation as Highly Efficient Oxygen Evolution Electrocatalysts. *Angew. Chemie - Int. Ed.* **56,** 5867–5871 (2017).

76. Song, F. & Hu, X. Exfoliation of layered double hydroxides for enhanced oxygen evolution catalysis. *Nat. Commun.* **5,** 1–9 (2014).

77. Fan, K. *et al.* Nickel-vanadium monolayer double hydroxide for efficient electrochemical water oxidation. *Nat. Commun.* **7,** 1–9 (2016).

78. Li, J. & Yang, Y. J. New type ternary NiAlCe layered double hydroxide photocatalyst for efficient visible-light photoreduction of CO 2 into CH 4. *Mater. Res. Express* **5,** 26204 (2018).

79. Lu, Z. *et al.* Ternary NiFeMn layered double hydroxides as highly-efficient oxygen evolution catalysts. *Chem. Commun.* **52,** 908–911 (2016).

80. Kim, S., Fahel, J., Durand, P., Andrï¿½, E. & Carteret, C. Ternary Layered Double Hydroxides (LDHs) Based on Co-, Cu-Substituted ZnAl for the Design of Efficient Photocatalysts. *Eur. J. Inorg. Chem.* **2017,** 669–678 (2017).

81. Yang, Y. *et al.* Highly Active Trimetallic NiFeCr Layered Double Hydroxide Electrocatalysts for Oxygen Evolution Reaction. *Adv. Energy Mater.* **8,** 1–9 (2018).

82. Zhang, J. *et al.* Single-Atom Au/NiFe Layered Double Hydroxide Electrocatalyst: Probing the Origin of Activity for Oxygen Evolution Reaction. *J. Am. Chem. Soc.* **140,** 3876–3879 (2018).

83. Gong, M. *et al.* An advanced Ni-Fe layered double hydroxide electrocatalyst for water oxidation. *J. Am. Chem. Soc.* **135,** 8452–8455 (2013).

84. Pavel, O. D., Cojocaru, B., Angelescu, E. & Pârvulescu, V. I. The activity of yttrium-modified Mg,Al hydrotalcites in the epoxidation of styrene with hydrogen peroxide. *Appl. Catal. A Gen.* **403,** 83–90 (2011).

85. Renfeng, X., Fan, G., Qian, M., Yang, L. & Li, F. Facile synthesis and enhanced catalytic performance of graphene-supported Ni nanocatalyst from a layered double hydroxide- based composite precursor †. *J. Mater. Chem. A* **2,** 7880–7889 (2014).

86. Zhou, Y.-H. *et al.* Hollow Nickel-Cobalt Layered Double Hydroxide Supported Palladium Catalysts with Superior Hydrogen Evolution Activity for Hydrolysis of Ammonia Borane. *ChemCatChem* **10,** 3206–3213 (2018).

87. Tang, D. *et al.* Carbon Quantum Dot/NiFe Layered Double-Hydroxide Composite as a Highly Efficient Electrocatalyst for Water Oxidation. *ACS Appl. Mater. Interfaces* **6,** 7918–7925 (2014).

88. Dong, S., Guan, W. & Lu, C. Quantum dots in organo-modified layered double hydroxide framework-improved peroxynitrous acid chemiluminescence for nitrite sensing. *Sensors Actuators, B Chem.* **188,** 597–602 (2013).

89. Cho, S., Hong, S. C. & Kim, S. Quantum dot-layered double hydroxide composites for near-infrared emitting codes. *J. Mater. Chem. C* **2,** 450–457 (2014).

90. Wang, J., Fan, G. & Li, F. Carbon-supported Ni catalysts with enhanced metal dispersion and catalytic performance for hydrodechlorination of chlorobenzene. *RSC Adv.* **2,** 9976–9985 (2012).

91. Liu, W. *et al.* Nickel-cobalt-layered double hydroxide nanosheet arrays on Ni foam as a bifunctional electrocatalyst for overall water splitting. *Dalt. Trans.* **46,** 8372–8376 (2017).

92. Puscasu, C. M., Carja, G., Mureseanu, M. & Zaharia, C. Mixed oxides derived from layered double hydroxides as novel catalysts for phenol photodegradation. *IOP Conf. Ser. Mater. Sci. Eng.* **227,** (2017).

93. Yuan, X., Jing, Q., Chen, J. & Li, L. Photocatalytic Cr(VI) reduction by mixed metal oxide derived from ZnAl layered double hydroxide. *Appl. Clay Sci.* **143,** 168–174 (2017).

94. Tang, H., Li, S., Gong, D., Guan, Y. & Liu, Y. Bimetallic Ni-Fe catalysts derived from layered double hydroxides for CO methanation from syngas. *Front. Chem. Sci. Eng.* **11,** 613–623 (2017).

95. Bianco, A., Kostarelos, K. & Prato, M. Applications of carbon nanotubes in drug delivery. *Curr. Opin. Chem. Biol.* **9,** 674–679 (2005).

96. Zhang, Q. *et al.* Advanced review of graphene-based nanomaterials in drug delivery systems: Synthesis, modification, toxicity and application. *Mater. Sci. Eng. C* **77,** 1363–1375 (2017).

97. Chertok, B. *et al.* Iron oxide nanoparticles as a drug delivery vehicle for MRI monitored magnetic targeting of brain tumors. *Biomaterials* **29,** 487–496 (2008).

98. Faraji, A. H. & Wipf, P. Nanoparticles in cellular drug delivery. *Bioorg. Med. Chem.* **17,** 2950–2962 (2009).

99. Wei, M. *et al.* Intercalation of l -Dopa into Layered Double Hydroxides: Enhancement of Both Chemical and Stereochemical Stabilities of a Drug through Host−Guest Interactions. *Chem. Mater.* **20,** 5169–5180 (2008).

100. Badar, M. *et al.* Controlled drug release from antibiotic-loaded layered double hydroxide coatings on porous titanium implants in a mouse model. *J. Biomed. Mater. Res. - Part A* **103,** 2141–2149 (2015).

101. Choi, S., Oh, J. & Choy, J. Anticancer drug-layered hydroxide nanohybrids as potent cancer chemotherapy agents. *J. Phys. Chem. Solids* **69,** 1528–1532 (2008).

102. Kim, T. H. *et al.* Anticancer drug-incorporated layered double hydroxide nanohybrids and their enhanced anticancer therapeutic efficacy in combination cancer treatment. *Biomed Res. Int.* **2014,** (2014).

103. Gao, X. *et al.* Intercalation and controlled release properties of vitamin C intercalated layered double hydroxide. *J. Solid State Chem.* **203,** 174–180 (2013).

104. Xu, Z. P. & Lu, G. Q. M. Layered double hydroxide nanomaterials as potential cellular drug delivery agents*. *Pure Appl. Chem.* **78,** 1771–1779 (2006).

105. Ping, Z., Hua, Q., Qing, G. & Bing, A. Inorganic nanoparticles as carriers for efficient cellular delivery. *Chem. Eng. Sci.* **61,** 1027–1040 (2006).

106. Chen, M., Cooper, H. M., Zhi, J., Bartlett, P. F. & Ping, Z. Reduction in the size of layered double hydroxide nanoparticles enhances the efficiency of siRNA delivery. *J. Colloid Interface Sci.* **390,** 275–281 (2013).

107. Choy, J., Kwak, S., Park, J. & May, R. V. Intercalative Nanohybrids of Nucleoside Monophosphates and DNA in Layered Metal Hydroxide. *J. Am. Chem. Soc.* **121,** 1399–1400 (1999).

108. Gu, Z. *et al.* In Vitro Sustained Release of LMWH from MgAl-layered Double Hydroxide Nanohybrids. *Chem. Mater.* **20,** 3715–3722 (2008).

109. Masarudin, M. J., Yusoff, K., Rahim, R. A. & Hussein, M. Z. Successful transfer of plasmid DNA into in vitro cells transfected with an inorganic plasmid – Mg / Al-LDH nanobiocomposite material as a vector for gene expression. *Nanotechnology* **20,** 045602(11pp) (2009).

110. Nakayama, H., Wada, N. & Tsuhako, M. Intercalation of amino acids and peptides into Mg – Al layered double hydroxide by reconstruction method. **269,** 469–478 (2004).

111. Wong, Y. *et al.* Efficiency of layered double hydroxide nanoparticle-mediated delivery of siRNA is determined by nucleotide sequence. *J. Colloid Interface Sci.* **369,** 453–459 (2012).

112. Ladewig, K., Niebert, M., Xu, Z. P., Gray, P. P. & Lu, G. Q. (Max). Controlled preparation of layered double hydroxide nanoparticles and their application as gene delivery vehicles. *Appl. Clay Sci.* **48,** 280–289 (2010).

113. Xu, Z. P. *et al.* Layered double hydroxide nanoparticles as cellular delivery vectors of supercoiled plasmid DNA. *Int. J. Nanomedicine* **2,** 163–174 (2007).

114. Chung, H. E., Park, D. H., Choy, J. H. & Choi, S. J. Intracellular trafficking pathway of layered double hydroxide nanoparticles in human cells: Size-dependent cellular delivery. *Appl. Clay Sci.* **65–66,** 24–30 (2012).

115. Oh, J. M., Choi, S. J., Lee, G. E., Kim, J. E. & Choy, J. H. Inorganic metal hydroxide nanoparticles for targeted cellular uptake through clathrin-mediated endocytosis. *Chem. - An Asian J.* **4,** 67–73 (2009).

116. Xu, Z. P. *et al.* Subcellular compartment targeting of layered double hydroxide nanoparticles. *J. Control. Release* **130,** 86–94 (2008).

117. Ladewig, K., Niebert, M., Xu, Z. P., Gray, P. P. & Lu, G. Q. M. Efficient siRNA delivery to mammalian cells using layered double hydroxide nanoparticles. *Biomaterials* **31,** 1821–1829 (2010).

118. Tyner, K. M. *et al.* Intercalation, delivery, and expression of the gene encoding green fluorescence protein utilizing nanobiohybrids. *J. Control. Release* **100,** 399–409 (2004).

Chapter 2: Instrumentation and Experimental Techniques

This chapter describes the concepts, instrumentation and techniques involved in our electron microscopy characterizations of the LDH nanomaterials. Many informative textbooks extensively describe the ideas and technicalities of these well established microscopy techniques such as 'Transmission Electron Microscopy: A Textbook for Materials Science' by D.B Williams and C.B Carter, 'Aberration corrected: Analytical Electron Microscopy' edited by R Brydson and 'Electron energy-loss spectroscopy in the Electron Microscope- Third Edition' by R.F. Egerton. In view of this, we will confine our discussions to the main concepts and methods of (scanning) transmission electron microscopy presented by these texts.

2.1 Transmission electron microscopy

As we have previously seen, the interactions of electrons with matter opens a world at the nanoscale with a vast amount of potential physical and chemical information. To exploit this, a demand for complex and capable instrumentation is required. The transmission electron microscope is a powerful characterization tool capable of studying materials at the nanoscale. This instrumentation passes a high energy electron beam through 'thin' specimens. The transmitted electrons can then be collected and used to form high spatial resolution images. This makes TEM an indispensable tool of materials characterization. A basic illustration and schematic of standard TEM image formation is shown in Figure 2.1. Figure 2.1 TEM configuration schematic and basic animated illustration of TEM along with associated x-ray and energy loss signals. Schematics were adapted from Williams and Carter.

A TEM column is comprised of an electron gun, electromagnetic lens system and a camera/detector system. The gun is either a heated tungsten filament, a lanthanum hexaboride (LaB_6) filament or a field emission gun (FEG). The electrons extracted from the gun are then accelerated down the TEM column and through the specimen. The transmitted electrons are then collected and an image is projected onto the camera or

detector. The whole TEM system is kept under high vacuum conditions in order to prevent electrons interacting with anything other than the inserted samples.

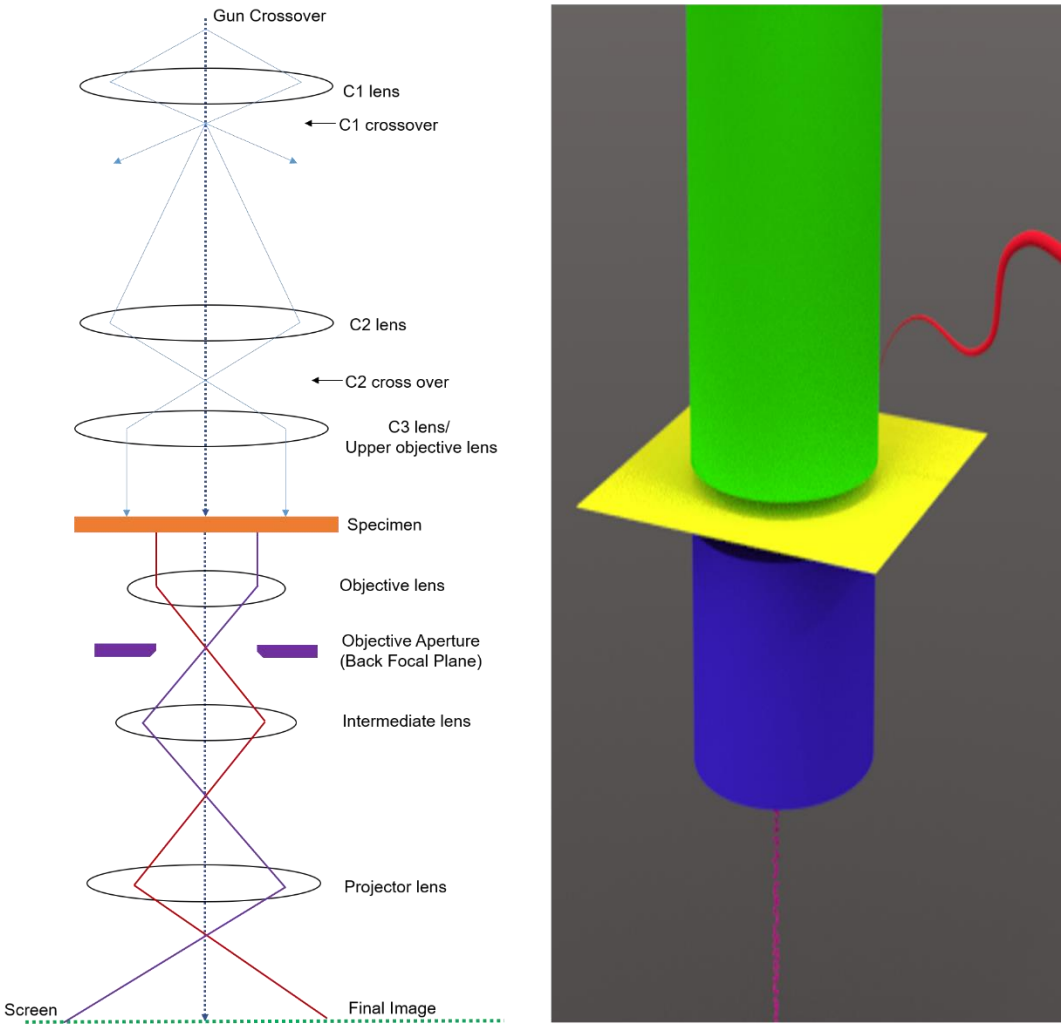

Figure 2.1 TEM configuration schematic and basic animated illustration of TEM along with associated x-ray and energy loss signals. Schematics were adapted from Williams and Carter.

In visible light microscopy, glass lenses are used to control the light paths and as such the focus, illuminations and magnifications of the images can be changed. Similarly, these principal operations of a TEM are also controlled by a lens system. However, glass lenses cannot influence the path of an electron. Hence we use electromagnetic lenses to control the path of the electron. An electromagnetic lens is composed of a cylindrically symmetrical soft iron core polepiece with a bore drilled through the middle. This is because the electrons 'ray paths' change their path when they experience a force in an electromagnetic field, governed by the Lorentz force,

$$\vec{F} = e\vec{E} + e\vec{v} \times \vec{B} \quad (14)$$

The electrons path passes through the bore in the centre of the lens. A current is established through the coils, which magnetizes the polepiece. This allows us to carry out focus and magnification changes by varying the currents in the electromagnetic lenses and hence a change in the lens focal length.

The lens system in a standard TEM system can be segmented into three separate section: the condenser system, the objective system and the projection system. The condenser system takes electrons from the electron source (i.e. electron gun) and creates a parallel column of electrons that illuminates the specimen using a parallel beam. This is depicted in our illustration by the green column onto the yellow planar specimen. The electrons exiting the sample are collected by the objective lens. It is worth noting that the focal plane of the objective lens is where the electron diffraction pattern is formed (i.e. the Fourier transform of the image). The collection and interpretation of the electron diffraction pattern will be discussed in the subsequent section. The electrons focussed by the objective lens are then passed through a projection lens system, either onto the phosphorous screen or the charge coupled device (CCD) camera. This is depicted by the blue column in our illustration (Figure 2.1 TEM configuration schematic and basic animated illustration of TEM along with associated x-ray and energy loss signals. Schematics were adapted from Williams and Carter.

The CCD is composed of an array of photodiodes where the current is represented in each pixel is displayed as an intensity within the software. For our research, DigitalMicrograph (Gatan Inc, USA) was the used software for TEM imaging and subsequent analysis. An important parameter in (S)TEM is the amount of defocus applied by the objective lens system. This is often used to create contrast between the background and specimen to highlight the features in the corresponding micrographs. The amount of defocus is illustrated by the nature of Fresnel fringes around the specimen. Conceptually, these fringes are produced from an interference pattern between scattered waves from the specimen and incident waves. Edge contrast can be produced by placing the image in slight underfocus giving bright Fresnel fringes at the

specimen edge. Conversely, dark fringes are a sign of overfocus where in practice, the features remain unclear. As such, the former is preferred when creating contrast using focus.

2.1.1 Electromagnetic lens aberrations

Our previous calculations showed that by using high-energy electrons we can attain resolutions of 0.1 nm. However, this is only the ideal situation and the actual achievable resolution is affected by the performance of our electron lenses.

It is noted that machinery, assembly and instrumentation imperfections can cause deviations from idealistic electron paths through the lens.[1,2] These are known as lens aberrations and come in three main forms: spherical aberrations, chromatic aberrations and astigmatism. These ultimately limit the achievable resolutions of our lenses and a brief description of each is described below.

Spherical aberrations, C_S, are caused by their differing paths as they travel through different parts of the lens. For example, the electrons passing through the optical axis in comparison to those travelling closer to the iron cores will experience different trajectories as they exit the lens.

Chromatic aberrations, C_C, are due to electrons of different energy being bent along different paths due to their different energies as they pass through the lens.

Astigmatism is caused when the electron experiences inhomogeneous magnetic field strength as they spiral through the optic axis of the lens. More often than not, this is due to fabrication of imperfect cylindrical symmetries including microstructure defects of the iron core lenses. In addition, the presence of apertures can also affect the local fields causing astigmatism. We can routinely correct for these aberrations such as condenser astigmatism (illumination system) and objective astigmatism (imaging system).[2]

Strikingly, the existence of these aberrations has not stopped physicists trying to improve the resolution capabilities with novel ideas and approaches. Perhaps one of the most revolutionary developments of TEM has been that of aberration correction. We briefly introduce the main concepts of this techniques with further detail of such

physical concepts available in the literature. Spherical aberrations can be eliminated in the (S)TEM by incorporating a quadrupole-octupole lens C_S corrector in the condenser lens system. This in essence, helps to reduce the STEM probe size giving enhanced sensitivity and greater spatial resolution.[3] On this point, monochromators help to relieve chromatic aberrations by reducing the energy spread of the incident electron beam. This has been shown to achieve single atom analysis in STEM.[4] Without doubt, these progressions have paved the way for atom level origins of materials and further understanding the true structure-property relationship of materials.[5,6]

In essence, any feature of a TEM image originates from some type of scattering event that the electron experiences as it transmits through the specimen. This is achieved by a close -to-parallel electron beam illuminates whole areas of interest of a specimen and an image is formed by the objective lens collecting the electrons post specimen.[7]

2.1.2 Electron diffraction

Periodicities in a crystallographic specimen can be studied with electron diffraction in TEM.[2] In parallel to TEM imaging, this type of data withholds vast amounts of structural information, such as if our materials exhibit crystalline or amorphous properties, to what extent these crystalline if the sample if monocrystalline or arranged by numerous grains i.e. polycrystalline. Detailed studies of the electron diffraction patterns reflect the atomic arrangements and orientations of the crystal.

As the parallel TEM beam transverses a crystal, they diffract through specific angles, i.e. Braggs law. In the context of electron microscopy, if the incident electron waves that are scattered of neighbouring atomic planes with a spacing *d* apart, are a whole path difference equal to that of an integral number of wavelengths nλ, and are scattered through angle θ, then they satisfy the Bragg law,

$$n\lambda = d_{hkl}\sin(\theta) \tag{15}$$

A reciprocal relationship can be established between spacing d and scattering angle θ. This allows us to calculate interplanar atomic planar spacings, an extremely useful method of characterization of crystallographic features of our nanomaterials.[2]

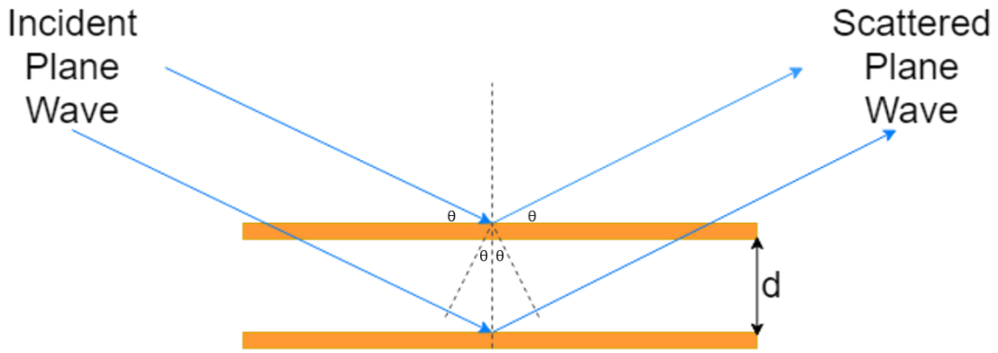

Figure 2.2 Schematic representation of the Bragg law diffraction concept, adapted from Williams and Carter.

2.1.3 Contrast in TEM

Contrast C in TEM is defined as the difference in intensity between two adjacent areas,[1]

$$C = \frac{I_2 - I_1}{I_1} = \frac{\Delta I}{I_1} \tag{16}$$

The reason why we can observe any feature in a TEM image is due to contrast, i.e. the difference in intensity between two image points. We next discuss various types of contrast generation: Mass-thickness, diffraction and phase contrasts.

This contrast arises because of the scattering of the incident beam. In relation to imaging techniques, the contrast is obtained by selecting specific electrons or excluding them from the imaging system[1]. There are various types of contrast mechanisms in TEM, such as Amplitude, Mass-Thickness, Diffraction and Phase contrast.

Amplitude contrast derives from the mass/thickness variations across the sample, due to the electron interacting with more material[1]. Images formed from amplitude contrast come from the selection of direct (bright field, BF) or diffracted (dark field, DF) beams, as seen in Figure 2.3.

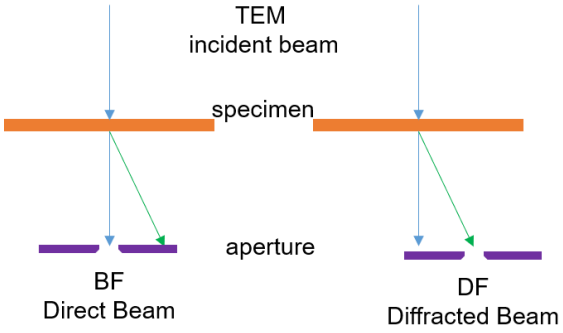

Figure 2.3 Side view of standard TEM set-up of bright field and dark field imaging using the objective aperture.

Mass-thickness contrast is due to incoherent (out of phase) elastic scattering (Rutherford scattering) of electrons.[1] By selecting the electrons at low scattering angles, the forward peaked Rutherford scattered electrons dominate and mass-thickness contrast becomes the primary contrast mechanism. Mass-thickness contrast plays a vital role in relation to biological specimens, a particular interest of this study. The lack of crystallinity in biological samples and polymers result in a lack of diffraction contrast. The mass-thickness contrast may be enhanced by the addition of heavy metal stains such as Os, Pb and U. These metals bind to bonds such as $C = C$ in cell tissues and polymers. However, these stains have their drawbacks, as they can alter specimen structure and composition as well as producing artefacts themselves. The Rutherford scattering cross section is dependent on atomic number Z. Furthermore, the number of elastic scattering effects increases with increasing thickness. These two properties lead to an insight of mass-thickness contrast mechanisms, where the high Z number regions scatter more than the low Z number regions of the specimen. Similarly, more electrons scatter in a thicker region than a thinner one.[1]

In relation to the selection of electrons, darker regions in BF images correspond to higher mass/thicker areas. Conversely, thinner regions appear brighter[1]. The opposite is true for DF images. It is noted that in DF images, although the contrast is greater than that of a BF image, the overall intensity is relatively lower.[1] Mass-thickness contrast can be influenced by the size of the objective aperture and the accelerating voltage i.e. kV. The size of the aperture controls the amount of scattered electrons that contribute to the image.[1] The kV affects the scattering angle and cross section, and

hence the electrons contributing to the image.

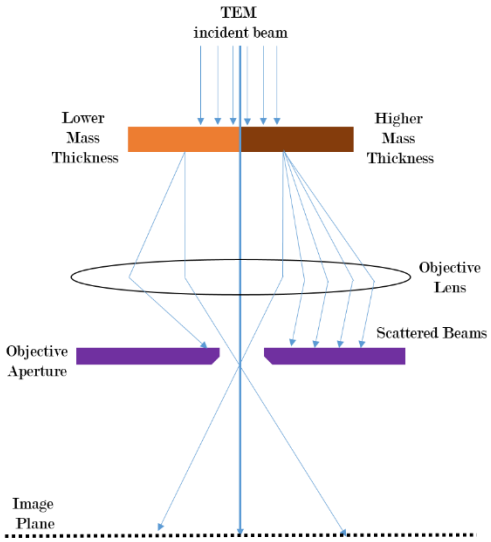

Figure 2.4 Representation of mass-thickness contrast in the TEM.

Diffraction contrast is due to coherent (in phase) elastic scattering. This is caused by Bragg diffraction which is determined from the crystal structure and orientation of the specimen. Moreover, diffraction contrast varies from mass-thickness contrast as difference in the beams arises from one diffraction beam being strong[1]. Since electrons are diffracted by a specific set of planes, the diffraction contrast derives from a specific orientation of the crystal, as opposed to the selection of general scattering information[1]. The objective aperture in TEM selects one Bragg-scattered beam. The selectivity of the objective aperture exceeds the mechanism of STEM detectors when diffraction contrast is discussed. There is less controllability with the ADF and HAADF detectors in STEM, as they collect many Bragg-scattered beams, subsequently reducing contrast.[1]

Phase contrast arises from the phase differences of the electron waves as they scatter through the thin specimen. It is dependent on many factors such as atomic scattering factors, thickness variations, orientations and focus and astigmatism of the objective lens. Phase contrast imaging varies from alternative types of contrast in the sense that more than one beam is required, and in general, increasing the number of beams increases the resolution. Phase contrast microscopy is more generally known as Lorentz microscopy. This is capable of imaging magnetic domains in magnetic thin

film samples. Foucault images are formed by using the split in electron diffraction spots caused by the domains themselves. Alternatively, Fresnel images can be constructed to capture domain wall features depending on how electrons are deflected towards or away from each other on the sides of the domain walls. However, this experimental set up requires a specifically designed low-field lens or the use of the intermediate lens to focus due to the internal field effect of the objective lens.

2.2 Scanning transmission electron microscopy

A scanning TEM ((S)TEM) has a differing lens configuration and image formation process to that of a TEM. Figure 2.5 shows the standard STEM instrumental set-up. The condenser lens system constructs a focussed electron probe. This point probe is then scanned across the sample in the x-y plane using scan deflector coils. A STEM image is formed by plotting the scattered intensity measured on the STEM detectors as a function of the probe position i.e. each pixel in the image.[7] In STEM imaging, our main concern is controlling which electrons that contribute to the image depending on their angles as they exit the specimen.[2] This is achieved by selecting electrons that are scattered through certain angles. Figure 2.5 depicts the basics of STEM image formation and detection. In this situation and in the case where the material is of the same thickness, regions of heavier Z elements are perceived as bright intensities whereas dark intensities are due to the lack of scattered electrons at these high angles (100+ mrad).

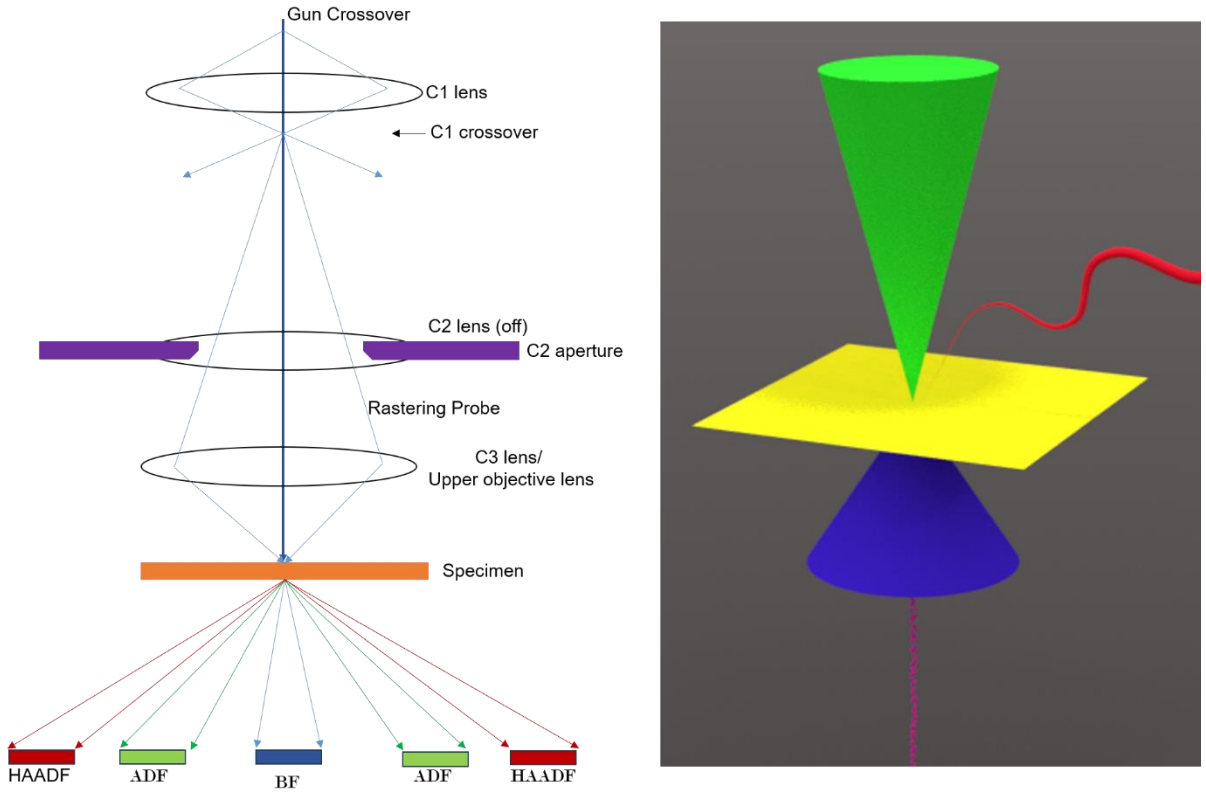

Figure 2.5 STEM configuration schematic and basic animated illustration of STEM along with associated x-ray and energy loss signals. Schematics were adapted from Williams and Carter.[2]

As we can see, electrons can scatter at high angles as they exit the specimen, and are collected by our bright field (BF), annular dark field (ADF) and high angle annular dark field detectors (HAADF) detectors. Although we also take advantage of scattered electrons to generate contrast in TEM, those that are collected by the objective lens are of a relatively smaller scattered Bragg angles (10-20 mrad). Electrons are also scattered by the atomic sites at a considerably large spread of angles as they exit the specimen. Electrons that are scattered at angles much greater than Bragg angles are found to have a greater dependence on the atomic number Z of the scattering centre. It is also noted that the dependence of these Bragg angle scattered electrons do not experience as strong a Z^2 dependence in Rutherford scattering due to screening effects. Hence, we see that heavier elements give rise to brighter intensities in ADF/HAADF STEM images, known as Z-contrast.[7]

The aforesaid mass-thickness contrasts also applies in STEM. In essence, a 'variable objective aperture' is created by varying the camera length L which in turn changes the collection angle of the detector and the electrons that contribute to the image[1]. In contrast to DF TEM images, the analogous annular dark field (ADF) collects most of the scattered electrons to form the image. There is also an additional benefit as there are no aberration effects from the lenses in the imaging system. Moreover, STEM contrasts are useful for the study of unstained polymers and beam sensitive materials. This is an important application in relation to the specimens analysed throughout this work. We also note that detector gain and black-level controls which can also affect the brightness and contrast in STEM image data.

Unsurprisingly, the choice of applying TEM, STEM or both to characterize the sample depends on what the properties of the samples are and what information is required. TEM is preferred over STEM for mass-thickness contrasts when resolution is concerned. However it can also be said that STEM mass-thickness contrast is more useful for thicker specimens and biological specimens.[8] Similarly, diffraction contrast generation is more suitable using TEM methods. The two-beam condition where contrast is generated with one strong diffraction beam and the central beam. This condition creates this strong contrast from specific set of (hkl) planes. In STEM, the diffraction contrast is poor as the ADF detector collects signals from several Bragg diffracted beams. STEM also holds unique Z-contrast imaging which can be seen right down the the atomic level resolutions. Images of this nature cannot be created in TEM as images will always contain some Bragg diffraction contrast. Moreover, STEM possesses superior control of the beam positions in comparison to TEM for more defined regions of interest for the experiment at hand. By nature, the STEM is a point-by-point method at high sensitivity using multiple signals.[7] The choice of TEM or STEM analysis can be swayed when the electron dose of the samples is important. In general, the same dose is required to create the same signal-to-noise ratios in image pixels. In TEM, the delivered dose is continuous. In contrast, the instantaneous dose is lower than the STEM method, which delivers the dose in a shorter time period but allows a longer relaxation time. On this note, the heating effect is generally less in

STEM as increased pathways are available for thermal energy diffusion into un-illuminated regions.[7]

2.3 TEM/STEM: A microanalytical tool.

As previously shown, the interactions of electrons with matter produce a diverse collection of interesting signals both above and below the specimen. This also holds true in the case of our established (S)TEM methodologies. In conjunction with structural information, the interacting electron beam in TEM methods can provide compositional and chemical information about the specimen. Indeed, the study of this using TEM methods validates this characterization as very commanding characterization tool at the nanoscale. This analysis is conducted in the (S)TEM by the acquisition of X-rays and inelastically scattered electrons, using efficient detectors and spectrometers.

2.3.1 Energy Dispersive X-ray spectroscopy

Energy dispersive x-ray spectroscopy (EDX) in the TEM is the study of characteristic x-rays produced from the beam-sample interaction. In this process, the electron beam causes a core-shell electron to be ejected from the atomic sites, thus creating a hole. This is subsequently filled by an electron in a higher energy state with the emission of a photon i.e. an X-ray. These fixed energy level transitions are characteristic of the atoms within the sample. This withholds compositional information, and a suitable collection of such x-rays allow us to identify certain elements as well as how they are distributed throughout the sample. EDX is indeed an efficient manner of identifying the chemical make-up of a material. This technique is useful in the identification and analysis of high Z number atomic species and thick samples. In addition, quantifiable studies can be performed given prerequisite knowledge of elemental scattering factors. Having said that, instrumental detectors collect a relatively low number of counts, which is also due to the application of windowed detectors. This detector design also introduces drawbacks as lighter elements such as Nitrogen and Lithium are made difficult or impossible to detect due to absorption within the spectrometer. Also, peak overlaps can be a cause of misinterpretations in EDX spectra and are also caused by

absorptions but also secondary electron generations. These implications often require in longer exposures in TEM and STEM dwell times to be employed for suitable statistics to be achieved. Thus, increasing likelihoods of specimen alterations and damages. Moreover, EDX falls short in the determination of local chemical environments and bonding information. This can be overcome by the study of the inelastic scattering of the accelerated electrons as they transverse the specimen, known as electron energy loss spectroscopy (EELS).

2.3.2 Electron energy loss spectroscopy

The characteristic loss in energy of transmitted electrons provides information of the local chemical environments of the atomic electrons. Hence a multitude of physical and chemical information can be yielded at very high spatial resolutions.[4,9] The associated EELS spectra can be looked at in two energy loss regimes. Firstly, the most intense peak of the EELS spectrum is the peak at 0 eV. This originates from the elastically scattered electrons that have lost no energy through the material, i.e. the 'zero-loss' peak. Up to 50 eV after the zero-loss peak defines the low loss region of the EELS spectrum. This involves interactions with weakly bound outer shell electrons, probing excitonic, plasmonic, local density of states and band gap properties.[10]

Higher energy features in the EELS spectrum reside in the core-loss regime, typically beyond 50 eV in electron energy loss. These edges arise from ionization of atomic core shell electrons, which correspond to the binding energy of the related atomic shell. These are superimposed on the background where the higher energy electrons have rapidly decreased in energy. They are found to take the form of edges as there is a sharp peak due to ionization of inner shell electrons by the incident beam causing them to be excited to a state above the Fermi level. This is then followed by a gradual fall off after this inner shell ionization feature. In greater detail, the study of the core loss regions also extends to fine structural features at about 40 eV after the core loss edge, known as energy loss near edge structure (ELNES).[11] Core loss ionization edges also contain a detailed amount of chemical information in their superimposed fine structure about 40 eV above the edge onsets, known as energy loss near edge structure (ELNES).[7]

Sample thicknesses may also be extracted from corresponding EELS spectra. This is calculated from the ratio of the zero-loss electrons to the transmitted electrons that have lost energy from a specimen interaction. This is described by the equation,

$$t = \lambda \ln\left(\frac{I_t}{I_0}\right) \tag{17}$$

Where t is the sample thickness, λ represents the mean free path of the electron through the specimen and the intensity ratio of the electrons that have lost energy, I_t and the zero-loss electrons, I_0.

The studies of EELS is idealistic for thin specimens and 2-D materials, which may be considered as a limitation of the technique. It is however quite useful for the study of lighter elements such as Carbon, Nitrogen and Oxygen, complimentary to EDX techniques. In comparison to the cases of EDX, cases can also arise of peak overlap in EELS. That being said, the much greater energy resolutions (1 eV in EELS as opposed to 100 eV in EDX) makes the peaks much more distinguishable. The interpretation of EELS spectra is inherently quite complex. It is often the case that small shifts in peaks as well as minute variations in fine structures may dictate sample information analysis. This requires expertise and knowledge by the experimental user to correctly determine the origin of peak features. To aid this, EELS signatures are routinely compared to elements in similar chemical environments.[12] Perhaps the time invested in EELS can reap its rewards, with greater experimental sensitivities, greater energy resolutions and enhanced information from the specimen.

In our FEI Titan microscope, EELS signals are collected using a post-column filter (GATAN Imaging Filter, Gatan, USA). Briefly, this is composed of a magnetic prism which bends the inelastically scattered electrons and separates them according to their energies onto a charge coupled device (CCD) camera.

The EELS spectra from our samples are acquired in (S)TEM characterizations using two primary approaches. Both methodologies reveal elemental distributions at the nanoscale and with new technologies such as chromatic aberration correctors, micro-analysis at single atom levels is now possible.[13,14] Firstly, energy filtered TEM (EFTEM) selects certain energy losses of the EELS spectrum using an energy slit window to

contribute to the image. There are certain drawbacks to such microanalysis EFTEM methods. Only one EELS feature is observable in any one EFTEM image. More than one map is required to assemble multiple element distributions.

Conversely, EEL spectra in STEM are acquired when the focussed STEM probe is placed at each pixel. In essence, a 'spectrum-image' can be acquired if an EEL spectra is recorded as the STEM probe scans across each pixel in the image. A favourable feature of this approach in STEM-EELS recordings is that large ranges of the loss spectrum can be acquired at each pixel, engulfing many spectral low loss and core loss edges as the STEM probe rasters across the sample. That being said, this requires long probe dwell times and long integrations times to build up counts and statistics. These conditions may lead to consequences to unrepresentative STEM-EELS maps if the sample is prone to drifts and damages.

EDX and EELS are truly superior in their own regard when acquiring chemical knowledge at high spatial resolutions.

2.4 *In-situ* transmission electron microscopy

A fast-growing and flourishing area of research not to be overlooked is in-situ TEM. Analysis of materials behaviour as they are subject to external stimuli is made possible by tailored in-situ TEM specimen holders. This thesis will look at how these various specimen holders can be used to further understand LDH materials properties in various environments. The evolution of in-situ TEM allows us to view nanoscale processes in a completely new way. The application of such instrumentation reveals nanoscale details of synthesis procedures, growth mechanisms and phase transitions under a range of different environments such as heat, gaseous or liquid. In addition, microanalysis experiments can be performed in real time, unveiling many important behaviours of nanomaterials as they are subjected to 'real' conditions. One of our in-situ TEM holders is a DENS Solutions Wildfire. This is a MEMS chip holder capable of heating samples in the TEM column over 1000°C. A schematic representation of the DENS heating chip is shown in Figure 2.6.

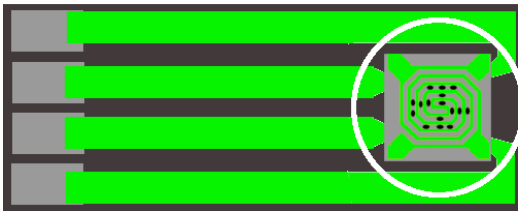

Figure 2.6 Schematic of standard in-situ TEM sample heating chip. White circle indicates magnified region. Image is not to scale. Adapted from DENS Solutions Inc..

The cooling of specimen to liquid nitrogen temperatures reduces ionization and heating damages to the specimen. This is conducted using an in-situ cryogenic TEM sample holder, where a dewar attached to the end of the holder shaft is in thermal contact with the tip hence cooling the specimen in the TEM column (Fischione Instruments, PA, USA).

The behaviour and properties of materials in liquid and gaseous conditions is always an interest in scientific areas such as materials science, chemistry and biology. Electron microscopy of materials in liquid phases has shown unique structural and chemical processes at high spatial resolutions.[15] However, one of the constraints is that standard TEMs are under low pressure vacuum systems. This prevention of imaging these systems in the TEM prompted many novel technological developments in this relatively new research field.[16,17] We give a brief introduction to the experimental techniques involved in liquid cell TEM and describe certain topics it has helped to address.

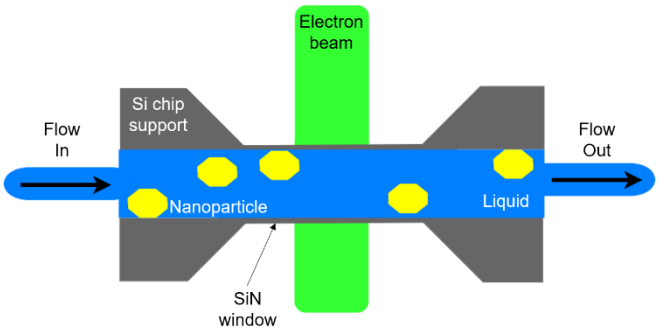

Figure 2.7 Schematic of cross-sectional view of imaging in liquid cell TEM. Figure adapted from De Jonge.[17]

A typical liquid cell set-up for TEM analysis is comprised of liquid dispersions encapsulated between two electron transparent windows. This means that the electron beam can pass through the liquid cell itself with detectable signals. At the same time, the windows are ideally mechanically strong enough to withstand the pressure differences and also resilient to electron beam damage as to avoid the liquid entering the vacuum environment of the TEM column. Graphene has been used in the past to establish such environments. These types of windows have minimal scattering and have previously shown to be capable of high resolution imaging and effective spectroscopic analysis.[18] However, they are prone to undesirable damages, which is not ideal for the TEM column environments. Silicon chips with SiN transparent windows have been more routinely fabricated for these types of experiments. In fact our own liquid cell holder from Hummingbird Scientific makes use of these SiN windows on Si chips (Hummingbird Scientific, WA, USA). The thickness of the cell is determined by 'spacer' chips, where thicknesses up to 1μm have been routinely imaged. Flow set-ups can also be achieved by creating liquid channels on the fabricated chips. This is useful for studies requiring liquid mixing, refreshing of liquids and solvent dependent reactions. The TEM study of materials in liquids also encounter their own experimental challenges. The set-up, acquisition and interpretation of data requires a careful and cautious approach by the experimental user. Technological difficulties include window membrane breaking, beam-induced effects to the liquid and contamination.

Numerous interesting studies can be performed using liquid cell TEM. In the context of our own work, research involving materials growth, dynamical processes, chemical reactions and imaging of biological systems are of interest.[19–22] Undoubtedly, potential liquid cell TEM experiments could provide unprecedented characterization of LDH based processes at the nanoscale in these environments.

2.5 Scanning electron and Helium Ion microscopy

Although the majority of the studies of this thesis were conducted using transmission electron microscopy methodologies, we also utilised scanning electron microscopy (SEM) and helium ion microscopy (HIM) as alternative methods. The description of

these related characterization methods is provided for completeness, but are kept to a rudimentary introduction.

2.5.1 Scanning electron microscopy

In SEM, an electron probe is created by a condenser lens system and are focussed by an objective lens. This probe is then scanned across the specimen surface. Signals from the corresponding beam-sample interaction such as backscattered, secondary and transmitted electrons (at higher acceleration voltages) can be used in the formation of images.[7]

2.5.2 Helium Ion microscopy

Helium ion microscopy (HIM) uses ions instead of electrons as an imaging source. The ion tip source is cryogenically cooled and exposed to high voltages in a helium gas environment. An ionized gas at the tip apex is created where one atom is used for imaging i.e. a single atom source.[23] The ions are then accelerated down the column where a beam is rastered across the sample. The detector system creates an image from the generated signals. In our case, secondary electrons are used to create micrographs.[24]

In comparison to SEM techniques, HIM offers greater spatial resolutions and depths of field. Moreover, it is more suitable technique in analysing insulating materials and biological samples.[23] This is assisted by the incorporation of an electron flood gun for charge compensation, allowing for samples to be imaged uncoated and closer to their native state.

2.6 Sample preparation

One important part of any TEM characterization study is the preparation of suitable samples. Fortunately, previous research in our group by Dr. Sonia Jaskaniec has led to many synthetic routes to generate high quality dispersions of layered double hydroxide materials. We acknowledge Dr. Jaskaniec for conducting several LDH synthesis and preparation of LDH dispersions during this PhD study.

2.6.1 TEM sample preparation for LDH samples

TEM samples were conventionally prepared using the 'drop-cast' method. This involves placing 3-5 μl of the dispersions onto lacey carbon Cu TEM grids (Ted Pella, USA). The nanoparticles were allowed to adhere for approximately 30 seconds and excess liquid was wicked away with filter paper. Samples were routinely subjected to baking in a vacuum oven (~80°C) overnight to remove surface hydrocarbons. This procedure was also used for the preparation of samples for in-situ TEM studies.

Similar procedures were also utilised for LDH nanocomposites with biological structures such as DNA based therapeutics. However in two latter cases, baking was not performed to prevent risk of thermal decomposition and biomolecule degradation and breakdown respectively.

2.6.2 Cell culture experimental details of LDH exposures

We would like to acknowledge Dr. Rosanne Raftery, TERG RCSI Dublin, for the cell culture experiments involving the Mg-Al LDH nanomaterials and mesenchymal stem cells. Further details of the plasmid DNA syntheses as well as the cell culture procedures can be found in the Appendix. Our gratitude also extends to Dr. Dania Movia, Trinity Molecular Medicine institute for conducting A549 cell culture experiments and optical characterizations involving the LDH materials. Brief details of the exposures are provided below,

LDHs exposed to mesenchymal stem cells: MSCs are isolated from murine sources, cultured and maintained in plastic well plates. In vitro experiments are conducted in At 1 hour prior to transfection, the cell media is removed and washed with phosphate buffer saline (PBS). Mg-Al LDH based vectors are mixed with transfection media and then exposed to the cultured MSC cells. After 4 hours, the transfection medium is removed and the cells are washed twice in PBS and cell media was then replenished. The cells were kept cultured for 7 days after which they were washed in PBS and then fixated using paraformaldehyde. Further details can be found in the Appendix.

LDHs exposed to A549 cells: Two culture exposures involving LDHs and A549 cells were conducted for this thesis. A549 lung adenocarcinoma cells were cultured in vitro

in plastic well plates. The Mg-Al LDH particles were then exposed to the A549 cells at a concentration of 50 μg μl^{-1}. After 14 hours, the transfection media is removed, cells were washed and then fixed in 2-4% glutaraldehyde.

Time-dependent exposures were also carried out in a similar fashion. In this case, cells were exposed to the Mg-Al LDH particles for 1 hour, 3 hours, 24 hours and 72 hours. After each time point, the transfection media was removed, cells were washed in PBS and fixed using 2-4% glutaraldehyde.

2.6.3 TEM sample preparation of biological cells

The conventional preparation of biological materials for any electron microscope should not be taken for granted. The vacuum environments of most EM characterizations is not directly suitable for the hydrated 'wet' cell culture samples. In particular, the requirements that samples must adhere to for effective TEM experiments lead to a complex procedure of sample preparation. Samples need to be fixated to terminate any continuing reactions in or outside of the cells, dehydrated to effectively remove the water content and stained with heavy metals such as lead citrate or uranyl acetate in order to improve TEM contrasts against the carbonaceous backgrounds of the resins. As well as this, the necessity of electron transparent samples leads to procedures of sample embedding in suitable resins. These resin samples are then ultramicrotomed where the blocks are mounted, sections are sliced by a diamond edge knife onto a water bath and collected onto TEM grids so as to produce appropriately thin (<100nm) electron transparent plastic sections containing the cultured cells.

2.7 Bibliography

1. Krivanek, O. L., Dellby, N. & Lupini, A. R. Towards sub-Å electron beams. *Ultramicroscopy* **78,** 1–11 (1999).

2. Willams, D. B. & Carter, C. B. *Transmission Electron Microscopy: A Textbook for Materials Science*. (Springer, 2009).

3. Batson, P. E., Dellby, N. & Krivanek, O. . Sub-angstrom resolution using aberration corrected electron optics. *Nature* **301,** 598–601 (2002).

4. Muller, D. A. Structure and bonding at the atomic scale by scanning transmission electron microscopy. *Nat. Mater.* **8,** 263–270 (2009).

5. Nellist, P. D. *et al.* Direct sub-angstrom imaging of a crystal lattice. *Science (80-.).* **305,** 1741 (2004).

6. Krivanek, O. L. *et al.* Atom-by-atom structural and chemical analysis by annular dark-field electron microscopy. *Nature* **464,** 571–574 (2010).

7. Brydson, R. *et al. Aberration-Corrected Analytical Transmission Electron Microscopy*. (John Wiley & Sons, Ltd, 2011). doi:10.1002/9781119978848

8. Williams, D. B. & Carter, C. B. *Transmission Electron Microscopy: A Textbook for Materials Science*. (Springer).

9. Hofer, F., Schmidt, F. P., Grogger, W. & Kothleitner, G. Fundamentals of electron energy-loss spectroscopy. *IOP Conf. Ser. Mater. Sci. Eng.* **109,** (2016).

10. Nerl, H. C. *et al.* Probing the local nature of excitons and plasmons in few-layer MoS2. *npj 2D Mater. Appl.* **1,** 2 (2017).

11. Egerton, R. F. *Electron Energy-Loss Spectroscopy in the Electron Microscope*. (Springer US, 2011). doi:10.1007/978-1-4419-9583-4

12. Tan, H., Verbeeck, J., Abakumov, A. & Tendeloo, G. Van. Oxidation state and chemical shift investigation in tmo by EELS. *Ultramicroscopy* **116,** 24–33 (2012).

13. Kothleitner, G. *et al.* Quantitative elemental mapping at atomic resolution using X-ray spectroscopy. *Phys. Rev. Lett.* **112,** 1–5 (2014).

14. Muller, D. A. *et al.* Atomic-scale chemical imaging of composition and bonding by aberration-corrected microscopy. *Science (80-.).* **319,** 1073–1076 (2008).

15. Holtz, M. E. *et al.* Nanoscale imaging of lithium ion distribution during in situ operation of battery electrode and electrolyte. *Nano Lett.* **14,** 1453–1459 (2014).

16. Liao, H.-G. & Zheng, H. Liquid Cell Transmission Electron Microscopy. *Annu. Rev. Phys. Chem.* **67,** 719–747 (2016).

17. De Jonge, N. & Ross, F. M. Electron microscopy of specimens in liquid. *Nat. Nanotechnol.* **6,** 695–704 (2011).

18. de Jonge, N., Peckys, D. B., Kremers, G. J. & Piston, D. W. Electron microscopy of whole cells in liquid with nanometer resolution. *Proc Natl Acad Sci U S A* **106,** 2159–2164 (2009).

19. Liao, H. G., Cui, L., Whitelam, S. & Zheng, H. Real-time imaging of Pt3Fe nanorod growth in solution. *Science (80-.).* **336,** 1011–1014 (2012).

20. Peckys, D. B., Veith, G. M., Joy, D. C. & de Jonge, N. Nanoscale imaging of whole cells using a liquid enclosure and a scanning transmission electron microscope. *PLoS One* **4,** 1–7 (2009).

21. Peckys, D. B. & De Jonge, N. Visualizing gold nanoparticle uptake in live cells with liquid scanning transmission electron microscopy. *Nano Lett.* **11,** 1733–1738 (2011).

22. Tan, S. F. *et al.* In situ Kinetic and Thermodynamic Growth Control of Au-Pd Core-Shell Nanoparticles. *J. Am. Chem. Soc.* **140,** jacs.8b05217 (2018).

23. Joens, M. S. *et al.* Helium Ion Microscopy (HIM) for the imaging of biological samples at sub-nanometer resolution. *Sci. Rep.* **3,** 1–7 (2013).

24. Notte, J. *et al.* An introduction to the helium ion microscope. *AIP Conf. Proc.* **931,** 489–496 (2007).

Chapter 3: Characterization of layered double hydroxides nanomaterials

This next chapter presents a comprehensive TEM, STEM and corresponding microanalysis characterization of Mg-Al LDH and Ni-Fe LDH nanomaterials.

3.1 Introduction

As previously discussed, the attention LDH materials have received in recent research is credited to their versatile physical and chemical properties. In addition, the flexibility and feasibility of their synthesis can also be viewed as one of the reasons they have attracted much attention. For example, the composition and ratio of the cationic sites in the brucite-like layers, nature of the interlayer species, lateral size and morphology can a have profound effect on their subsequent performances across a range of applications. In fact, previous work led by Dr. Sonia Jaskaniec, a current post-doctoral fellow of the Nicolosi group, has established how the synthesis parameters and experimental procedures can tailor the production of these LDH materials for a diverse range of sizes, morphologies and compositions, which we will see in future chapters.

Due to their prospective applications in ongoing and future research, two particular layered double hydroxide materials were elected to be synthesized and characterized by our research group. A magnesium-aluminium (Mg-Al) LDH and a nickel-iron (Ni-Fe) LDH cationic combination of the layers in a cationic site ratio of 3:1 were elected to be studied using TEM methods.[1–5] Mg-Al LDHs have been successfully employed across many areas such as cancer treatment methods and flame retardants.[6,7] Elsewhere, Ni-Fe LDHs also had broad applications in electrocatalysis, water oxidation and oxygen evolution.[8–10] Further details of their roles in these applications will be provided in subsequent experimental chapters. However, since these LDH nanomaterials were synthesized in our own research laboratories, an emphasis was placed on the thorough characterization of their physical and chemical properties. Previous studies throughout the literature as well as work by our group, also led by

Dr. Jaskaniec, successfully characterized these materials using techniques such as Fourier Transform Infrared spectroscopy (FTIR), X-ray diffraction (XRD), UV-Vis spectroscopy and atomic emission spectroscopy (AES). FTIR and TGA analysis of our synthesized LDH materials can be found in the Appendix. This information certainly provided much needed physicochemical information of the LDH synthesized in our labs. However, in consideration that many applications of nanotechnology involving LDH nanomaterials require optimizations and information at smaller length scales, advanced characterization was sought after. We employed electron microscopy (EM) to probe these physical features at greater spatial resolutions. Although previous research has utilised EM methodologies to characterise LDH materials, there is a lack of application of advanced state-of-the-art techniques to fully understand their physical properties in great detail at the nanoscale.

This chapter provides a full in-depth EM characterization of the LDH nanomaterials. We compare and contrast the physical features of LDH nanostructures of Mg-Al and Ni-Fe compositions. The advanced TEM techniques of EDX, EFTEM and EELS can be applied to extend the characterizations of these lamellar structures. Furthermore, as with any TEM characterizations, the impact of the electron beam on the LDH properties and behaviours must be credibly assessed. In this regard, this evaluation of the role of the incident high energy electrons on the LDH structure will assist in the credibility that the findings are inherent of the LDH materials themselves. The information yielded from the application of these high-end techniques will provide key information for the evaluation of LDH materials in both scientific and industrial applications. Ultimately, it is crucial to fully understand the as-synthesized material properties to investigate and verify their behaviours in future applied situations such as catalysis and drug delivery.

3.2 Experimental Methods

3.2.1 TEM sample preparation

The LDH samples studied in this chapter were synthesized in our own CPAM research labs (TCD) by Dr. Sonia Jaskaniec, who kindly provided numerous samples for TEM analysis. A detailed description of the associated synthesis procedures can be found in our labs publication by Hobbs *et. al*[11] and Jaskaniec *et. al.*[12] Due to the aggregating nature of LDH particles in aqueous solutions, dispersions intended for TEM analysis were sonicated in an ultrasonic bath to create a homogenous dispersions that would result in particles sparsely deposited on the TEM sample girds. These samples were then prepared by placing approximately 5µl of the synthesized materials onto lacey-carbon film Cu TEM grids (Ted Pella, USA). The material was allowed to adhere to the grids for approximately 30 seconds before excess sample was wicked away using filter paper. Subsequently, the grids were allowed to air dry overnight and were then subject to low temperatures (<100°C) under vacuum to remove surface contamination which may obscure TEM results.[13–15]

3.2.2 TEM characterization experimental details

The primary TEM characterization in this chapter was conducted using an FEI Titan80-300. The main body of the results of this chapter were analysed at 300 kV, due to the relatively greater resolutions achievable at this alignment. Experiments were also conducted at 80kV where required. A detailed EDX and EELS spectroscopic analysis of the LDH materials was conducted in the FEI Titan TEM using an equipped Si-Li EDAX detector for EDX analysis. A Gatan Imaging Filter (Gatan Inc., USA) was used to characterise the materials using EELS and EFTEM methods. STEM characterizations were primarily focussed on HAADF signals, collected on a Fischione HAADF detector (E.A Fischione Instruments, PA, USA).

TEM characterization of Mg-Al and Ni-Fe LDHs: Standard core loss EELS spectra from the Mg-Al and Ni-Fe LDHs were recorded in TEM mode using the Gatan Imaging Filter (GIF). The C K,O K, Fe $L_{2,3}$ and Ni $L_{2,3}$ edges were recorded with a 5 mm entrance

aperture and a dispersion of 0.2 eV/channel. The corresponding core-loss edges occurring at <100eV were analysed with a 0.1 eV/channel dispersion.

Electron beam induced degradation STEM-EELS experiments: Beam induced degradation STEM- EELS studies of the O K edge and Fe $L_{2,3}$ edge at standard and cryogenic temperatures in-situ. For these experiments, a STEM probe current of 0.46 nA with a 8 mrad convergence angle and a 21 mrad collection angle (camera length 38mm) was used. A dispersion of 0.1 eV/channel was established on the spectrometer and an energy resolution measured from the FWHM of the zero-loss peak was 1.1 eV. At each time interval, area scans of 200nm x 200nm were acquired on the Ni-Fe LDH platelet with an integration time of 5 seconds summing 3 spectra.

3.3 TEM and STEM characterization of Mg-Al and Ni-Fe LDH nanomaterials.

3.3.1 Mg-Al LDH nanomaterials

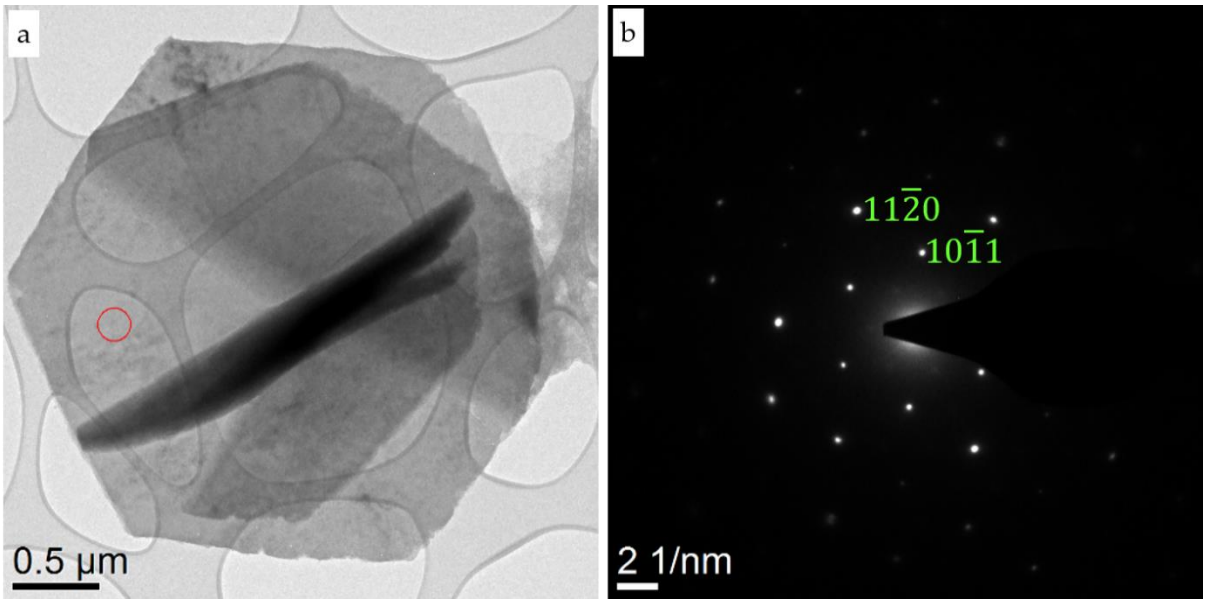

Figure 3.1 (a) Bright Field TEM images of Mg-Al LDH respectively. (b) Associated SAED patterns of Mg-Al LDH. Red circle in (a) and (b) represents region SAED was recorded from.

This section provides a thorough TEM characterization of the Mg-Al LDH nanomaterial. Figure 3.1 depicts a representative BFTEM micrograph and corresponding SAED pattern from the central region of the large platelet. The BFTEM

showed that these hexagonal platelets attain a large lateral dimension of approximately 3.25 μm. In general, the platelets exhibit a uniform thickness. This is depicted from the generally uniform contrast across the platelet areas that are orientated in the basal plane (i.e. in the same plane as the incident TEM electron beam) on the lacey carbon support TEM grid. This feature was commonly observed across many studies involving related LDHs.[16,17] The dark contrast region across the centre of the platelet represent another platelet, or perhaps numerous platelets, orientated on its side and adhered to the platelet lying flat in the basal plane. In addition the areas of darker contrast indicate multiple layers adhered to each other. These sample aggregations were found to occur across many regions of the TEM sample grid. Selected area electron diffraction was used to record an electron diffraction pattern from specified region of the LDH nanoplatelets. This was achieved by using a selected area aperture where the region selected only contributed to the recorded diffraction pattern. In the case of these LDHs, the pattern exhibits a clear single crystal exhibiting hexagonal symmetry with reciprocal lattice distances of 2.67 nm and 1.55 nm, corresponding to the (100) and (110) planar families of the Mg-Al LDH structure (Figure 3.1 (b)). The hexagonal symmetries correlate well with previous studies in the literature.[17,18]

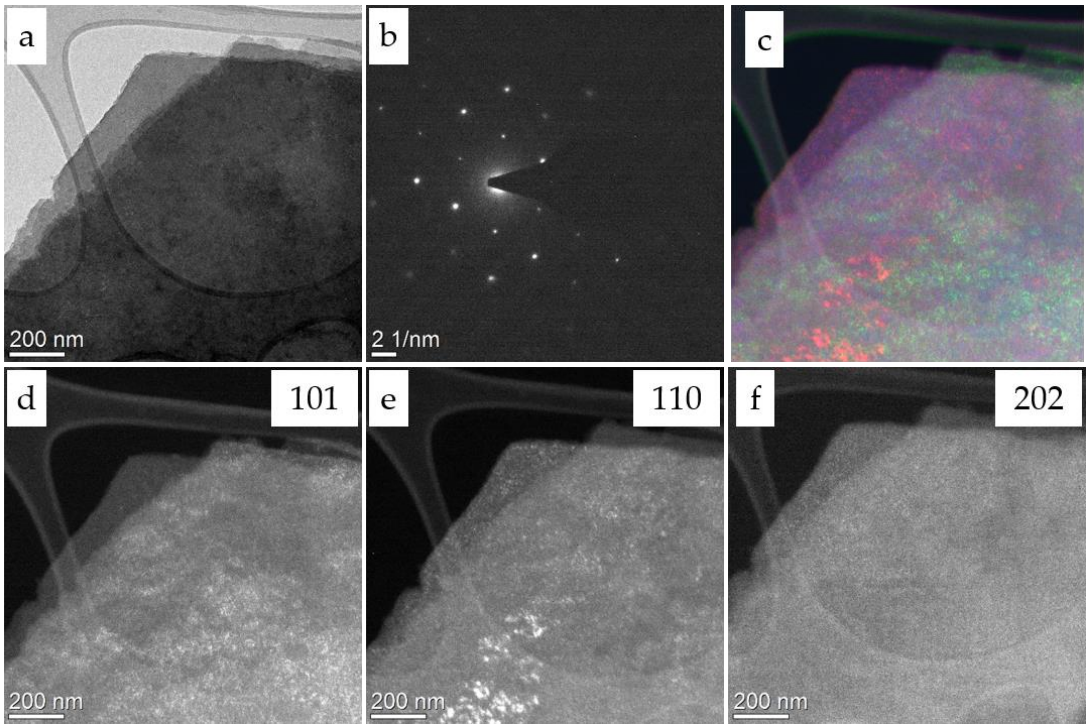

Figure 3.2 Dark field imaging of Mg-Al LDH platelet. (a) BFTEM TEM image and (b) SAED pattern. (c) Colour composite representation image of (d) (101), (e) (110) and (f) (211) dark field images, corresponding to the spots in the acquired SAED pattern in (b).

Figure 3.2 depicts dark field TEM images which were taken from specific diffraction spots in the SAED pattern. These images are achieved by adjusting the objective aperture such that only diffracted beams from certain LDH crystallographic planes (i.e. diffraction spots) contribute to the image. Hence, the intensity in dark field images corresponds to the selected crystallographic planes. Overall, a uniform contrast is viewed in the dark field images from the (101), (110) and (202) diffraction spots. However, it can also be seen that there are regions of brighter intensities in certain regions of the dark field images (Figure 3.2 (d) and (e)). This contrast shows that there is a presence of crystallite domains of this orientation that are lying on axis in the basal plane direction. The colour composite image also highlights that the domains from different planar families ((101) in green and (110) in red)) do not arrange on axis in similar regions of the large platelet, suggesting that the LDH platelets are composed of an arrangement of randomly orientated domains (Figure 3.2 (c)). Similar dark field TEM features in related LDH materials were also presented by Roelofs *et. al*.[19]

This data prompted the investigation into the possible morphological arrangements of the Mg-Al LDH platelets. In fact, an important characteristic of LDH nanomaterials is their height or thickness i.e. one of the main reasons as to why we can classify LDHs as 2-D nanomaterials. The thickness of the LDH platelets were characterized using EELS/EFTEM methods. The ratio of the inelastically scattered electrons to those that have not lost energy through interaction with the LDH material (i.e. zero loss electrons) can be used to effectively map the thickness variation across the LDH nanomaterials. Figure 3.3 presents a BFTEM image and corresponding EELS thickness map of the Mg-Al LDH. The relatively uniform contrast evidences a constant thickness across the platelets. The slight variations are believed to be due to surface adhered contamination originating from the material synthesis procedures. A $t\backslash\lambda$ thickness evaluation shows that the central regions are relatively 2.2 times thicker that the platelets edge (Figure 3.3 (c)).

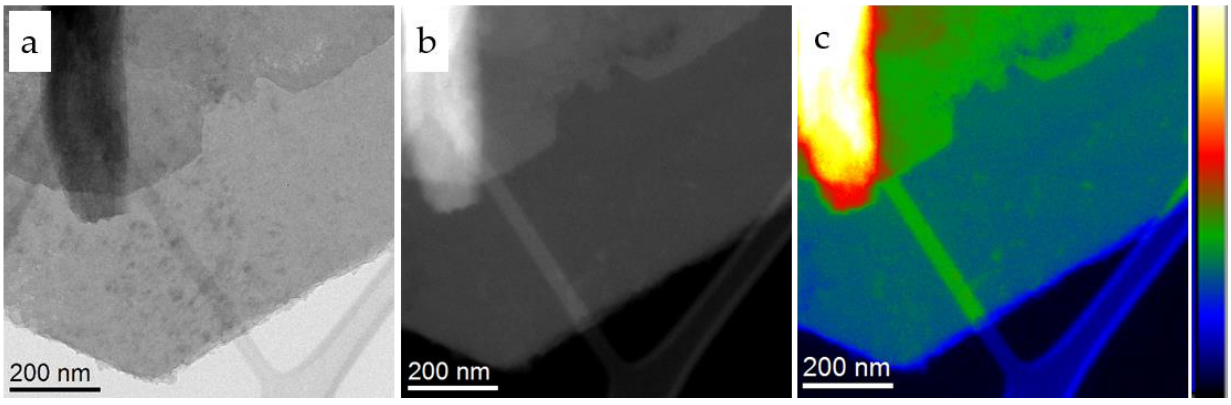

Figure 3.3 (a) BFTEM and (b) EELS thickness map of Mg-Al LDHs. (c) Colour contrast representation of the thickness map in (b). The contrast range is in t/λ values from -0.01 to 1.51.

The elemental composition of the Mg-Al LDH material was characterized via EDX and EELS methods. Figure 3.4 shows representative EDX spectra of the Mg-Al EDX spectra recorded from platelet regions using transmission electron microscopy methods.

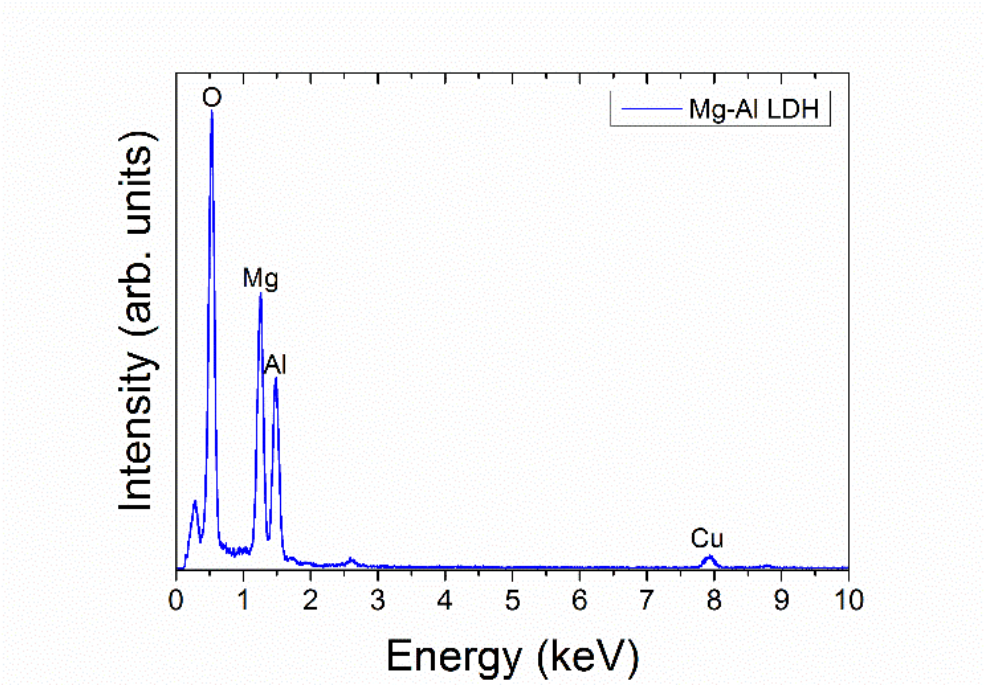

Figure 3.4 EDX spectra of the Mg-Al LDH platelets using TEM methods.

In the case of the Mg-Al LDH nanomaterials, the EDX spectrum showed significant peaks at 1.25 keV, 1.49 keV and 0.52 keV, deriving from Mg, Al and O of the LDH structures respectively. The additional peaks in the EDX spectra at 1.74 keV, 2.62 keV and 8 keV are attributed to Si, Cl and Cu respectively. The Copper originates from the sample grid and the Silicon and Chlorine peaks were deemed to be artefacts from sample synthesis and preparation procedures.

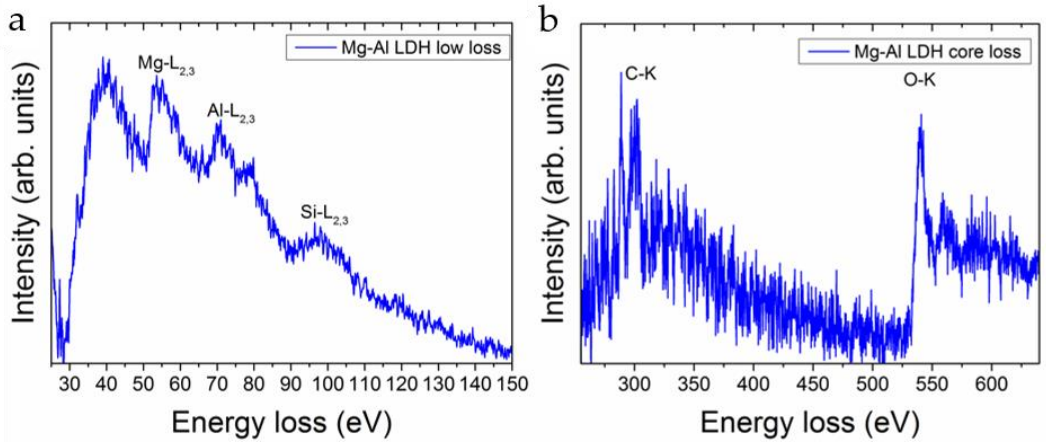

Figure 3.5 (a) Core loss Mg-$L_{2,3}$, Al-$L_{2,3}$ and (b) C-K and O-K EELS edges of Mg-Al LDHs. Intensities were normalized between 0 and 1 in both cases.

Figure 3.5 shows both the core loss TEM EELS spectra of the Mg-Al LDH nanomaterial. In the higher energy core loss region, the delayed K edges of carbon and oxygen are found at 301 eV and 540 eV respectively. The C edges originate from carbon species such as CO_3^{2-} located in between the layers. It is also possible that there may be carbonaceous artefacts absorbed to the surfaces of the LDHs themselves as well as the carbon based TEM support. The Oxygen signals derive from water in the inter layers or adhered to the surface and oxygen octahedral sites. However, there is also a significant oxygen source of the hydroxyl bonds of the metallic sites in the cationic interlayers of the LDHs. The Mg and Al $L_{2,3}$ edges are also observed in the lower energy regimes of the core loss regions (<100eV) at approximately 54 eV and 71eV and respectively.[20] These originate from the individual cationic sites in the layered structures. These M edge profiles can be related to similar materials such as Mg-Al composite alloys or aluminium oxide, where comparable bonding environments are common to both.[21,22] Mg and Al core loss K edges were not analysed due to their relatively large energy losses (1305 eV and 1560 eV respectively) which would require long exposures to attain a suitable signal to noise ratio in an EEL spectrum. This experimental condition was deemed as an unsuitable analysis in consideration of the beam sensitivity of the Mg-Al LDH. The acquisition of spectra at these energies were also experimentally limited to due to the large unsuitable shift on the drift tube of the EELS spectrometer.

3.3.2 Aging characteristics of Mg-Al LDH nanomaterials

TEM was employed to understand the aging properties of the Mg-Al LDH platelets. During this process, the metal reagents are subject to hydrothermal treatment to promote the formation of the LDH structures in the form of platelets. We chose to study how the temperatures used in this hydrothermal treatment could affect the evolution of the Mg-Al LDH. For this study, we used Mg-Al platelets with lateral dimensions of approximately 50nm. Samples for TEM were prepared at intermittent stages during this procedure of the material synthesis. Three samples of the co-precipitated metal reagents were selected and separately aged for 28 days at room

temperature, heated at 50°C for 7 days followed by 21 days at room temperature and analogously, heated at 85°C for 7 days followed by 21 days at room temperature.

Figure 3.6 compares the morphological properties as a result of differing thermal aging conditions for 3 days of the Mg-Al LDH starting metal reagent co-precipitated solutions.

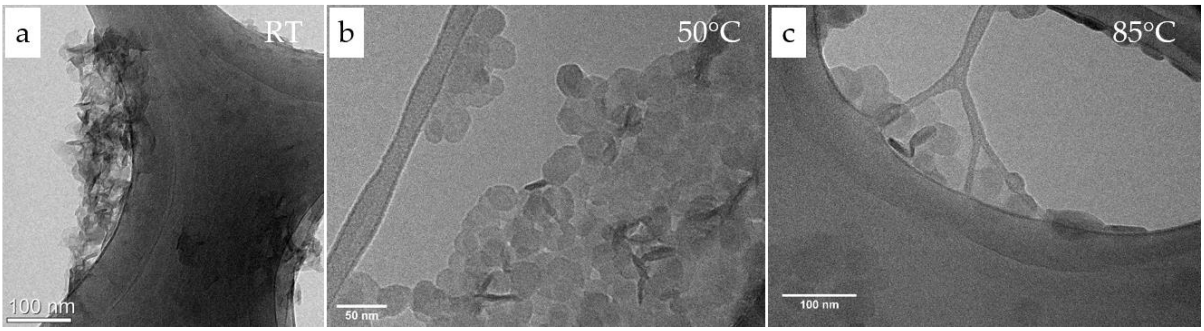

Figure 3.6 TEM study of the formation of Mg-Al LDH platelets at various temperatures of hydrothermal treatments. BFTEM images showing the co-precipitated solution aged for 3 days at (a) Room temperature (RT), (b) 50°C and (c) 85°C.

This contrast in the TEM images of these particles infer that the material is relatively thin, with an approximate lateral dimension of 50nm. These findings correspond well to the previous findings from the Mg-Al LDH nanomaterials as well as past studies (Figure 3.1).[23] Additionally, the morphology of the LDH materials at this time point appear to be independent of the temperature at which the solution is aged. We next continued this by prolonging the aging time at these temperatures to 7 days and subsequently 21 days at room temperature. Figure 3.7 and Figure 3.8 present the TEM findings from both these time points respectively. After 7 days at room temperature and 50°C, the LDH morphology becomes more refined into their hexagonal arrangements. Similar features are retained after a subsequent aging for 21 days at room temperature (Figure 3.7). However when the Mg-Al LDH platelets are heated at 85°C for 7 days and then subsequently aged at room temperature for a further 21 days, the particles attain a difference in morphology (Figure 3.7 (c) and Figure 3.8 (c)). The uniform contrast still suggests that they are relatively thin, however there are irregular jagged features at edges of the platelets with a more rounded platelets being formed. This is evidenced from the regions of darker contrast at the platelet edges compared to

their centres. It is speculated to be a degradation of the edge regions due to their locally different crystallographic environments at the platelet boundaries. There are more active sites due to the open bonds at the edges of the basal planes which could be more susceptible to thermal degradations, and also perhaps a greater chance of being oxidised in the aqueous solution. Moreover, this alteration to the platelet boundaries could perhaps be a reconstruction of the LDH materials, known as the memory effect. The induced thermal damages caused by heating may result in the partial breakdown of the LDH structures and then subsequently reconstructed due to the presence of available hydroxyls from the aqueous solutions.

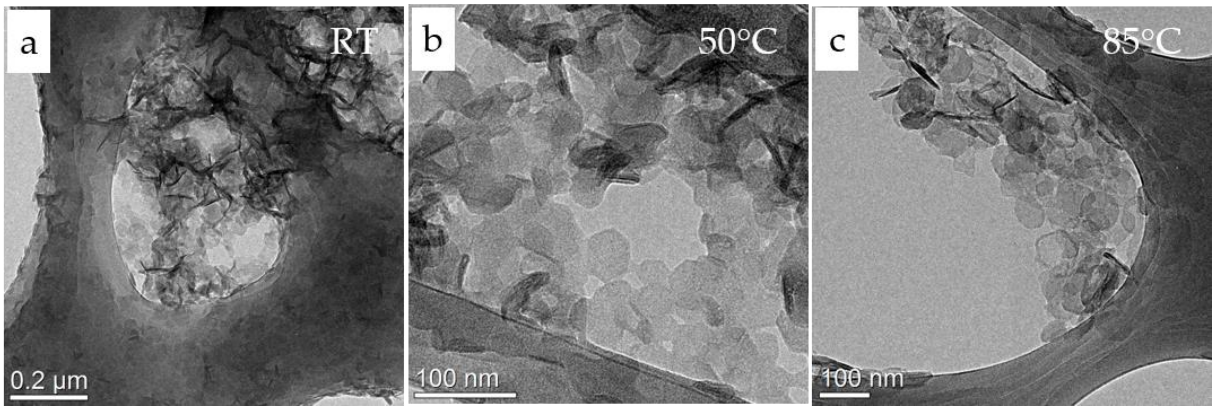

Figure 3.7 TEM study of the formation of Mg-Al LDH platelets at various temperatures during hydrothermal treatment. BFTEM images showing the co-precipitated solution aged for 7 days at (a) RT, (b) 50°C and (c) 85°C.

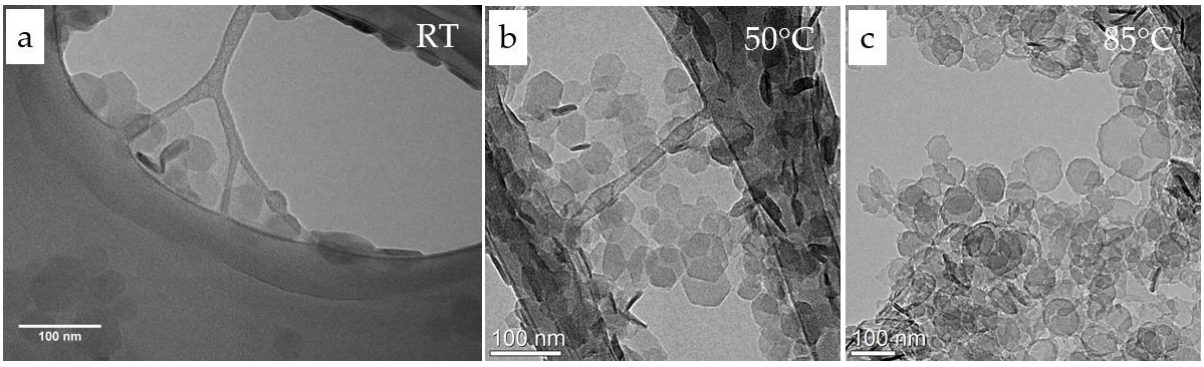

Figure 3.8 BFTEM imaging of the Mg-Al LDH materials aged for 7 days at (a) RT, (b) 50°C and (c) 85°C and then subsequently aged in solution at room temperature for a following 21 days.

3.3.3 Ni-Fe LDH nanomaterials

The selectivity of the species and ratios of the metallic sites in the cationic layers of LDH nanomaterials has led to widespread applications across nanoscale research. Moreover, these attributes of the LDH materials themselves have also been the subject of many synthesis studies involving coprecipitation, reconstruction and exfoliation methods. Previous research in our laboratories developed direct synthesis routes to produce high-quality applicable dispersions of a variety of LDH structures. One such synthesis approach involved the production of LDH nanomaterials of Ni and Fe composition, in a ratio of 3:1, intended for applications in energy storage and oxygen evolution reactions. This following section extensively characterizes these layered materials using transmission electron microscopy techniques.

Figure 3.10 shows representative BFTEM image and corresponding SAED pattern of the synthesized Ni-Fe LDH materials. Firstly, the morphology resembles that of the Mg-Al LDH counterpart. The platelets attain a relatively smaller lateral dimension of approximately 700nm and the overall uniform contrast highlights a thin platelet material. A hexagonal crystal symmetry is observed via the electron diffraction pattern, as was also viewed in the Mg-Al case. The Ni-Fe LDH platelets exhibit reciprocal lattice vectors at 2.69 nm and 1.57 nm, corresponding to the {100} and {110} planar families respectively.[4] The observed TEM contrasts and crystal symmetries also agree well with similar LDH structures in related studies.[24] The darker regions giving rise to the inhomogeneous contrasts are speculated to be due to mass thickness contrast effects caused by adhered surface water, hydrocarbons or artefacts from the sample synthesis such as triethanolamine and urea. The variation in platelet thickness was also investigated using EELS thickness maps, as shown in Figure 3.11 (b). The uniform contrast again indicates that the overall platelet thickness is relatively consistent, and was also comparable to the Mg-Al platelets. From this analysis, it is evident that even changing the composition of the LDH platelets retains similar morphological and crystallographic properties. As was the case with the Mg-Al LDHs, thickness maps using EELS demonstrates a homogenous contrast for the Ni-Fe LDH composition, implying a uniform thickness across the platelets. It was also interesting

to see a slight variation in thickness between the edge and central regions of the platelets (Figure 3.11 (c)). These intensity distributions indicate that the edge regions are relatively thinner than the central parts of the platelet. This also correlates well with the darker contrast regions of the corresponding BFTEM image. Due to the diverse range of elements in the LDH structures (C, O, H, Ni and Fe), it was beyond the scope of this study to evaluate an accurate electron mean free path for quantitative thickness calculations. Also, a suitable mean free path for such samples could not be found in the literature. Nevertheless, a relative thickness was interpreted. An evaluation of the relative thickness yields that the central regions are approximately 1.5 times thicker than the edge. This correlates very well to previous atomic force microscopy studies conducted in our own group. The AFM line profiles are shown in Figure 3.9, reprinted from our studies in Nature Scientific Reports.[25]

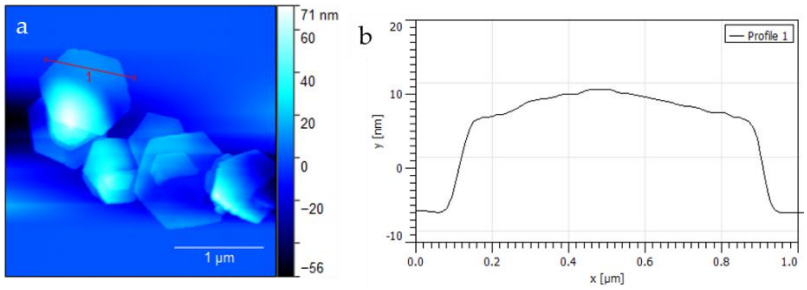

Figure 3.9 AFM image and line profile from a typical Ni-Fe LDH platelet. Data adapted from our publication in Nature Scientific Reports led by Dr. Jaskaniec.[25]

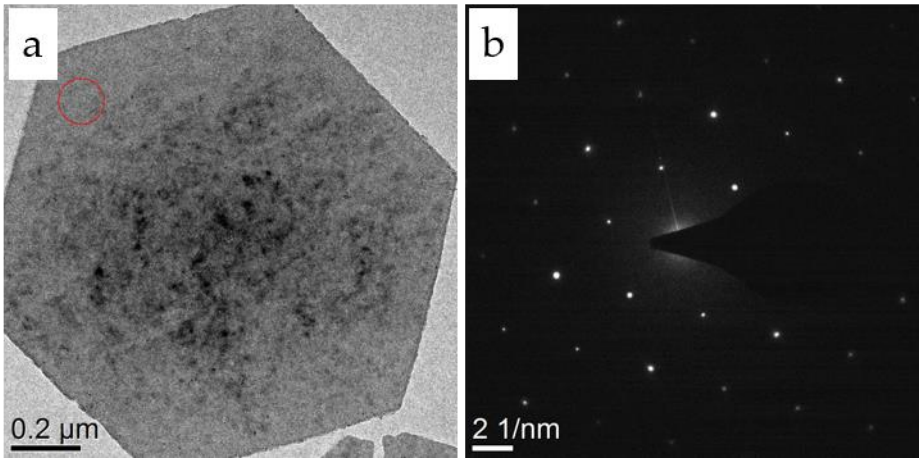

Figure 3.10 (a) Bright Field TEM image of Ni-Fe LDH nanomaterials. (b): Associated SAED pattern Ni-Fe LDHs. Red circle in (a) represents the region from which the SAED pattern was recorded.

Similar comparisons can also be made of the relative crystallographic properties of the LDH nanomaterials, as shown in Figure 3.10 (b). Both materials exhibit a well-defined crystallographic electron diffraction pattern with hexagonal symmetry. An arrangement of these distinct reciprocal space vectors is shown by the bright spots in the electron diffraction pattern. The reciprocal lattice vector distances from these symmetries were evaluated as 2.69 nm and 1.52nm , and are assigned to the (100) and (110) LDH crystallographic planes respectively.[4,26,27]

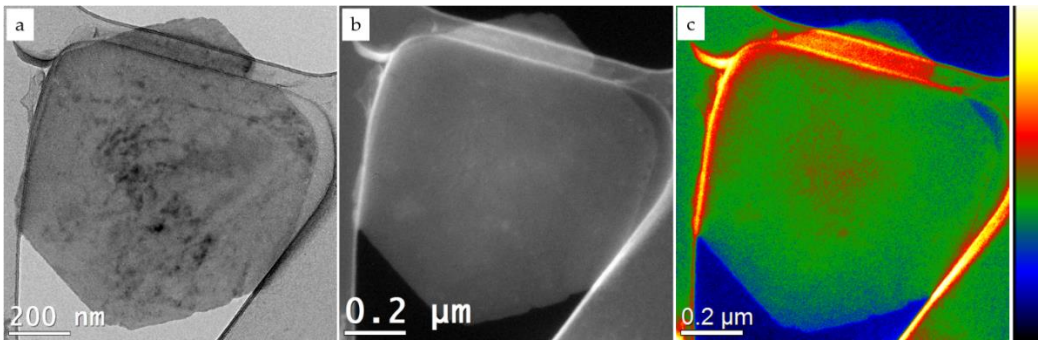

Figure 3.11 (a) BFTEM and (b) EELS thickness map of Ni-Fe LDHs. (c) Colour contrast representation of the thickness map in (b). The contrast range is in t/λ values from -0.02 to 0.49.

Figure 3.12 presents selected dark field images from different reciprocal lattice vectors (i.e. (hkl) planes) in the electron diffraction pattern that contribute to the image.

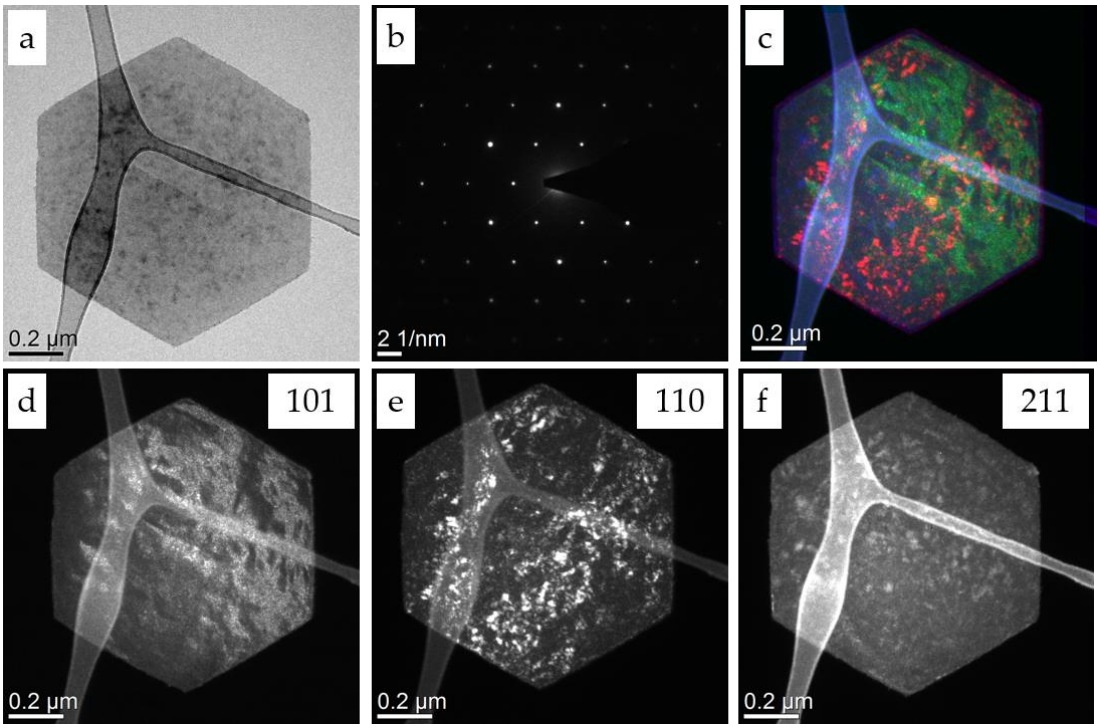

Figure 3.12 Dark field imaging of Ni-Fe LDH platelet. (a) BFTEM TEM image and (b) SAED pattern of platelet. (c) Colour composite representation image of (d) (101), (e) (110) and (f) (211) dark field images, corresponding to the crystallographic planes that contribute to the individual micrographs.

The variance in contrast when comparing dark field images (Figure 3.12 (d) – (f)) immediately shows that the Ni-Fe LDH structure does not arrange as a lamellar sheet of single orientation. The displayed contrast of the dark field images infers that different regions of the platelets exhibit different orientations of the crystal. Although, the platelet as a whole can be considered as a single crystal due to the defined crystallographic hexagonal structure (Figure 3.10 (b)). Further interpretation of these images suggests that the Ni-Fe LDH platelets are composed of smaller randomly orientated crystallite domains. This is viewed by the bright regions of intensity in each of the individual DFTEM images (Figure 3.12 (d)-(f)). From this data, it may also be interpreted that the LDH morphology exists in a somewhat 'wrinkled' fashion, and not a homogenously 'flat' 2-dimesional lamellar sheet.

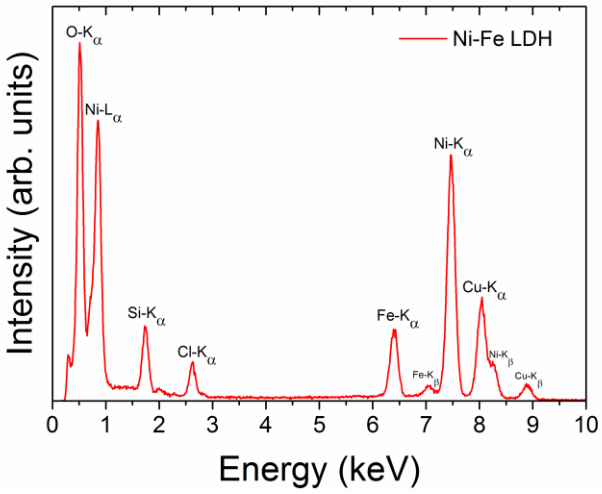

Figure 3.13 EDX spectra of Ni-Fe LDH platelet acquired using TEM methods.

Core loss EELS spectra in two energy ranges were recorded for the Ni-Fe LDH material, shown in Figure 3.14. The Ni $M_{2,3}$ edge at approximately 70 eV and core-loss $L_{2,3}$ edge at 855 eV could be easily identified in the EEL spectra. Correspondingly, the peaks at 58 eV and 714 eV derive from the Fe $M_{2,3}$ and $L_{2,3}$ and edges respectively. Analogously, peaks at 6.44 keV and 7.47 keV in the EDX spectra are representative of the Fe K_α and Ni K_α EDX lines respectively, deriving from Ni-Fe nanoplatelets derive from the respective metallic sites in the LDH materials.

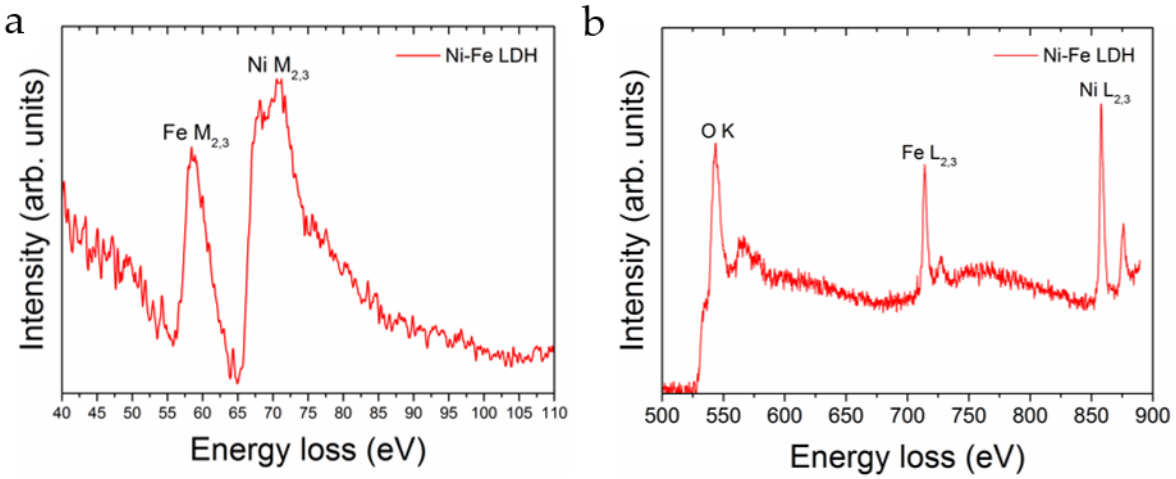

Figure 3.14 Core loss EELS spectra of Ni-Fe LDH.

A direct visualisation of these planes was imaged using high resolution TEM (HRTEM). An analysis of fast Fourier transform patterns from varying regions of the sample highlight the orientation of the crystallographic planes in the LDH nano-sheets.

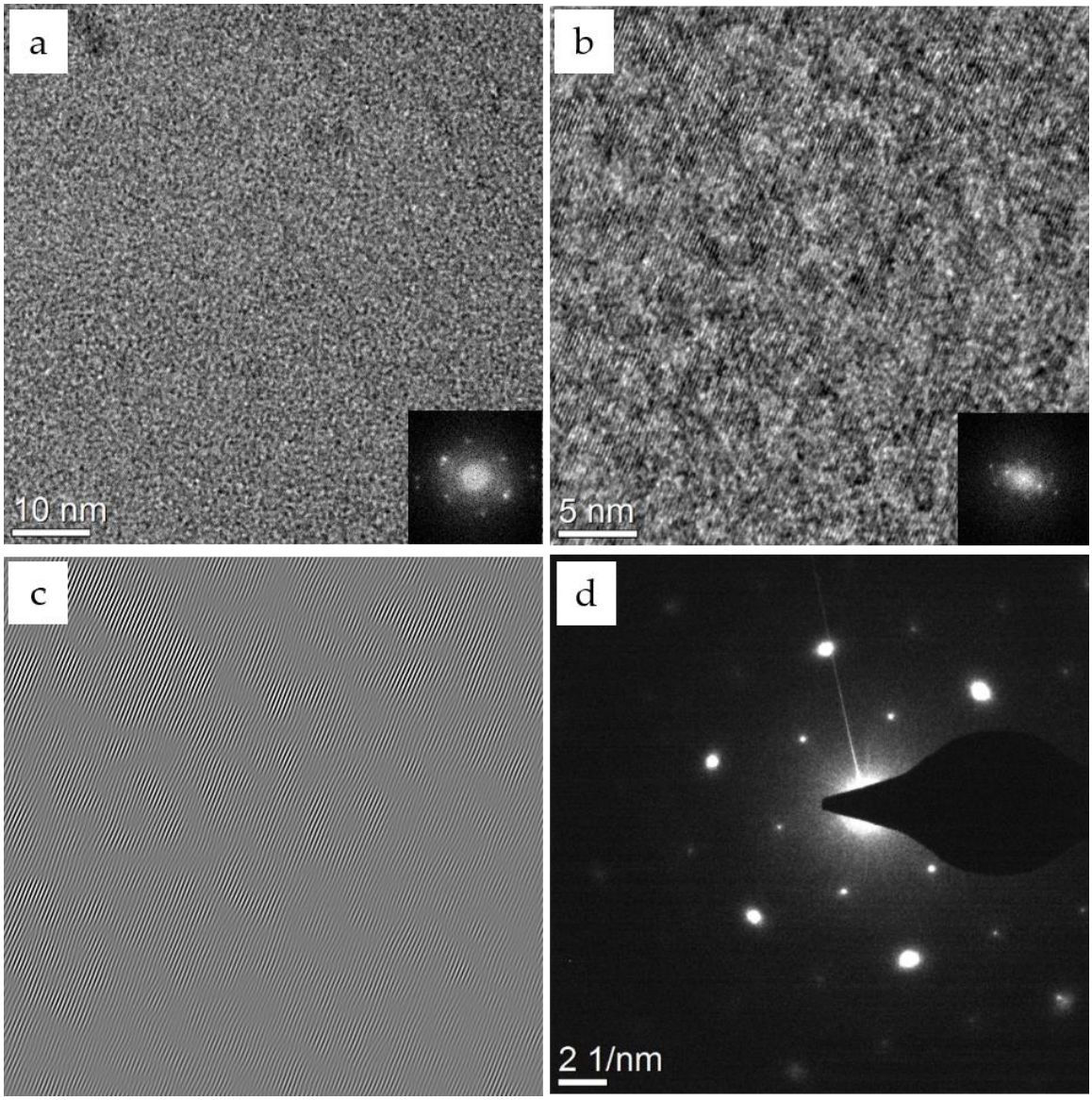

Figure 3.15 HRTEM imaging of Ni-Fe LDH nanomaterial. (a) Lattice imaging of a Ni-Fe nanoplatelet. (b) Higher magnification images of same regions. (c) Inverse FFT image of masked FFT of the {100} reflection in (b). FFT of whole imaged region are presented as insets in image (a) and (b). (d) SAED pattern acquired from analysed region after HRTEM imaging.

The lattice spacings of the observed planes were calculated from the distances between the reciprocal lattice vector spots in the generated FFT pattern (Figure 3.15 (a) and (b) insets). These spacings were measured as 2.5 nm in both cases. In addition, these same *d* spacing values also corroborated the recorded SAED pattern d-spacings evaluations, as shown in Figure 1.5 (b). An electron diffracted pattern was recorded from the imaged region after HRTEM analysis. This evaluated the effect on the LDH platelets when using a higher dose rate in HRTEM experiments due to higher magnifications.

Figure 3.15 (d) shows an obvious broadening of the intensity in the spots, indicating a crystallographic breakdown in the sample. It is also noted however that the partial retention of the diffraction spots indicate that the material is not entirely amorphous as a result of the electron beam irradiation during HRTEM analysis. Nonetheless, we could quantify these degradations by comparing the intensity profiles from the associated diffraction patterns. Intensity line profiles of selected (100) and (110) diffraction spots of the LDH SAED patterns before and after HRTEM imaging can be found in the Appendix. A striking result is the evident broadening of the spots due to the imaging conditions of HRTEM. More precisely, the FWHM of the (100) and (110) diffraction spots were evaluated as 0.08 nm^{-1} and 0.12 nm^{-1} in the Ni-Fe LDH before HRTEM imaging. In contrast, the FWHM of the respective planes after HRTEM studies were evaluated as 0.16 nm^{-1} and 0.32 nm^{-1}. This streaking effect of the spots after HRTEM is indicative of crystal distortions of the LDH lattices. This infers that the electron beam could be breaking down the lattice structures in the LDH material. As well as this, the broadening of the spots results in a more polycrystalline electron diffraction pattern which may also infer platelet twist and rotations. Alternative layered materials such as He-irradiated graphene exhibited similar electron diffraction effects.[28]

To push the limits into what we can observe from the LDH materials from a resolution perspective, we elected to characterize the Ni-Fe LDH platelets using our NION aberration corrected ultraSTEM at 200 kV. One remarkable benefit of using aberration corrected STEM is the use of a rastering STEM probe capable of imaging with atomic resolution. This high-end characterization technique was applied to understand the atomic scale features of the Ni-Fe LDH structure. Figure 3.16 presents HAADF ac-STEM imaging of the LDH platelet previously studied using TEM. FFT analysis of the depicted region are also presented as insets in each figure.

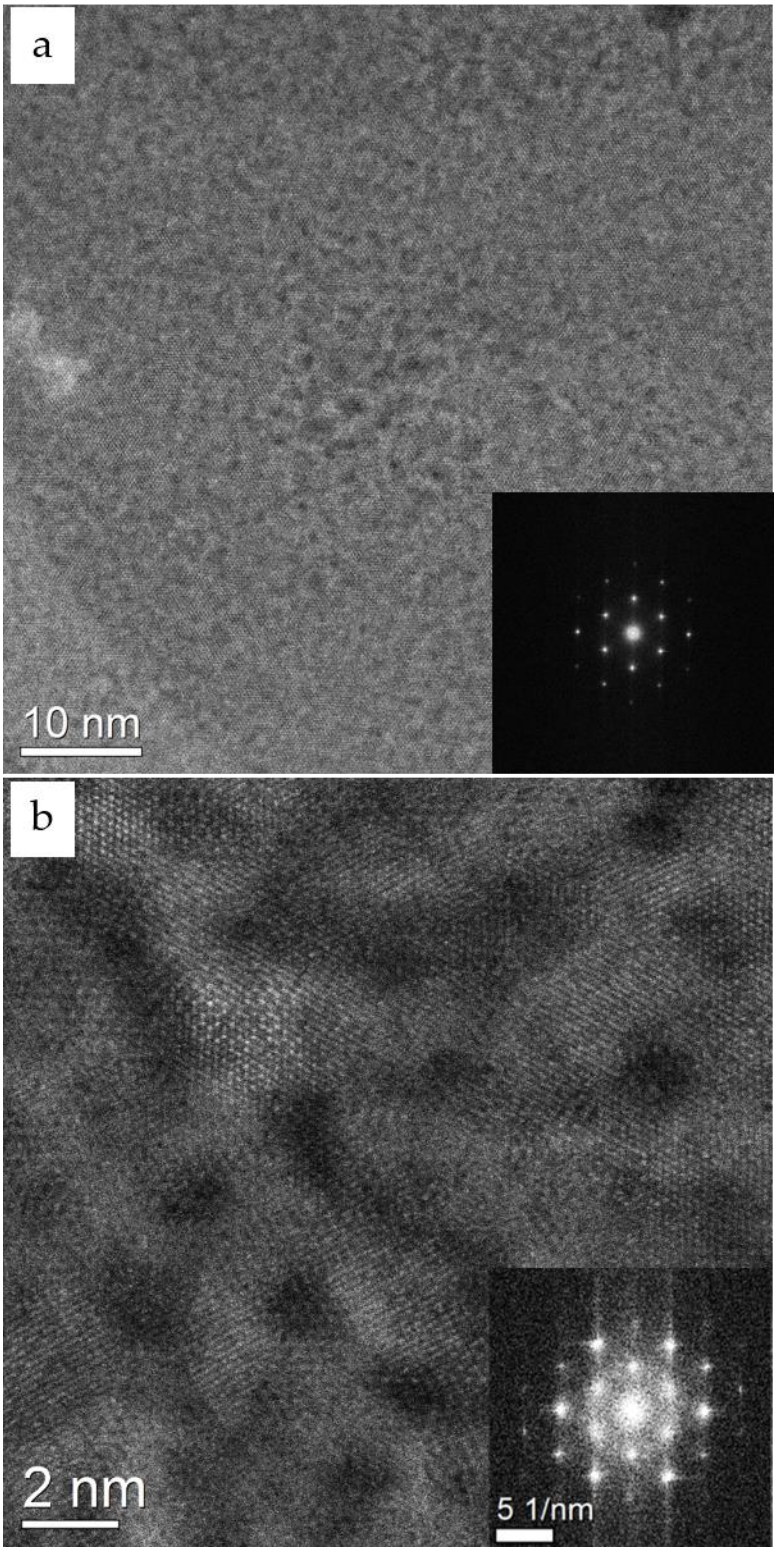

Figure 3.16 (a) Aberration corrected STEM imaging of Ni-Fe LDH. (b) Higher magnification image. Inset are FFTs generated from whole imaged regions in (a) and (b).

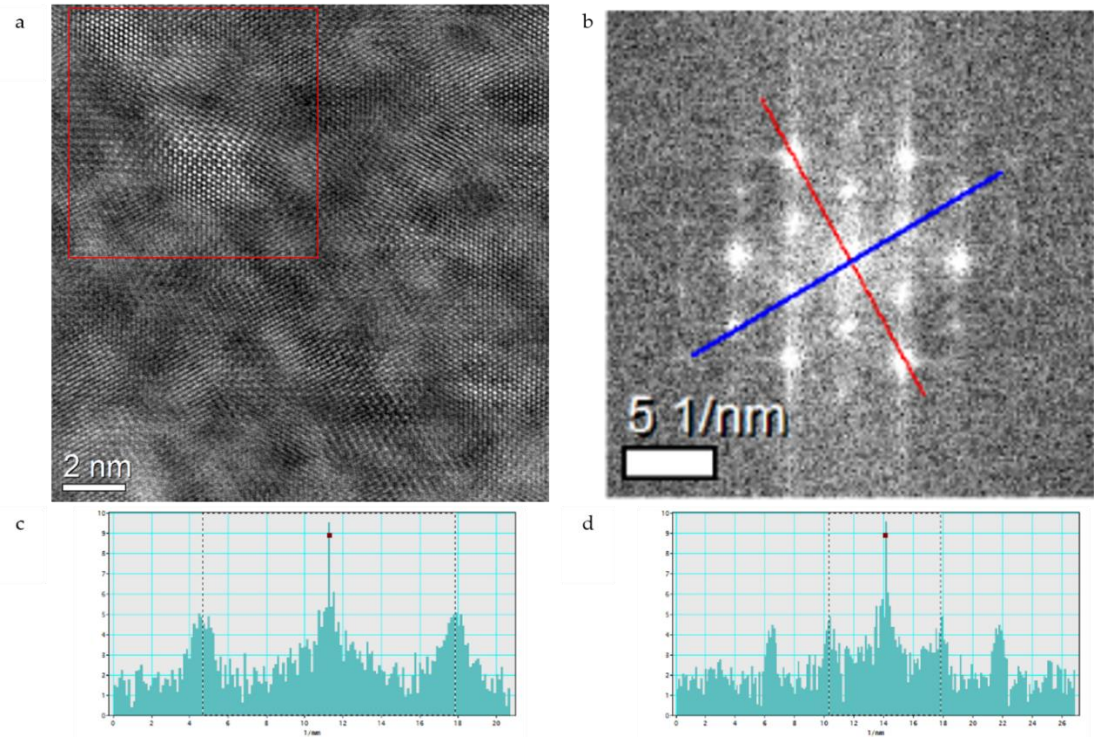

Figure 3.17 Fast Fourier Transform analysis of ac-STEM image of Ni-Fe LDH platelet. (a) ac-STEM image as viewed previously. Image has been filtered for noise reduction and further clarity. Red square indicates region the FFT pattern was calculated from in (b). (c) and (d) represent intensity line profiles acquired from the FFT pattern. Region of intensity for line profile in (c) is annotated on FFT pattern.

Firstly, the atomic hexagonal pattern of the LDH structure is observed in real space (Figure 3.16 (b)). It is also noted that the relative z-contrast in STEM imaging between the Ni and Fe sites in the LDH structure is difficult to distinguish as there is very little difference in the z-number of these elements. However, an inspection of the STEM imaging intensities in Figure 3.17 (a) shows a variation in contrast between atomic sites. It is speculated that this relative contrast difference is due to the presence of the Oxygen sites in the LDH structure, due to its relatively lower Z-contrast in comparison to that of the Ni and Fe metallic sites. Further analysis of this data yields an identification of the crystallographic planes. In addition, the crystallite arrangements corroborates the dark field imaging interpretations (Figure 3.12). The potential case of randomly orientated sheets stacked on top of each other was also considered. However further inspection overlooked this possibility due to the lack of periodicity in the image as well as the absence of Moiré fringe effects from multiple sheets.[29] The calculated FFT (red square in Figure 3.17 (a)) also highlights the hexagonal

crystallographic features. The *d* spacing values were calculated from the intensity line profiles from the generated FFT pattern. The distances were calculated as 2.65 nm and 1.52 nm (Figure 3.17 (c) and (d) respectively). These were ascribed to the {100} and {110} planar families of the Ni-Fe LDH structure, comparing well to previous studies and our own electron diffraction data.[30] Moreover, the findings from ac-STEM also agrees well with the SAED patterns in TEM analysis. This suggests that the observed atomic scale information is indeed intrinsic of the LDH structure and not an effect caused by the interacting ac-STEM probe. The arrangement of the crystallographic planes of the LDH materials also highlights that the LDH structures are not arranged in one single orientation across the nano-platelet, as also seen using DFTEM analysis (Figure 3.12).

3.3.4 The aging properties of Ni-Fe LDHs

In compliment to the aging mechanisms and characteristic of the Mg-Al LDHs, a similar experiment was conducted in the case of the Ni-Fe LDH nanomaterials. The aging properties of the Ni and Fe salt emulsion was characterized at various time points during the synthesis of the LDH materials. Small amounts of liquid dispersions of the reagents were Samples were taken during the hydrothermal treatment at 100°C at the beginning of the treatment and after 30 minutes, 2 hours, and 18 hours. Each sample was prepared for TEM analysis as per our standard approach, previously described in the Experimental Methods chapter. Figure 3.18 displays BFTEM imaging and SAED analysis of this aging process of the Ni and Fe reagents solution.

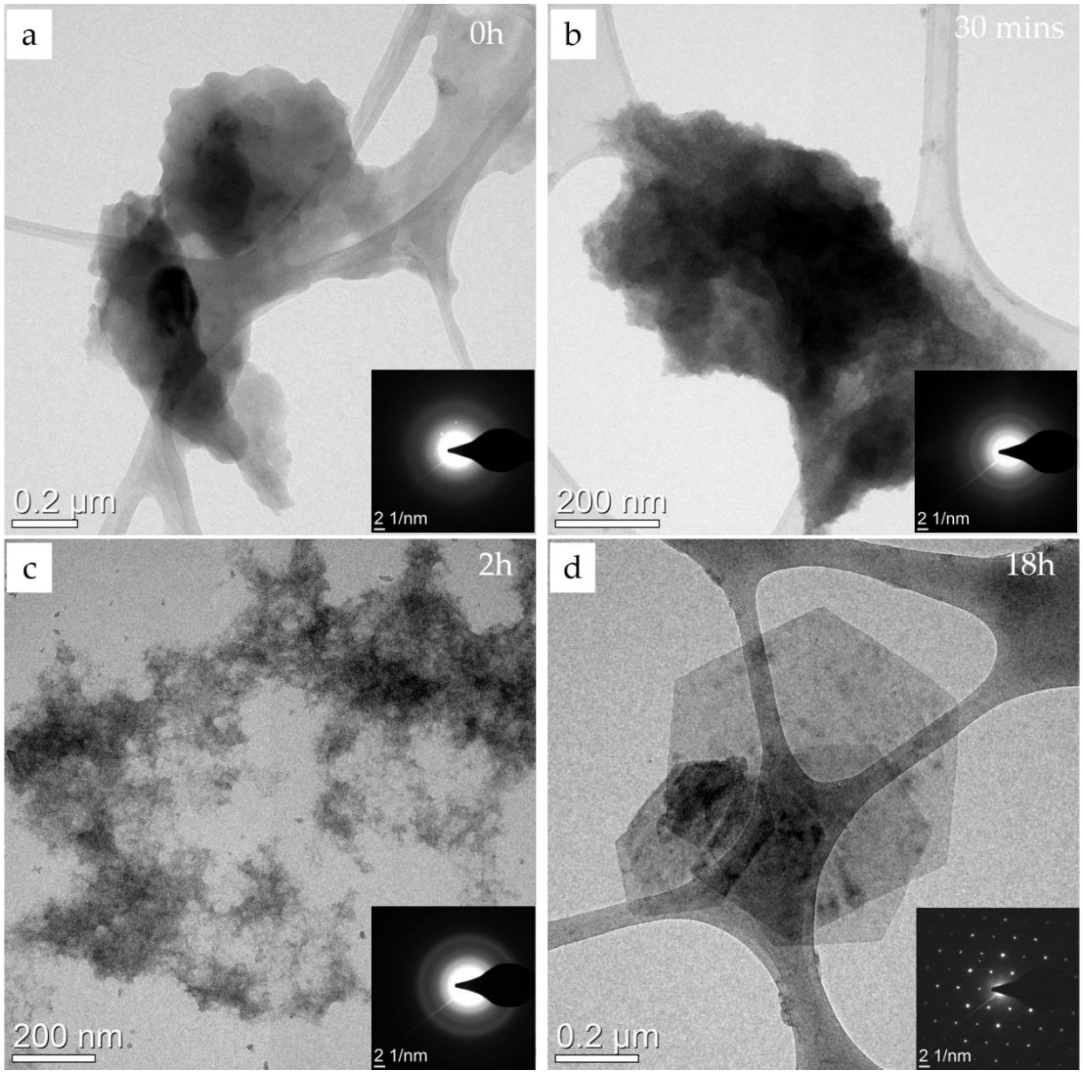

Figure 3.18 Aging properties of Ni-Fe LDH nanomaterials. Samples were characterized using BFTEM after (a) 0 mins, (b) 30 mins, (c) 2 hours and (d) 18 hours. Each image has a corresponding SAED pattern, shown inset.

Before hydrothermal treatment, the material in the reaction solution was found to be of a relatively thick irregular morphology as shown by BFTEM (Figure 3.18(a)). Furthermore, the initial starting material was deemed to be of an amorphous nature, as indicated by the lack of diffraction spots in the SAED pattern. As the suspension is heated at 100°C for 30 minutes, we saw similar features from our TEM analysis. Likewise, the aging solution has amorphous tendencies after 2 hours of aging at this temperature (Figure 3.18 (c)). However having established this, it was seen that the material has become much more dispersed on the TEM grids. The decrease in contrast at this time point shows that the material has become less agglomerated at this time

point. This perhaps suggests that the material is beginning to arrange itself toward an LDH crystal phase.

At longer timescales at 100°C, the metal salt suspension was viewed to undergo drastic changes. This was seen in both BFTEM and SAED analysis. The contrast in the TEM images show that the thin LDH hexagonal flakes have formed as a result of this hydrothermal treatment in solution. Correspondingly, the SAED patterns depict a well-defined hexagonal crystal structure, which we previously saw in the direct characterizations of the Ni-Fe LDHs in the previous section. We can also compare these aging behaviours to their Mg-Al counterpart. Despite the conflicting sizes of the Mg-Al and Ni-Fe platelets that were analysed, it is clear that the aging temperature has a pivotal role in the successful synthesis of these structures. In fact, the Ni-Fe LDH platelets rely on the elevated temperature, in this case 100°C, to attain such LDH crystal phases. On the contrary, we judged that elevated temperatures of the Mg-Al composition has a detrimental effect on the materials formation (Figure 3.8 (c)). Not only does the temperature affect the quality of the particle formed, it also can be seen that the Ni-Fe LDH platelets form at a much quicker rate than the smaller Mg-Al platelets. To illustrate this, the Mg-Al LDHs are fully formed into well-defined hexagonal morphologies when aged at 50°C, however this is on a time scale on the order of a days to occur (Figure 3.7 (b)). Conversely, the Ni-Fe LDH platelets of larger lateral dimension, attain this morphology in a matter of hours, as we have previously seen in Figure 3.18. On an additional note, these established aging properties may play a role in future developments, optimizations and up-scalability properties of such materials.

3.4 Electron beam interaction with LDHs

It was regularly observed that the all of the LDH materials underwent alterations, and more often than significant changes during TEM and STEM experiments. Figure 3.19 highlights a range of observed effects to both the Mg-Al and Ni-Fe LDH samples that occurred throughout the EM characterizations up to this point.

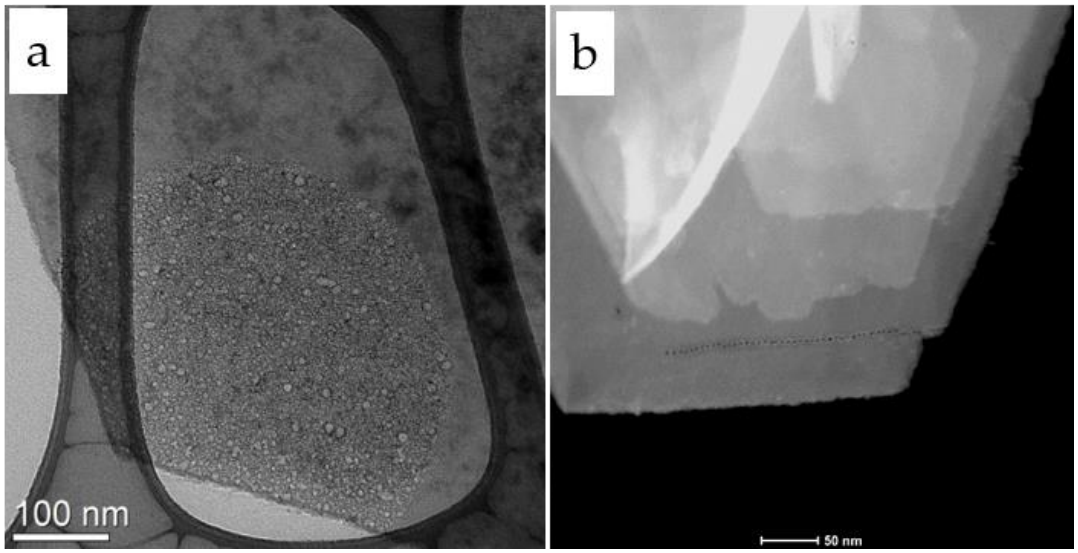

Figure 3.19 Typical (S)TEM observations of beam induced alterations and damages in LDH nanomaterials.

During the TEM experiments under such parameters, damages to the sample due to the incident electrons were clearly evidenced. Figure 3.19 displays typical damages to the LDH material after HRTEM and STEM analysis. When imaging at higher magnifications and at relatively higher dose rates in TEM, there was a rapid damage to the LDH material in imaged region (Figure 3.19 (a)). Also, the use of longer dwell times during EDX and EELS microanalysis experiments in STEM, often resulted in significant damage to the LDH specimen in the form of holes being formed in the platelets where the electron probe was incident on the sample (Figure 3.19 (b)). This provided motivation to investigate how the electron microscopes imaging conditions could be revised to determine if the observed features were indeed inherent of the material itself. As such, reducing the accelerating voltage of the electron gun results in incident electrons of lower energy and also a reduction in 'knock-on' damage to the sample. However by doing so, imaging at a lower incident voltage potentially promotes heating damage and further radiolysis to the sample.

These effects motivated the studies of this next section to understand how the electron beam can affect the physical and chemical features of both LDH compositions as well as mechanisms involved in these clear alterations and potential transformations to the material. A greater detailed study of the LDH interactions with the beam is provided using the Ni-Fe LDH sample. This was favoured over the Mg-Al LDH due to the

sample quality and study the Ni and Fe EELS edges that were in a suitable range for our experimental set-up to study potential elemental and bonding information. The Ni and Fe core loss L edges are abrupt well-defined features in the core loss EELS spectra and can be readily analysed with a reasonable drift tube shift of our Gatan GIF EELS spectrometer. In addition, these K edges are also relatively closer to the O K edge compared to the high energy losses of the Mg and Al K edges (both >1000eV). This deemed the Ni and Fe K core losses to be further suitable as they could be simultaneously acquired with the Oxygen K edge data with the available energy dispersions of the EELS spectrometer.

Recent infrastructure developments have permitted the alteration of the environmental conditions in which the Ni-Fe LDH could be characterized in the electron microscope using in-situ TEM specimen holders. These state-of-the-art technologies allows us to image and analyse the sample in many different environments as discussed in previous chapters. In relation to these experiments, we chose to apply the in-situ cryogenic sample holder, permitting characterizations of the specimens to be conducted at liquid nitrogen temperatures.

The influence of the electron beam on the crystalline nature of the Ni-Fe LDH platelets was investigated using dark field imaging in TEM, as shown in Figure 3.20. The sample was continuously exposed to the electron beam at an electron dose rate of 1.51 x 10^4 $e^-nm^{-2}s^{-1}$ and was repeatedly imaged at various time points. Figure 3.20(a) presents the initial dark field TEM image of the {100} plane. As previously found, this is due to the randomly orientated {100} domains across the whole LDH platelet.

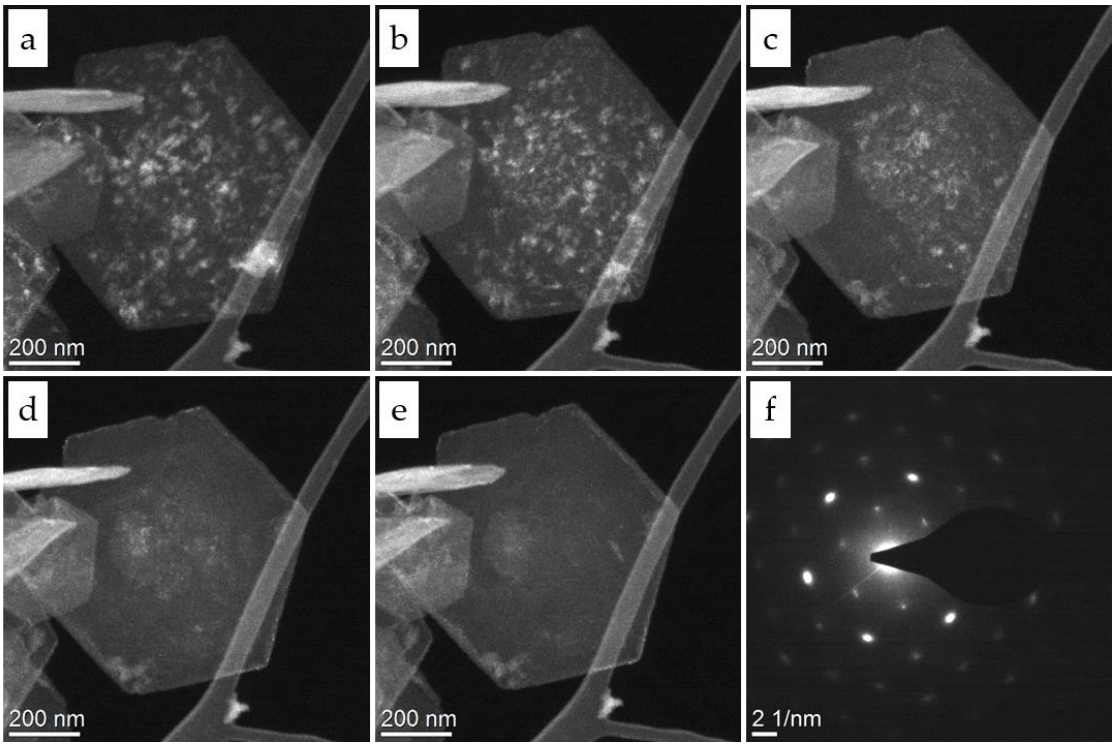

Figure 3.20 Dark field TEM of Ni-Fe LDH platelet corresponding to the {110} planes. Images were acquired after (a) 0 s, (b) 540 s, (c) 1800 s, (d) 2520 s and (e) 3600 s as they were subject to a continuous electron beam exposure at 300kV. (f) SAED pattern recorded from central platelet region after beam exposure of 3600 seconds.

The intensity of the dark field images reflects the crystalline decay of the material as it is subject to electron beam exposure. Initially, the bright intensity regions highlights the crystalline orientations of the {110} planes across numerous regions of the Ni-Fe LDH platelet (Figure 3.20 (a)). As the samples is exposed to the electron beam, the diminished intensity in the dark field images indicates a degradation of the LDH crystal (Figure 3.20 (e)). This behaviour can also be evidenced in the electron diffraction pattern recorded after the prolonged beam exposures. The intensity of the {100} spots is attenuated, suggesting a loss in crystal structure with regards to this family of planes. Although the existence of the diffraction spots post-imaging show that the LDHs have not been completely transformed to fully amorphous phases. However, the elongation and attenuated intensities of the {100} and also the {110} diffraction spots is indicative of a reorientation of the crystal and crystal degradation. Using similar approaches to our HRTEM studies (Figure 3.15), the effect of the beam degradations of the intensity profiles on these diffraction spots was studied, as shown

in Figure 3.23. The FWHM of the (100) and (110) diffraction spots were measured as 0.55 nm^{-1} and 0.54 nm^{-1} after the 300kV electron beam exposure. The effect of the previously mentioned intensity drop off was also effectively shown in the case of the (100) planes. In addition to the previously observed effects during HTREM (Figure 3.15), the periodicity of long-range order diffraction spots in the basal planes were also observed to disappear after the electron beam exposure. More precisely, the intensity of the {100} planes was observed to be reduced by the electron beam. This is studied more quantitatively later in this section. The {100} and {110} planar spacings were measured as 2.48 nm and 1.48 nm respectively (Figure 3.20 (f)), indicating a preservation of these inter-planar distances even after exposure to the electron beam as well as the overall main hexagonal symmetry.

We have previously established that a lower acceleration voltage of the electrons in the TEM beam results in greater heat induced damage but a reduction in atomic displacement of the sites in the studied material.[31] We chose to study this effect by subjecting the Ni-Fe LDH material to similar electron dose rates at 80 kV, monitoring the effect on the LDH crystalline properties using dark-field TEM imaging as above. Figure 3.21 presents the use of dark field TEM imaging to illustrate the effect of the electron beam on the crystalline properties of the Ni-Fe LDH nanomaterials.

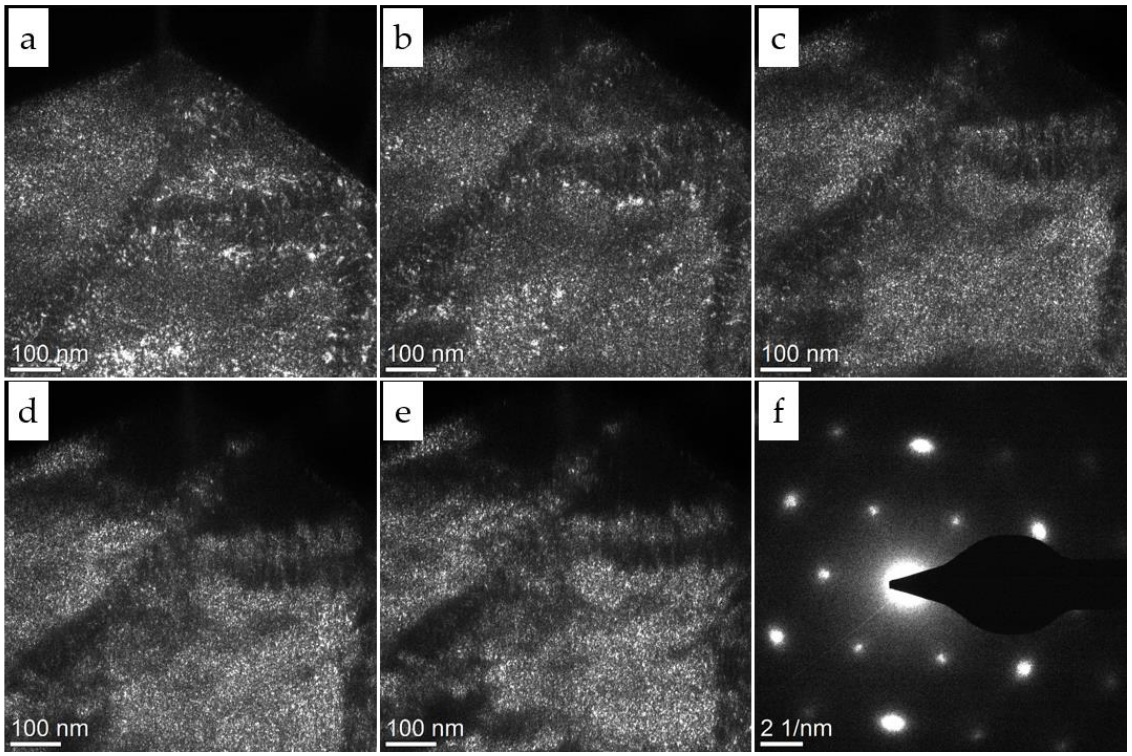

Figure 3.21 Monitoring beam degradations using dark field TEM imaging of Ni-Fe LDH platelet at 80 kV corresponding to the {110} planes. Images, corresponding to the {110} plane, were acquired after (a) 0 s, (b) 720 s, (c) 1620 s, (d) 2220 s and (e) 2820 s as they were subject to a continuous electron beam exposure. (f) SAED pattern recorded after exposures to the electron beam for 2820s.

The {110} plane was imaged in dark field as the sample was subjected to the electron beam at a dose rate of 1.31 x 10^4 $e^-nm^{-2}s^{-1}$. Over a time period of 2820 seconds, the variation in contrast of the dark field images (Figure 3.21 (a) and (e)) show that the crystallographic properties are indeed being altered, an effect we also observed at 300 kV (Figure 3.20). This is also illustrated in the electron diffraction pattern which was acquired after the prolonged electron beam exposure (Figure 3.21 (f)). The elongation of the diffraction spots also signifies a degradation of the LDH structure. To investigate the role of heat damage to the Ni-Fe LDHs crystal structure, we mirrored this degradation study at cryogenic temperatures in-situ. In fact, previous studies have also utilised cryogenic TEM sample holders as a method of prevention of beam-induced decompositions for hydride powder samples such as MgH_2. This also applies to the case of our LDHs which are prone to dehydrogenations by the electron beam. Figure 3.22 presents a similar timescale of electron beam exposure and simultaneous dark field images acquired after 0s, 720s, 1560s, 2160s and 2760s. In this case the platelets

were subjected to a similar dose rate of 1.21 x 10^4 $e^-nm^{-2}s^{-1}$ in comparison to non-cryogenic conditions at 80 kV. An analysis of the electron diffraction spot intensity profiles yielded FWHM evaluations of 0.39 nm^{-1} and 0.52 nm^{-1}. This contrasts the FWHM of the pristine material FWHM of 0.08 nm^{-1} and 0.12 nm^{-1}, highlighting the broadening and attenuation and hence distortion of the LDH lattice. Similar behaviours of the electron diffraction features were also observed at 300 kV (Figure 3.21).

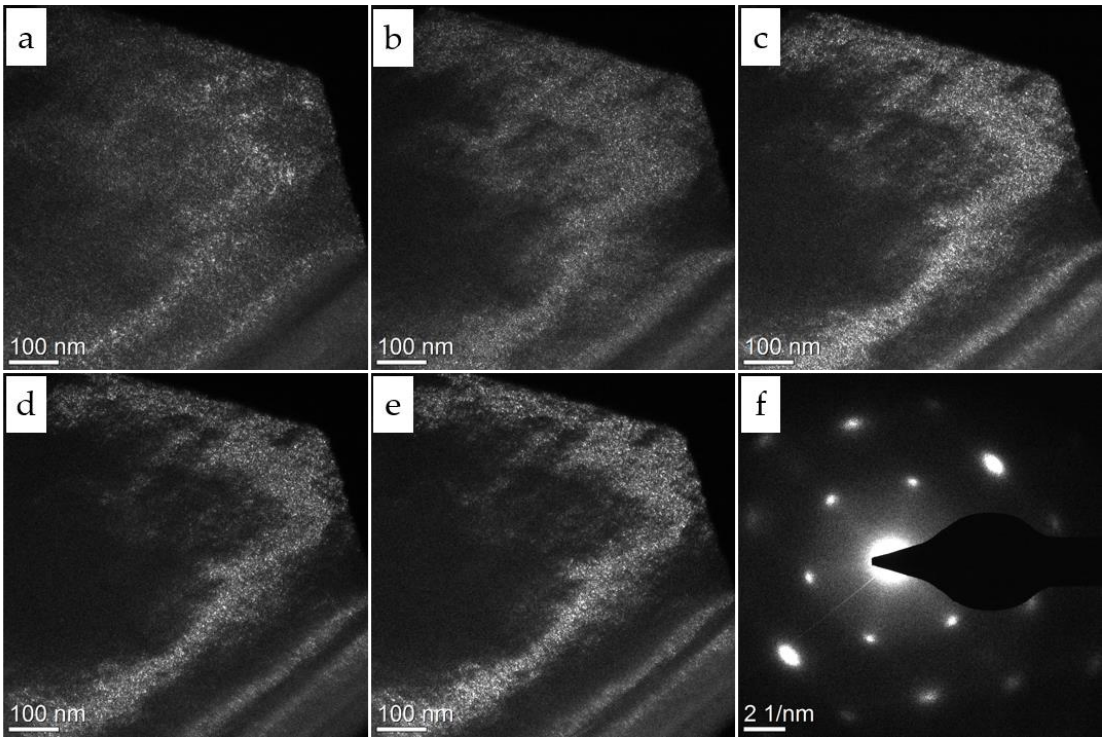

Figure 3.22 Monitoring beam degradations using dark field TEM imaging of Ni-Fe LDH platelet at 80 kV corresponding to the {110} planes at cryogenic temperatures. DFTEM images of the {110} plane were recorded after (a) 0 s, (b) 720 s, (c) 1560 s, (d) 2160 s and (e) 2760 s. (f) SAED pattern recorded after exposures to the electron beam for 2760s.

As the beam is exposed to the specimen, the loss of contrast on certain central platelet regions indicates a degradation of the {110} crystal plane structure of the Ni-Fe LDH. Once again, this is further reflected in the electron diffraction patterns recorded after the exposure, where a diffusion and elongation of the {110} diffraction spot denotes a crystallographic degradation of these planes. Moreover, further inspection of the electron diffraction pattern also shows an intensity attenuation of the {100}, which

shows that it is not just the higher order {110} planes that are subjected to damage. Even at lower acceleration voltages and lower temperatures, parallel behaviours are observed where the beam has induced a crystallographic rearrangement. This is signified by the FWHM of the {100} planes as
0.45 nm^{-1} and {110} as 0.59 nm^{-1}.

It is interesting to note that these effects occur at similar timescales both at column temperatures and cryogenic temperatures. It is hence speculated that the damages observed are not due to heating effects of the electron beam, and perhaps radiolysis and atomic displacement play a more prominent role in damaging the LDH structure.

The effect of the electron beam on the electron diffraction patterns was studied in a more quantitative fashion. Figure 3.23 presents intensity line profiles were acquired from the (100) and (110) diffraction spots after each experimental condition. Each pattern was acquired on the same FEI Titan microscope, at the same camera lengths and camera acquisition parameters so as to avoid any experimental discrepancies in comparing intensity profiles. Each data set intensities were normalized to highlight the effect of the broadening of the diffraction spots after each experimental condition.

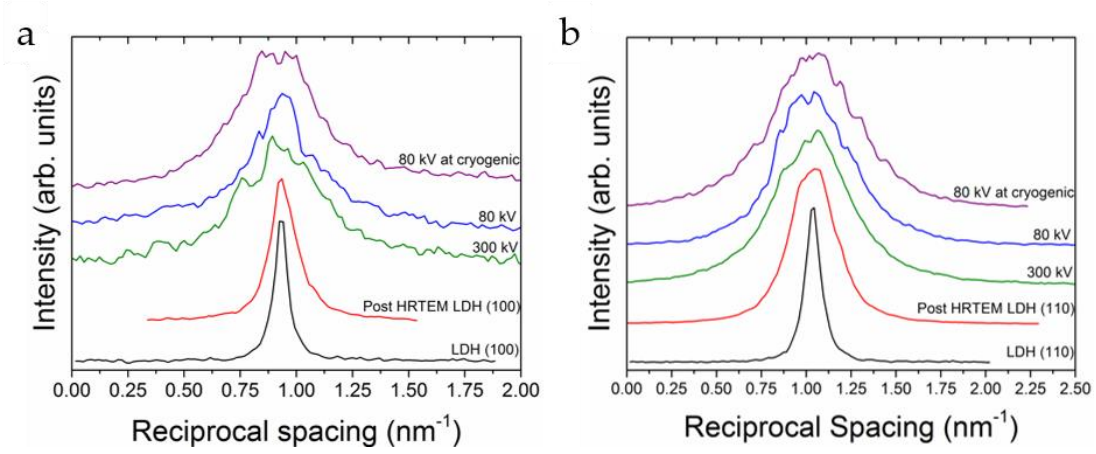

Figure 3.23 Intensity profiles of the (a) LDH (100) and (b) LDH (110) spots from the corresponding electron diffraction patterns acquired after different experimental conditions. Intensity values were normalized to compare broadenings of the diffraction spots. The different experimental conditions are presented as follows: LDH before imaging (black), after HRTEM experiments (red), beam degraded LDHs at 300 kV (green), beam degraded at 80 kV (blue) and beam degraded at 80 kV at cryogenic temperatures (purple).

Table 3.1 displays the FWHM of the (100), (110) and their respective intensity ratios in each case. A graphical representation of the intensity ratios can be found in the Appendix.

FIGURE	Experimental Condition	FWHM LDH(100) (nm^{-1})	FHWM LDH(110) (nm^{-1})	Intensity Ratio $\frac{I_{100}}{I_{110}}$
Figure 3.10 (b)	LDH only	0.08	0.12	0.62
Figure 3.15 (d)	Post HRTEM analysis	0.16	0.32	0.43
Figure 3.20 (f)	Beam degradations 300 kV	0.55	0.54	0.16
Figure 3.21 (f)	Beam degradations 80 kV	0.39	0.52	0.19
Figure 3.22 (f)	Beam degradations 80 kV(cryogenic)	0.45	0.59	0.21

Table 3.1 Full width half maximum and intensity ratios of the Ni-Fe LDH (100) and (110) diffraction spots as they are subjected to the different experimental conditions we have imposed in this section.

The FWHM of the (100) and (110) diffraction spots from the Ni-Fe LDH were observed to be of similar values irrespective of the beam conditions during induced degradation studies. In the (100) case, the FWHM increased from 0.08 nm^{-1} to 0.55 nm^{-1}, 0.39 nm^{-1} and 0.45 nm^{-1} for the 300 kV, 80 kV and 80 kV at cryogenic temperature experiments. Correspondingly, the FWHM of the (110) plane was initially evaluated as 0.12 nm^{-1}. This was observed to increase to 0.54 nm^{-1}, 0.52 nm^{-1} and 0.59 nm^{-1} for the 300kV, 80 kV and 80 kV at cryogenic temperature degradation studies respectively.

The intensity ratio of the (100) and (110) planes exhibited comparable features to the FWHM observations. Similar ratio values for the 300 kV (0.16), 80 kV (0.19) and 80 kV at cryogenic temperatures (0.21) were evidenced. This was attenuated from the 0.62 ratio value in the initial LDH characterizations. This suggests that the differing beam conditions did not significantly alter the extent of LDH sample degradations.

It must also be noted that the degradation studies occurred over a much longer time scale in comparison to HRTEM experiments, which may suggest a reasoning for the

less pronounced broadening in this case. This indicates that there are changes to the atomic positions within the structures unit cell but the overall lattice is preserved.

3.4.1 Low Dose Imaging of Ni-Fe LDHs

The previously established influences of the electron beam on the LDHs, raises the concern that these materials are indeed subject to structural alterations and even irreversible damage in some cases using these electron doses, as highlighted by TEM and STEM. In light of this, we characterized the LDH materials using a relatively lower electron dosage of incident electrons. This was achieved in TEM using a smaller condenser aperture to limit the number of incident electrons as well as reducing the current of the electron beam. It is also noted that in order to achieve sufficient signal beyond noise on the CCD camera at these lower dose rates, relatively longer image acquisition times were required (~10 seconds). By adopting such approaches to imaging the LDH samples assisted in verifying that the material properties were indeed inherent of the LDHs and not a beam induced effect. Figure 3.24 and Figure 3.25 display TEM images of the Ni-Fe LDH regions. We imaged the Ni-Fe LDH platelets at the same magnification where the latter was acquired at a 5 times lower dose rate (in units of e $nm^{-2}s^{-1}$).

Figure 3.25 presents a HRTEM image of the Ni-Fe LDH acquired using a low dosage approach. The arrangement of the lattice planes was still resolvable using this low dose approach. The corresponding inset FFT pattern presented a hexagonal symmetry with a lattice plane spacing of 2.64 nm. This was previously observed via electron diffraction methods, which was assigned the {101} planar families.

A similar case can also be viewed for the Mg-Al LDHs (Figure 3.26). The FFT pattern in this case resulted in a d-spacing evaluation of 2.61 nm. This same feature was also seen in the electron diffraction patterns of the Mg-Al material, corresponding to the {101} planes. Hence, imaging at lower electron doses confirms the previous findings are indeed inherent properties of the LDH materials. The images are enlarged for clarity and are found on the following page.

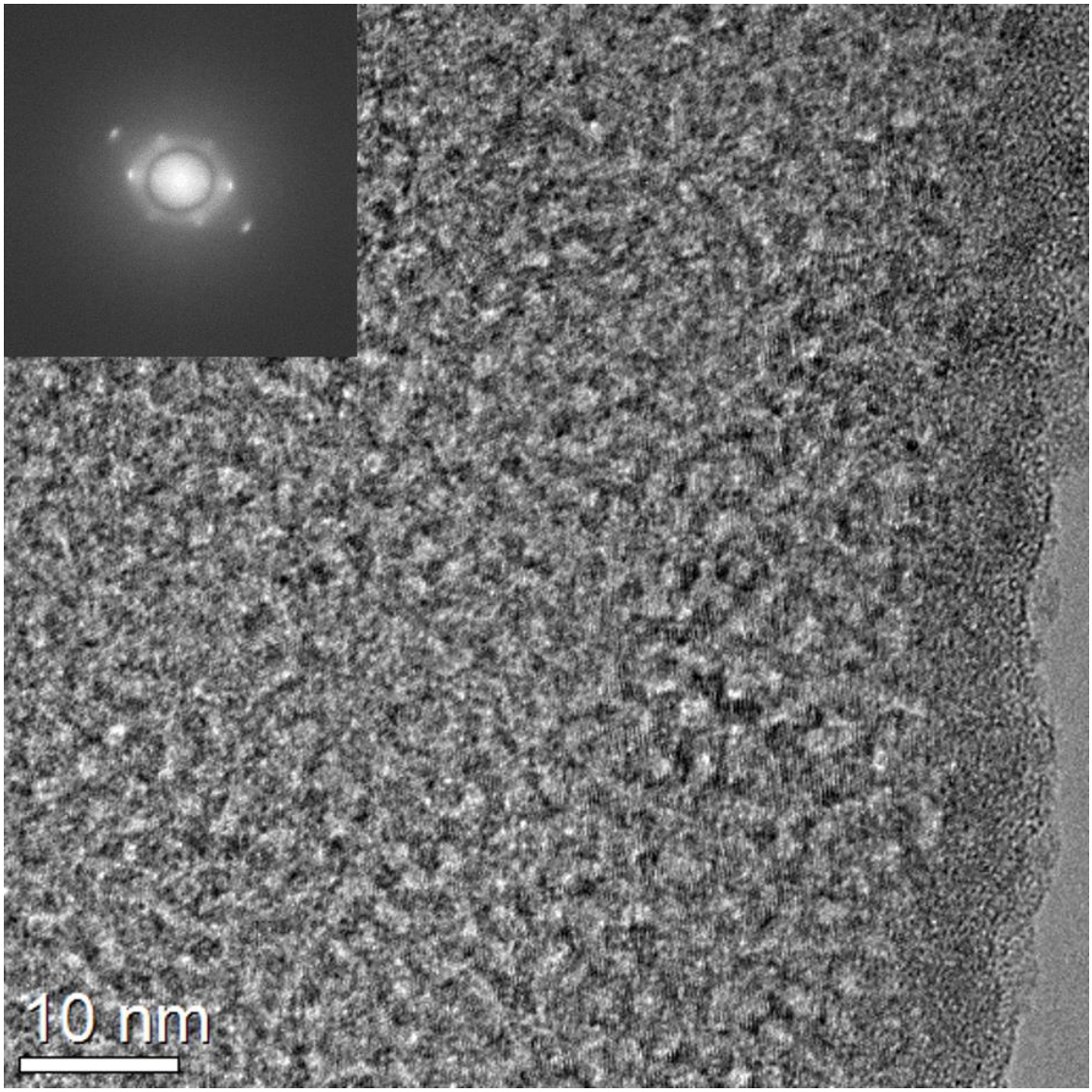

Figure 3.24 Standard dose HRTEM imaging of Ni-Fe LDH platelet. FFT of the image is inset. Reciprocal spots in the FFT correspond the {100} planes of the LDH structure. Image is purposely enlarged for clarity.

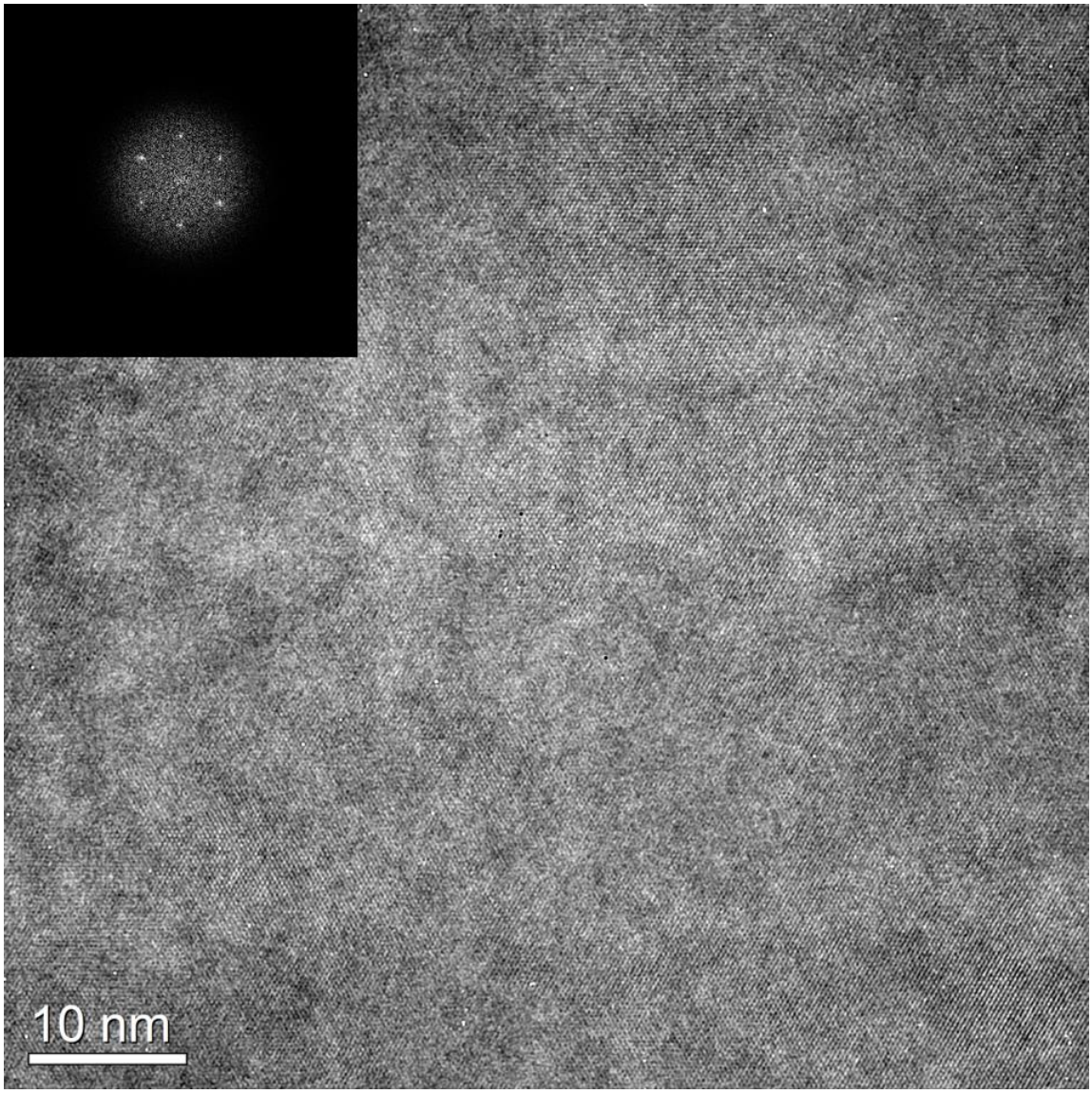

Figure 3.25 Low dose HRTEM imaging of Ni-Fe LDH platelet. Inset is the FFT of the whole image region. Reciprocal spots in the FFT correspond the {100} planes of the LDH structure. Image is purposely enlarged for clarity.

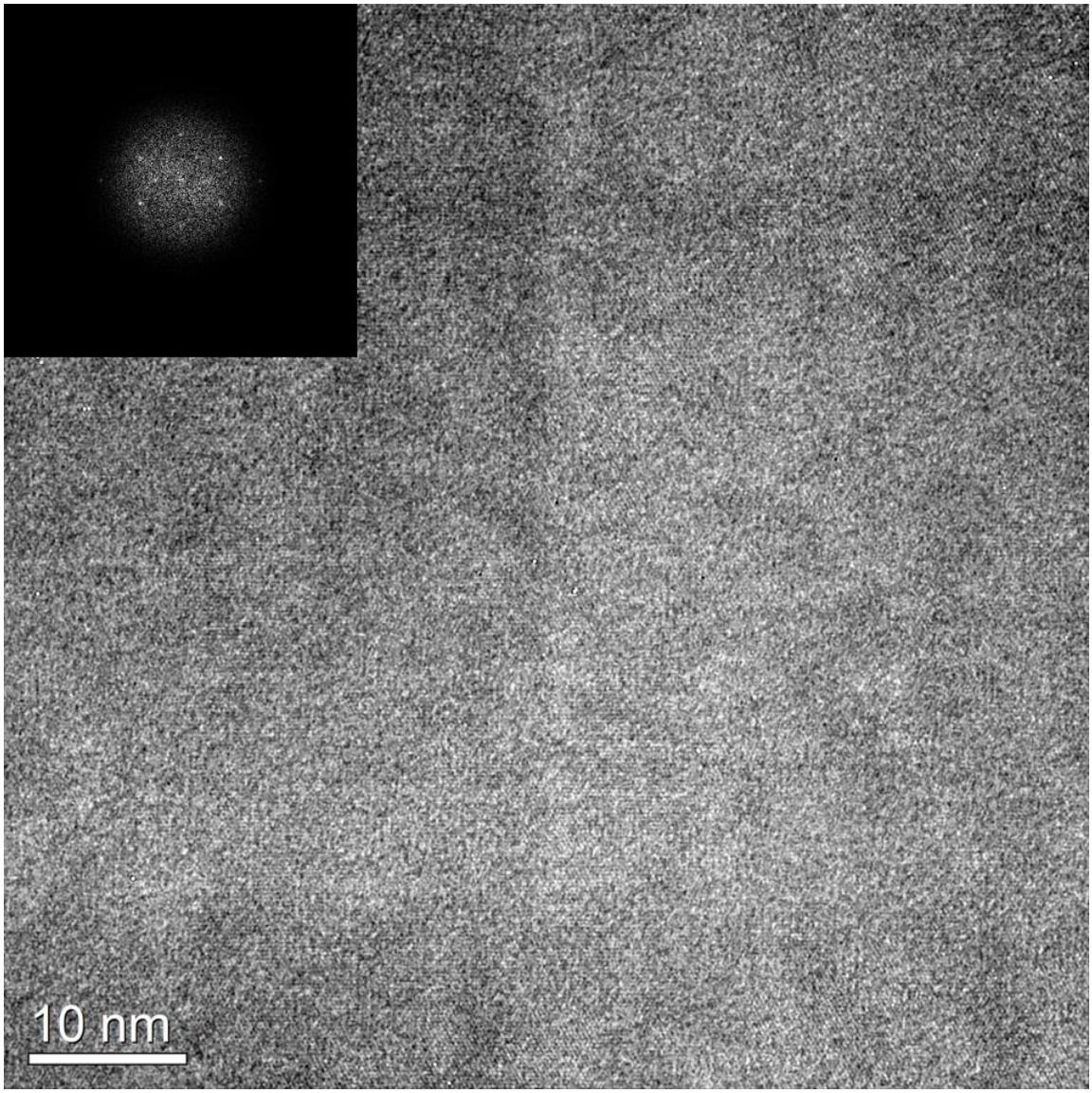

Figure 3.26 Low dose TEM imaging of Mg-Al LDH nanoplatelets. BFTEM image, with FFT inset, of the Mg-Al LDH material. Image is enlarged for easier visualisation of the resolved lattice planes. Image is purposely enlarged for clarity.

3.5 Electron beam effect on Ni-Fe LDH EELS spectra

It is clear that the influence of the electron beam has a profound effect on the structural properties of the Ni-Fe and Mg-Al LDH materials. In addition to the studies of the electron beam irradiation effect on the physical structure of the LDH materials, we also investigated its influence on the spectroscopic EELS features. This was conducted by continuously exposing a region of the Ni-Fe LDH to the scanning electron probe in STEM and acquiring EELS spectra of the Oxygen K-edge. In this setup, the LDH material was subjected to a STEM probe beam current of 0.46 nA. The Fe L_3 edge was also acquired to track any potential shift in the O K edge peaks. Figure 3.27 displays the EELS spectra at subsequent times during the electron beam irradiation.

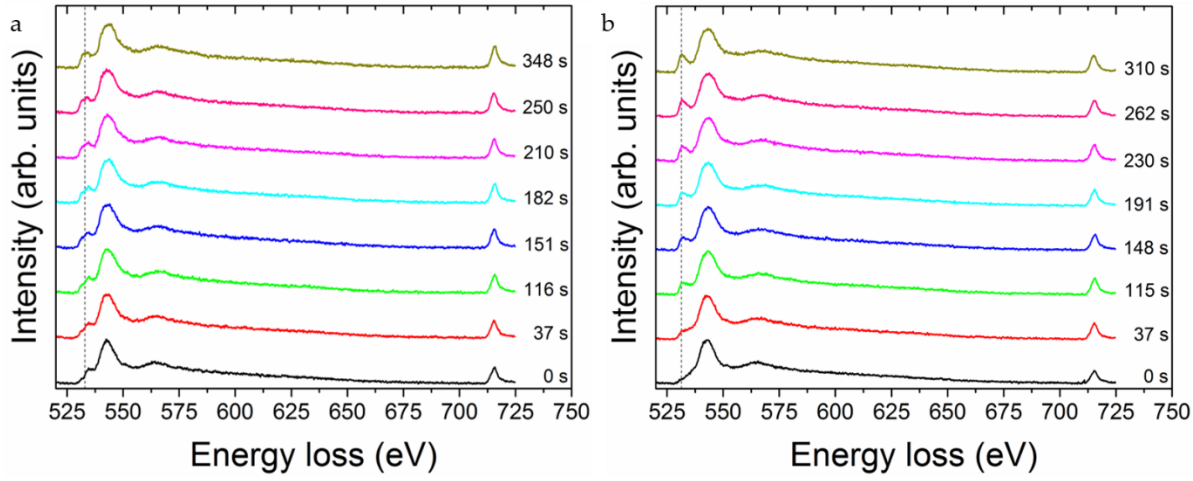

Figure 3.27 Evolution of the EELS O K-edge of Ni-Fe LDH due to electron beam irradiation. (a) STEM-EELS spectra recorded at evolving time points as the LDH sample was exposed to the electron beam column temperature. (b) STEM-EELS spectra acquired at successives time points after a new LDH platelet was exposed to the electron beam at cryogenic temperatures in-situ.

Firstly, at column temperatures, a shoulder in the delayed Oxygen K edge exists due to the presence of either Ni and/or Fe transition metal oxide bonding in the LDH structure. As the sample is exposed to the STEM probe, there is an evident change in the features of the oxygen K edge. In particular the shoulder of the O K edge appears to become more pronounced the longer the beam is irradiating the sample. In fact, this

shoulder progresses into its own peak, as is seen after 348 seconds of electron beam irradiation.

The species of oxide is difficult to determine due to the presence of both Ni and Fe transition metals in the initial LDH material. As well as that, the similarities in the EELS features of many different Fe oxide species further complicate the interpretation of such spectral features.[32] It is noteworthy that the evolved well-defined peak at 532 eV could derive from Fe_2O_3 or even Fe_3O_4 (magnetite) species, or even perhaps a NiO species.[33]

In order to further assess the transformation mechanisms involved in the electron beams effect on the LDH materials, a parallel study was carried out where the specimen was cooled to cryogenic temperatures using the in-situ cooling specimen holder. This would attenuate any transformation caused by localised heat damage by the scanning electron probe. Similar trends of evolution of the EELS peak before the Oxygen K-edge were also observed at cryogenic temperatures (Figure 3.27 (b)). It could be argued that the evolved peak becomes more pronounced at a quicker rate, suggesting that there is a different environment when imaging at low temperatures.

The electron beam irradiation effect on the EELS features at the Fe $L_{2,3}$ and M edges as well as Ni $L_{2,3}$ and M edges was also analysed using a similar approach. STEM- EELS spectra were acquired using a STEM probe current of 0.46 nA, with a convergence angle of 8 mrad and collection angle of 21 mrad. To highlight the fine structure EELS features, a dispersion of 0.05 eV/channel with an entrance aperture of 2mm was chosen on the GIF spectrometer. The zero loss FWHM was measured as 1.1 eV. 10 scans of each spectral region was recorded over the same 200nm x 200nm area. The integration times for the O K edge and Ni/Fe M edges were 4 secs and 0.4 secs summing over 5 and 3 spectra respectively. The Ni $L_{2,3}$,and Fe $L_{2,3}$ edges were acquired for 10 seconds summing 5 spectra in each scan.

Figure 3.28 shows the evolution of the Ni and Fe $L_{2,3}$ edges as the platelet is subjected to repeated scans over the same area of a Ni-Fe platelet. It is noted that in each case a fresh area of the Ni-Fe platelets was used to avoid any previous from prior EELS edge analyses.

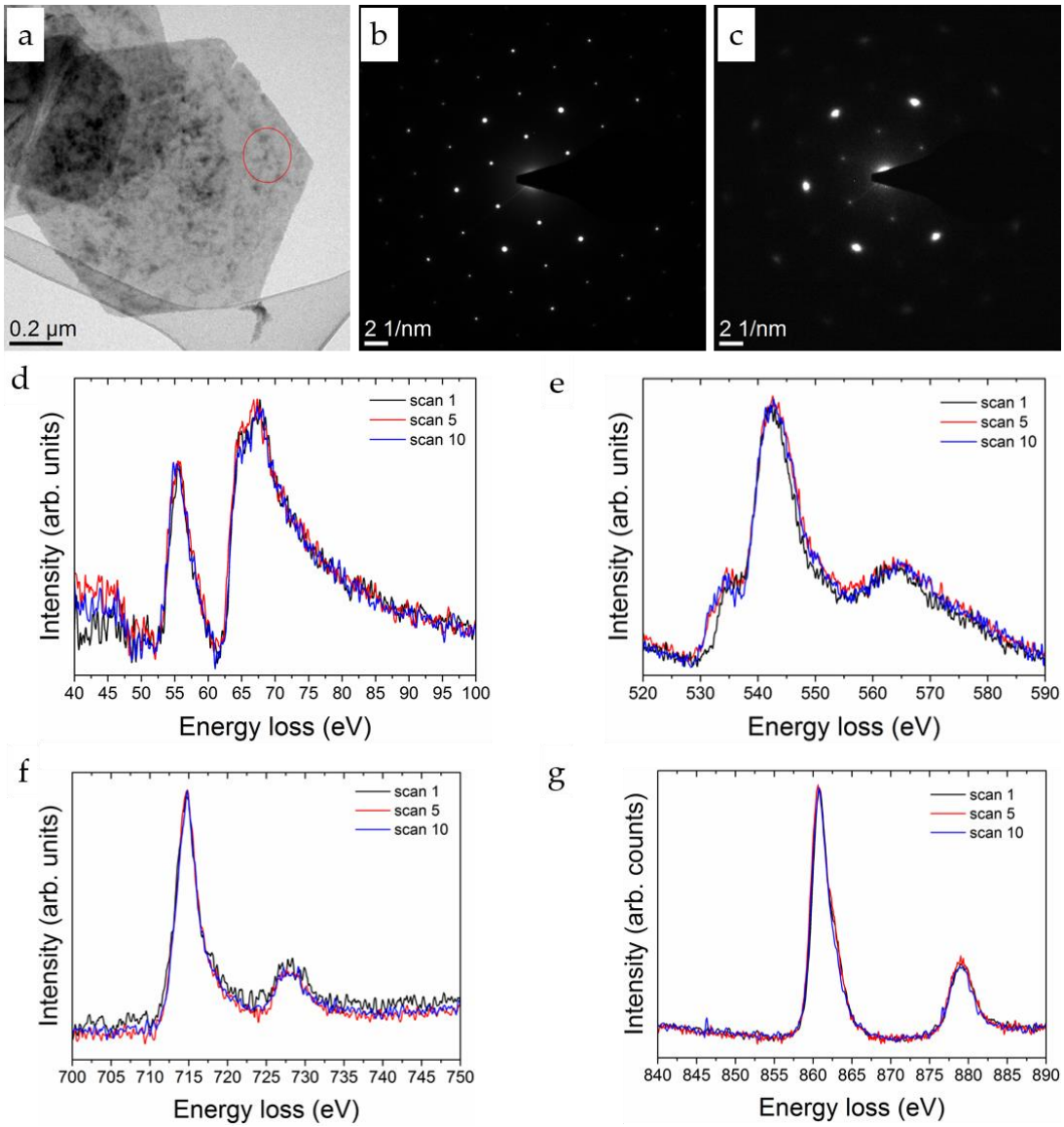

Figure 3.28 Fine structure EELS analysis of beam induced effects in Ni-Fe LDHs. (a) BFTEM image of the Ni-Fe LDH platelet studied using STEM-EELS. (b) and (c) present SAED patterns before and after EELS analysis respectively. (d) – (g) show EELS spectra of the Ni and Fe M edges, O K edge, Fe $L_{2,3}$ edge and Ni $L_{2,3}$ edge respectively as they are subjected to repeated scan acquisitions using STEM.

The Fe $L_{2,3}$ edge does not undergo any apparent transformation as it more scans are incident on the specimen. This preservation of the edge profile is also mirrored in the Ni $L_{2,3}$ edge (Figure 3.28 (b)). This indicates that there is no evident change in the bonding characteristics of the Fe sites in the LDH structures. Also, the distance between the L_2 and L_3 peaks and the white line ratio of these transition metals EEL spectra is maintained throughout the periods of electron irradiation, suggesting there

is no change in the oxidation states of either the Ni or Fe as a result of the electron irradiation.

3.5.1 Energy filtered TEM of Ni-Fe LDHs

Energy filtered TEM used to investigate the distribution of Ni and Fe and O throughout the Ni-Fe LDH sample. Figure 3.29 presents EFTEM maps of Ni-Fe LDH platelet regions. The EFTEM composite map highlights a random distribution of iron (red) and nickel (green) across the platelet. The greater intensities of Iron in Figure 3.29 (b) is speculated to be surface adhered excess iron and oxygen, possibly due to the formation of ferrihydrite or metal reagents used as precursors to synthesize the LDHs themselves. An analysis of the EFTEM O map (Figure 3.29 (d) and (e)) using an averaged intensity profile shows a greater intensity at the borders. A measurement of this oxygen rich region yields a thickness of approximately 6.5 nm. This effect is potential oxidation of the layer edges due to the greater accessibility of metallic sites relative to central regions of the Ni-Fe LDHs.

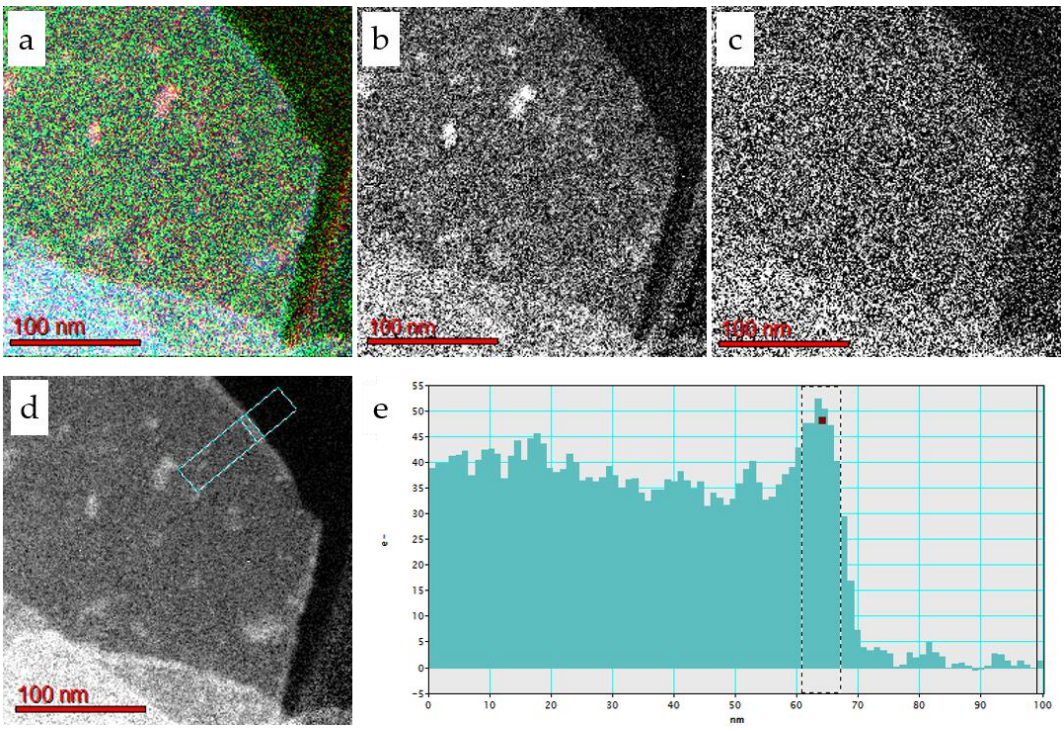

Figure 3.29 EFTEM studies of Ni-Fe LDH platelet. (a) Colour composite map of Fe (red), Ni (green) and O (blue). (b)-(d) Separate EFTEM maps of Fe, Ni and O respectively. (e) Extracted line profile from O EFTEM map in (d).

During EFTEM map acquisitions, the sample is subject to a prolonged exposure to the electron beam in order for a significant signal to noise ratio of the Ni, Fe and O signals in the acquired EELS spectra. As a consequence, the induced damage to the specimen was of concern when interpreting results of elemental distribution across the LDH platelet. The effect of the beam on the LDH material properties after EFTEM maps is highlighted in Figure 3.30.

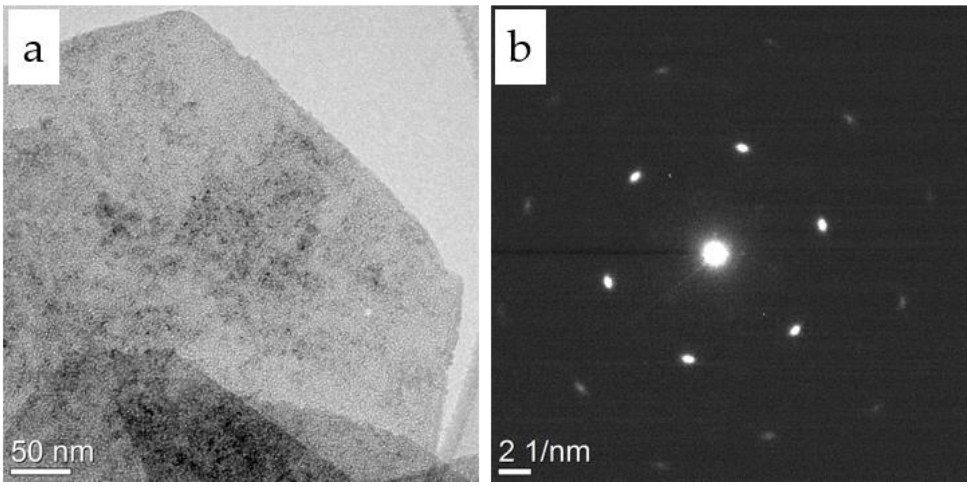

Figure 3.30 (a) BFTEM image and (b) SAED pattern after the EFTEM maps were acquired.

The effect of the electron beam was analysed post-acquisition of the EFTEM maps, as shown in Figure 3.30. BFTEM images of the mapped platelet showed a significant alteration to the sample. In addition, the electron diffraction pattern presents a loss of diffraction spots and the remaining spots appear diffused and elongated, suggesting a loss in crystal structure towards an amorphous material re-shuffling of ordered material. This also parallels the degradation study using dark field TEM (Figure 3.20). To validate these elemental distribution properties, we decided to utilise EDX mapping techniques in the SEM to avoid damages to the sample. The LDH platelets were imaged at 15 kV, a sufficient incident voltage to produce the K line x-rays of the Fe, Ni and O in the LDH layers. Although there is a drop off in resolution using this incident voltage, the desired information could be extracted from the elemental map data. Figure 3.31 highlights a homogenous distribution of Fe, Ni and O across the platelets, as was corroborated in the previous EFTEM data (Figure 3.29). In addition,

the LDH morphology appeared to be well preserved even after the SEM EDX map experiments. This structural preservation is shown by imaging the sample after the EDX map was acquired (Figure 3.31).

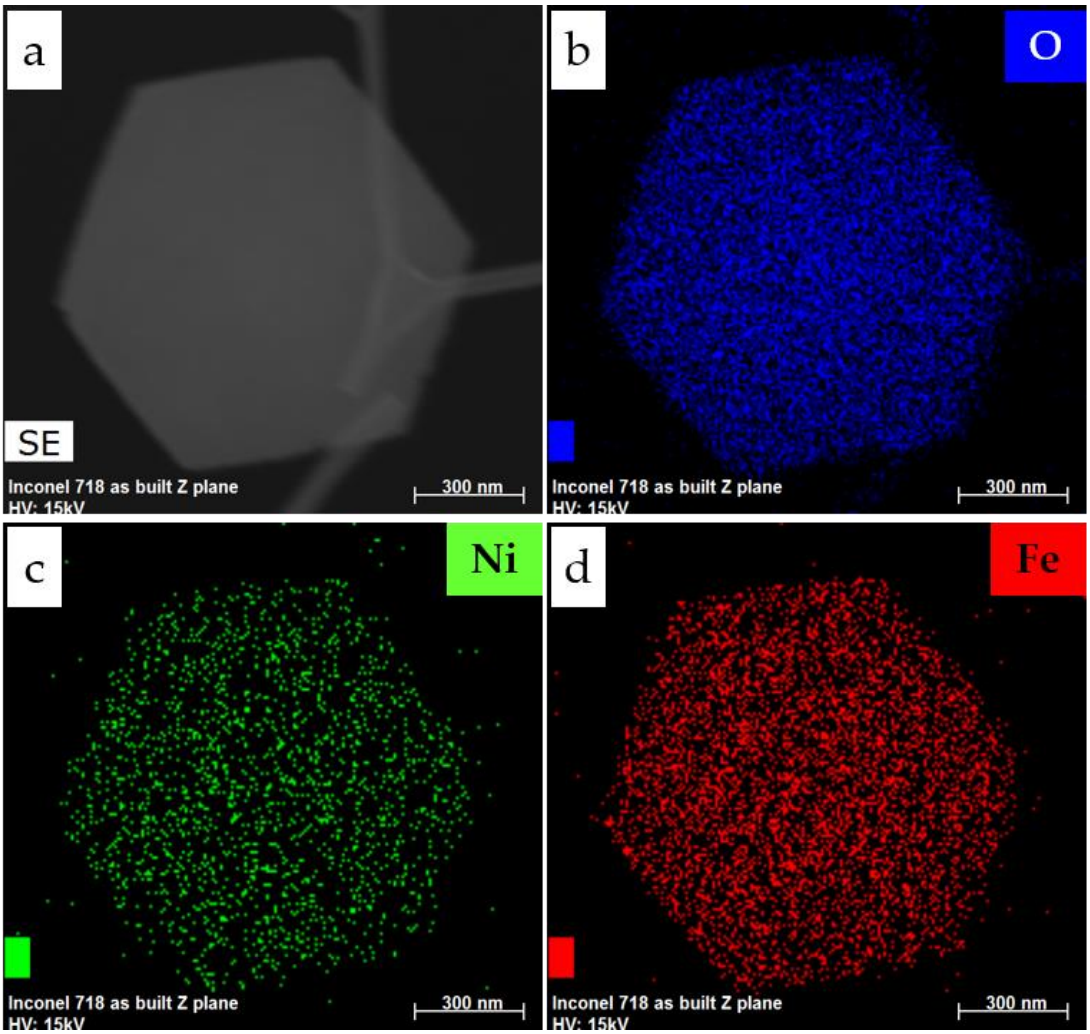

Figure 3.31 SEM EDX map of Ni-Fe LDH platelets at 15kV. (a) Standard secondary electron image of mapped region. Elemental maps of (b) Oxygen, (b) Nickel and (c) Iron are displayed as blue, green and red respectively. The scale bar in each image is 300nm.

3.6 Conclusions

Mg-Al and Ni-Fe LDH nanomaterials were extensively characterised using TEM/STEM approaches, including EDX and EELS. The LDH materials were found to attain a hexagonal morphology of single crystalline nature with a well-defined hexagonal symmetry. These features were found to be independent of the cationic layer metallic species. Moreover, dark field TEM and ac-STEM characterizations showed that the Ni-Fe LDH, although still single crystalline, was composed of randomly arranged crystallite domains.

In both compositions, the LDH materials were found to be susceptible to damage due to the electron beam interaction. Electron diffraction and dark field TEM studies showed that the electron beam degraded the crystalline qualities of both the Mg-Al and Ni-Fe LDH materials. This behaviour was observed at both 300kV and 80kV, as well as imaging at cryogenic temperatures. Hence it was found that the TEM imaging conditions did not significantly vary the damaging mechanisms of the LDH materials.

The synthesized LDH materials could also be studied via EM spectroscopic techniques such as EDX, EFTEM and EELS. EFTEM and EDX maps showed that the Ni, Fe and O were randomly distributed across the LDH nanosheet as well as a potential oxidation at the edge of the platelets. Moreover, different features in the EELS spectra were due to the compositional difference between the Mg-Al and Ni-Fe LDHs. A noteworthy difference was the presence of a pre-shoulder in the oxygen edge for the Ni-Fe LDH. The electron beam also had a significant effect on the EELS spectra, particularly in the O K edge of the Ni-Fe LDH sample. The pre-shoulder of the delayed O K edge was found to evolve into an independent peak as a consequence of electron beam irradiation. This evolution was seen to occur both at column temperatures as well as cryogenic temperatures in-situ. This oxygen edge shoulder evolved into an independent peak highlighting the existence of a transition metal oxide after electron beam exposure. This effect was speculated to be a dehydration of the hydroxyl groups and interstitial water in the Ni-Fe LDH sample.

The features unveiled in this chapter will provide excellent reference point and comparisons of the material when they are applied in future chapters of this thesis. The collective EM findings and data interpretations also provide an adequate establishment of the material properties for future chapters to progress the studies involving both Mg-Al and Ni-Fe LDH nanomaterials. Ultimately, this chapter will serve as a basis for future studies of this thesis where we take the synthesized LDHs and probe their behaviours in more applied but also more realistic environments in nanotechnology.

3.7 Bibliography

1. Vijaikumar, S., Dhakshinamoorthy, A. & Pitchumani, K. L -Proline anchored hydrotalcite clays : An efficient catalyst for asymmetric Michael addition. *Appl. Catal. A Gen.* **340,** 25–32 (2008).

2. Dumbre, D. K. *et al.* Thermally decomposed mesoporous Nickel Iron hydrotalcite : An active solid-base catalyst for solvent-free Knoevenagel condensation. *J. Colloid Interface Sci.* **441,** 52–58 (2015).

3. Zhou, T. *et al.* Preparation and Characterization of Layered Precursor Nickel - Iron Hydrotalcites and Magnetic Materials. *Acta Chim. Sin.* **60,** 1078–1083 (2002).

4. Boukraa, F. B. D. S., Su, B. & Bettahar, N. Nickel – iron layered double hydroxide (LDH): Textural properties upon hydrothermal treatments and application on dye sorption. *J. Hazard. Mater.* **165,** 206–217 (2009).

5. Mourad, M. C. D. *et al.* Activation and local structural stability during the thermal decomposition of Mg / Al-hydrotalcite by total neutron scattering. *J. Mater. Chem.* **21,** 15479–15485 (2011).

6. Matusinovic, Z. & Wilkie, C. A. Fire retardancy and morphology of layered double hydroxide nanocomposites : a review. *J. Mater. Chem.* **22,** 18701–18704 (2012).

7. Dai, C., Tian, D., Li, S. & Li, X. Methotrexate intercalated layered double hydroxides with the mediation of surfactants : Mechanism exploration and bioassay study. *Mater. Sci. Eng. C* **57,** 272–278 (2015).

8. Gong, M. & Dai, H. A mini review of NiFe-based materials as highly active oxygen evolution reaction electrocatalysts. *Nano Res.* **8,** 23–39 (2015).

9. Gong, M. *et al.* An advanced Ni-Fe layered double hydroxide electrocatalyst for water oxidation. *J. Am. Chem. Soc.* **135,** 8452–8455 (2013).

10. Dionigi, F., Reier, T., Pawolek, Z., Gliech, M. & Strasser, P. Design Criteria , Operating Conditions , and Nickel – Iron Hydroxide Catalyst Materials for Selective Seawater Electrolysis. *ChemSusChem* **9,** 962–972 (2016).

11. Hobbs, C. *et al.* Structural transformation of layered double hydroxides : an in situ TEM analysis. *npj 2D Mater. Appl.* **2,** (2018).

12. Jaśkaniec, S., Hobbs, C., Seral-ascaso, A. & Co, J. Low-temperature synthesis and investigation into the formation mechanism of high quality Ni-Fe layered double hydroxides hexagonal platelets. 4–11 (2018). doi:10.1038/s41598-018-22630-0

13. Dieckmann, Y., Colfen, H., Hofmann, H. & Petri-fink, A. Particle Size Distribution Measurements of Manganese-Doped ZnS Nanoparticles. *ACS Anal. Chem.* **81,** 3889–3895 (2013).

14. Michen, B. *et al.* Avoiding drying-artifacts in transmission electron microscopy : Characterizing the size and colloidal state of nanoparticles. *Sci. Rep.* **5,** 9793 (2015).

15. Domingos, R. F. *et al.* Characterizing Manufactured Nanoparticles in the Environment : Multimethod Determination of Particle Sizes. *ACS Environ. Sci. Technol.* **43,** 7277–7284 (2009).

16. Song, F. & Hu, X. Exfoliation of layered double hydroxides for enhanced oxygen evolution catalysis. *Nat. Commun.* **5,** 1–9 (2014).

17. Lin, H., Zhang, Y., Wang, G. & Li, J. B. Cobalt-based layered double hydroxides as oxygen evolving electrocatalysts in neutral electrolyte. *Front. Mater. Sci.* **6,** 142–148 (2012).

18. Hu, G. & O'Hare, D. Unique layered double hydroxide morphologies using reverse microemulsion synthesis. *J. Am. Chem. Soc.* **127,** 17808–17813 (2005).

19. Roelofs, J. C. A. A., Bokhoven, J. A. Van, Dillen, A. J. Van, Geus, J. W. & Jong, K. P. De. The Thermal Decomposition of Mg ± Al Hydrotalcites : Effects of Interlayer Anions and Characteristics of the Final Structure. *Chem. Eur. J.* **24,** 5571–5579 (2002).

20. Ahn, C. C. & Krivanek, O. . *EELS Atlas: a reference collection of electron energy loss spectra covering all stable elements*. (Warrendale : Gatan, 1983).

21. Sieber, I. *et al.* Preparation of thin polycrystalline silicon films on glass by aluminium-induced crystallisation—an electron microscopy study. *Thin Solid Films* **427,** 298–302 (2003).

22. Feldhoff, A., Pippel, E. & Woltersdorf, J. Interface engineering of carbon-fiber reinforced Mg-Al alloys. *Adv. Eng. Mater.* **2,** 471–480 (2000).

23. Xu, Z. P., Stevenson, G., Lu, C.-Q. & Lu, G. Q. (Max). Dispersion and Size Control of Layered Double Hydroxide Nanoparticles in Aqueous Solutions. *J. Phys. Chem. B* **110,** 16923–16929 (2006).

24. Liang, H. *et al.* Hydrothermal Continuous Flow Synthesis and Exfoliation of NiCo Layered Double Hydroxide Nanosheets for Enhanced Oxygen Evolution Catalysis. *Nano Lett.* **15,** 1421–1427 (2015).

25. Jaskaniec, S. *et al.* Low-temperature synthesis of high quality Ni-Fe layered double hydroxides hexagonal platelets. *Sci. Rep.* **8,** 4–11 (2018).

26. Han, N., Zhao, F. & Li, Y. Ultrathin nickel-iron layered double hydroxide nanosheets intercalated with molybdate anions for electrocatalytic water oxidation †. *J. Mater. Chem. A* **3,** 16348–16353 (2015).

27. Abellán, G., Coronado, E., Martí-Gastaldo, C., Pinilla-Cienfuegos, E. & Ribera, A. Hexagonal nanosheets from the exfoliation of Ni2+-Fe3+LDHs: A route towards layered multifunctional materials. *J. Mater. Chem.* **20,** 7451–7455 (2010).

28. Pan, C. T. *et al.* In-situ observation and atomic resolution imaging of the ion irradiation induced amorphisation of graphene. *Sci. Rep.* **4,** 1–7 (2014).

29. Kim, J. H., Kim, K. & Lee, Z. The Hide-and-Seek of Grain Boundaries from Moiré Pattern Fringe of Two-Dimensional Graphene. *Sci. Rep.* **5,** 1–9 (2015).

30. Forticaux, A., Dang, L., Liang, H. & Jin, S. Controlled Synthesis of Layered Double Hydroxide Nanoplates Driven by Screw Dislocations. *Nano Lett.* **15,** 3403–3409 (2015).

31. Willams, D. B. & Carter, C. B. *Transmission Electron Microscopy: A Textbook for Materials Science*. (Springer, 2009).

32. Colliex, C., Manoubi, T. & Ortiz, C. Electron-energy-loss-spectroscopy near-edge fine structures in the iron-oxygen system. *Phys. Rev. B* **44,** 11402–11411 (1991).

33. Mitterbauer, C. *et al.* Electron energy-loss near-edge structures of 3d transition metal oxides recorded at high-energy resolution. *Ultramicroscopy* **96,** 469–480 (2003).

Chapter 4: Structural characterization of LDH materials in thermal environments

4.1 Introduction

Our TEM characterizations in the preceding chapter provided a substantial wealth of physical information of the LDH nanomaterials. Now looking forward, we will investigate where these nanomaterials can be applied in nanotechnology as well as their behaviours in such fields. Even a brief perusal into the literature shows that LDHs are fast becoming a leading candidate across many fields of industrial and academic research.[1–3]

Having said that, a further exploration into the world of layered double hydroxides research reinforces the diversity and applicability of this class of nanomaterials. In addition to the range of inherent properties of LDHs utilised in applications such as medicine and energy storage, these materials can also be used as a precursor to generate new structures. Primarily, these new phases are achieved by subjecting the precursor LDH materials to thermal treatments at elevated temperatures. In fact, this calcination of LDH materials in general has received an abundance of attention from both an applications and scientific perspective.

As we have previously mentioned, these calcinations have been exhausted in catalysis. In particular, these metal oxides and spinel structure composites contribute to the enhancement of catalytic properties across several related fields including nanocatalyst design,[4–6] hydrogenation[7] and photocatalysis.[8–10]

Beyond catalysis, the thermal treatment of LDH materials has also found recent success in the other areas such as flame retardants. The incorporation of the lamellar structures into polymer materials has shown beneficial results of thermal stability, melting temperatures, smoke suppression as well as an attenuation of peak heat release rate in a number of cases[11–16]. This is owed to the favourable thermal decomposition mechanisms of H_2O and CO_3^{2-} release as well as char coating formation which reduces fuel availability and heat release.[17,18]

The calcination of LDHs have also been used in magnetic applications.[19] The enhanced magnetic stabilities are due to strong interfacial interactions between thermally evolved phases.[20]

In the literature, the thermal degradation procedures themselves have also been well established and described via a complex procedure of dehydration, dehydroxylisation and decarbonisation of the lamellar material. It is also conveyed that factors such as composition, morphology,[21] structure[22] and atmospheric conditions[23] can affect these calcination mechanisms. More generally, many studies have utilized this in their calcination procedures for applications in oxygen evolution,[24] photocatalysis,[25] and catalytic supports.[26,27] Evidently, the thermal decomposition of the LDH structures plays an important role in both catalytic performance, flame retardant properties and magnetic stabilities of LDH nanocomposites.

Despite this extensive work throughout such areas of research, the majority of these reports have largely relied on macroscopic characterization techniques such as X-ray diffraction (XRD), Fourier transform infrared spectroscopy (FTIR) and thermogravimetric analysis (TGA).[23,28–31] A fall-back of the related literature is the lack of in-depth EM based characterization to understand the thermal evolutions of the LDH materials. Most studies have only focussed on SEM techniques as well as post-calcination analysis using basic TEM imaging. In addition to these characterization techniques, research on this subject has been limited to this pre- and post- mortem EM information. However, this approach cannot elucidate on how to optimize the processes that occur under real time conditions at single nanoparticle level. As a consequence, far too little attention has been paid to how the LDHs attain such transformed phases and its ability to recover their phases from mixed metal oxides. This in turn has led to controversial opinions in the literature about the rehydration mechanisms of calcined LDHs.[32,33] As such, an understanding of the mechanisms of such calcination procedures is of critical importance for the optimization of materials development as well as prospective applications of LDH materials in future applications. Determining the correct structure-property-function relationships requires a detailed description of the material in its working state. In light of this past,

current and divisive research, we aspired to understand the effect of thermal environments on the properties of LDH nanomaterials by applying afore mentioned high-end techniques of in-situ transmission electron microscopy. Fortunately, recent technological advances in EM allow us to image materials with a range of *in-situ* techniques that have been developed to follow the evolution of materials in the presence of such external stimuli. In addition to observing materials in their working state, *in-situ* techniques can also capture important intermediate transitional forms that may be involved in phase transformations. As such, previous research acknowledges that these exact transformations in which the LDH decomposes are not fully understood.[34–36]

This experimental chapter aims to unravel the nanoscale behaviours surrounding the thermal decomposition of our previously studied Mg-Al and Ni-Fe LDHs using in-situ transmission electron microscopy. An additional aim of this chapter is to assess how the conditions of thermal treatment of the LDH nano-platelets affects the structural properties of the calcined products at the nano and atomic scales. EM characterizations from ex-situ heating experiments for both LDH compositions will be presented to parallel the studies from the in-situ TEM work. In addition, the properties of the thermally treated LDH material, in both from both in-situ and ex-situ cases, are investigated using the high-end techniques of transmission electron microscopy which were utilised in the previous chapter.

This study provides an exciting opportunity to take advantage of previously learned knowledge of our LDH materials and the knowledge of our instrumentation capabilities. In doing so, we will bring the LDH materials to life at the nanoscale in these real environments.

4.2 Experimental Details

4.2.1 TEM sample preparation

In-situ TEM experiments: Samples were prepared by suspending the synthesised LDH materials in deionized water and sonicating for 30 minutes. Subsequently, 5µl of the associated samples were subsequently placed on DENSsolutions Nano-chips™ for *in-*

situ experiments respectively. Excess sample was wicked away using filter paper and then air dried for approximately 30 minutes each before TEM analysis. *Ex-situ* heated Ni-Fe samples were prepared for TEM analysis by directly depositing the powder forms of the materials onto lacey Carbon TEM Cu grids (TED Pella Inc., USA).

Ex-situ heated samples and preparation: Samples were also heated using a furnace where powders of the sample were heated using this heating ramp set-up. To prepare TEM samples, powders were lightly placed onto the TEM grids. The grids were also placed face up onto powder samples for approximately 60 secs. Excess powder was removed using gentle N_2 gas flow on the grids. Similarly, we prepared ex-situ heated samples by first drop-casting the same dispersion of Ni-Fe LDHs from in-situ experiments onto a SiN window. This grid was the heated at 850°C for 6 hours in a conventional laboratory oven.

4.2.2 In-situ TEM experimental conditions

Transmission electron microscopy (TEM) was used to characterize the overall morphology and crystallographic structure of the associated LDH samples. TEM and selected area electron diffraction (SAED) were conducted on a FEI Titan300 (FEI, Oregon, USA), operated at 300kV. For comparative purposes of the *in-situ* heating experiments, TEM magnifications and electron diffraction camera lengths were kept constant. *In-situ* heating TEM experiments were conducted using a DENS Solutions Wildfire™ TEM holder (DENSsolutions, Delft, The Netherlands). This experimental *in-situ* TEM sample holder set up consists of a microelectricalmechanical systems (MEMS) chip design with electron transparent Silicon Nitride windows onto which the sample is deposited.

LDH materials were subject to 250°C for 2 hours followed by an increment to 450°C for 2 hours, held at 450°C for 2 hours and then followed by an increase to 850°C at a rate of 10°C/min. The heating ramp was held at this temperature for 2 hours also. A visualisation of such heating protocols can be viewed in Figure 4.1.

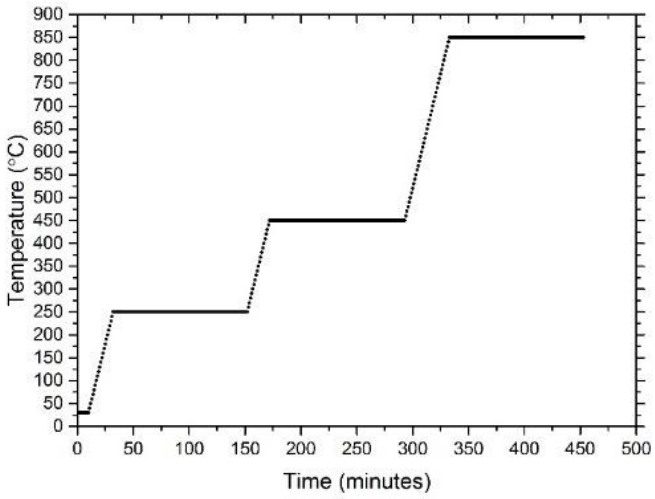

Figure 4.1 Graphical representation of heating ramp conditions applied in both in-situ and ex-situ experiments.

4.2.3 Microanalytical EELS experimental details

Thermal evolution of EELS spectra: The thermal evolution of the O K, Fe $L_{2,3}$ and Ni $L_{2,3}$ core loss edges was studied using the DENS Wildfire in-situ TEM holder and the Gatan Imaging Filter. The Ni-Fe LDH was heated up to 850°C in increments of 50°C and held at each interval for 10 minutes. For the EELS analysis, the STEM probe current was approximately 0.46 nA and had a 10 mrad convergence angle and 21 mrad collection angle (camera length 38mm). A 2mm entrance aperture was used with a dispersion of 0.5 eV/channel and an energy resolution of 1.05 eV. The associated spectra at each temperature gradient from a 200nm x 200nm region with an integration time of 5 seconds, summing over 5 spectra in each measurement. New regions of interest were used at each temperature stage.

EELS characterizations of ex-situ calcined platelets: STEM-EELS studies were performed using the GIF. A STEM probe of 0.46 nA with respective convergence and collection angles of 8 mrad and 21 mrad were used. The energy resolution was 1.1 eV and a 0.05 eV/channel was set up on the spectrometer. Area scans of 50nm x 50nm were acquired from 4 different platelet regions for the respective O K, Fe $L_{2,3}$, Ni $L_{2,3}$ and M EELS edges.

4.3 Experimental Results and Discussion

In-situ and *ex-situ* heating TEM experiments were comparatively carried out in parallel to fully understand the development of LDHs thermally induced degradation, as well as the various crystallographic transitions occurring before that. For this purpose, the as-synthesized LDH samples were subject to identical heating ramp conditions both in *ex-situ* and *in-situ* experimental set ups. Further details can be found in the Methods section.

This parallel set up will determine if the behaviours of LDH transformations are independent of the different *in-situ* and *ex-situ* experimental conditions. For example, the significant pressure variations as the samples are heated may impact the thermal behaviours of the LDH nanomaterials. More importantly, full TEM characterization of the various LDH samples were performed pre- and post *ex-situ* heating experiments, as well as during *in-situ* analysis; this comparison was of crucial importance in order to rule out any electron beam-contribution during the *in-situ* experiments. It has in fact been well established that there can be a significant contribution of radiation beam damage (in the form of radiolysis or knock-on) or Joule sample heating when the electron beam interacts with the sample.[37] In view of these possible issues, comparative *ex-situ* heating experiments were conducted to rule out any eventual electron beam-induced transition. We sought to investigate if the LDH degradation processes are dependent on both the composition and platelet size of the material. As such, the structural transformation of a Ni-Fe LDH material was also investigated via the application of *in-situ* heating TEM.

4.3.1 In-situ heating TEM experiments: Mg-Al LDH

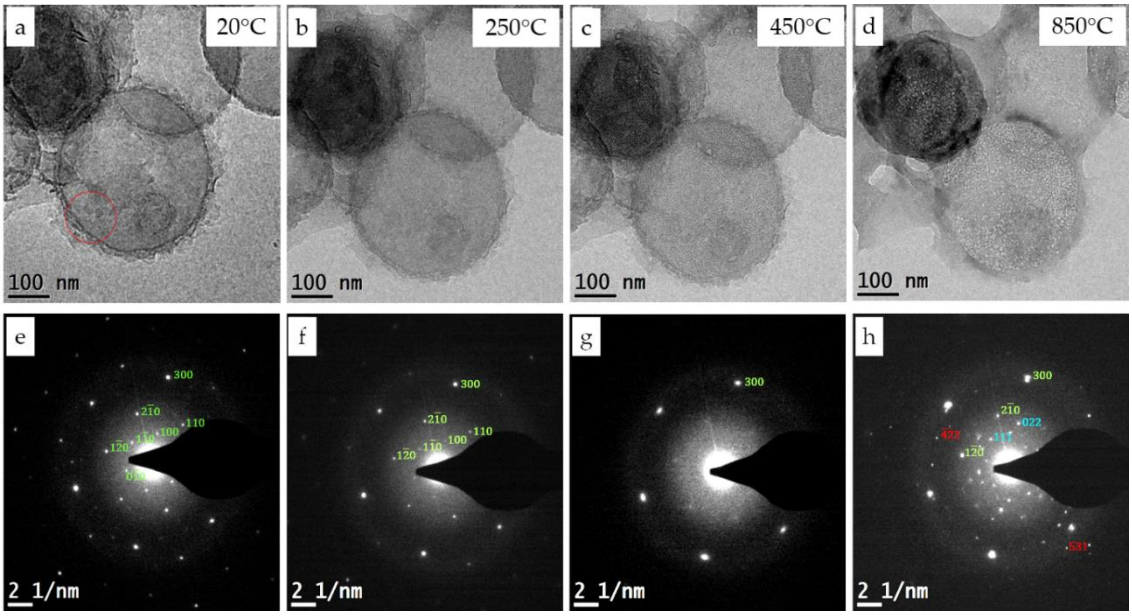

Figure 4.2 BFTEM and associated SAED patterns from various stages of the in-situ heating experiments of the smaller Mg-Al LDH, synthesized by Dr. Mourad. (a)-(d) BFTEM and (e)-(h) SAED patterns corresponding to column temperature 20°C, end of 250°C step, end of 450°C step and end of 850°C step respectively. Red circle in (a) denotes where SAED pattern was recorded from.

Figure 4.2 displays the TEM findings from *in-situ* heating of an Mg-Al LDH material, where the previously mentioned heating ramp was imposed (Figure 4.1). Initially the material appears to have well-defined platelet structures however they portray width of approximately 350nm and rounded morphology, as shown by BFTEM (Figure 4.2). Moreover, the crystallographic phases can be seen via the existence of well-defined {100}, {110}, {120} and {330} planar families of the LDH structure (Figure 4.2(e)).[38,39]

An overall examination of the LDH platelets as they are subject to the *in-situ* heating ramp reveals an inhomogeneous contrast and a porous structure develops within the platelets (Figure 4.2 (d) and Movie V2). These porous structures evolve in an irregular, somewhat random, fashion on the hydrotalcite materials. The borders of the platelets are not observed to have the same behaviours, possibly due to their different crystallographic environments when compared the central domains of the materials. In contrast, they develop a denser frame on the outer regions of the heated material. This

is consistent with similar LDH materials investigated previously.[40] Indeed, it is indicative that the composition and dimension of LDH materials has an influential effect on its thermal degradative properties. Similar features of the Mg-Al LDH degradation, in particular the evolution of a porous matrix, were also evidenced in the recent independent studies of Warringham *et.al.*[41] Their analysis via *in-situ* BFTEM emulates the findings of this study. The Mg-Al LDH morphology and crystalline structures are maintained as they are subject to *in-situ* heating up to 250°C, as demonstrated by the TEM micrographs and electron diffraction patterns in Figure 4.2 (b) and (f). An intensity attenuation in the {100} and {110} diffraction spots occurs. The loss in periodicity of these planes suggest a crystallographic rearrangement of the LDH structures and is accredited to the loss of H_2O from the interstitial layers and a dehydroxlisation of the octahedral layers.[42–47]

As the continuation of the *in-situ* heating ramp regime reached 450°C, Mg-Al platelets demonstrated increased porosity with an evident rearrangement taking place, as shown in BFTEM (Figure 4.2 (c)). The overall morphology of the LDH remained intact but an amorphization occurred. This was evidenced by *in-situ* SAED patterns via the loss of intensity and broadening of the {100}, {110} and {120} LDH diffraction spots (Figure 4.2 (f) and (g)).

At the 850°C step, the emergence of new diffraction spots in the associated SAED patterns provide direct experimental evidence of a crystallographic transformation from an LDH material to a combination of α-Al_2O_3 and $MgAl_2O_4$ spinel structures (Figure 4.2 (h)). This is evidenced by the existence of the associated {111} and {022} reflections of the α-Al_2O_3 and {422}, {531} and {444} of $MgAl_2O_4$ spinel.[48,49] This evolution to mixed metal is also similar to previous work.[42,44,46,50,51] These *in-situ* methods show that a complete decomposition does not occur via the existence of the {110}, {120} and {300} LDH planes ((h)).

We next elected to inspect whether the platelet dimensions had an influential role to play on the thermal evolution of the Mg-Al LDH nanomaterial. Figure 4.3 presents an identical heating experiment of Mg-Al LDHs of larger lateral dimensions.

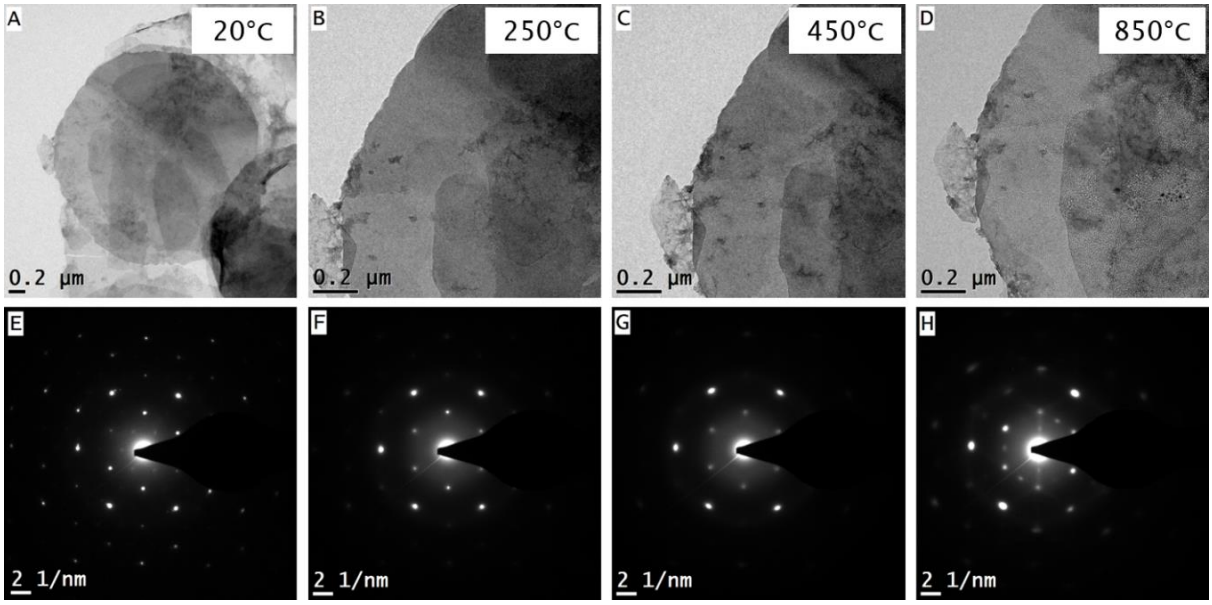

Figure 4.3 BFTEM and SAED patterns of larger Mg-Al LDH during in-situ TEM experiments at various temperatures. (a)-(d) BFTEM and (e)-(h) SAED patterns corresponding to column temperature 20°C, end of 250°C step, end of 450°C step and end of 850°C step respectively. Selected area aperture was used when recording SAED patterns.

Similar thermal degradations were observed of these larger platelets. The thermal evolution of the Mg-Al LDH was found to be independent of the platelet lateral sizes.

4.3.2 Thermal evolution of a LDH different composition: Ni-Fe LDH

Subsequently, we decided to mirror the heating experiments with the Ni-Fe LDH nanomaterial, characterized in Chapter 3. This revealed insight into the role of the cationic composition has on the LDH thermal degradation.

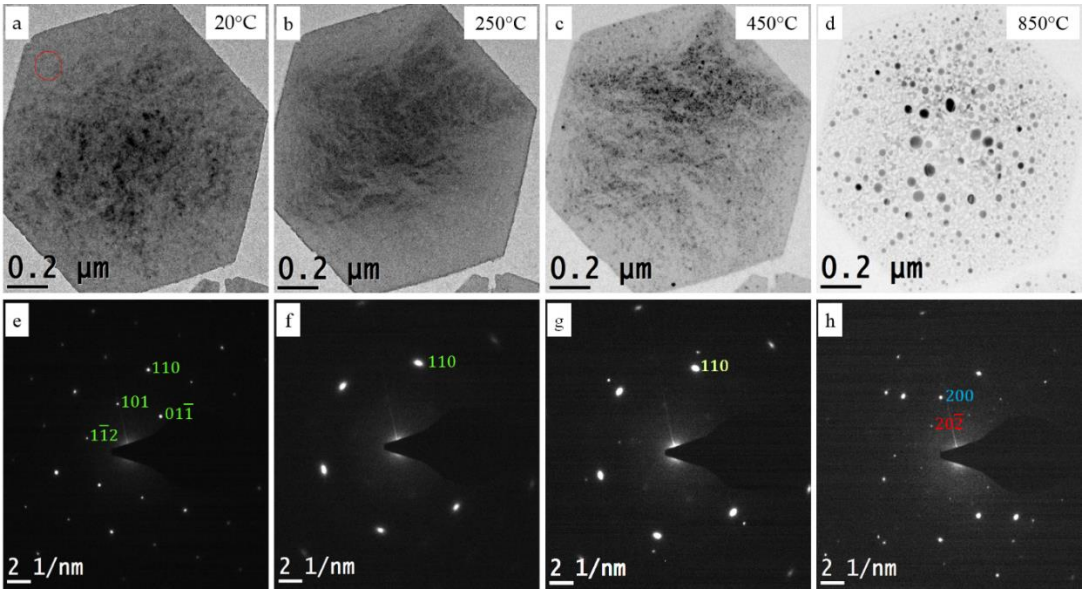

Figure 4.4 BFTEM and associated SAED patterns from various stages of the in-situ heating experiments of the Ni-Fe LDH. (a)-(d) BFTEM and (e)-(h) SAED patterns corresponding to column temperature, end of the 250°C step, end of the 450°C step and end of the 850°C step.

Figure 4.4 displays the BFTEM and associated SAED patterns at various stages of the *in-situ* heating experiments for the Ni-Fe LDH material. Initially, the material was synthesized to have a well-defined hexagonal morphology with a lateral dimension on the order of microns, as seen in the preceding chapter. This starting material was found to have an LDH crystallographic structure, with the associated SAED pattern revealing the (101), $(01\bar{1})$, $(1\bar{1}2)$ and (110) crystallographic planes. Upon heating, both a morphological and crystallographic change is evidenced. As the sample reaches 250°C, the loss of the (101), $(01\bar{1})$, $(1\bar{1}2)$ reflections indicates a collapse in the crystal structure towards an amorphous phase, whilst still retaining its hexagonal morphology. The loss of such planes are also believed to be due to the dehydration of the interstitial galleries. Moreover, the contrast variations of BFTEM images (Figure 4.4 (a) and (b)) indicate a surface alteration at this temperature, possibly as a consequence of the additional dehydration of water from the surface of the material. As we increased the heating environments 450°C, the well defined hexagonal morphology is still retained (Figure 4.4 (c)). However, the evolution of spherical particles, less than 50nm in size, are seen to generate and randomly distribute themselves onto the hexagonal parent material. There appears to be minimal crytallographic

tranformations from 250°C to 450°C. This is indicated by the conservation of the (110) LDH plane (Figure 4.4 (g)). Moreover, there is parity in this Ni-Fe LDH crystallographic transition however amorphization was found to occur at approximately 250°C when compared to the Mg-Al degradations, which display amorphization tendencies at 450°C (Figure 4.4 (f)). Hence, it is believed that the Mg-Al LDH structural transformations are less susceptible to degradations at higher temperatures.

As the sample is calcined to 850°C, there is clear evidence of a further generation of these particles. These have become more numerous, increased in size and randomly distributed themselves across the hexagonal LDH platelet (Figure 4.4 (d)). The SAED pattern of the calcined sample at 850°C indicates a change in the crystal structure (Figure 4.4 (h)). In contrast to the patterns recorded at 250°C and 450°C, there is an generation of new reflections in the diffraction pattern, corresponding to newly arranged crystallographic planes. The evolution of such particles and a variance in the diffraction patterns during the calcination procedures confirms a rearrangement of the LDH structures ino a new crystallographic form. It is believed that this is a topotactic transformation caused by the *in-situ* heating effects. The SAED patterns recorded at 850°C from *in-situ* TEM experiments (Figure 4.4 (h)) portrayed the emergence of the {200} and {220} family of planes of the NiO and trevorite structures respectively (Figure 4.4 (h)). The reflections occurring at 13.1 nm^{-1} could also derive from the parent LDH structure, suggesting that certain LDH planes are retained even after thermal degradation procedures. Furthermore, the SAED findings in this regard reveal an evolution to a mixed phase of LDH, metal oxides and trevorite structures. In contrast to the Mg-Al LDH thermal degradation, the Ni-Fe LDH does not develop a morphological variation along the borders of the platelets (Figure 4.2 (d) and Figure 4.4 (d) respectively). Moreover, the development of a porous structure of the Ni-Fe LDH is not as pronounced as the Mg-Al counterpart.

4.3.3 (S)TEM and microanalysis of thermally treated Ni-Fe LDHs

To investigate the variation in the orientation of the metal oxides, we employed electron diffraction in STEM mode (Figure 4.5). The experimental set-up to record the diffraction patterns is credited to Mr. Clive Downing, a technical staff member of the Advanced Microscopy Laboratory, TCD. This overcame the drawback of SAED techniques in TEM, where the dimensions of the selected area apertures are limited to recording diffractions from regions of minimum 100nm in size approximately. Whereas the application of electron diffraction using a 'parallel' STEM electron probe permitted the characterization of features of approximately 10nm i.e. the size range of the products of calcination procedures. Furthermore, the application of diffraction studies via an electron probe in STEM allowed us to investigate the crystallographic orientations across the calcined Ni-Fe structures. The variations in the recorded patterns show that the NiO particles assemble with various orientations relative to the basal plane of the LDH platelet. (Figure 4.5 (c) and (e)). This can also be viewed in the case of the $NiFe_2O_4$ trevorite regions of the structure (Figure 4.5 (b) and (d)). It is deduced that the products of mixed metal oxides derived from the Ni-Fe LDH calcinations arrange themselves randomly throughout the parent material.

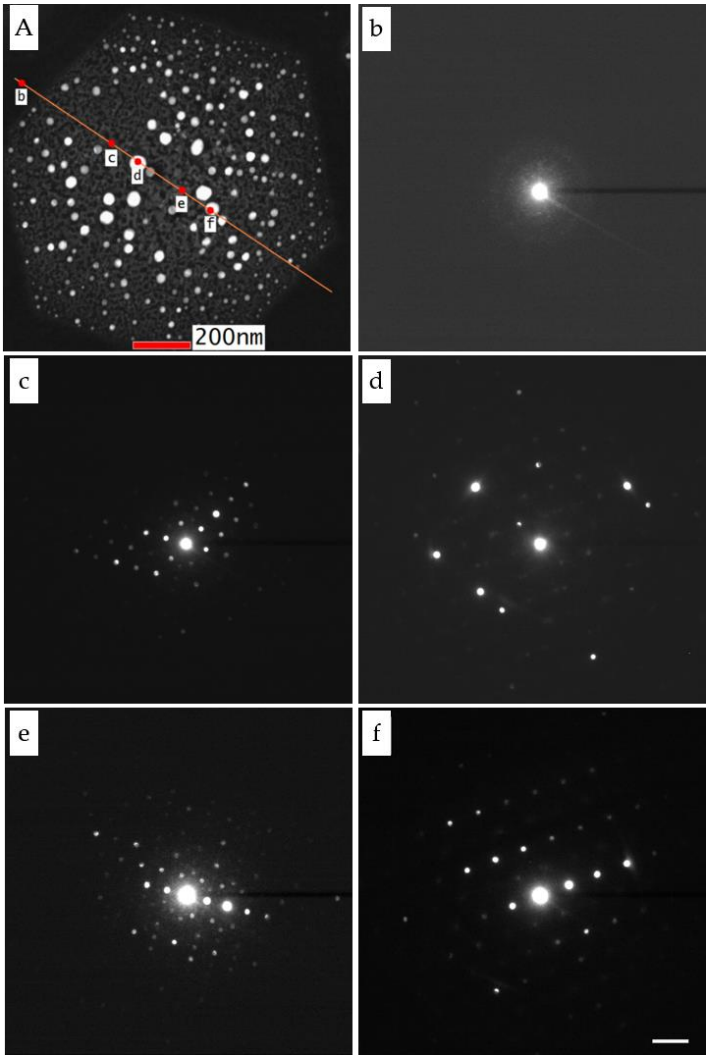

Figure 4.5 Electron diffraction patterns recorded across calcined Ni-Fe LDH using 'parallel nanoprobe' in STEM. (A) STEM image with line scan (orange) from which the diffraction patterns were recorded across the calcined NiFe LDH material post-heating. Images (b)-(f) are patterns acquired from the labelled red regions (b)-(f) indicated in STEM image (A). Scale bar in (f) is 5 nm^{-1} and applies to diffraction patterns (b)-(f).

The thermally evolved platelets from the in-situ TEM experiment was studied using HRTEM analysis, as shown in Figure 4.6 . This analysis also showed the presence of the $NiFe_2O_4$ trevorite lattice structure surrounding the spherical particles resulting in a heterogeneous structure (Figure 4.6 (e)).

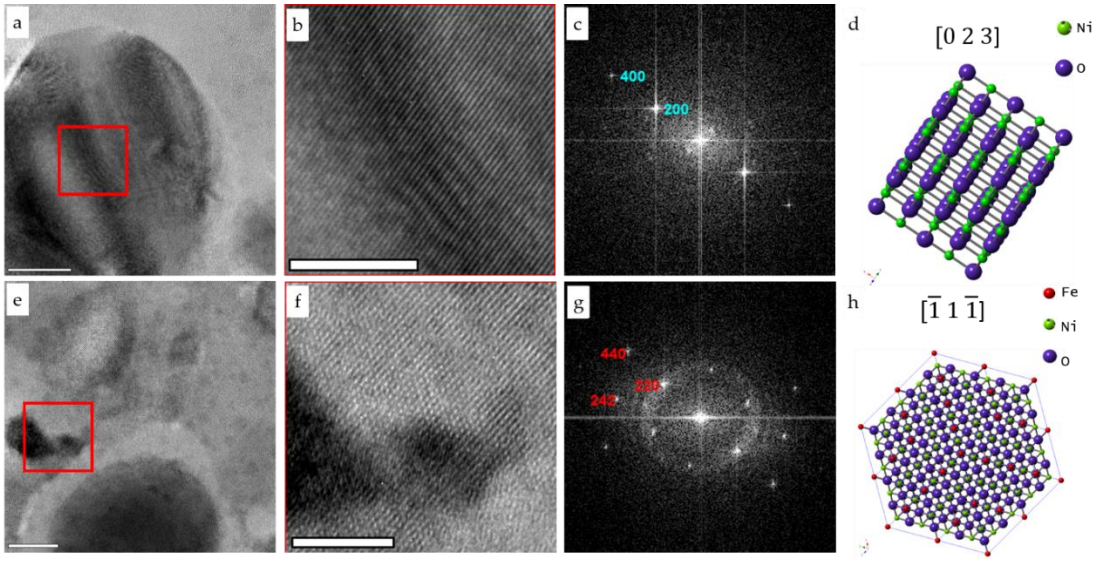

Figure 4.6 (a) and (e) HRTEM images of various regions after in-situ TEM heating experiments. (b) and (f): zoomed in images of square regions as indicated in (a) and (e). (c) and (g): Calculated FFT from square red region as indicated on the TEM micrograph in (a) and (e). Blue and Red annotations ((c) and (g)) represent labelled NiO and trevorite crystallographic planes respectively. (d) and (h): Schematic representations of the respective crystalline structures, viewed along the [0 2 3] (d) and [$\bar{1}$ 1 $\bar{1}$] (h) directions. Scale bars are 10 nm for micrographs (a) and (e) and 5 nm for (b) and (f). Structures (d) and (h) were visualised using CrystalMaker™.

FFT analysis of the associated regions (Figure 4.6 (g)) confirmed the presence of the {220} and {242} family of planes (indicated by red indices in Figure 4.6 (g)), where the crystallite region has a [$\bar{1}$ 1 $\bar{1}$] orientation . This can also be corroborated to the Fe signal as found by EFTEM methods (Figure 4.7 (a)). Similar analysis of the spherical nanoparticles directly resolves the lattice spacings attributed to the {200} planes of the NiO structure with an orientation along the [0 2 3] axis, hence confirming the evolution of metal oxide particles as a result of the calcination of the Ni-Fe LDH structure. These findings also correlate to similar calcined LDH materials (Zn-Al) presented by Cho and Lee[52] and Carriazo *et. al.*[53] However, there is a discrepancy in the correlation of the STEM nanoprobe diffraction and HRTEM of similar particle regions, whereby the (1 1 $\bar{1}$) family of planes found in the STEM nanoprobe acquisitions fully coincides with the FFT analysis of our HRTEM data (Figure 4.6 (c) and Figure 4.5 (f)). We perceive this to be due to the evolution of a non-stoichiometric Nickel oxide

compound as opposed to a pure NiO phase. The existence of non-stochiometric Nickel oxides has been previously investigated by Da Rocha and Rougier.[54]

We post-analysed the Ni-Fe LDH samples using energy filtered TEM (EFTEM) (Figure 4.7) to understand the elemental distribution of the metallic species across the platelet. Initially, EFTEM was favoured over scanning transmission electron microscopy (STEM) spectroscopic techniques such as energy dispersive x-ray and electron energy loss spectroscopy (EELS) to reduce the risk of inducing a transformation due to the beam-sample interaction and not as a consequence of applied thermal environments.

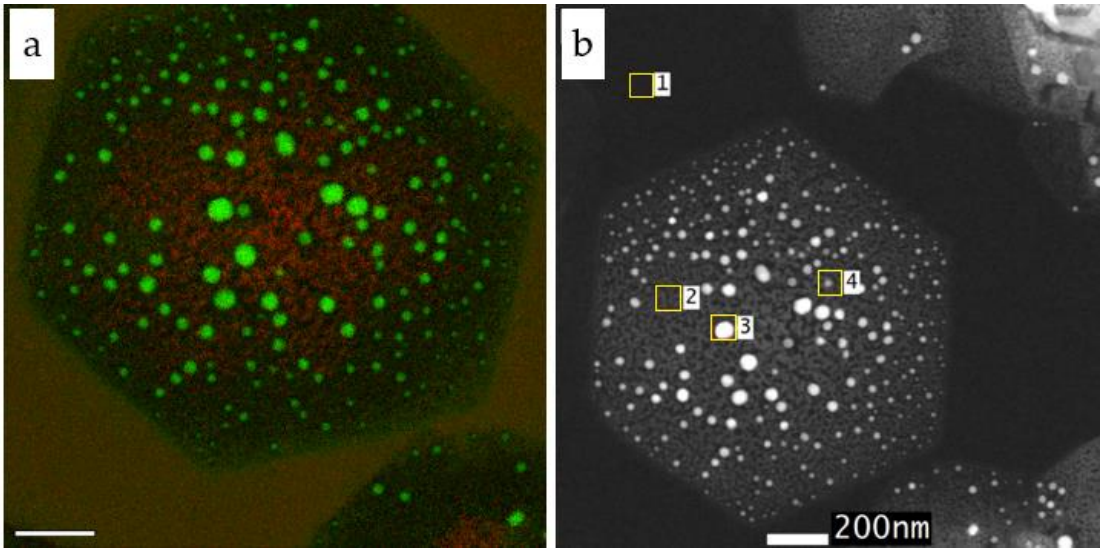

Figure 4.7 (a) Energy filtered TEM image of Ni-Fe LDH sample post-heating. Ni and Fe signals are represented by the colours green and red respectively. (b) Scanning transmission electron microscopy image of the same platelet. Area 1 – Area 4 indicated in (b) represent EDX recording regions. Scale bar in (a) is 200nm.

Furthermore, the application of EFTEM allowed for the direct analysis of the Ni and Fe from the whole platelet via the acquisition of two EFTEM maps (Figure 4.7 (a)). This application was preferable over STEM acquisitions where a longer timescale for spectroscopic acquistions are required for such platelet regions. STEM methods may have introduced issues of drift and potential alterations of crystallographic environments and, in turn, would have impacted the true reflection of the Ni-Fe LDH calcination behaviours. EFTEM also revealed the distribution of Ni and Fe throughout the calcined products (Figure 4.7 (a)). In contrast to the Ni evolution, Fe was found to

have a more regular distribution across the platelet, with a localisation in the centre of the calcined material. In addition, larger NiO particles tend to form on the central sections of the platelets, with smaller NiO crystallites arranged on the platelets edge regions. This may be due to the non-uniform local crystallographic environments of the cationic sites, whereby the different environments at the edge-regions of the platelets affect the growth of both $NiFe_2O_4$ trevorite and NiO oxide nanoparticles. Moreover, it is perceived that the catalytic activity at these edge-regions are not only influenced by Fe sites[55] but are also influenced by smaller sized NiO particles.

Area / Element	Ni (Atomic %)	Fe (Atomic %)
1	0.00	0.00
2	8.19	2.37
3	10.67	2.63
4	11.16	2.55

Table 4.1 Relative amounts (atomic %) of Ni and Fe in from STEM-EDX spectra recorded in Areas 1 -4 in Figure 4.7(b).

Imaging with an energy slit width to contain the Ni L_3 EELS edge yielded a direct visualisation of the Ni-Fe thermal transformations (Figure 4.8 and Movie V1 Supporting Information).[56] The intensity in such video representations derive solely from the Ni L_3 EELS edge signals. As the platelets were subject to 850°C, the evolution of Ni containing particles was clearly evidenced. Particles initially evolved and migrated in a random fashion on the platelet surfaces. Further exposure at this temperature leads to a sudden transformation where the remaining material transforms to an array of smaller similar Ni containing particles (Figure 4.8 (e)). This somewhat restricted size is perhaps due to the limited local availability of Ni cations after the initial transformations occurred.

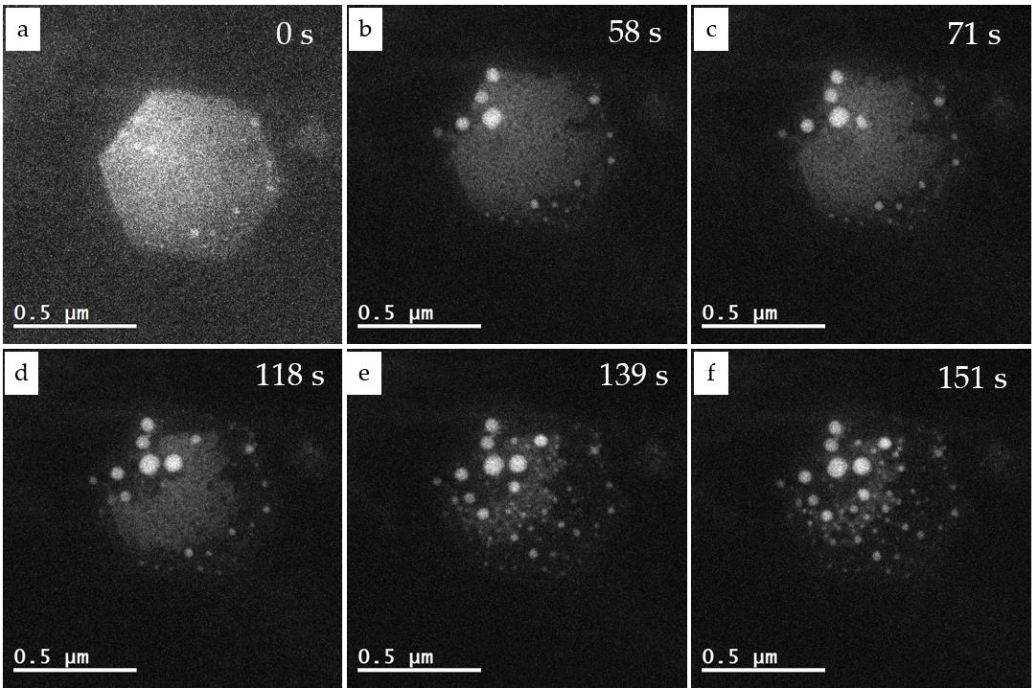

Figure 4.8 EFTEM images of Ni-Fe LDH were subjected to 850. Subsequent frames taken from the EFTEM video Movie V1. (a) – (f) show EFTEM images after certain time points after 850°C exposure.

We employed energy dispersive x-ray spectroscopy (EDX) in STEM to quantitatively assess the elemental distribution of the calcined products from Ni-Fe LDH degradations. Whilst the Fe content appears to be ubiquitously distributed, STEM-EDX revealed that there is a significantly higher Ni content on the thermally evolved spherical particles (Figure 4.7 (b) and Table 4.1). This yields further evidence that the evolved particles are that of NiO, and also correlates well with the data acquired by EFTEM methods. The varying Nickel/Iron ratios ascross the platelet are speculated to be due to the migration of Nickel as a consequence of the thermal evolution from the LDH structure to mixed oxide phases (Table 4.1). Areas 3 and 4 present respective atomic % ratios of 4.06 and 4.38 due to the presence of the Nickel particle in the acquisition regions. In contrast, Area 2 demonstrates a ratio of 3.26, where the region of interest only encapsulates the $NiFe_2O_4$ regions.

4.3.4 STEM-EDX/STEM-EELS mapping of thermally evolved Ni-Fe LDHs

During EFTEM analysis and HRTEM imaging, we observed that the calcined Ni-Fe LDH was rather resilient to the electron beam and was not subject to immediately induced damages. The effects of the electron irradiation were not as pronounced as compared to the case of the parent LDH structures. Hence, we decided to perform elemetal maps using STEM-EDX and STEM-EELS techniques to enhance the compositional information of the calcined materials. Figure 4.9 presents STEM-EDX maps of annealed Ni-Fe LDH nanomaterials. The EDX maps show regions of Nickel and Iron signals, as was seen using EFTEM anaylsis. The oxygen appears to be quite unformly distributed across the mapped region, where the lack of signal is more than likely due to the presence of pores throughout the calcined platelets (Figure 4.9 (b)). The spherical particles are seen to be largely composed of Nickel , evidenced by the location of the intense map signals. (Figure 4.9 (c)). Moreover, these Ni containing particles appear to be surrounded by regions largely composed of Iron (Figure 4.9 (d)). However, the detected signals in the Iron map which coincide with the intense Nickel signals of the particles could be perceived as false artifacts when evaluating map regions. The 7.11 keV Fe-K_β x-ray signal is close in proximity to the Ni-K_α x-ray peak at 7.47 keV in the recorded EDX spectra. This may lead to the apparent signal of Fe x-rays in the Fe maps when in fact it is a count deriving from the shoulder or background of the Ni-K x-ray peak in the EDX detector.

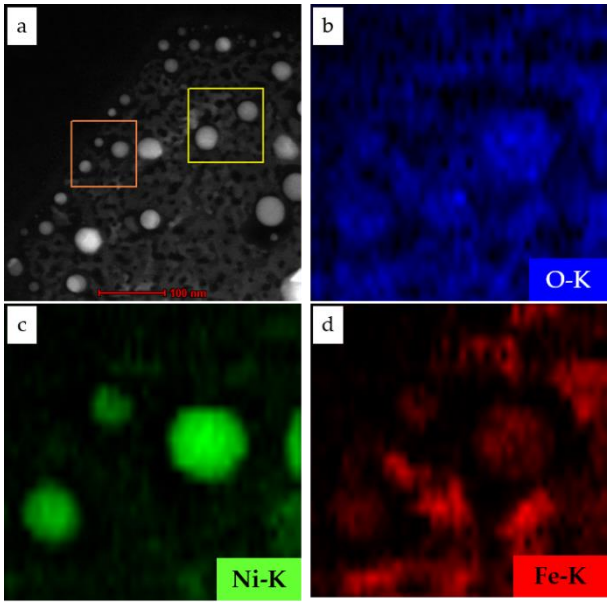

Figure 4.9 STEM-EDX mapping of calcined Ni-Fe LDH nanomaterials after in-situ TEM experiments. (a) STEM image of calcined LDH platelet. Orange square represents mapped region. Yellow square denotes the image region for drift correction during map acquisitions. Extracted elemental maps of (a) oxygen, (b) nickel and (c) iron are represented by the colours blue, green and red respectively.

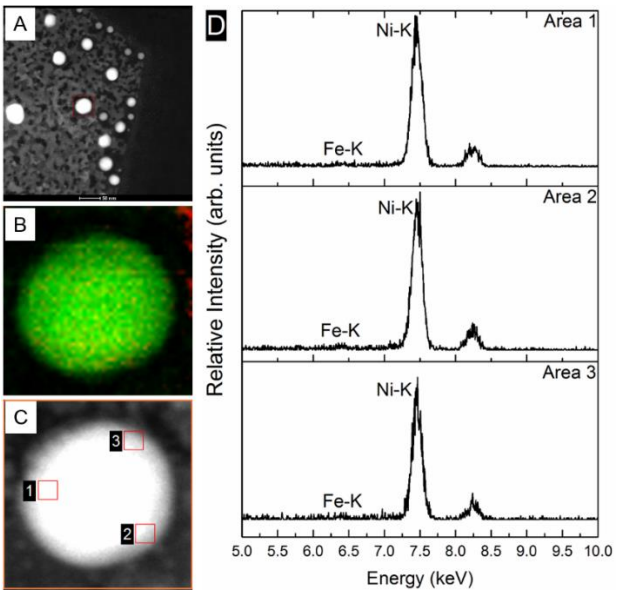

Figure 4.10 STEM-EDS mapping analysis of the calcined Ni-Fe LDH material. (A) STEM image of calcined LDH platelet. Red square denotes EDS map area acquisition. (B) Superimposed Ni (green) and Fe (red) elemental maps of the analysed region. Spherical particle is largely dominated by Ni EDS peak signals. (C) Sum EDS spectra from various locations (denoted 1-3) across the analysed particle. (D) Displayed sum EDS spectra from areas 1-3, Ni-K and Fe-K peak locations at 7.4 keV and 6.4 keV respectively are shown on the sum spectra.

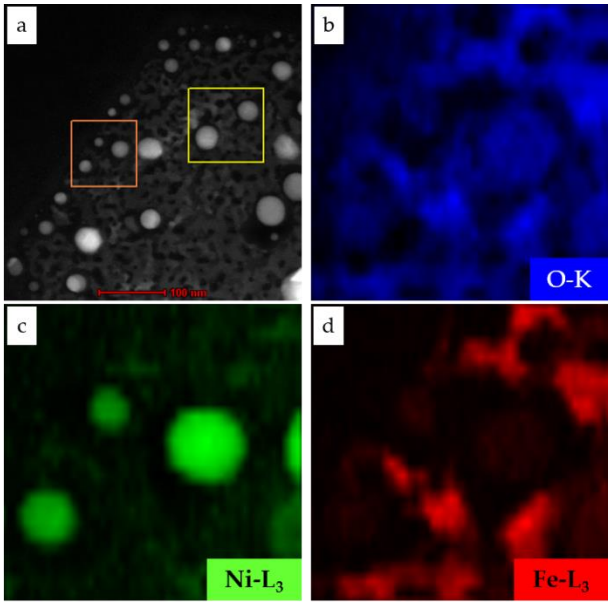

Figure 4.11 STEM-EELS mapping of calcined Ni-Fe LDH nanomaterials after in-situ TEM experiments. (a) STEM image of calcined LDH platelet. Orange square represents mapped region. Yellow square denotes the image region for drift correction during map acquisitions. Extracted elemental maps of (a) oxygen, (b) nickel and (c) iron are represented by the colours blue, green and red respectively.

Hence, the simultaneous acquisition of a STEM-EELS map of the same region was exploited for a more representative compositional map (Figure 4.11). In the core loss spectrum, and indeed as we have previously seen with the precursor Ni-Fe LDH material, there is a significant energy loss difference between the Fe $L_{2,3}$ (707 eV) and Ni $L_{2,3}$ (855 eV) edges. This difference negates any possible ambiguities in the calculated STEM-EELS maps. The Ni L edge EELS maps is consistent with the previous EDX maps and EFTEM data, highlighting the Nickel composition of the evolved spherical particles. However, the Fe is non-existent in these areas, corroborating the EFTEM signals that there is no Fe containing material where the spherical Nickel particles are located. Moreover, the formation of Fe containing domains around the Ni particles is more pronounced in the STEM-EELS maps compared to the acquired STEM-EDX data. In addtion, the stability of the calcined structures was assessed by analysing the same flake from in-situ TEM studies, 40 days after it was carried out. Figure 4.12 displays BFTEM, SAED, HRTEM and a corresponding FFT pattern of the calcined Ni-Fe LDH platelet. It was clearly evident that the structures remained stable after this time. The spherical particle array still exists and a revert to the LDH crystal phase is not

observed. The existence of a spinel phase is also viewed by HRTEM analysis, where the {220} planes are shown in the FFT pattern.

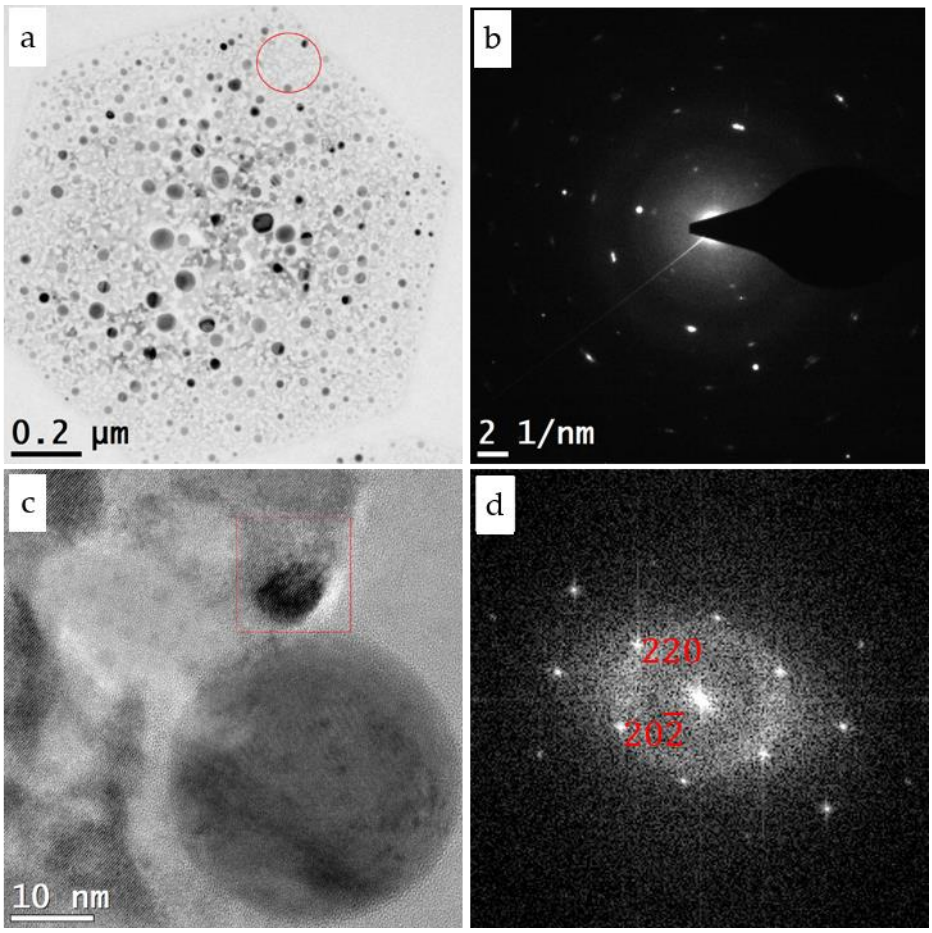

Figure 4.12 (a) BFTEM image of Ni-Fe LDH 40 days after in-situ heating experiment. (b) SAED pattern recorded from red region indicated in (a). (c) HRTEM image of material. (d) Associated FFT calculated from red region indicated in (c). Red labels indicate trevorite crystallographic planes in (d).

4.3.5 Core loss EELS study of Ni-Fe LDHs in in-situ thermal environments.

In-situ heating techniques were also utilised to investigate the effect of elevated temperatures on the core-loss EELS spectra of Ni-Fe LDHs. In this experimental set-up, the Ni-Fe LDH nanomaterials were subjected to 50°C and subsequent increments of 100°C up to 850°C, each for 10 mins, using our DENS Solutions in-situ TEM sample holder. At the end of each interval, O K edge, Fe $L_{2,3}$ and Ni $L_{2,3}$ edge EELS spectra were

recorded on the GATAN GIF in STEM mode over a 200 nm x 200 nm area. The FWHM of the zero loss peak before EELS analysis was 1.05 eV. New regions of interest were analysed at each temperature stage to avoid any unwanted effects of the electron beam on the EELS spectra. Figure 4.13 shows the O K , Fe $L_{2,3}$ and Ni $L_{2,3}$ core loss EELS edges at each temperature, as stated on the associated graphs.

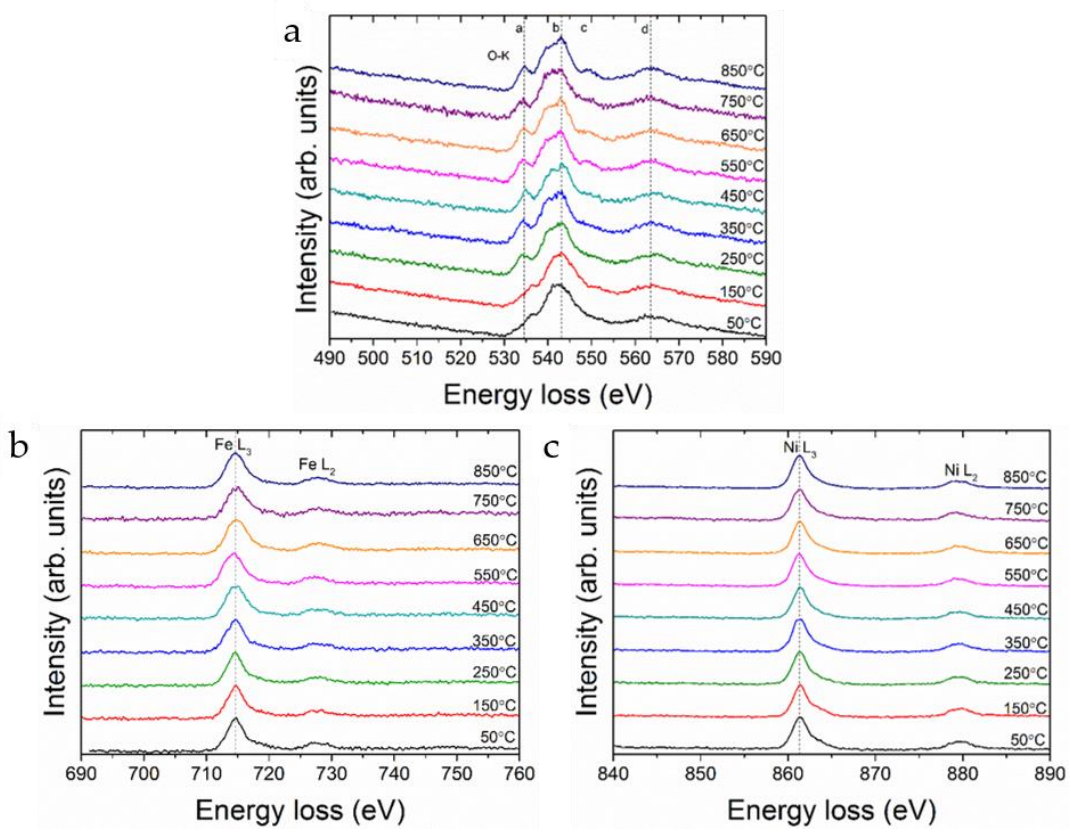

Figure 4.13 STEM-EELS core loss spectra recorded at incrementing temperatures during in-situ heating experiments. (a)-(c) show the O K , Fe $L_{2,3}$ and Ni $L_{2,3}$ edges respectively. The temperature at which each EELS spectra was recorded is shown on each figure (a) – (c).

Firstly, a significant variation in the O K edge was identfied as the Ni-Fe LDH platelets were exposed to higher temperatures. Initially at 50°C, there is a distinct shoulder in the pre peak of the delayed Oxygen K edge at 536.4 eV. This is due to the existence of the transition metal bonding to the hydroxyl groups in the cationic layers of the Ni-Fe LDH structure. This shoulder is also evident in similar layered Fe and Ni oxyhydroxides.[57] Moreover, this feature has also been shown in EELS and x-ray absorptions spectroscopy (XAS) studies of various transition metal oxide nanomaterials such as Cr_2O_3, CoO, CuO and NiO.[58–60] As these LDHs are subjected to

temperatures up to 850°C, this pre-shoulder evolves into a more intense independent peak (Figure 4.13 (a)). This is accompanied with a peak shift from the shoulder at 536.4 eV to 534.6 eV (Figure 4.13 (a) peak a). The increase in the peak's intensity is believed to be due to the dehydration of the LDH structure, causing a breakdown of the hydroxyl groups, a liberation of Hydrogen from the material and hence a change in the transition metal bonding to the oxygen sites.[61,62] Coupled with this evolution, there are extra fine structure feature changes with the development of new peaks at 539.5eV and 543.1 eV (Figure 4.13 (a) peak b). Also, a newly developed peak at 549.4 eV is seen at 550°C (Figure 4.13 (a) peak c). This may be attributed to the generation of a NiO phase, which would corroborate the previous findings from post in-situ TEM, HRTEM and EELS characterizations (Figure 4.6 and Figure 4.11).[63] Moreover, the EELS profile also agrees very well with NiO films analysed by Grunes *et. al*.[60] On the other hand, these spectral attributes may also be judged to derive from iron oxide phases as a result of the thermal enviroments.[64] In combination with the Fe $L_{2,3}$ findings in the literature, it can be discerned that the phases are FeO or Fe_3O_4 as opposed to an Fe_2O_3 structure. The studies of Chen et. al highlight a pre-shoulder in the Fe L_3 peak of the Fe_2O_3 which was not observed in our case of the LDHs.[61] These EELS behaviours also support the previous mechanistic thermal degradation explanations, where the LDH structure undergoes a dehydration of intersitial and surface H_2O as well as from the hydroxyl bonds of the cationic layers.

In contrast to these changes, the Ni and Fe $L_{2,3}$ edges show no significant change in the fine structure features with increasing temperature. A shoulder in the Ni L_3 peak may be seen to develop which would potentially imply an evolution to a NiO phase.[60] A similar case is presented for the Fe $L_{2,3}$ edge where no ample variation in the spectra features is distinguishable even at 850°C where a change in material phase was previously clearly evidenced.

4.3.6 TEM studies of thermally treated Ni-Fe LDHs: heating ex-situ.

The thermal evolution behaviours and the properties of the calcined products deriving from Ni-Fe LDHs via in-situ TEM heating approaches were thoroughly characterized

in the electron microscope. However, one major drawback of this approach is that the conditions in the TEM column may not reflect annealing conditions in large scale or even industrial volumes. Indeed from an applications perspective, the heating of single nanoparticles as well as these vacuum environments is not particularly feasible due to the demand on the production of large quantities. As such, we paralleled the in-situ TEM analysis with ex-situ heating of bulk powders as well as single LDH nanomaterials to investigate the role of the heating environments of the LDHs thermal behaviours. This approach also validates the credibility of our *in-situ* EM methodologies to characterize such behaviours as well as providing reference for the effect of the electron beam on the LDHs thermal evolution.

Figure 4.14 presents BFTEM and SAED of ex-situ calcined Ni-Fe LDH materials, paralleled from the in-situ studies. Ni-Fe LDH powders were annealed at 250°C for 2 hours, then subsequently at 450°C for 2 hours and finally 850°C for 2 hours.

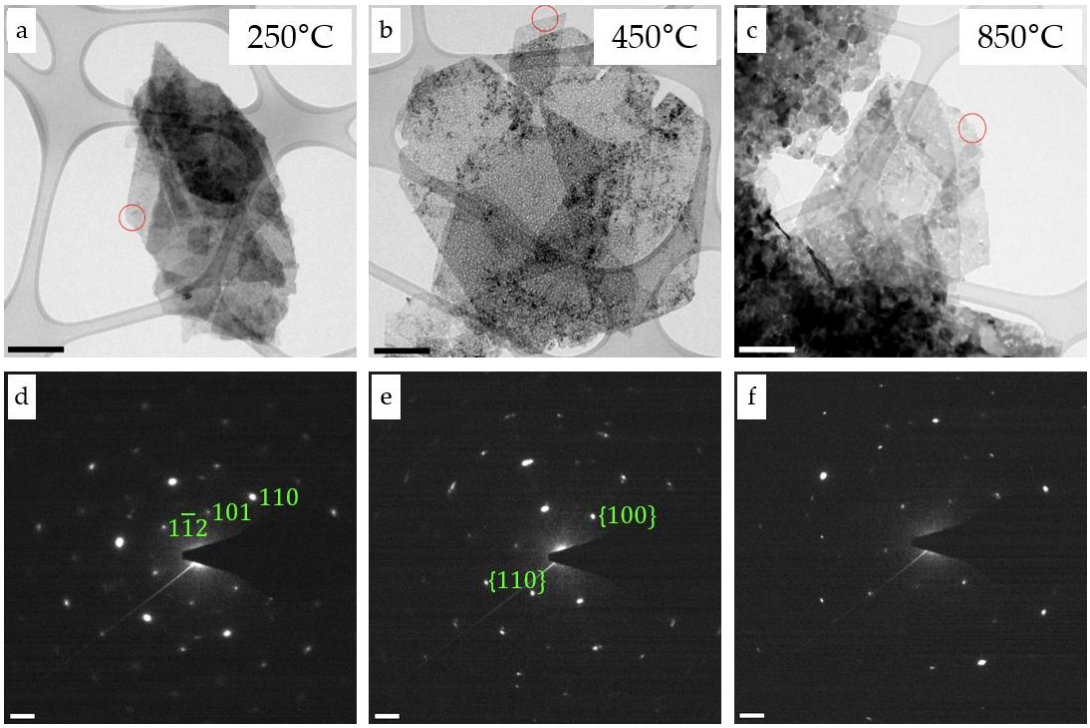

Figure 4.14 BFTEM and associated SAED patterns of *ex-situ* heating experiments of the Ni-Fe LDH. (a)-(c) BFTEM and (d)-(f) SAED patterns corresponding to the end of the 250°C step, end of the 450°C step and end of the 850°C step of the applied heating ramp respectively. Green annotations ((d) and (e)) represent labelled LDH crystallographic planes. Scale bars for TEM micrographs (a)-(c) and SAED patterns (d)-(f) are 200 nm and 2 nm^{-1} respectively.

The samples heated to 250°C *ex-situ* present an irregular platelet morphology (Figure 4.14 (a)). This evidently contrasts the precursor LDH platelets as well as the LDH materials heated to 250°C using *in-situ* methods (Figure 4.4 (a) and (b) respectively). The corresponding SAED pattern show that these irregular sheet-like materials display an LDH crystalloraphic structure, demonstrated by the {101} and {110} planes (Figure 4.14 (d)). Similarly, these crystallographic planes are also evidenced as the sample is heated to 450°C using *ex-situ* methods (Figure 4.14 (e)). The BFTEM findings (Figure 4.14 (b)) are also consistent with *in-situ* studies at this temperature, in particular the irregular morphology and formation of particles on the platelets surface (Figure 4.14 (b)). The morphology demonstrates an arrangement of smaller crystallite regions at 850°C (Figure 4.14 (c)) with similar crystallographic features (Figure 4.14 (f)). These LDH features observed at elevated temperatures as a result of *ex-situ* heating of materials may also be perceived as a reconstructed LDH due to its exposure to aqueous environments, i.e. the LDH 'memory effect'.[65] The hexagonal symmetry in the associated SAED patterns may highlight a partial revert to the LDH structure but could also be a regeneration of the LDH phases via a direct synthesis mechanism (Figure 4.14 (f)).[32] We also identified the existence of the spinel phase using HRTEM analysis (Figure 4.15).

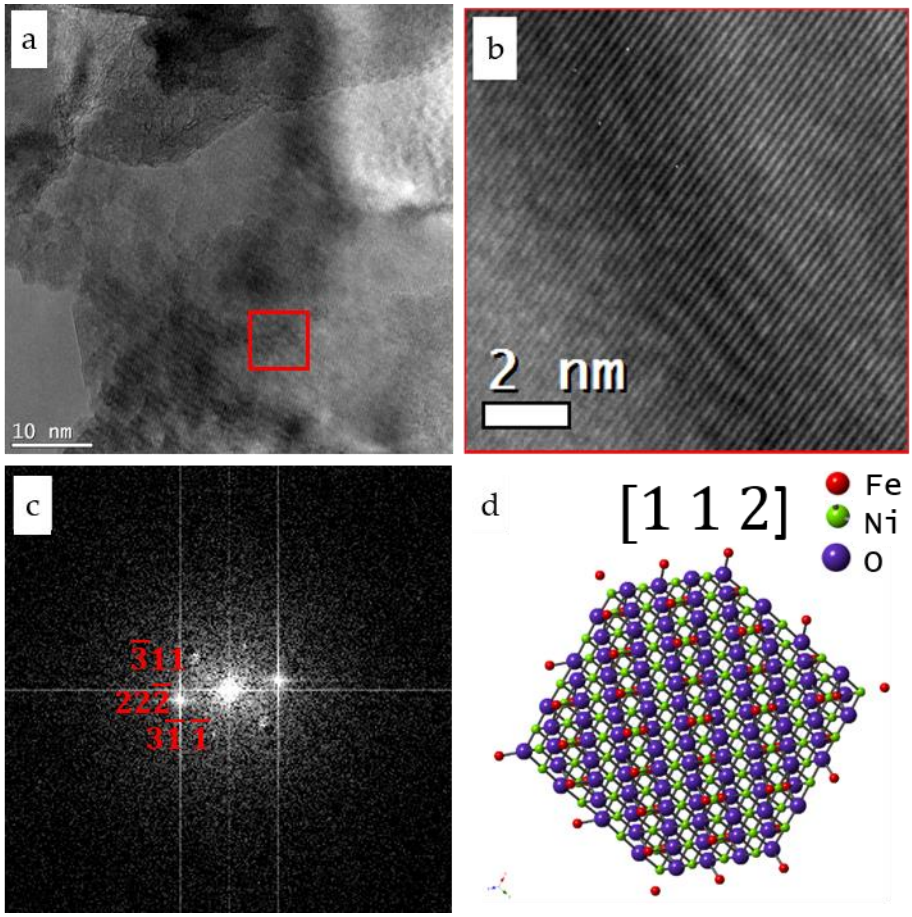

Figure 4.15 (a) HRTEM image of Ni-Fe LDH sample region after ex-situ heating experiments at 850°C. (b) Zoomed in region of square region as indicated in (a). (c) Calculated FFT from square red region as indicated in (a). (d) Schematic representations of the trevorite structures, viewed along the [1 1 2] direction. (Structures in (d) were visualised using CrystalMaker™.)

Figure 4.16 shows combinative EFTEM images of the *ex-situ* heated sample up to 850°C highlighted an even distribution of Ni and Fe throughout the material. This is evidenced by the ubiquitous EFTEM intensities of Ni (green) and Fe (red) respectively (Figure 4.16). The non-specific location of either Ni or Fe contrasts the EFTEM findings from *in-situ* experiments (Figure 4.7(a)). This is acknowledged to be the effect of rehydration of the heated LDH material due to its exposure to moist air conditions as a consequence of sample preparation, where the Ni and Fe sites would revert back to an LDH structure. However it is noted that this conflicts previous in-situ data where samples heated at 850°C in the TEM remained stable (Figure 4.12). STEM-EDX quantitative data demonstrates a greater Ni content in the analysed region, which is also paralleled in the in-situ case (Area 3 and 4 in Figure 4.16 (b) and Table 2).

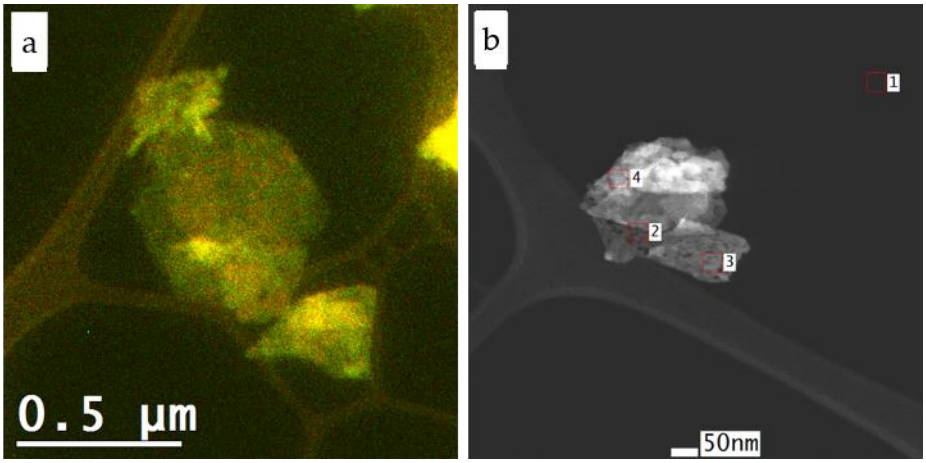

Figure 4.16 (a) Combinative energy filtered TEM image of Ni-Fe LDH sample post heating ex-situ. Ni and Fe signals are represented by the colours green and red respectively. (b) Scanning transmission electron microscopy image of sample heated to 850°C ex-situ. Area 1 – Area 4 indicated in (b) represent regions from which EDX spectra were acquired.

Area	Ni (Atomic %)	Fe (Atomic %)
1	0.00	0.00
2	11.75	2.35
3	9.70	0.36
4	16.79	6.92

Table 4.2 Relative amounts (atomic %) of Ni and Fe in from STEM-EDX spectra recorded in Areas 1 -4 in Figure 4.16 (b).

Despite maintaining the focus of interest on the nanoscale features responsible for the thermal evolution of these LDH samples, it is also acknowledged that the above findings may not reflect their bulk material counterparts. Hence, we investigated and compared these behaviors via the application of X-ray diffraction (XRD). To exclude any possibility of afore mentioned reconstruction to an LDH structure due to water-exposure, we performed XRD using samples in powder form. The crystallographic features of bulk Ni-Fe LDH samples were investigated using in-situ and ex-situ XRD methods, as shown in Figure 4.17.

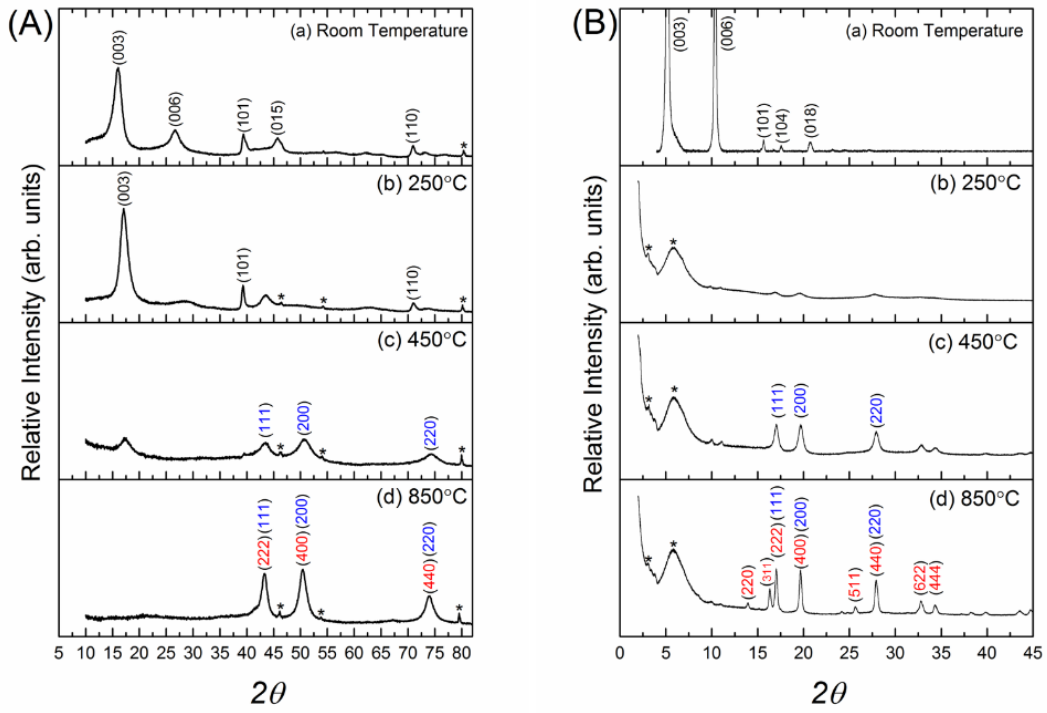

Figure 4.17 In-situ and (B) ex-situ XRD measurements of Ni-Fe LDH samples at (a) room temperature (b) 250°C for 2 hours (c) 250°C for 2 hours followed by 450°C for 2 hours and (d) 250°C for 2 hours, 450°C for 2 hours and 850°C for 2 hours. Black, blue and red labels indicate planes from LDH, NiO and trevorite structures respectively. Peaks indicated by * come from the XRD sample holder set up.

Ex-situ samples were analysed at intermediate temperature stages of afore mentioned heating protocols. In particular, XRD was strategically conducted firstly at room temperature then samples were heated to 250°C for 2 hours followed by 450°C for 2 hours and finally to 850°C for 2 hours and post-analysed at each stage (Figure 4.17(B) (a) – (d) respectively). At room temperature, the XRD peaks at 2θ angles 5.3°, 10.32°, 15.7°, 17.6° 20.7° are related to the (003), (006), (101), (104) and (018) planes of the Ni-Fe LDH crystallographic planes, complimenting previous work[66]. Upon heating to 250°C, the loss of the (006), (101), (104) and (018) peaks indicate a breakdown in the Ni-Fe LDH crystal structure. This collapse is attributed to the dehydroxylisation of the associated LDH material. At this temperature, the XRD patterns also show a decreasing and broadening of the (003) peaks indicating an alteration in basal spacings (Figure 4.17 (B)). The transitions of the LDH structures reported by XRD were also consistent with the EM studies of this work (Figure 4.4). The evolution of the NiO (111), (200) and (220) planes and the $NiFe_2O_4$ (220), (311), (222), (400), (511), (440), (622)

and (444) planes are evidenced at 450 °C and 850°C respectively (Figure 4.17 (c) and (d) respectively). The NiO {200} and $NiFe_2O_4$ {220} planar families were also evidenced both in the SAED patterns recorded during *in-situ* experiments. However, there is an ambiguity in selected XRD peaks of the calcined samples as they could correspond to either oxide or trevorite structures. The XRD peaks at 2θ angles 17.0°, 19.7° and 27.9° could be hypothesized to derive from the respective NiO (111), (200) and (220) or $NiFe_2O_4$ (222), (400) and (440) family of planes. This has also been observed by previous work[67]. Furthermore, this ambiguity in the possible source of XRD peaks validates our motivation of applying the techniques of SAED and HRTEM. The observed correlations between XRD macroscopic techniques and EM analysis indicate that the bulk features derive from the LDH nanoscale transformations.

4.3.7 TEM characterization of single particle calcined Ni-Fe LDH nanomaterials

Further work was undertaken to characterize the newly generated material as a result of thermally treated Ni-Fe LDH nanomaterials. This added information on the transformed LDH nanomaterials to mixed oxides and spinels.

Up until this point, bulk samples were heated ex-situ for TEM analysis by heating powders of the Ni-Fe LDH material. It is noted that this data must be interpreted with caution. As was previously addressed, the possibility of the ex-situ heating powders to recover LDH phases due to exposure to hydrous enviroments such as air or water may not truly reflect the material properties and therefore skew results. Also from a sample preparation viewpoint, difficulties arose when dispersing dry powders onto TEM grids. A homogenous dispersion of sample was next to impossible to achieve via this method. More importantly, numerous regions of these samples were deemed to be too thick and not sufficiently 'electron transparent' for TEM imaging and analysis.

We elected to drop cast a sample for a uniform distribution of the nanoplatelets and heat the LDH materials on SiN TEM grids at 850°C for 6 hours at atmosphere in a furnace. This allowed for a relatable comparison to in-situ experiments as well as being able to analyse annealed single nanoplatelets as opposed to placing bulk powders onto the lacey carbon TEM grids. In addition, the MEMS chips for the DENS in-situ heating

sample holder are not compatible with other standard sample holders or the NION UltraSTEM cartridges. Hence this alternative sample preparation and analysis method was also chosen from an experimental apparatus and infrastructure standpoint. Figure 4.18 (a) displays a representative STEM image of the calcined Ni-Fe LDHs. The platelets were observed to have a porous morphology, comparable to the calcined samples using an in-situ approach. However in contrast to the in-situ calcinations, the ex-situ thermally treated samples on the TEM grid did not have an array of spherical nanoparticles dispersed across the original platelet, rather an array of facets across the original platelet outlines.

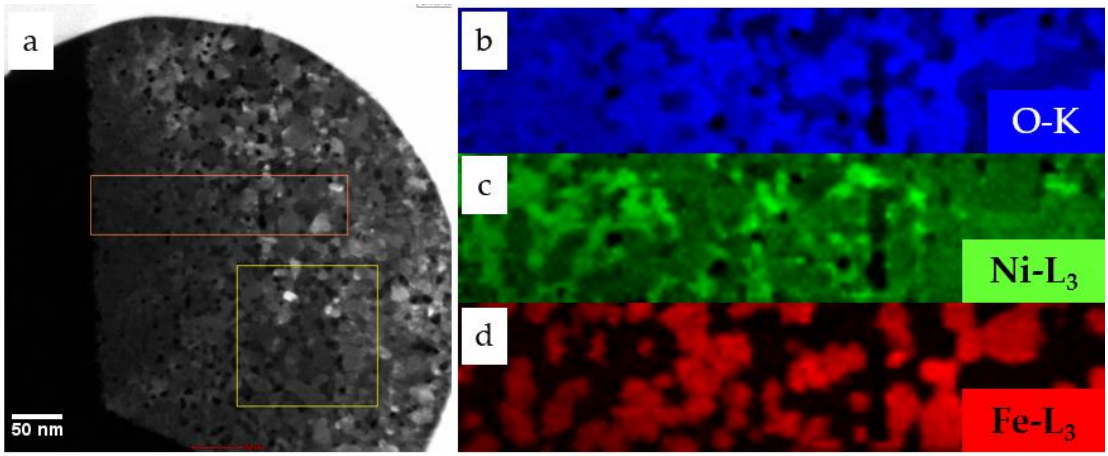

Figure 4.18 STEM-EELS map of calcined Ni-Fe LDH nanomaterials after ex-situ heating in a furnace at 850°C for 6 hours. (a) STEM image of thermally treated material. Orange rectangle represents mapped region. Yellow square denotes the image region for drift correction during map acquisitions. Scale bar is 50nm. (a) Oxygen (blue), (b) Nickel (green) and (c) Iron (red) elemental maps calculated from the O-K, Ni-L_3 and Fe-L_3 EELS edges respectively.

Beyond understanding the calcination processes of the LDH nanostructures, the generation of these new materials require their own characterizations to fully understand their structural properties. This thermal degradation procedures results in a new structure to be characterized. This section presents the application of TEM/STEM methodologies to probe the physicochemical properties of the thermally transformed Ni-Fe LDH material as a result of in-situ and ex-situ heating environments. A comprehensive understanding of this evolved material is crucial for optimization of future calcination processes as well as providing pivotal information in

relation to future catalytic and flame retardant applications.

A STEM-EELS map of the ex-situ calcined Ni-Fe LDH deposited on the SiN grid is shown in Figure 4.18. The Fe map demonstrates a prominent segregation of Fe rich domains, with a complete absence of Fe in some areas. However in the case of Nickel, the signal appears to be more ubiquitous but the regions of greater intensity also indicate the presence Nickel rich regions as well. This may be due to the formation of Ni containing particles which does not have any Iron content along with the formation of $NiFe_2O_4$ where there is a co-existence of the Ni and Fe and indeed O signals in the STEM-EELS maps.

High resolution TEM and STEM further characterized the atomic scale make-up of the calcined Ni-Fe LDH material. Figure 4.19 presents HRTEM and STEM analysis of the ex-situ calcined Ni-Fe LDH on the SiN grids. Copious regions of the sample were found to be highly crystalline in nature, as can be seen directly in the HRTEM data (Figure 4.19 (b)). Likewise to the in-situ experimentations, the LDH platelets underwent a phase transformation. This was confirmed by comparing crystallographic properties from FFT calculations. In particular, the calcined samples exhibit am orthorhombic symmetry with reciprocal lattice vector lengths of 2.51 nm and 2.94 nm. These crystal symmetries also agree well with the STEM nanoprobe diffraction data of the calcined materials from in-situ experiments (Figure 4.5 (f)). The highly crystalline features were also mirrored in STEM imaging, where atomic scale features could be resolved (Figure 4.19 (e)). Having said that, a varying crystal symmetry was exhibited from the corresponding FFT analysis. This revealed a hexagonal symmetry with a spacing of 2.91 nm. This is believed to be due to the formation of spinel-like structures rather than an LDH phase retention due to the prolonged thermal annealing at 850°C for 6 hours. Moreover, the findings related to the FFT analysis also correlate well with XRD and electron diffraction characterizations of similar spinel-like materials.[68,69] Without question, this data enhances our in-situ methodologies where similar structures were found to evolve upon thermal annealing. A notable feature from the STEM imaging is the presence of imperfections in the calcined crystallites of the material (Figure 4.19 (e)). One possible explanation of such irregularities may be the existence of grain boundary formations as a result of the ex-situ heating protocols.

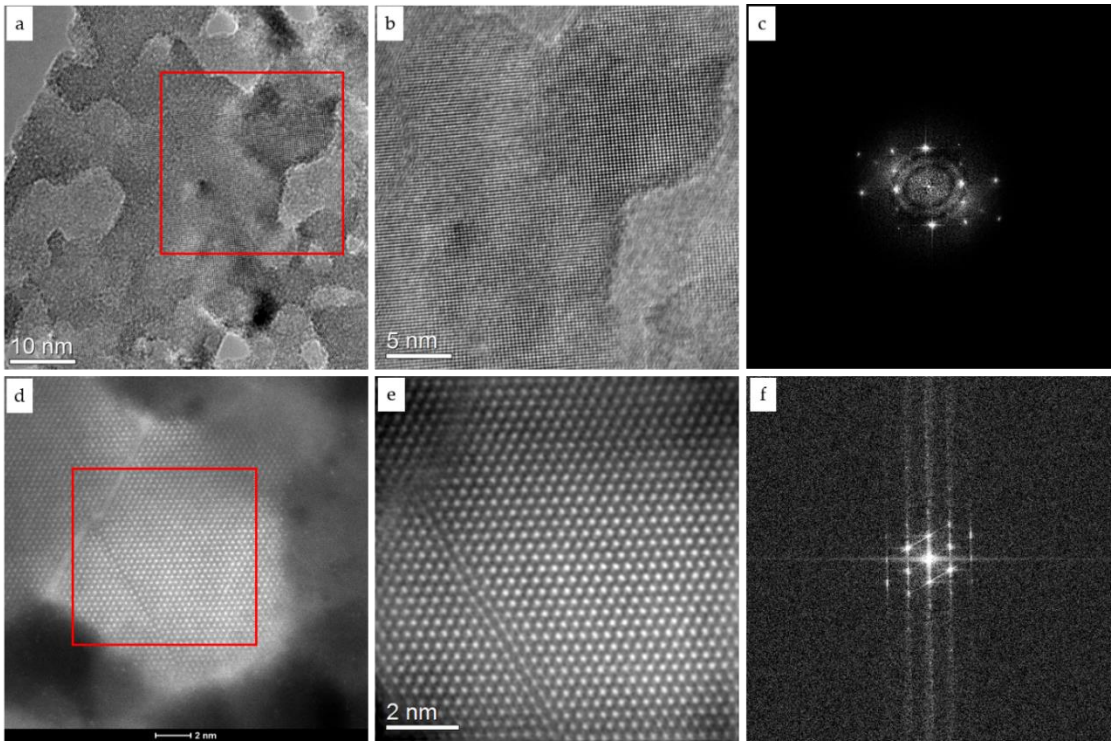

Figure 4.19 (a) HRTEM and (d) HRSTEM images of calcined LDH platelets. Red squares in each image represent region of filtered (b) HRTEM and (e) HRSTEM images. (c) and (f) present FFTs recorded from red square regions from HRTEM and HRSTEM images in (a) and (d) respectively.

Another striking observation to emerge from this HRTEM and STEM analysis was the stability of these calcined materials under the electron beam. This also accords well with earlier observations with regards to the calcined Ni-Fe LDHs in-situ. Hence, the properties of the ex-situ calcined materials were further investigated using our aberration corrected NION ultraSTEM. As previously addressed, this methodology uses significantly greater probe currents to image such materials but also holds the benefit of having more efficient EDX detectors as well as greater energy resolutions for potential EELS studies. Figure 4.20 shows both lower and higher magnification images of the calcined Ni-Fe LDHs. In accordance with the previous HRTEM data, a faceted morphology is also observed. Our previous results have illustrated that the calcined platelet was composed of randomly orientated crystallites before thermal annealing. However, the calcined products are composed of facets which appear to have a regular triangular morphology surrounding the porous regions. Furthermore, this data also agrees well with the previous HRTEM experiments using the FEI Titan (Figure 4.19). FFT were also used in this case to understand the crystalline features and in doing so,

we also are able to validate the findings from the previous HRTEM data. An orthorhombic symmetry is once again observed from the calculated FFT with reciprocal lattice vectors corresponding to d-spacings of 2.53 nm and 2.96 nm. These were found to compare very well with those found from TEM Titan experiments.

Surprisingly, there was also an existence of single atoms that were randomly and ubiquitously dispersed across the calcined morphologies. This is depicted by small regions of greater contrast, owed to the Z-contrast in STEM imaging (Figure 4.20). During this analysis, these 'heavy' atoms were observed to randomly migrate on the facet surface under the electron beam and were hence difficult to capture from an imaging perspective. Although what is more profound from this observation is that these atoms were not believed to be incorporated into the calcined structures but rather adhered to their surfaces.

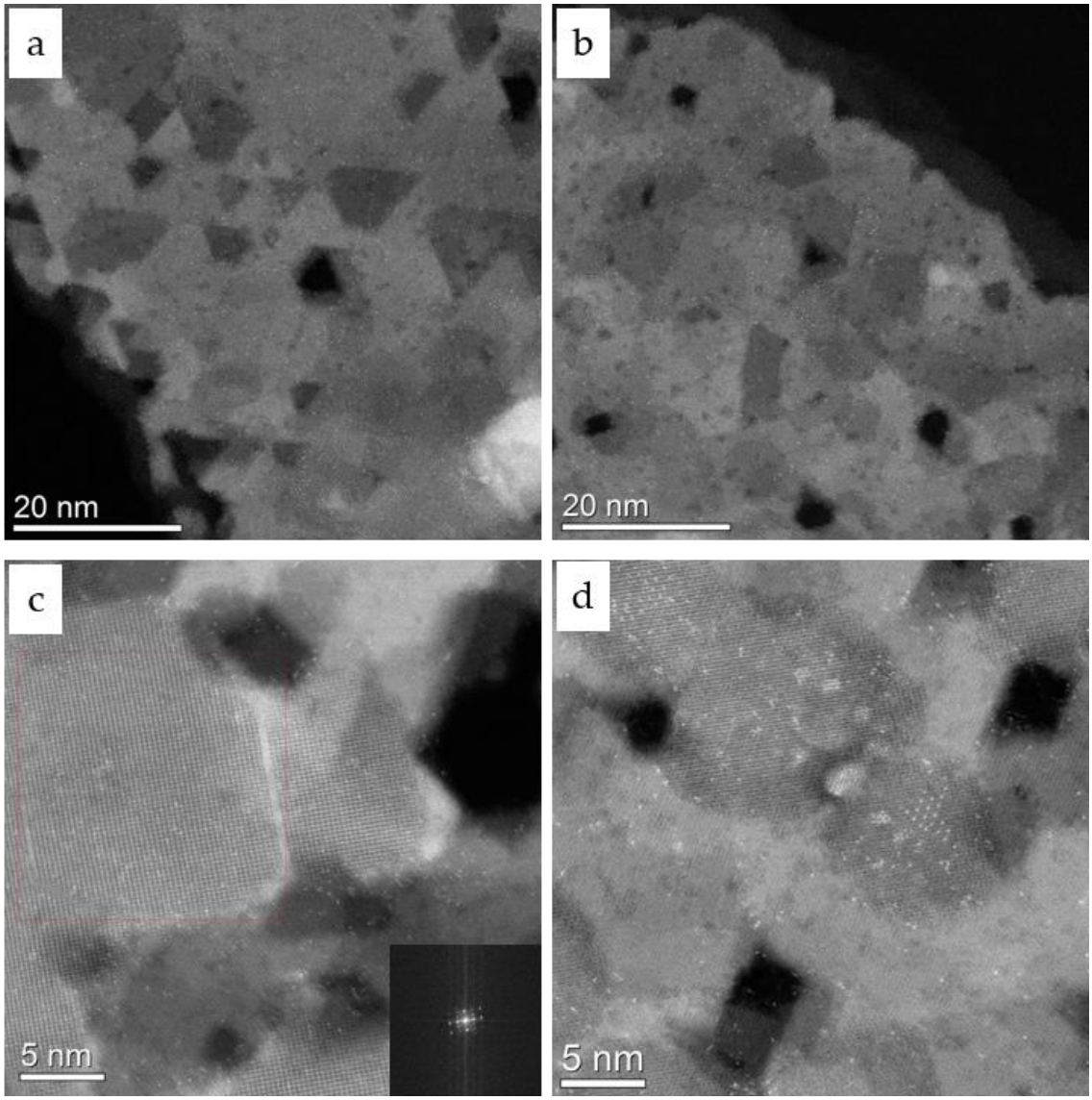

Figure 4.20 Characterization of the ex-situ calcined Ni-Fe LDH using NION ultraSTEM. (a) and (b) present lower magnification images of the calcined structures showing overall morphology. (c) and (d) present higher magnification images highlighting the atomic scale structure of the calcined material.

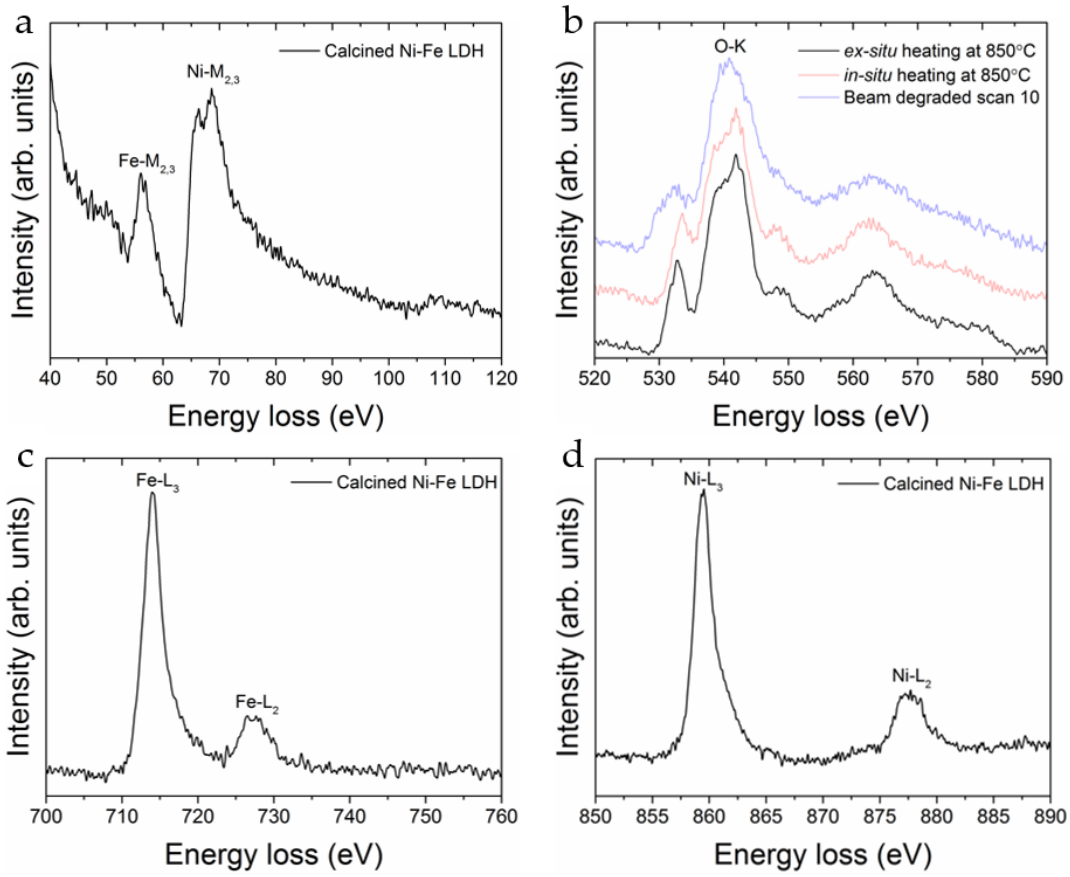

Figure 4.21 Core-loss EELS spectra recorded from ex-situ calcined platelets. Spectra (a) depicts the Ni and Fe M edges. Similarly, (b) represents the O K edge, with EELS spectra from previous beam degradation (blue) and in-situ heating (red) experiments shown for comparative purposes. (c) EELS spectra showing the Fe $L_{2,3}$ edge and (d) Ni $L_{2,3}$ edge of the calcined Ni-Fe LDH.

The features of the core-loss EELS edges of the ex-situ calcined Ni-Fe LDH were examined. The EELS spectra were acquired in STEM from the thermally treated platelets, similar regions to those previously shown in Figure 4.18(a).

The acquired spectra were recorded with a 2mm aperture and a dispersion of 0.05 eV/channel to try to resolve near edge fine structures in the core-loss peaks. The FWHM of the zero-loss peak for these experiments was 1.1 eV. Figure 4.21 presents the core-loss EELS spectra taken from the ex-situ calcined Ni-Fe LDH materials. Firstly, the Fe and Fe M edges are identifiable in the lower loss regimes of the core-loss spectrum present peaks at 56.2 eV and 67.5 eV respectively. This is believed to be due to the respective M edges of the Fe and Ni sites in the thermally treated LDH materials. Moreover, the nature of the doublet at 67.5 eV was also observed in a NiO thin film by Ahn and Krivanek (Figure 4.21 (a)).[70] This suggests that the calcined metallic sites are

of a NiO nature, which corroborates previous HRTEM and STEM-EELS of LDH platelets that were calcined in the electron microscope (Figure 4.6 (b) and Figure 4.11 (b) respectively). More interestingly, the O K edge substantially differs from the related K-edge of the parent Ni-Fe LDH material, as seen in Chapter 3. There exists an independent pre-peak before the Oxygen K edge in the calcined structures at 532.8 eV. This contrasts the shoulder feature of the K edge of the LDH material before calcination which was previously observed. We speculate that this peak is due to the presence of transition metal oxides. Moreover, there also appears to be the differences in the near edge fine structure of the delayed K-edge, with the existence of two peaks at 539.8 eV and 541.8 eV contrasting the rounded edges of the pristine material. These peaks observed in the Oxygen K edge also corroborate to previous research. The work of Mitterbauer *et. al* also present similar O K-edge signatures due to the presence of nickel oxide.[58] However, near edge x-ray absorption fine structure studies led by Park *et. al*, claiming these spectral shapes derive from an iron-oxide type material such as Fe_2O_3 or Fe_3O_4.[71] Likewise, the features of the O K edge from in-situ and ex-situ calcinations are also similar to analogous spinel materials in the literature.[72] This suggests that our EELS studies could be used to highlight the presence of particular phases, overcoming the numerous ambiguities and overlaps in the crystallographic analysis.

A natural progression from the O K edge studies was to determine whether alternative edges in the core loss EELS spectrum demonstrated similar behaviours. In our material, it is entirely possible that many possible physical phases can be due to the presence of both Ni and Fe in the calcined structures. Hence the Ni and Fe $L_{2,3}$ edges were also investigated in an attempt to further clarify the nature of such potential structures. Figure 4.21 (c) and (d) present the Ni $L_{2,3}$ and Fe $L_{2,3}$ core-loss edges from the calcined LDH materials. Upon first inspection, it is seen that there is no major alteration in either $L_{2,3}$ peaks after the LDH nanoplatelets have been thermally treated, in comparison to similar spectra recorded from the pristine LDH material in the preceding chapter.

Both the L_2 and L_3 can be easily observed in the Ni and Fe core-loss spectra from these thermally treated materials, as was similar to the case of the Ni-Fe LDHs before calcination experiments. More precisely, the spectra shape of the Ni $L_{2,3}$ edge compares well with previous studies, further highlighting the existence of NiO in the calcined materials. There is however conflicting EELS spectra features in the Fe L_3 edge in comparison to the literature, where a sharp pre peak occurs from the presence of Fe_2O_3 oxides.[64] Past studies of the $L_{2,3}$ edge in Fe based oxides have shown that there is a significant shoulder peak occurring in the L_3 peak.[73] In fact, the absence of the pre-peak in the Fe $L_{2,3}$ edge, as well as a similar shape to the Fe species studied by Leapman *et. al* propose that the nature of Fe in our ex-situ calcined platelets is that of Fe or FeO as opposed to the Fe_2O_3 configurations.[74]

If we now turn to the O K edge, the recorded EEL spectra from the calcined material using ex-situ approaches exhibits very similar signatures in comparison to the thermally treated LDHs from in-situ experiments (Figure 4.21 (b)). On a more general overlook, it can be deduced from these findings that both the thermal and beam radiation effects result in dehydration mechanisms of the LDH structure. Having said that, the features from the beam degradation from the sample are not as pronounced (Figure 4.21 (b)). For instance, even though the evolution of the pre-peak shoulder is evidenced in all three of these separate experimental procedures, the shape and intensity are not as appreciable when compared to the thermal cases. Also, the peak at 549.5eV after the delayed O K edge is only distinguished when the LDH is elevated to higher temperatures using thermal approaches. This indicates that the radiolytic damages of electron beam irradiation cause a different mechanism of dehydration in such transition metal LDH nanomaterials. Moreover, it can be inferred that applying thermal environments accelerates the generation of this transition metal oxide phases relative to beam irradiation methods. These findings may stir greater interest in the applications world of catalyst development or future catalyst support materials.

4.4 Conclusions

The main goal of this chapter was to use *in-situ* TEM to investigate and compare the thermal degradation behaviours of LDH materials. The application of *in-situ* heating

techniques in the transmission electron microscope revealed the morphological and crystallographic integrity of individual LDH platelets as well as the nanoscale behaviours and progression mechanisms involved in their thermal degradation.The decomposition mechanisms of both Ni-Fe and Mg-Al LDH compounds exhibited similar behaviours but also had unique signatures in their own right. The *in-situ* heating of Ni-Fe LDH material resulted in the transformation into a coexistence of Ni oxide type particles arranged throughout a $NiFe_2O_4$ trevorite matrix, confirmed by EFTEM, HRTEM and STEM-EDX methods. In addition, the thermal degradations were also paralleled via *ex-situ* and XRD methods, exhibiting identical phase transformations, verifying the observed behaviours are due to the inherent properties of the LDH materials. It was found that the calcined Mg-Al LDH evolved into Al_2O_3 and $MgAl_2O_4$ structures, effectively charaterized by HRTEM and SAED. However, the transition of the Mg-Al material occurred via a different mechanism, with a development of a porous matrix as opposed to the generation of spherical particles. The application of selected area electron diffraction *in-situ* effectively characterized the crystallographic transitions involved in the degradations of both Ni-Fe and Mg-Al of LDH materials, an important factor in evaluating their applications as catalysts and flame retardants respectively.

The applicability of our experimental methodologies was confirmed by our analysis of LDH materials of a different compositions, establishing a suitable *in-situ* approach to characterize the LDH thermal transformation behaviours. Undoubtedly these findings have raise research questions worth pursuing with further scientific investigation. It would be interesting to study if alternative LDH compositions and varying divalent/trivalent ratios have an affect of the thermal decompositions properties.

The environment of the heating experimental protocols, particularly those between in-situ and ex-situ approaches had an effect on the morphology of the calcined materials. It was shown that ex-situ heating of the nanoplatelets resulted in the formation of a contrasting faceted morphology in comparison with in-situ heating methods. Although there were no spherical particles observed, the segregation of Ni and Fe regions still resulted from the ex-situ heating environments. HRSTEM and AC-STEM showed that the facets of segregated iron and nickel are highly crystalline

domains of varying phases and orientations. STEM analysis also illustrated the existence of grain boundaries and defects in these faceted regions.

A significant finding to emerge from the EELS analysis combined with the in-situ heating methods is that different features in the O K edge EELS spectra emerge as the platelets were subject to elevated temperatures. STEM-EELS experiments illustrated that the pre-shoulder of the O K edge evolved into its own independent peak from 250°C. This is comparable to the case of EELS spectra evolution induced by the electron beam as discussed in the previous chapter. An additional peak at 549.5 eV after the delayed O-K edge was also seen to evolve from 550°C. It was also found that the EEL O K edge spectra of the calcined materials from ex-situ heating of the Ni-Fe LDHs exhibited very similar features to the case of the in-situ heated materials. The results of this study indicate that although there may be varying particle morphologies due to thermal annealing conditions, the electronic structure and chemical bonding of calcined materials are consistent, regardless of in-situ or ex-situ approaches. This work contributes to the existing depths of EELS knowledge by providing further spectra signatures from single nanoparticles of transition metal – oxygen environments for a range of temperatures up to 850°C. A natural progression could be to use low loss EELS to analyse if the annealing environments affect the electronic excitations such as excitonic and plasmonic features.

Overall, future research in this field would be of great help in the design of devices derived from calcined LDH nanomaterials of all types. In addition, studies could progress this area of research to advance our knowledge and the reasoning behind the enhanced material properties due to calcination. This would be of certain interest across many fields of research such as photocatalysis, flame retardants and gas adsorbents.

4.5 Bibliography

1. Fan, G., Li, F., Evans, D. G. & Duan, X. Catalytic applications of layered double hydroxides : recent advances and perspectives. *Chem. Soc. Rev.* **43,** 7040–7066 (2014).

2. Xu, Z. P., Zhang, J., Adebajo, M. O., Zhang, H. & Zhou, C. Catalytic applications of layered double hydroxides and derivatives. *Appl. Clay Sci.* **53,** 139–150 (2011).

3. Baig, N. & Sajid, M. Applications of layered double hydroxides based electrochemical sensors for determination of environmental pollutants: A review. *Trends Environ. Anal. Chem.* **16,** 1–15 (2017).

4. Fan, Q. *et al.* Double-Confined Nickel Nanocatalyst Derived from Layered Double Hydroxide Precursor : Atomic Scale Insight into Microstructure Evolution. *ACS Chem. Mater.* **28,** 6296–6304 (2016).

5. Liang, R., Tian, R., Liu, Z., Yan, D. & Wei, M. Preparation of Monodisperse Ferrite Nanocrystals with Tunable Morphology and Magnetic Properties. *Chem. - An Asian J.* **9,** 1161–1167 (2014).

6. Li, S., Mo, S., Wang, D., Wu, X. & Chen, Y. Synergistic effect for promoted benzene oxidation over monolithic CoMnAlO catalysts derived from in situ supported LDH film. *Catal. Today* (2018). doi:10.1016/j.cattod.2018.08.014

7. Abelló, S., Verboekend, D., Bridier, B. & Pérez-ramírez, J. Activated takovite catalysts for partial hydrogenation of ethyne , propyne , and propadiene. *J. Catal.* **259,** 85–95 (2008).

8. Zhao, Y. *et al.* Oxide-Modified Nickel Photocatalysts for the Production of Hydrocarbons in Visible Light. *Angew. Chemie Int. Ed.* **55,** 4215–4219 (2016).

9. Zou, L. *et al.* Self-generated Template Pathway to High-Surface-Area Zinc Aluminate Spinel with Mesopore Network from a Single-Source Inorganic Precursor. *Chem. Mater.* 5852–5859 (2006).

10. Yuan, X., Jing, Q., Chen, J. & Li, L. Photocatalytic Cr(VI) reduction by mixed metal oxide derived from ZnAl layered double hydroxide. *Appl. Clay Sci.* **143,** 168–174 (2017).

11. Manzi-nshuti, C., Wang, D., Hossenlopp, M. & Wilkie, C. A. Aluminum-containing layered double hydroxides : the thermal , mechanical , and fire properties of (nano) composites of poly (methyl methacrylate) †. *J. Mater. Chem.* **18,** 3091–3102 (2008).

12. Edenharter, A., Feicht, P., Diar-bakerly, B., Beyer, G. & Breu, J. Superior flame retardant by combining high aspect ratio layered double hydroxide and graphene oxide. *Polymer (Guildf).* **91,** 41–49 (2016).

13. Nyambo, C., Songtipya, P., Manias, E., Jimenez-gasco, M. M. & Wilkie, C. A. Effect of MgAl-layered double hydroxide exchanged with linear alkyl carboxylates on fire-retardancy of PMMA and PS. *J. Mater. Chem.* **18,** 4827–4838 (2008).

14. Chem, J. M. *et al.* Polypropylene / layered double hydroxide nanocomposites. *J. Mater. Chem.* **22,** 19113–19121 (2012).

15. Nagendra, B., Mohan, K. & Gowd, E. B. Polypropylene/Layered Double Hydroxide (LDH) Nanocomposites: Influence of LDH Particle Size on the Crystallization Behavior of Polypropylene. *ACS Appl. Mater. Interfaces* **7,** 12399–12410 (2015).

16. Xu, W., Zhang, B., Xu, B. & Li, A. The flame retardancy and smoke suppression effect of heptaheptamolybdate modified reduced graphene oxide / layered double hydroxide hybrids on polyurethane elastomer. *Compos. Part A* **91,** 30–40 (2016).

17. Gao, Y., Wu, J., Wang, Q., Wilkie, A. & Hare, D. O. Flame retardant polymer / layered double hydroxide nanocomposites. *J. Mater.* **2,** 10996–11016 (2014).

18. Zammarano, M., Franceschi, M., Bellayer, S., Gilman, J. W. & Meriani, S. Preparation and flame resistance properties of revolutionary self-extinguishing epoxy nanocomposites based on layered double hydroxides. *Polymer (Guildf).* **46,** 9314–9328 (2005).

19. Lee, C.-G. & Kim, S.-B. Magnetic alginate-layered double hydroxide composites for phosphate removal. *Environ. Technol.* **34,** 2749–2756 (2013).

20. Zhao, X., Xu, S., Wang, L., Duan, X. & Zhang, F. Exchange-Biased NiFe2O4/NiO Nanocomposites Derived from NiFe-Layered Double Hydroxides as a Single Precursor. *Nano Res.* 200–210 (2010). doi:10.1007/s12274-010-1023-3

21. Lei, X. *et al.* Activated MgAl-layered double hydroxide as solid base catalysts for the conversion of fatty acid methyl esters to monoethanolamides. *Appl. Catal. A* **399,** 87–92 (2011).

22. Sideris, P. J., Nielsen, U. G., Zhehong, G. & Grey, C. P. Mg/Al Ordering in Layered Double Hydroxides Revealed by Multinuclear NMR Spectroscopy. *Science (80-.).* **321,** 113–118 (2008).

23. Perez-Ramirez, J., Mul, G., Kapteijn, F. & Moulijn, J. A. In situ investigation of the thermal decomposition of Co ± Al hydrotalcite in different atmospheres. *J. Mater. Chem.* **11,** 821–830 (2001).

24. Li, Y. *et al.* In-grown structure of NiFe mixed metal oxides and CNT hybrid catalysts for oxygen evolution. *Chem. Commun.* **52,** 1439–1442 (2016).

25. Zhao, X. *et al.* Fabrication and Photocatalytic Properties of Novel ZnO / ZnAl 2 O 4 Nanocomposite with ZnAl 2 O 4 Dispersed Inside ZnO Network. *AIChE* **58,** 573–582 (2012).

26. He, S. *et al.* A Surface Defect-Promoted Ni Nanocatalyst with Simultaneously Enhanced Activity and Stability. *ACS Chem. Mater.* **25,** 1040–1046 (2013).

27. Li, C., Wei, M., Evans, D. G. & Duan, X. Recent advances for layered double hydroxides (LDHs) materials as catalysts applied in green aqueous media. *Catal. Today* **247,** 163–169 (2015).

28. Puttaswamy, N. S. & Kamath, P. V. Reversible thermal behaviour of layered double hydroxides : a thermogravimetric study. *J. Mater. Chem.* **7,** 1941–1945 (1997).

29. Tsyganok, A. & Ã, A. S. Incorporation of transition metals into Mg – Al layered double hydroxides : Coprecipitation of cations vs . their pre-complexation with an anionic chelator. *J. Solid State Chem.* **179,** 1830–1841 (2006).

30. Yan, D. *et al.* In Situ Polymerization of the 4-Vinylbenzenesulfonic Anion in Ni - Al - Layered Double Hydroxide and Its Molecular Dynamic Simulation. *J. Phys. Chem. A* **112,** 7671–7681 (2008).

31. Vaysse, C., Guerlou-Demourgues, L. & Delmas, C. Thermal Evolution of Carbonate Pillared Layered Hydroxides with (Ni, L) (L = Fe , Co) Based Slabs: Grafting or Nongrafting of Carbonate Anions? *Inorg. Chem.* **41,** 3831–3839 (2002).

32. Mascolo, G. & Mascolo, M. C. On the synthesis of layered double hydroxides (LDHs) by reconstruction method based on the 'memory effect'. *Microporous Mesoporous Mater.* **214,** 246–248 (2015).

33. Kowalik, P. *et al.* Memory effect of the CuZnAl-LDH derived catalyst precursor - In situ XRD studies. *Appl. Catal. A Gen.* **464–465,** 339–347 (2013).

34. Mohapatra, L. & Parida, K. A review on the recent progress , challenges and perspective of layered double hydroxides as promising photocatalysts. *J. Mater. Chem. A* **4,** 10744–10766 (2016).

35. Radha, A. V, Thomas, G. S., Kamath, P. V. & Antonyraj, C. A. Thermal decomposition of Co – Al layered double hydroxide : Identification of precursor to oxide with spinel structure. *Bull. Mater. Sci.* **33,** 319–324 (2010).

36. Matusinovic, Z. & Wilkie, C. A. Fire retardancy and morphology of layered double hydroxide nanocomposites : a review. *J. Mater. Chem.* **22,** 18701–18704 (2012).

37. Egerton, R. F., Li, P. & Malac, M. Radiation damage in the TEM and SEM. *Micron* **35,** 399–409 (2004).

38. Arakcheeva, A. V., Pushcharovskii, D. Y., Rastsvetaeva, R. ., Atencio, D. & Lubman, G. U. Crystal structure and comparative crystal chemistry of Al2Mg4(OH)12 (CO3)·3H2O, a new mineral from the hydrotalcite-manasseite group. *Crystallogr. Reports* **41,** 972–981 (1996).

39. Downs, R. T. & Hall-Wallace, M. The American Mineralogist crystal structure database. *Am. Mineral.* **88,** 247–250 (2003).

40. Yilmaz, G., Yam, K. M., Zhang, C., Fan, H. J. & Ho, G. W. In Situ Transformation of MOFs into Layered Double Hydroxide Embedded Metal Sulfides for Improved Electrocatalytic and Supercapacitive Performance. *Adv. Mater.* **1606814,** (2017).

41. Warringham, R. *et al.* Mapping the Birth and Evolution of Pores upon Thermal Activation of Layered Hydroxides. *ACS Chem. Mater.* **29,** 4052–4062 (2017).

42. Constantino, V. R. L. & Hnnavaia, T. J. Basic Properties of Mg2 + 1 ,Al3+, Layered Double Hydroxides Intercalated by Carbonate , Hydroxide , Chloride , and Sulfate Anions. *Inorg. Chem.* **34,** 883–892 (1995).

43. Roelofs, J. C. A. A., Bokhoven, J. A. Van, Dillen, A. J. Van, Geus, J. W. & Jong, K. P. De. The Thermal Decomposition of Mg ± Al Hydrotalcites : Effects of Interlayer Anions and Characteristics of the Final Structure. *Chem. Eur. J.* **24,** 5571–5579 (2002).

44. Camino, G., Maffezzoli, A., Braglia, M., Lazzaro, M. De & Zammarano, M. Effect of hydroxides and hydroxycarbonate structure on fire retardant effectiveness and mechanical properties in ethylene-vinyl acetate copolymer. *Polym. Degrad. Stab.* **74,** 457–464 (2001).

45. Bellotto, M. *et al.* Hydrotalcite Decomposition Mechanism : A Clue to the Structure and Reactivity of Spinel-like Mixed Oxides. *J. Phys. Chem.* **3654,** 8535–8542 (1996).

46. Yang, W., Kim, Y., Liu, P. K. T., Sahimi, M. & Tsotsis, T. T. A study by in situ techniques of the thermal evolution of the structure of a Mg – Al – CO 3 layered double hydroxide. *Chem. Eng. Sci.* **57,** 2945–2953 (2002).

47. Mokhtar, M., Inayat, A., Ofili, J. & Schwieger, W. Thermal decomposition , gas phase hydration and liquid phase reconstruction in the system Mg / Al hydrotalcite / mixed oxide: A comparative study. *Appl. Clay Sci.* **50,** 176–181 (2017).

48. Grazulis, S. *et al.* Crystallography Open Database – an open-access collection of crystal structures. *J. Appl. Crystallogr.* 726–729 (2009). doi:10.1107/S0021889809016690

49. Allmann, R. Magnesium Aluminium Carbonate Hydroxide Tetrahydrate: A discussion. *Am. Mineral.* **53,** 1057 (1968).

50. Sun, G. *et al.* From Layered Double Hydroxide to Spinel Nanostructures : Facile Synthesis and Characterization of Nanoplatelets and Nanorods. *J. Phys. Chem.* **110,** 13375–13380 (2006).

51. Chai, R. *et al.* Free-Standing NiO-MgO-Al 2 O 3 Nanosheets Derived from Layered Double Hydroxides Grown onto FeCrAl-Fiber as Structured Catalysts for Dry Reforming of Methane. *ACS Sustain. Chem. Eng.* **5,** 4517–4522 (2017).

52. Cho, S. & Lee, K. Formation of zinc aluminum mixed metal oxide nanostructures. *J. Alloys Compd.* **509,** 8770–8778 (2011).

53. Carriazo, D. *et al.* Zn , Al hydrotalcites calcined at different temperatures : Preparation , characterization and photocatalytic activity in gas – solid regime. *J. Mol. Catal. A* **342–343,** 83–90 (2011).

54. Rougier, A. & Da Rocha, M. Electrochromism of non-stoichiometric NiO thin film : as single layer and in full device. *Appl. Phys. A* **122,** 1–7 (2016).

55. Hunter, B. M., Hieringer, W., Winkler, J. R., Gray, H. B. & Mu, A. M. Effect of interlayer anions on [NiFe]-LDH nanosheet water oxidation activity. *RSC Energy Environ. Sci.* **23,** 1734–1743 (2016).

56. Hobbs, C. *et al.* Structural transformation of layered double hydroxides : an in situ TEM analysis. *npj 2D Mater. Appl.* **2,** (2018).

57. Lim, C. S. *et al.* Layered transition metal oxyhydroxides as tri-functional electrocatalysts. *J. Mater. Chem. A* **3,** 11920–11929 (2015).

58. Mitterbauer, C. *et al.* Electron energy-loss near-edge structures of 3d transition metal oxides recorded at high-energy resolution. *Ultramicroscopy* **96,** 469–480 (2003).

59. De Groot, F. M. F. *et al.* Oxygen 1s X-ray-absorption edges of transition-metal oxides. *Phys. Rev. B* **40,** 5715–5723 (1989).

60. Grunes, L. A., Leapman, R. D., Wilker, C. N., Hoffmann, R. & Kunz, A. B. Oxygen K near-edge fine structure: An electron-energy-loss investigation with comparisons to new theory for selected 3d transition-metal oxides. *Phys. Rev. B* **25,** 7157–7173 (1982).

61. Chen, S.-Y. *et al.* Electron energy loss spectroscopy and *ab initio* investigation of iron oxide nanomaterials grown by a hydrothermal process. *Phys. Rev. B* **79,** 104103 (2009).

62. Garvie, L. A. J. Can electron energy-loss spectroscopy (EELS) be used to quantify hydrogen in minerals from the O K edge? *Am. Mineral.* **95,** 92–97 (2010).

63. Koyama, Y., Mizoguchi, T., Ikeno, H. & Tanaka, I. Electronic Structure of Lithium Nickel Oxides by Electron Energy Loss Spectroscopy. *J. Phys. Chem. B* **109,** 10749–10755 (2005).

64. Colliex, C., Manoubi, T. & Ortiz, C. Electron-energy-loss-spectroscopy near-edge fine structures in the iron-oxygen system. *Phys. Rev. B* **44,** 11402–11411 (1991).

65. Wong, F. & Buchheit, R. G. Utilizing the structural memory effect of layered double hydroxides for sensing water uptake in organic coatings. *Prog. Org. Coatings* **51,** 91–102 (2004).

66. Abelló, S., Bolshak, E. & Montané, D. Ni – Fe catalysts derived from hydrotalcite-like precursors for hydrogen production by ethanol steam reforming. *Appl. Catal. A Gen.* **450,** 261–274 (2013).

67. Xiao, T., Tang, Y., Jia, Z., Li, D. & Hu, X. Self-assembled 3D flower-like Ni2+-Fe3+ layered double hydroxides and their calcined products. *IOP Nanotechnol.* **20,** 475603 (2009).

68. Jadhav, H. S., Kalubarme, R. S., Jadhav, A. H. & Seo, J. G. Iron-nickel spinel oxide as an electrocatalyst for non-aqueous rechargeable lithium-oxygen batteries. *J. Alloys Compd.* **666,** 476–481 (2016).

69. Zheng, J. *et al.* Enhanced Li+ ion transport in LiNi0.5Mn1.5O4 through control of site disorder. *Phys. Chem. Chem. Phys.* **14,** 13515 (2012).

70. Ahn, C. C. & Krivanek, O. . *EELS Atlas: a reference collection of electron energy loss spectra covering all stable elements*. (Warrendale : Gatan, 1983).

71. Park, T.-J. *et al.* Electronic Structure and Chemistry of Iron-Based Metal Oxide Nanostructured Materials: A NEXAFS Investigation of BiFeO3, BiFe4O9, alpha-Fe2O3, gamma-Fe2O3, and Fe/Fe3o4. *J. Phys. Chem. C* **112,** 10359–10369 (2008).

72. Nyquist, S. & Hålenius, U. An EELS study of near edge structures of the oxygen K-edge in spinels. *Phys. Chem. Miner.* **41,** 255–265 (2014).

73. Almeida, T. P. *et al.* Visualized effect of oxidation on magnetic recording fidelity in pseudo-single-domain magnetite particles. *Nat. Commun.* **5,** 1–6 (2014).

74. Leapman, R. D., Grunes, L. A. & Fejes, P. L. Study of the L23 edges in the 3d transition metals and their oxides by electron-energy-loss spectroscopy with comparisons to theory. *Phys. Rev. B* **26,** 614–635 (1982).

Chapter 5: Characterization of Mg-Al LDH materials as a delivery vector to biological cells

5.1 LDH materials in bioengineered samples

Up to this point, we have learned a great deal about the properties of LDHs and in the previous chapter, their related behaviours in applied thermal environments. The application of in-situ TEM revealed processes at the nanoscale which could not be resolved using bulk techniques. The calcination behaviours could be analysed with enhanced spatial resolutions, as well as probing LDH behaviours at nano and even atomic scales. In view of this, we chose to uncover alternative avenues of LDH research where these EM characterizations could greatly assist in the understanding of these materials in so-called 'real world' systems.

A revision of the literature highlights numerous studies where LDH based nanomaterials are employed in the areas of biological based fields of nanotechnology such as drug and gene delivery, cancer therapy, skin repair, implants and antimicrobial treatments.[1–9] In particular, the recent employment of layered double hydroxide nanomaterials as therapeutic delivery agents to biological cells has shown great promise in areas such as gene delivery vectors, controlled release agents and cancer therapy diagnostics[10–18]. This is largely due to the numerous beneficial properties of LDHs for these applications such as high biocompatibility, low cytotoxicity, accessible surface areas, high loading capacity, suitable size distributions, controlled release and anion exchange properties[19–21]. Interestingly, their ability to intercalate a range of loaded drugs/genes such as single stranded RNA and methotrexate into their interlayers has attracted research interest[22,23]. The inclusion of the substituted load can introduce a beneficial positive surface charge to the vector which enhances the interaction with the negative cell membranes as well as protecting of the biomolecules from enzymatic degradation within the cells[24,25]. In contrast, other types of biomolecules such as supercoiled plasmid DNA structures exhibit an

alternative interaction via a surface adherence to outer LDH layers resulting in particle aggregation.[26] These unique properties have resulted in the development of LDH materials as effective drug/gene delivery vehicles for a range of therapeutics.[26–32]

It has further been shown that LDH materials can successfully transfect and deliver therapeutics to a broad range of cell types such as tendon cells, tumour cells, cancer cells and even plant cells.[33–36] Previous work has addressed the mechanisms of biomolecule interaction and cellular delivery using LDH nanomaterials as vectors using a variety of physical and biological analytical techniques[15,37–40].

The general outlook on the published work related to LDH nanoparticle delivery to date is somewhat problematic from a nanoscale characterization point of view. Whilst this provides useful and crucial information for healthcare applications, the majority of the works centre around the impact of the applied LDHs have on the biological systems at hand such as cancer cell impacts or gene therapy applications. A considerable overlook of these studies is the structural role, behaviour and ultimate fate of the LDH nanoparticles in the cellular environments. Even though past studies recognise the manner of uptake and delivery of single LDH nanoparticles is not fully understood, little characterization to investigate such mechanisms has been conducted.[41] This inadequacy indeed needs to be addressed in order to comprehensively understand our entire system. Hence, a thorough assessment of these systems includes the knowledge of the LDH materials behaviours at all scales in these environments, something which EM characterizations can adequately provide. Only then can we truly evaluate and optimize these LDH materials in the most efficient manner. Many features of EM methods are advantageous relative to complimentary optical microscopy techniques. Firstly, the interaction of the electron with the sample provides greater spatial resolution. This allows us to analyse the physical and morphological features of LDH related particles can be assessed when subject to MSC environments. In addition, the electron-sample interaction generates crystallographic information from subcellular regions, studied by electron diffraction. The use of a selected area aperture permits the recording of diffraction patterns from intracellular regions of the cell. A further benefit of utilising EM techniques is the

generation of X-ray signals. The acquisition and identification of these X-rays is conducted in energy dispersive x-ray spectroscopy. Hence, elemental analysis can be conducted at nanometre resolution from various regions across the associated samples. This complete nanoscale characterization of the interaction of LDH nanomaterials with biological specimens is a critical necessity for the evaluation of their suitability to be employed as the next generation of therapeutic materials in regenerative medicine.

As we have previously seen, EDX and EELS can provide unique chemical information about our nanomaterials. These too can elucidate information about specimens of a biological nature. The specialized microanalytical techniques inherently characterize materials at a subcellular level, revealing a new wealth of information about biological systems. Firstly, EELS is considered as a useful technique for analysis of light elements such as carbon, nitrogen and oxygen. This is of particularly advantageous for the study of organic molecules such as proteins and nucleic acids which are made up of such light elements.[42–44] Moreover, metallic atoms with sharp $L_{2,3}$ edges such as calcium and iron can also be probed in subcellular compartments using EELS approaches.[45–48] A further benefit of applying these spectroscopic studies to such systems is the study of elemental distributions within biological specimens. EFTEM is an accurate method for large-area distribution studies within cellular bodies. For example, previous literature has shown the distribution of nitrogen, phosphorous and sulphur in mouse pancreatic islets.[49] In the more precise context of the work of this thesis, EFTEM has also been used to study the uptake and localisation of iron oxide,[50] titanium dioxide[51] and quantum dot[52] particles in their respective cellular systems.

Although the microanalysis of biological structures and cellular physiological processes can elucidate interesting information, experiments of such nature have its own limitations. First of all, EELS based studies are valued as high-end analytical tools of EM. Along with this, the availability of suitable advanced instrumentation and skill levels by the experimentalist are required to carry out such analysis. Furthermore, the extent of the microanalytical studies largely depend on the quality of the sample and its preparation. The conventional embedding procedures can cause major alterations to cellular content and structure.[53] Hence, any spectroscopic data needs to be interpreted

with great caution. In relation to plastic embedded samples, radiation damage can be a significant limiting factor for microanalytical experiments. Multiple frame acquisitions in EFTEM and long pixel dwell times in
STEM-EELS studies are often a stipulation in order to achieve significant statistical counts. This however may be beyond the dose threshold of plastic embedded samples, leading to further specimen alterations, sample resin destructions and unfortunate useless data. The thickness of sections from plastic embedded samples can also impair the outcome and even possibilities of EFTEM or EELS experiments. If sections are too thick, the signal-to-noise ratios are too low to achieve any substantial experimental data.

We have seen that there are several studies of LDH nanoparticles applied as delivery vectors to a wide range of cell lines. This has often resulted from the successful uptake of the related LDH based vectors into the cells. Also a number of researchers have reported the ultrastructural features involved in the uptake and localisation of LDH particles at the subcellular scale.[54–56] However, this research is restricted to a morphological outlook from conventional TEM imaging and interpretation. In fact, there is a clear lacking of comprehensive microanalytical based studies of LDH nanomaterials as they as employed in biological environments. Also, these studies do not consider the behaviour of the LDHs themselves in such systems. EFTEM and EELS can progress the fields of research of LDH particles applied as drug delivery vectors. These microanalytical studies can elucidate any uncertainty in the uptake and localisation of LDH based nanoparticles as well as revealing their structural information in biological systems.

Here, we applied EM methods such as (scanning) transmission electron microscopy ((S)TEM), selected area electron diffraction (SAED) and energy dispersive x-ray spectroscopy (EDX) to observe and understand the nanoscale LDH materials structural properties as they are employed as gene delivery vectors to mesenchymal stem cells (MSCs) and A549 lung adenocarcinoma cancer cells. As well as providing pivotal information regarding the delivery roles involved in LDH delivery, our approach will have a critical impact on pharmaceutical and clinical applications.

The aims of this chapter are two-fold. Firstly, we investigate the nanoscale properties of LDH interactions with DNA based biomolecules, plasmid DNA and single stranded RNA. We then also seek to characterize the LDH physical behaviours and intracellular fate in two differing cell lines i.e. mesenchymal stem cells and lung A549 lung carcinoma cells.

5.2 Experimental Methods

5.2.1 Mg-Al LDH synthesis

Mg-Al LDH were synthesized to have a smaller platelet dimension than the samples previously synthesized in Chapter 3. The Mg-Al LDH delivery vectors were prepared using 343 g (1.68 mol) $MgCl_2 \cdot 6H_2O$ and 136 g (0.56 mol) $AlCl_3 \cdot 6H_2O$ and were dissolved in 100 ml deionized water. Similarly, a second reactant mixture was prepared by dissolving 180 g (4.5 mol) NaOH pellets and 30 g (0.28 mol) Na_2CO_3 in 100 ml deionized water. Subsequently, the reactant mixtures were pumped together within 30 minutes with a syringe pump into a beaker, containing another 150 ml deionized water, under heavy shear-mixing using an ultraturrax rotor-stator-mixer. The reaction product was subsequently washed five times with deionized water. Then, solid-liquid separation was conducted by gravitational sedimentation i.e. centrifugation. Eventually, the washed LDH particles were re-dispersed in 1500 ml of deionized water and heated at 80°C for 4 days.

Mg-Al LDH and plasmid DNA (pDNA) composites were synthesized using the anion exchange methods.[28] In our case, 100 µl of plasmid-DNA solution (1 µg/µl) (TERG, RCSI, Dublin) was added to 500 µl of LDH solution (1 mg/ml) (CRANN, TCD, Dublin) in a sealed septum. This was purged with N_2 flow to prevent carbonation of the anionic interlayer. The sample was placed in an oil bath at 37°C for 3 days.

5.2.2 TEM preparation of cell cultures samples

In preparation for TEM analysis, cell pellets were fixed in 2% glutaraldehyde for 1 hour and washed twice with phosphate buffer saline (PBS) solution. These were then post-fixed in OsO_4 for 1 hour. Samples were then dehydrated through an ethanol:H_2O ratio series of 50% , 60%, 70%, 80%, 90%, 95% and 100% for 10 minutes. There were

two variations of embedding media used in this study. For the MSC cell exposures, LR White resin (Agar Scientific, USA) was used. Conversely, the LDHs that were exposed to A549 cells were embedded in epoxy resin (Agar Scientific, USA). Resin embedding was imposed using LR White Resin (Agar Scientific, USA). The dehydrated samples were exposed to an ethanol:resin ratio of 1:1 twice and subsequently embedded in 100% LR White resin. Curing of the resin blocks was conducted overnight at 4°C under ultraviolet light exposure. Samples embedded in epoxy based firstly in a 1:1 ratio of ethanol:resin at 37°C for 2 hours followed by 100% epoxy resin at 60°C overnight. Ultramicrotomy was conducted using a Leica UC6 ultramicrotome (Leica, Germany) equipped with a Diatome diamond knife. The resin blocks were microtomed and sections were collected on 200 mesh Cu TEM grids (Sigma-Aldrich, USA)). A selection of sample grids of the LDH – MSC exposures were post-stained with uranyl acetate for 30 seconds to enhance TEM contrast.

5.2.3 TEM characterization experimental details

TEM and STEM characterization of results presented in this chapter was performed on an FEI Titan aligned at 300 kV.

LDHs exposed to A549 cells: STEM-EELS and EFTEM experiments were carried out on a Gatan Imaging Filter (GIF) and a 1.1 eV energy resolution. A 5mm entrance aperture was used in this case to maximise the signals from the core-loss edges.

STEM-EELS of the Nitrogen and Oxygen core-loss edges were recorded using a 0.1 eV/channel dispersion. A STEM probe current of 0.06 nA was again used with a convergence angle of 8 mrad, collection angle of 21 mrad (camera length 38mm). Area scans of 500nm x 500nm were recorded and an integration time of 6 seconds (summing 10 spectra) was used.

Analogously, STEM-EELS of the Carbon and Oxygen core-loss signals were acquired with a 0.2 eV/channel dispersion to encapsulate both signals simultaneously. A probe current of 0.03 nA with convergence and collection angles as above. The spectra were acquired over a 530nm x 530nm region with an integration time of 5 seconds.

The Mg and Al $L_{2,3}$ edges of the LDH were acquired with a 2mm entrance aperture due to a better energy resolution. A 0.05 eV/channel dispersion was chosen in this case. EFTEM of the Oxygen K edge was conducted by first tuning the GIF and then using a 60 second exposure time for map acquisitions.

5.3 Mg-Al LDH only characterization

5.3.1 Mg-Al LDHs of smaller dimensions

The first step of this study was to select a suitable candidate for the intended cell culture experiments. Firstly, the Mg-Al LDH composition was favoured over the Ni-Fe counterpart due to the potential undesirable cytotoxic effects of Nickel related particles.[57] Adding to this argument, the literature has shown many previous studies of utilising the Mg-Al composition for such applications, which provided valuable reference points and comparisons to our own work. On the other hand, the majority of the Mg-Al materials we have already studied in previous sections were, although suitably thin, were of large lateral dimensions (approximately 3μm). This was deemed limitation in relation to biocompatibility for endocytic uptake.[58,59] As such, research conducted in our group refined the synthesis to produce Mg-Al LDHs of smaller more appropriate lateral dimensions.

Figure 5.1 shows a TEM image and a corresponding SAED pattern of the as-synthesized LDH material respectively. TEM micrographs of the synthesized LDH material reveal that the nanoplatelets attain a well-defined hexagonal morphology and are below 100nm in lateral dimension.

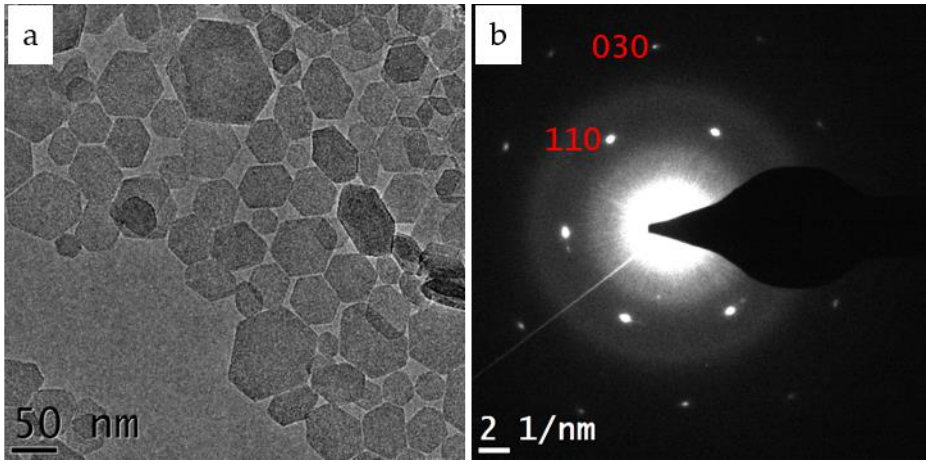

Figure 5.1 (a) TEM and (b) SAED analysis of the LDH particles prior to cell exposure experiments. The hexagonal symmetries in the associated pattern represent an LDH crystal structure with diffraction spots corresponding to the {110} and {100} families.

These features are favourable for their candidacy as gene delivery vectors due to their suitable size ranges for biological cellular uptake.[60] The recorded SAED pattern from the associated LDH platelets is presented in Figure 5.1(b).

From a crystallographic viewpoint, a hexagonal symmetry is exhibited, consisting of the {100} and {110} planes of the LDH structure (crystallographic plane indices are shown in red in Figure 1B). The reciprocal lattice symmetries are in agreement with previously investigated LDH materials[61,62]. Energy dispersive x-ray spectroscopy (EDX) analysis of the LDH particles exhibits peaks at 1.25 keV and 1.5 keV respectively, originating from the Mg and Al metallic cations in the LDH layers.

5.3.2 Mg-Al LDH interaction with plasmid DNA structures

To act as successful gene delivery vectors, LDHs must be successfully complexed with gene therapeutics such as nucleic acids. More details on the functionalisation methods can be found in the Supplementary Information. Figure 2 shows the TEM images of the LDH particles after their interaction with plasmid DNA (pDNA) encoding green fluorescent protein (pGFP), which resulted in a bio-functionalized nanohybrid (LDH-pGFP). The functionalised LDH material exhibited increased aggregation as shown in bright field TEM (Figure 5.2 (a)). Furthermore, Figure 5.2 (c) presents STEM-EDX analysis of similar regions of these hybrid materials. The peak in the EDX spectrum at

2 keV indicates the presence of Phosphorous, a signature of the pGFP plasmids and not the LDH material itself. This is attributed to the phosphate backbone of the pDNA structure. We perceive that the pGFP adheres to the positively charged LDH platelet surfaces, resulting in an aggregation of the platelets. These findings confirm results from previous reports by Ladewig *et. al*[26] and Xu *et .al* using similar TEM methods[63]. However, the former overlooks spectroscopic interactions to confirm such interactions whilst the latter relies on a STEM-EDX point acquisitions. This results in low EDX counts and makes the existence of Phosphorous, and hence a pDNA interaction, difficult to interpret.

The application of EDX microanalysis methods in STEM to evaluate the composition of the LDH-pDNA composite materials. The acquired EDX spectra shows an additional peak at

2 keV in comparison to the pristine Mg-Al LDH material. This is believed to come from the phosphate backbone of the plasmid DNA structures, confirming an interaction between the layered material and the introduced biomaterial.

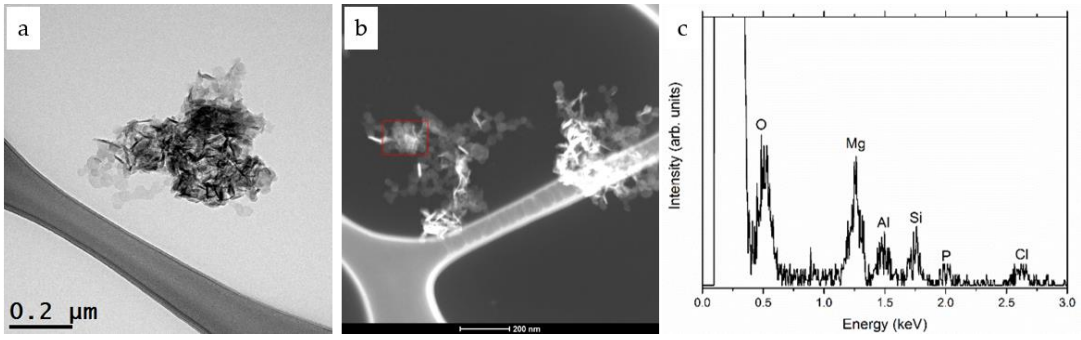

Figure 5.2 (a) Bright field TEM and (b) annular dark field STEM images of the LDH-pGFP nanohybrid gene delivery vectors. LDH particles are observed to aggregate into complexes when interacting with pGFP. Red box indicated region from which the (c) EDX spectrum was recorded, exhibiting spectrum peaks at 0.5 keV, 1.2 keV, 1.5 keV and 2.0 keV. These peaks are attributed to O, Mg, Al and P respectively.

5.3.3 Mg-Al LDH interaction with single stranded RNA

We hence decided to investigate the interaction of a smaller biomolecule, single stranded RNA (siRNA), with the Mg-Al LDH particles. This is a much smaller therapeutic relative to the pDNA and hence a better likelihood of being intercalated

between the Mg-Al cationic layers. Figure 5.3 illustrates the interaction of siRNA biomolecules with the LDH nanoparticles. The BFTEM image shows large aggregations of the material. This could be due to the interaction of the siRNA with the LDHs themselves. However, due to the nature of hydrotalcite materials, it is more likely that the aggregations are a cause of LDH agglomeration over time. This was often seen even with LDH particle dispersions themselves where large precipitates would form over time. The EDX spectra highlights a peak at 2 keV deriving from the presence of Phosphorous in the samples. Much like the case of the LDH-pDNA, we believe this is due to the interaction of the Phosphorous backbone of the siRNA strands. On the other hand, the existence of significant Cl and K peaks at 2.6 keV and 3.3 keV were not expected during the synthesis of these particles. This artefact peaks could be a cause of the nature of the siRNA sample or saline solutions used in the synthesis and as buffers of the siRNA strands themselves.

Although it was planned to look at the LDH-siRNA behaviours in mesenchymal stem cell environments, the current experiments could not be completed in time before thesis submission deadlines. The prospective experiments will be discussed in subsequent chapters.

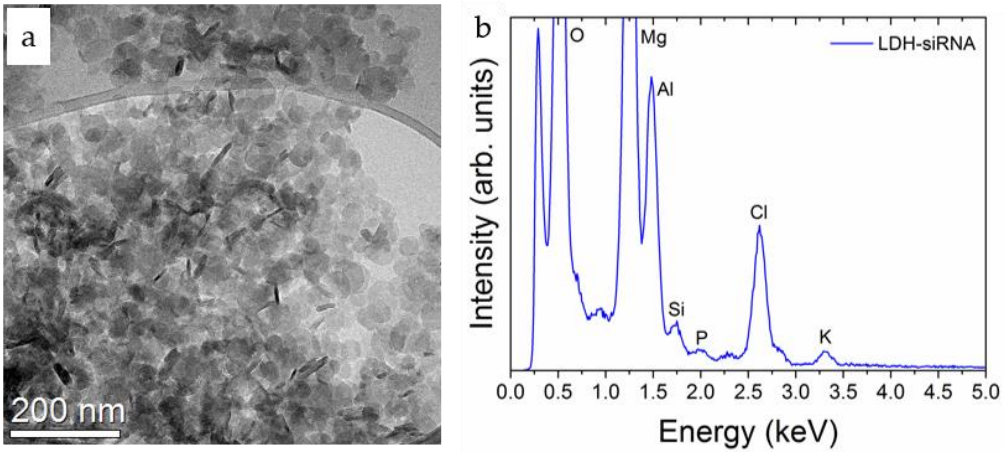

Figure 5.3 LDH interaction with single stranded RNA. (a) BFTEM image of the LDH-siRNA composite. (b) Corresponding EDX spectra of the nanocomposite.

5.4 Mg-Al LDH uptake and intra-cellular behaviour in mesenchymal stem cells

Next we proceeded to study the LDHs inside the MSCs. Figure 5.4 displays (S)TEM images of MSC sections. The ultrastructure of the MSC sections shows that the cell remains intact with various features such as nuclei, vesicles and cell membrane structures of the cells being revealed (yellow arrows in Figure 5.4).

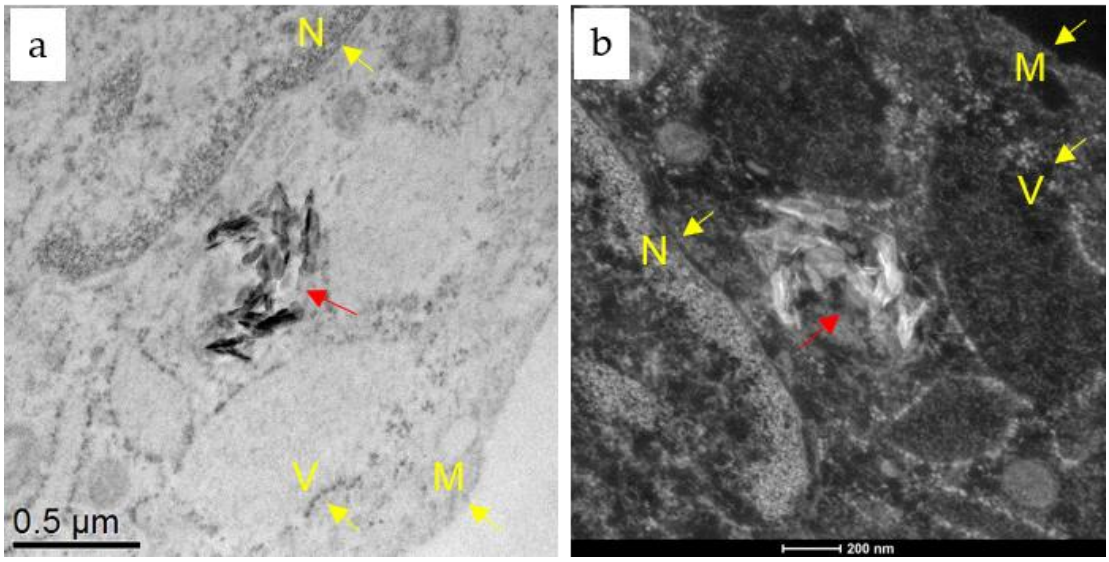

Figure 5.4 Direct observation of the LDH-pGFP aggregated up-taken by MSCs. (a) TEM and (b) scanning TEM images of LDH vectors located in MSCs. Both images recorded from the same sample region. Cellular components such as the nucleus (N), vesicles (V) and membranous structures (M) are indicated by the yellow arrows. LDH-pGFP nanohybrids are indicated by red arrows.

Comparable ultrastructural features via TEM analysis were also reported by Wu *et. al*[54], however the intrinsic properties of the LDH material itself was overlooked in this MSC study (such properties will be discussed later in this section). Similar to our case, the LDH vectors can be located in the cytoplasmic regions of the MSC sections (red arrows in Figure 5.4). Higher magnification images of such regions display how these agglomerates consist of individual nanoplatelets. Moreover, MSC cells appear to uptake aggregates of the LDH delivery vectors rather than individual nanoplatelets.

The hexagonal morphology of the LDH structures was observed, indicating retention of the LDH material structure within the MSCs (Figure 5.4 and Appendix).

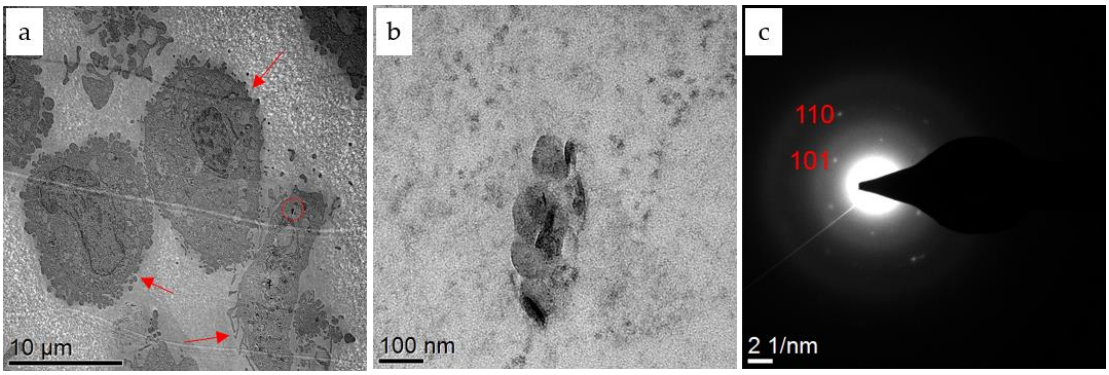

Figure 5.5 Low magnification TEM image of MSC resin section. The ultrastructure of whole cells are observed (indicated by red arrows). (b) Higher magnification image from red circle region displayed in (a), revealing an example of LDH-pGFP uptake by MSCs (red arrow). (c) Recorded SAED pattern from LDH agglomerate in (b). Hexagonal symmetries of the {110} planes of the LDH structure are observed.

Using electron diffraction to study the MSC resin sections permitted the analysis of the crystallographic features from intracellular components of the cells. SAED patterns were recorded from the LDH agglomerates within the cell. The existence of the {100} and {110} crystallographic planes is viewed in the SAED patterns (Figure 5.5 (c)). This confirms a periodicity of lattice planes within the LDH layers. Moreover, it is noteworthy that these structures remain present after interaction with pGFP and exposure to MSCs. This suggests that the synthesized hydrotalcite materials are capable of withstanding the harsh cellular cytoplasmic environments even after 72 hours of exposure to the cells. The fact that the LDHs retain their structural integrity inside of the MSCs is a further indication of their suitability to act as a gene delivery vector where longer lifetimes of vectors are required[64]. This is an important result in relation to numerous aspects of efficient drug delivery such as cellular toxicity, cellular proliferation and drug delivery vector optimization.

The intracellular accumulation of nanoparticles in cells can have a profound effect on cell physiological behaviours. This has been previously seen in the literature. For example, aggregations of silica nanoparticles over extended time periods have caused lysosomal dysfunction and impairment, which could affect basic cell functions.[65] Also, gold nanoparticle accumulations within the cell has induced inhibition of uptake

mechanisms, even ceasing further uptake.[66] Similarly, gold nanoparticle aggregate uptake can slow down excretion rates and cause cytotoxic effects in the epithelial cells. These intracellular accumulations can also affect the adhesion, migration and division of cells.[67] More closely related to our experiments, LDH accumulations from intravenous injections have been seen to cause immediate death in previous in vivo experimentation.[68] From this, we suggest that this observation of LDHs in the MSCs should not be overlooked, especially when the biosafety and human body applications are being evaluated.

5.4.1 Microanalysis of Mg-Al LDHs in MSCs

Next, we analysed the materials integrity and composition via STEM-EDS which provides a reliable chemical characterization technique. Figure 5.6 shows STEM-EDX of LDH agglomerates within the MSCs. The signals of Mg, Al and O are found to occur in coherent fashion across the analysed region (Figure 5.6 (d)).

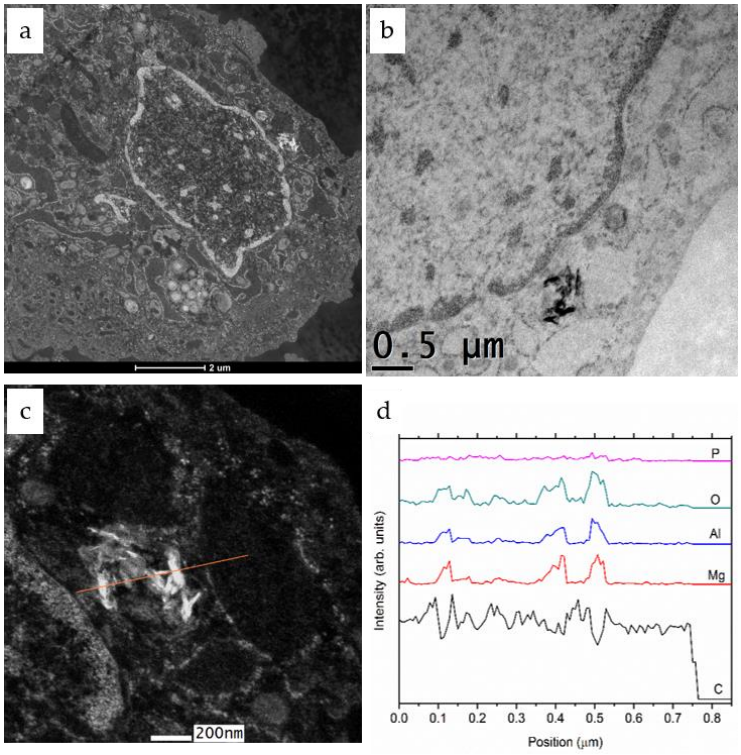

Figure 5.6 EDX analysis of LDH delivery vectors in MSCs. (a) STEM and (b) TEM images of LDHs internalized into MSC cells. (c) STEM-EDX line scans of suspected nanoparticle region (d) EDX spectra acquired from line scans, highlighting coexistence of Mg, Al and O of the LDH structure.

The parallel existence of these elements is attributed to the LDH materials, suggesting that they have preserved their structure as opposed to a random distribution of the LDH elemental components throughout the cellular regions as a result of their breakdown. An EDX line scan was favoured over a EDX map acquisition due to the damage the electron beam can cause to the sample. The damage caused by heating of the sample through prolonged exposure to the electron beam can cause uneven shrinkage of the cell sections and damage of the resin. It can also introduce a drift and lead to a total destruction of the section (such as the drilling of holes).[69] Hence, a line scan collection was chosen over a full STEM-EDX map to extract as many EDX counts as possible whilst limiting beam-sample interaction and minimising potential beam induced damage.

Our SAED and STEM-EDX findings also elucidate the possible delivery mechanisms involved in the LDH nanoplatelets to the stem cells. The reciprocal lattice symmetries exhibited in the SAED patterns (Figure 5.5 (c)) compare well to those recorded from the pristine LDH material (Figure 5.1 (b)). This establishes that the crystalline in-planar structures of the LDH-pGFP vectors are retained in the MSC environments. This perhaps suggests that a reverse anion exchange procedure of delivery is possible, as opposed to breakdown and atomic dissolution release mechanisms of the LDH structures. Furthermore, it is speculated that enzymatic degradation may have affected the surfaced adhered pGFP instead of the LDH materials themselves, as evidenced by the relatively low Phosphorous signals from the STEM-EDS data. Alternatively, given that the pGFP is adhered to the LDH nanoplatelet surfaces, it is also possible that the biomolecule is subject to enzymatic degradation before the LDH carriers, leaving the particle structure in-tact.

5.5 Mg-Al LDH as a deliver agent to A549 cancer cell lines

5.5.1 Mg-Al LDH synthesized in endotoxin free water

The previous section established how Mg-Al LDHs interact with therapeutics such as pDNA and siRNA. This was followed by a thorough study of how these composite materials interact with MSC cells and moreover how the Mg-Al LDHs themselves behave in these environments. Whilst retaining the study of the LDHs from this angle, we chose to investigate how the Mg-Al LDH properties behave in other types of cell lines with various intended usages. This next section probes the properties of the Mg-Al nanomaterials as they are exposed to A549 lung cancer cell lines, utilising the same high-end EM techniques as discussed above.

As before, there was a necessity to effectively characterise the LDHs before they were applied to the A549 cells. It was a concern for LDH nanomaterials in relation to cancer cell line exposures that the synthesized LDHs were free from any source of infection or unwanted contamination that would affect the cell behaviours. Hence, the Mg-Al LDH material was synthesized using the above procedures however this time in contrast, endotoxin free water was used. Figure 5.7 shows a TEM image with corresponding SAED pattern of the LDHs prior to exposures with the A549 cancer cell lines. The SAED pattern highlighted a polycrystalline nature with reciprocal lattice distances from the radii evaluated as 9.59 nm^{-1} and 13.4 nm^{-1}. EELS was also used to characterize the composition of the material, whilst providing spectral signatures which could be compared in future experiments. Figure 5.8 shows the Mg and Al $L_{2,3}$ edge at 58eV and 76 eV respectively, as well as the O K edge at approximately 540 eV. These peaks as well as their spectral features also compare well with other Mg-Al LDH materials, indicating that synthesizing the materials in the endotoxin free water and at smaller dimensions does not change the LDH properties.

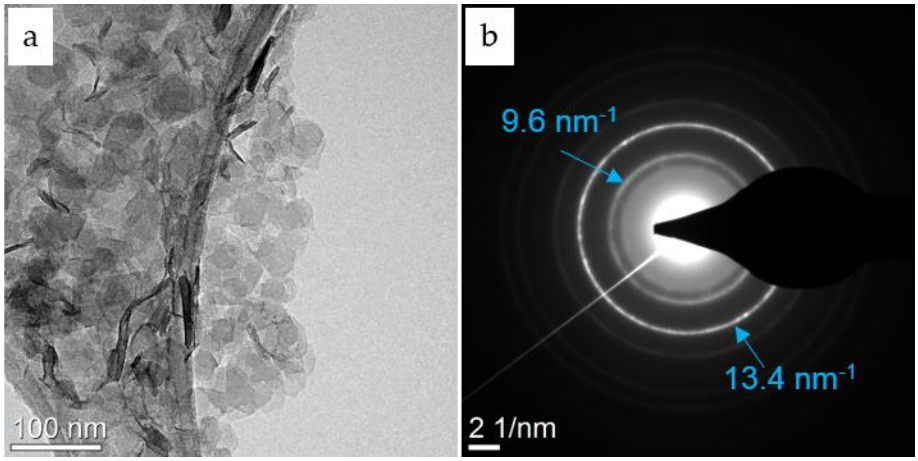

Figure 5.7 (a) BFTEM and (b) SAED pattern of Mg-Al LDHs synthesized in endotoxin free water.

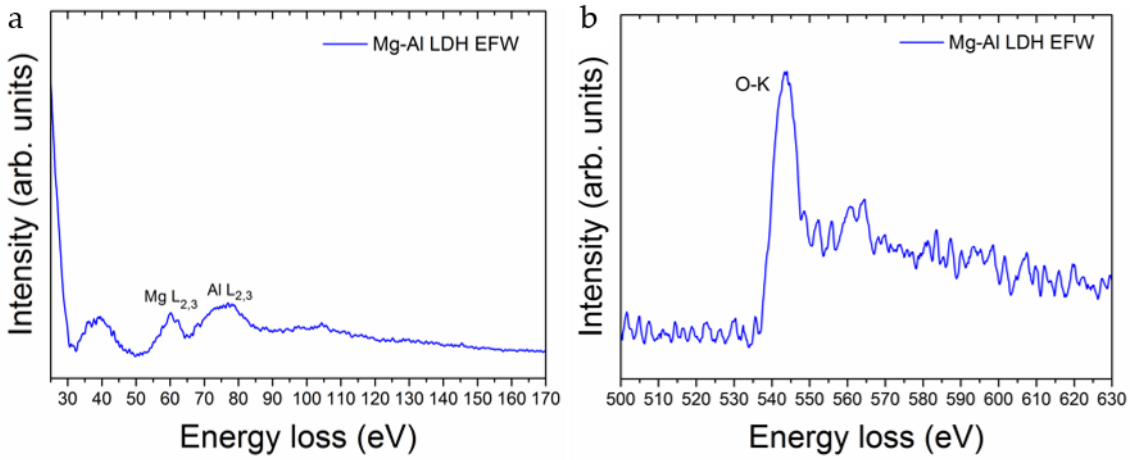

Figure 5.8 Core loss EELS spectra of the (a) Mg and Al $L_{2,3}$ edges and the (b) O K edge of Mg-Al LDHs synthesized in endotoxin free water.

5.5.2 Mg-Al LDH interaction with A549 lung cancer cell lines.

Previous research has established how LDH nanoparticles can be used as drug delivery vectors in the treatment of cancer cells. The application of LDH nanomaterials to transport chemotherapy drugs such as methotrexate to various cancer cell lines has led to the enhanced delivery of these therapeutic drugs.[22,34,70] We decided to further the scope of this field by investigating the interaction of Mg-Al LDHs with the A549 lung cancer cell line. The nanoscale behaviours of these LDH materials in cellular

environments will provide important information into their interaction with cell membranes as well as the intracellular fate of the LDH material. Moreover, the behaviours of these materials may also impact their future performance as a drug delivery mechanism in these types of cell lines. We employed TEM methods to investigate how the features of the LDHs are affected in the A549 cells, as well as how their physical properties progress over time in these biological environments.

Initially, we chose to expose the Mg-Al LDH nanomaterials to the A549 cell line at 50 μg μl^{-1} and were subsequently fixed after 14 hours. This was carried out to verify the cytotoxic effect of the Mg-Al LDHs on the A549 cells. Firstly, Figure 5.9 displays STEM images of untreated A549 lung cancer cells in epoxy resin sections on lacey carbon TEM grids. Although the visualisation of the ultrastructural details are somewhat hindered due to the type of TEM grid, features such as the cellular membranes (yellow arrows) and intracellular components can be resolved. Furthermore, an absence of LDH nanoparticles around the cell membranes and within the intracellular regions is also observed.

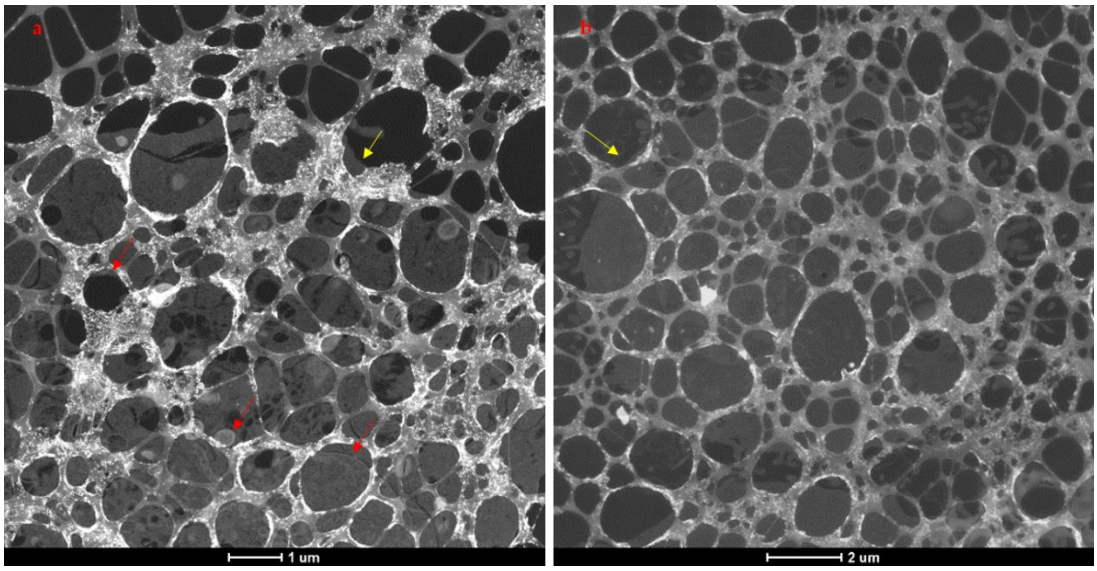

Figure 5.9 STEM imaging at low magnification of untreated A549 cells. Untreated cells were embedded into resin and ultramicrotomed sections were placed onto lacey carbon TEM grids.

Following on from this control experiment, Figure 5.10 shows STEM images of resin sections in which Mg-Al LDH nanoparticles were exposed to A549 lung cancer cells. In

contrast to the unexposed specimens, the presence of LDHs can be seen at the cellular membranes and in intracellular vesicles within the cell regions (red arrows). A significant interaction of LDH platelets with the cell membranes is possibly due to electrostatic interactions of the positively charged LDHs with the negative charges of the membranes.

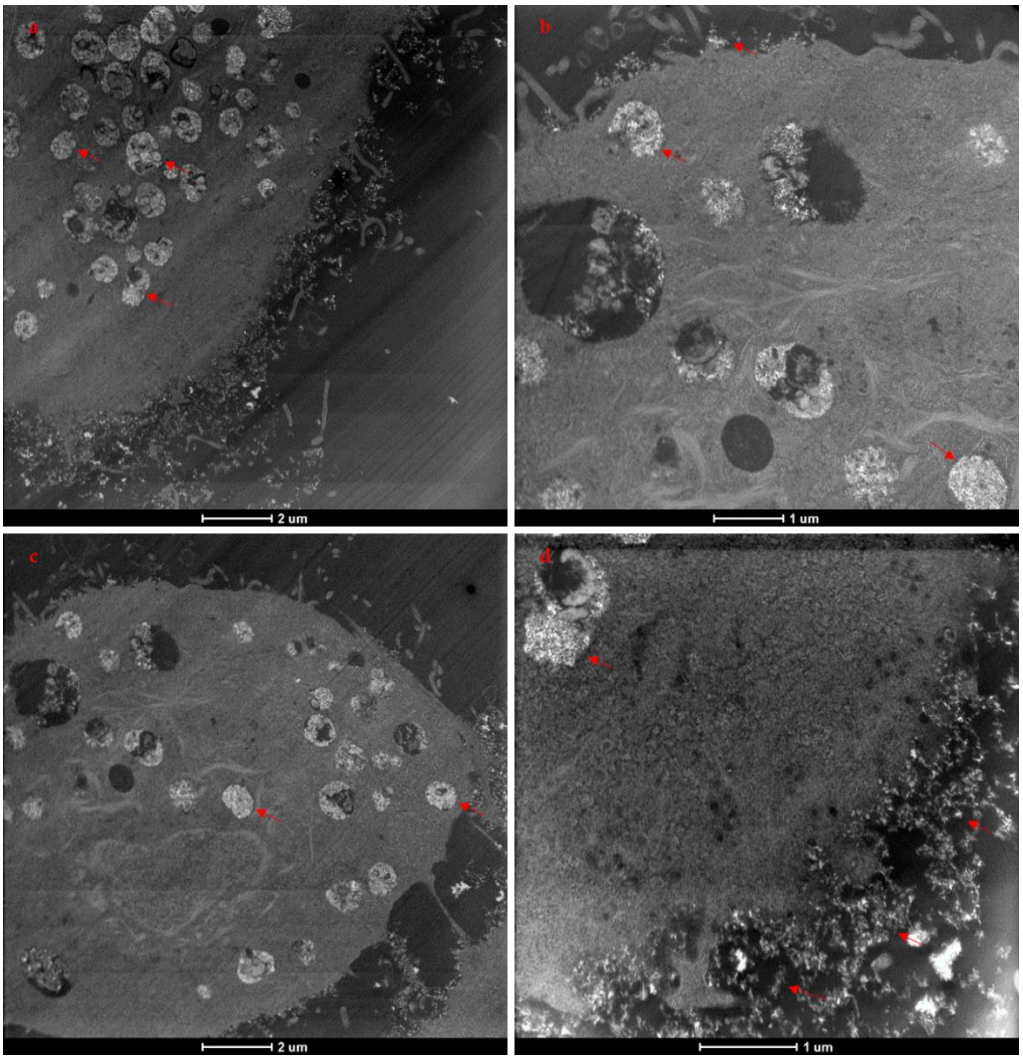

Figure 5.10 STEM imaging of resin sections of A549 cells exposed to Mg-Al LDHs at 50 µg µl^{-1}. (a) and (c) represent lower magnification images, with (b) and (d) presenting higher magnifications of (a) and (b) respectively. Regions of greater intensity are the interacting and up-taken LDH nanomaterials.

With the identification of the LDH nanoparticle transfection, further study into the intrinsic LDH properties was undertaken using EM methodologies. Figure 5.11 presents dark field TEM and electron diffraction studies of similar cells exposed to the

LDH nanoparticles at the same time point of fixation (14 hours). Dark field images were formed by placing the objective aperture in regions away from the zero order spot and onto other diffracted spot regions in the diffraction pattern. Figure 5.11 (b) shows bright intensities where the LDH nanoparticles occur. This contrast originates from the crystalline nature of the LDHs, indicating that there is some retention of crystallographic features of the LDHs in the cellular vesicles.

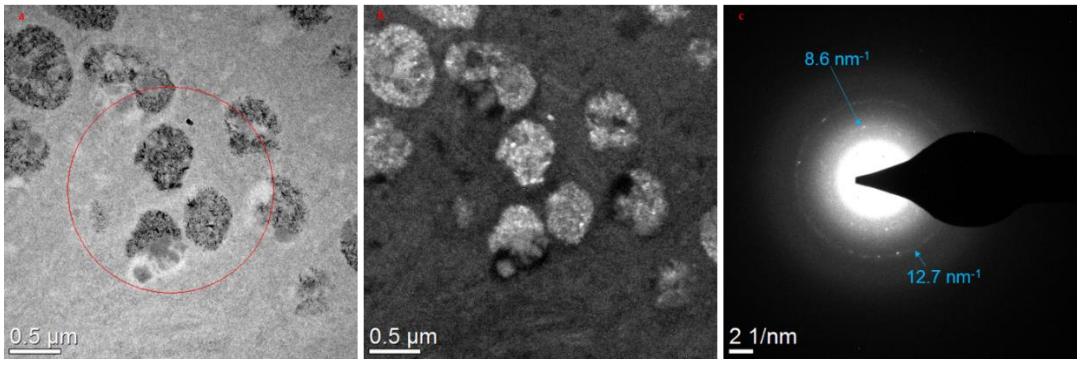

Figure 5.11 (a) BFTEM, (b) DFTEM and (c) SAED pattern of the Mg-Al LDHs in the cellular environments. Red circle in (a) denotes the region from which the diffraction pattern was recorded.

Electron diffraction patterns themselves were also recorded from the same cellular regions. Figure 5.11 (c) exhibits polycrystalline features owing to the random orientation of the platelets in the vesicles in the cell and also hence confirms a retention of LDH structure. The lattice vectors occurred at 8.56 nm^{-1} and 12.71 nm^{-1}, which compare well to the case of the LDH material before it was exposed to the cells (Figure 5.7) and XRD standards. The slight discrepancy in the measured distances suggest a potential alteration to the lattice structure perhaps induced by the acidic nature of the cytosol endosomes. Nevertheless, the stark existence of these polycrystalline rings indicates the LDHs retain some regular structure, and do not undergo complete dissolution within the A549 cells.

5.5.3 Time study of LDHs in A549 lung cancer cells

To study the uptake behaviours of LDHs in A549 cells with respect to time, we performed TEM characterization experiments on samples that were fixated after certain time points after initial exposures. This sample set provided a way to further understand how the material properties would be affected due to their exposure to the

cellular environments. In particular, an assessment of the material properties over these time points would give a better extent of the capability of these Mg-Al LDHs to perform as delivery vectors in these A549 cells. Moreover, the TEM data from these studies also yield information on the potential delivery mechanisms of drugs or genes by these types of layered nanomaterials.

In this study, samples were fixed after 1 hour, 3 hours, 24 hours and 72 hours. Each sample was subjected to our standard TEM preparation protocol described in the Experimental Methods section 5.2. Figure 5.12 displays BFTEM findings at each time point. It is noted that there were limited amounts of cells in the resin sections of these samples and as such few cells could be analysed. As well as this, there were also experimental drawbacks during imaging whereby the sections would immediately destroy under the electron beam resulting in a lack of sample to be potentially analysed. This was deemed to be due to poor resin sections cut with the ultramicrotome. This sample preparation method often caused the sections to have holes or tears in the plastic sections due to sub-standard ultramicrotome knife conditions and knife marks or poorly polymerised resin blocks themselves. The existence of knife marks and ultramicrotome artefacts were regularly seen throughout all samples from this experiment set (see Appendix), resulting in low number of quality areas that could be analysed. Nevertheless we proceeded to image as many regions as possible to attain a clear picture of the on-goings in the systems involving LDH nanoparticles and A549 cancer cells.

Even after short time scales of 1 hour of exposure, the LDH particles were observed to be transfected across the cell membranes, located in the cell cytoplasm (Figure 5.12 (a)). This was similarly observed after 3 hours. The LDH particles are seen to interact with the cell membranes in this case. In fact, the uptake mechanism process could also be directly observed in this case. This is believed to be an endocytic pathway of the LDH particles.[71] In addition, we see that the LDHs are localised in cellular vesicles, probably endosomes formed as a result of the uptake processes. The identification of endosomes involving similar uptake mechanisms of silver nanoparticles has been previously shown by Uygur et. al.[72]

These findings of the LDHs in the cytosol are also consistent with previous research.[38] There were indeed numerous cases of this endosomal formation as the LDHs were exposed to the cells for 24 hours and 72 hours (Figure 5.12 (c) and (d) respectively).These vesicles were found to contain large aggregations of the LDH particles. They appear to remain in the cytoplasm regions even after 72 hours of continuous exposure. Similar time scales of LDH survival are also viewed in past research where LDH could be used to increase the efficiency of A549 tumour cell suppression using methotrexate-LDH compsosites.[34] The findings of this experiment are also mirrored in previous observations of the LDH exposures to the A549 cells, where they were fixed after the shorter time period of 14 hours (Figure 5.10). Moreover, the acidic pH environments of the cell did not appear to cause a significant breakdown of the LDH structures, with the platelet aggregations still observed after 72 hours (Figure 5.12 (d)). This bodes well for the concepts where the LDHs 'protect' their intercalated biomolecule cargos in relation to delivery mechanisms. It can be proposed from these results that the delivery of associated genes or drugs occurs via a reverse anion exchange as opposed to releases by layer disassociation by acidic environments.

These results give an indication of the life time and survival of the LDHs in the A549 cytosols, yielding important information from a biological perspective such as timescales of delivery, applicability of controlled release mechanism and cytotoxicity implications.

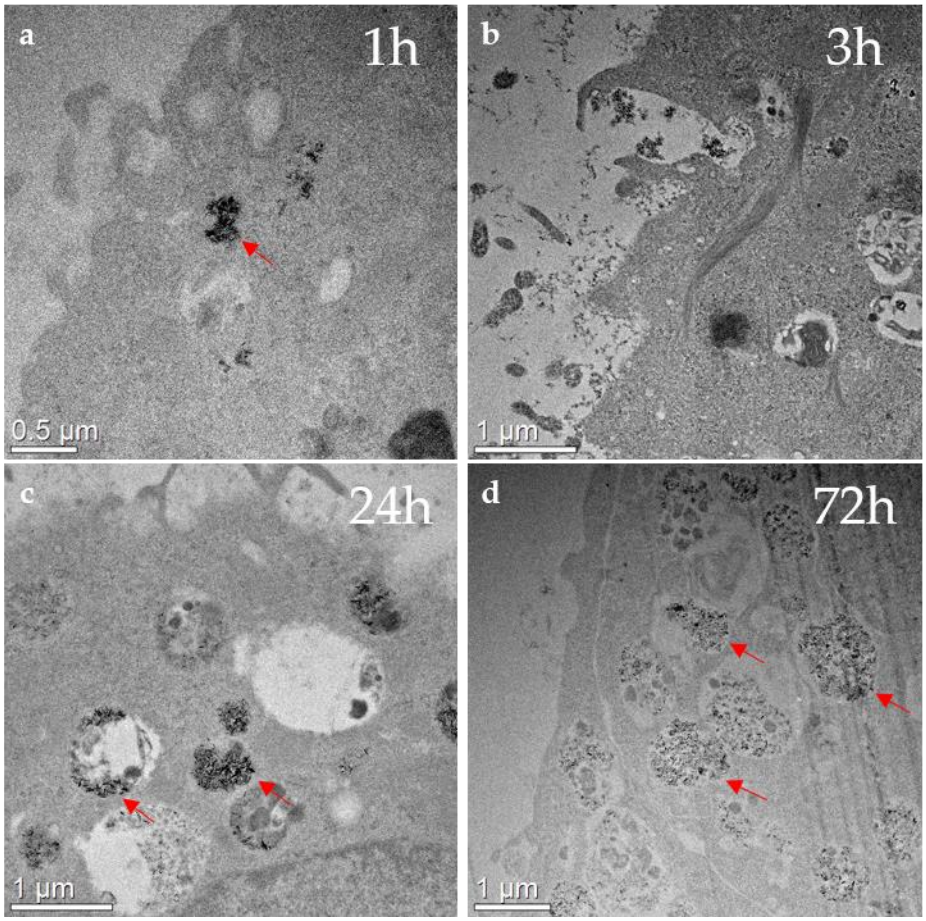

Figure 5.12 TEM images of Mg-Al LDHs exposed to A549 cells fixated after (a) 1 hour, (b) 3 hours, (c) 24 hours and (d) 72 hours post-exposure of the nanomaterials to the cells. LDH uptake is indicated by the red arrows.

5.5.4 Microanalysis of LDH properties in A549 cells using EFTEM and STEM-EELS techniques

LDH materials appeared to be transfected as well as structurally stable in the cell cytosol regions even after 72 hours. Analogous to the case of the LDHs exposed to MSCs in section 5.4.1, we elected to apply the high-end EM techniques of EFTEM and EELS to further the understanding of the intracellular properties of these LDHs when they have been transfected into the A549 cells.

The selection of microanalytical technique in samples of this nature can be absolutely crucial in the experiment. As we have previously seen, the radiation damage of the electron beam is very much so a limiting factor in the EM characterizations of the resin embedded samples (see Appendix). As well as that, the techniques of EFTEM and EELS often require prolonged exposures of the electron beam to achieve sufficient

levels of interpretable scientific data. In particular, the core loss spectrum at higher energy ranges require sufficient signals for the K edge peaks to be identified above background, an undesirable necessity that does not bode well for samples which are prone to beam alterations and damages. In addition, when imaging with the energy filter, multiple exposures are often necessary to conduct effective elemental map distributions for multiple elements in the EELS spectrum. On the other hand, STEM-EELS is favourable as large energy ranges of the EELS spectrum may be recorded with just one exposure. It must be said however, that this technique indeed has its inherent drawbacks, as the timescale for similar area map acquisitions can be much longer relative to EFTEM. Notwithstanding, the issues of sample drift and stability also come into play during STEM-EELS map collections, which unfortunately can result in specimen destruction. Further information on this topic has been discussed in detail by Leapman and Andrews.[53] This section thus, in parallel with the acquired physical information related to the LDHs behaviours, can also assess the application of the associated microanalytical techniques to samples of this kind.

It is clear that there are many substantial factors that determine the experimental approaches related to the resin embedded A549 cell samples. None more so than the suitability of the EELS edges that are to be studied. In the case of the Mg-Al samples, these metallic K edges occur at 1305 eV and 1560 eV for Mg and Al respectively. These were neglected as potential edges to be analysed due to unsuitable. Also, they reside at high energies in the core loss spectra which would require large exposure times to achieve significant signal to noise ratios, not ideal for our electron beam sensitive sections. Upon further inspection of potential EELS studies, there also exists Mg and Al $L_{2,3}$ edges at 51 eV and 73 eV.[73]

We chose to use the initial exposures of LDHs to the A549 cells as a primary study using EELS based characterizations (Figure 5.10).

Figure 5.13 presents Mg and Al $L_{2,3}$ edge STEM-EELS spectra of different cellular regions containing the LDH particles, from the initial exposures of LDH to the A549 cells, as previously shown in Figure 5.10.

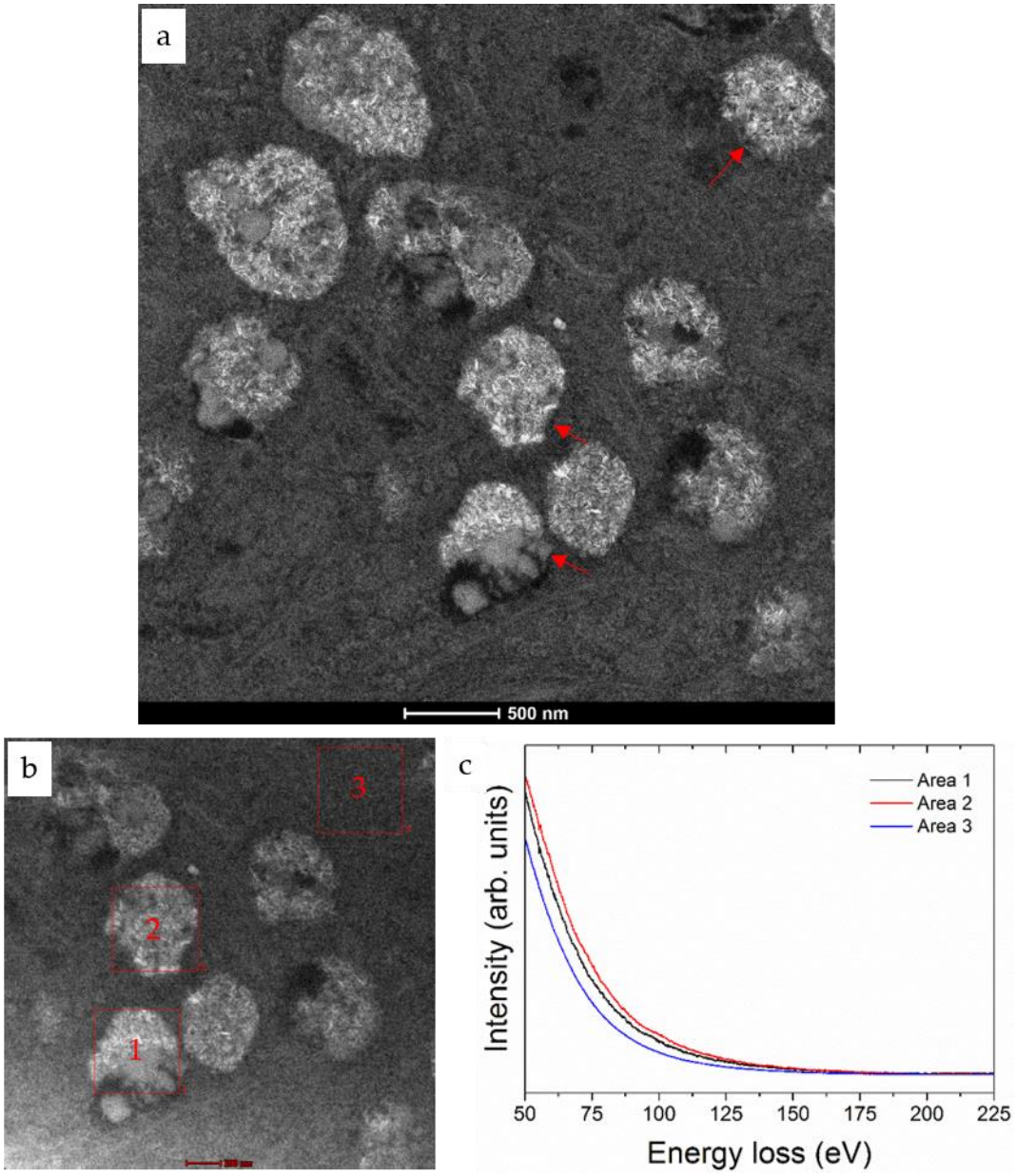

Figure 5.13 STEM-EELS area scans from various cellular regions involved in the Mg-Al LDH interaction during the Mg-Al LDH exposures, fixated after 14 hours. (a) STEM image of region before EELS acquisitions. Red arrows indicate areas of Mg-Al LDH nanoparticles. (b) STEM image incorporating regions of EELS scans. (c) Mg and Al $L_{2,3}$ edge region EELS spectra from Area 1 – Area 3 in (b).

Even though these Mg and Al $L_{2,3}$ edges could be identified in the case of the pristine material, as seen in Chapter 3, the same signatures could not be resolved from the LDHs embedded in the cell environments and resin section. This can be explained by the nature of interaction with these resin embedded samples, and perhaps highlights one of the drawbacks of the EELS technique. The LDH particles in these resin sections

lie in the epoxy based sections that are approximately 80nm in thickness. This results in a large number events of plural scattering of the electrons as they transmit through the sample. This appears in the EELS spectra as a significant fall off from the zero loss in the plasmonic regions up to about 100 eV. This unfortunately encapsulates the Mg and Al $L_{2,3}$ edges and whilst they may occur, they cannot be distinguished above this background.

In light of these limitations, alternative elemental EELS edges were considered and assessed as a way to characterize the LDH behaviours. There is an abundance of oxygen in the LDH materials, which is a suitable element to study using EELS approaches. Moreover, the oxygen K-edge occurs at an experimentally reasonable energy at 532 eV. This is an ideal edge to study with our spectrometer as it occurs high enough in the core loss spectrum to be resolved above plural scattering from the resin sections as well as being located at appropriate energies for drift tube settings on our EELS spectrometer. Core loss EELS spectra were recorded from 3 separate intracellular regions to identify and compare the elements present in various areas of LDH treated A549 cells. The nitrogen and oxygen edges were elected to be recorded as both are intrinsic to the LDH structure. Moreover, the closeness of the K edges (nitrogen is at 401 eV and oxygen is at 532 eV) allowed for their simultaneous acquisition using a suitable energy resolution and spectrometer channel dispersion. Figure 5.14 portrays STEM-EELS studies of the nitrogen and oxygen K edges from various cellular regions from the previous cell region used to study the Mg and Al $L_{2,3}$ edges, as shown in the related STEM image.

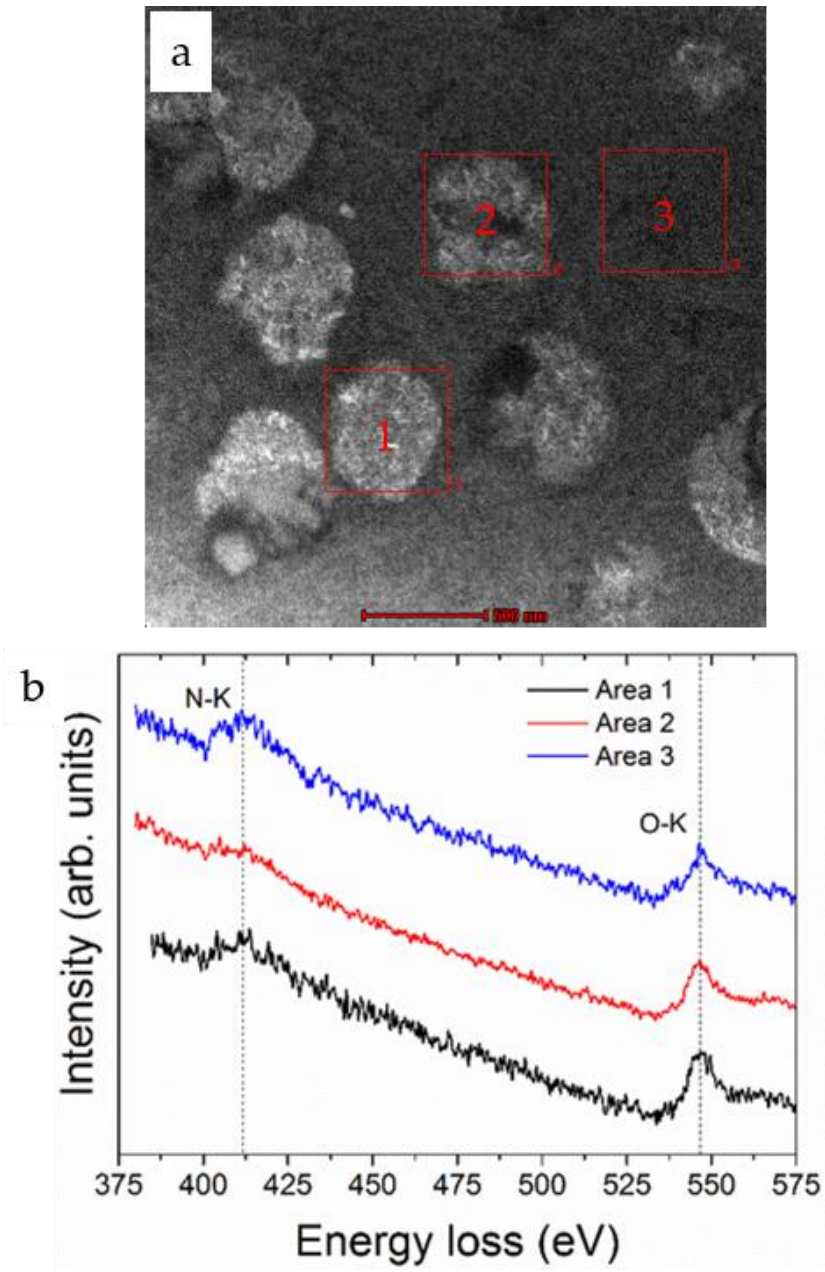

Figure 5.14 STEM-EELS area acquisitions of the nitrogen and oxygen K-edges in the LDH-exposed A549 cells. (a) STEM image representing area acquisition regions. (b) Core loss EELS spectra acquired from various areas. Each core loss spectra is acquired using STEM methods from indicated square regions in (a).

The existence of the nitrogen signals (the delayed edge at approximately 410 eV) derive from the cellular component compositions. The same can also be said in the case of oxygen. There does however appear to be a more prominent oxygen signal in regions containing the transfected nanoparticles, believed to originate from the oxygen sites in the layered structures (Figure 5.14 (b) Area 2 and Area 3).

Table 5.1 shows the integrated peak intensity ratios of the nitrogen and oxygen signals from the three regions of spectral acquisitions in Figure 5.14. This was evaluated from the standard EELS quantification in DigitalMicrograph (Gatan, USA). We observe that the particles have a significant greater oxygen: nitrogen ratios. This may indicate the existence of the oxygen sites in the LDH structures, corroborating the crystallographic data of similar regions. However, these quantification studies are only intended for relative comparisons. The absolute quantification from EELS quantification methods require more detailed attention and is beyond the scope of our study.

	Nitrogen (%)	Oxygen (%)
Area 1	10.6	89.4
Area 2	21.8	78.2
Area 3	37.5	62.5

Table 5.1 EELS relative quantifications of the nitrogen and oxygen core loss signals in the studied regions of the A549 cells.

We next chose to investigate the nature of the carbon K-edge of the LDHs in these A549 cells. Figure 5.15 shows the STEM-EELS area scans of the from similar regions. Firstly, the C K edge is evidently seen in all four EELS acquisitions. This is mainly due to the carbon based materials not only of the cell itself but also the epoxy resins in which the cells were embedded. More interestingly, EELS spectra from the regions containing the particles show a peak at 540 eV, indicating the presence an O K edge. These signals are believed to derive from the up-taken LDH sites interacting with the A549 cell and also compliments our previous EFTEM data (Figure 5.15 (b)).

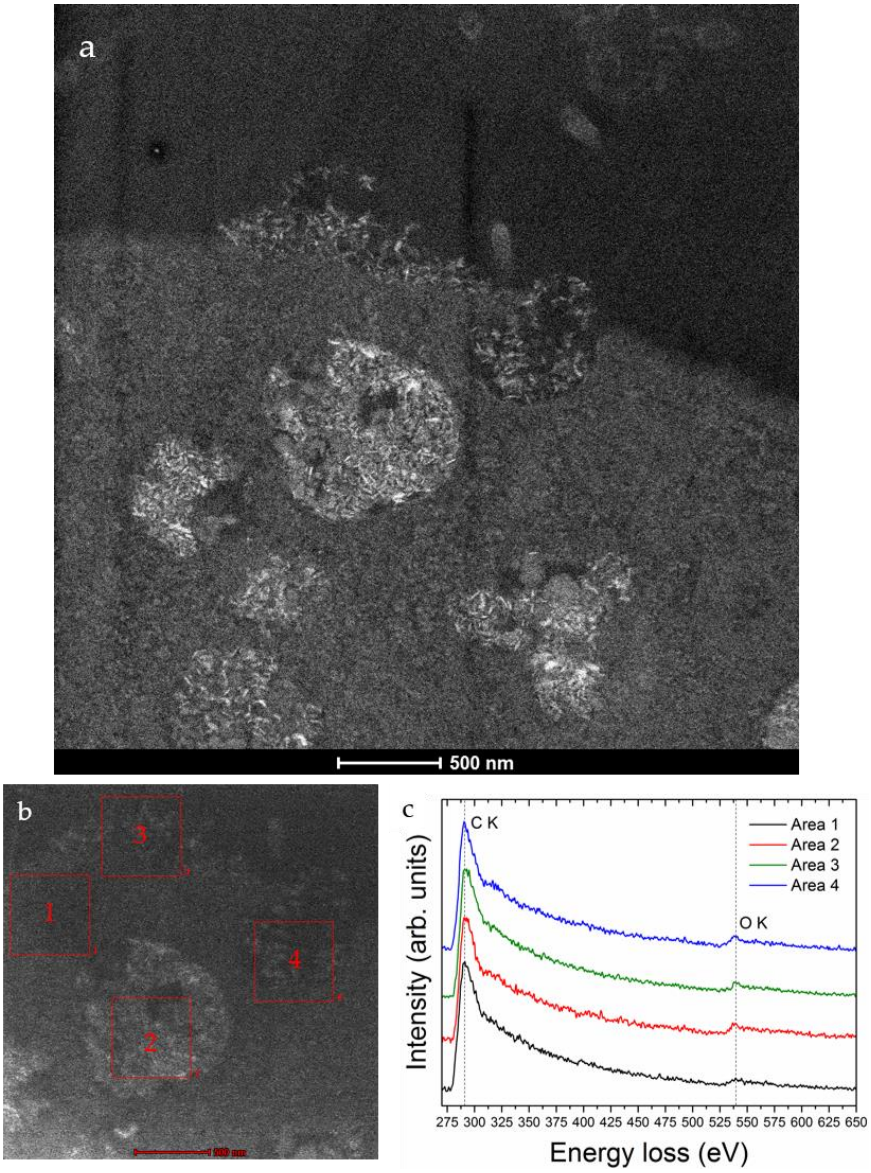

Figure 5.15 STEM-EELS area scans from various cellular regions involved in the Mg-Al LDH interaction. (a) STEM image of region before EELS acquisitions. Faster dwell times used during STEM EELS analysis to avoid resin section alteration and damage. (b) STEM image incorporating regions of EELS scans. (c) C K edge and O K edge EELS spectra from Area 1 – Area 4 in (b).

Similar to the case of the 14-hour fixed samples, we performed peak intensity ratio analysis of the associated carbon and oxygen signals. This was also carried out using standard relative EELS quantifications in DigitalMicrograph.

	Carbon (% content)	Oxygen (% content)
Area 1	85.1	14.9
Area 2	75.7	24.3
Area 3	81.6	18.4
Area 4	77.6	22.4

Table 5.2 EELS relative quantifications of the carbon and oxygen core loss signals in the studied regions of the A549 cells in Figure 5.15.

Again, we see a slightly greater oxygen content in regions of suspected Mg-Al LDH uptake (Areas 1-3 in Figure 5.15). Moreover, we compare oxygen contents between particles on the cell regions before and after internalizations. There is a similar peak intensity ratio, suggesting that the LDH structure has not been affected by the uptake processes of the cell.

5.5.5 EFTEM analysis of LDHs in A549 cell environments

Figure 5.16 (a) presents BFTEM image of the Mg-Al LDHs exposed to the A549 cells after 72 hours, with a corresponding oxygen K-edge EFTEM map. The BFTEM shows what looks like the LDH nanoparticles interacting with the cell membrane as well as aggregations transfected across the cell membrane. Correspondingly, Figure 5.16 (b) depicts an oxygen K edge EFTEM map of the same region. A temporal intensity histogram is used to highlight the presence of the O K edge signal in the mapped region. As speculated, the regions of higher intensity indicate a presence of greater oxygen K edge signals. This indicates that the particles involved in the interaction are of greater oxygen content relative to the cell itself, more than likely due to the inherent oxygen sites of the LDH lamellar structures.

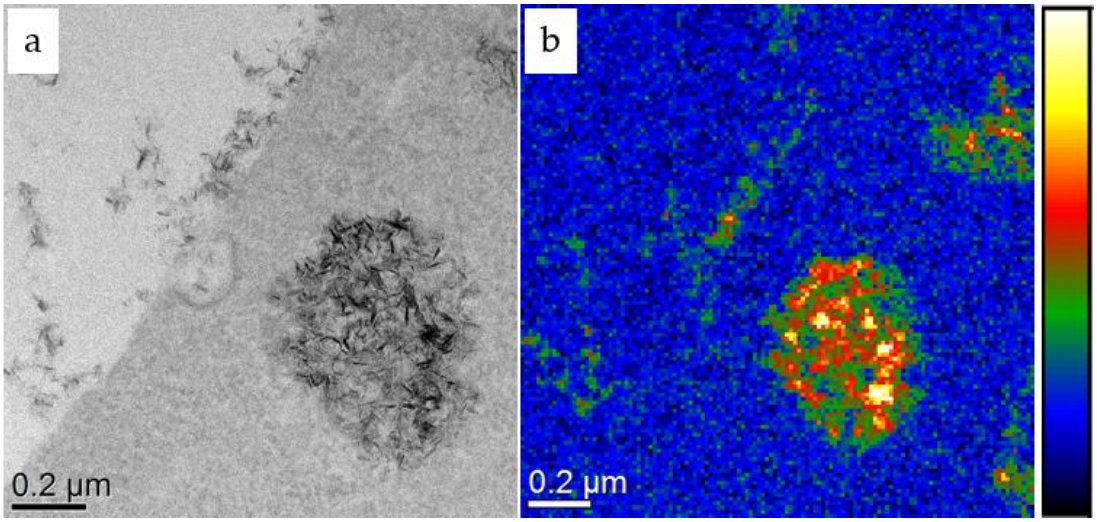

Figure 5.16 EFTEM analysis of A549 cells with 50 µg µl^{-1} LDH exposure. (a) BFTEM image of cell membrane showing cell interaction and uptake of LDH nanoplatelets. (b) Oxygen EFTEM map of the same region. Regions of bright intensity representative of greater Oxygen content.

These findings were also mirrored in STEM-EELS analysis. Figure 5.15 shows a representative STEM image of the interaction, uptake and cytosol distribution of the LDH nanoparticles with the A549 cell after 72 hours. The beam damage cause by the rastering probe during imaging is evident in the section by the dark streaks in the STEM image. Nevertheless, we opted to record core loss EELS spectra of the C K edge and O K edge from various regions of the cell at hand (Figure 5.15 (b)). The areas 1 – 4 denoted by the red square regions correspond to the EELS spectra 1 – 4 in Figure 5.15 (c). This analysis also corroborates the EFTEM maps previously seen in our previous STEM-EELS area scans Figure 5.14.

The presence of oxygen in our EFTEM and EELS studies may also derive from sample preparation artefacts such as osmium tetroxide fixation, alcohol dehydration and epoxy embedding. It would be of interest to compare TEM sample preparations in similar cases but removing OsO4 fixation steps to eliminate potential ambiguities in data interpretation. Although in doing so, (S)TEM contrast in the sections may be hindered as a result. In this case, it may be possible that Mg-Al LDHs themselves could provide significant Z-contrast (scaling with Z^2) relative to the carbonaceous backgrounds of the cell. However, such samples were not prepared by these methods and were not studied in the context of this thesis work.

A natural follow up experiment to this study was to investigate if the oxygen EELS signatures of the Mg-Al LDHs remained constant after longer times spent in the cell environments. Hence, we chose to utilise the studies of STEM-EELS of the 72 hour resin-embedded sample. Figure 5.17 displays STEM-EELS maps of the O K edge from LDHs exposed to A549 cells after 72 hours.

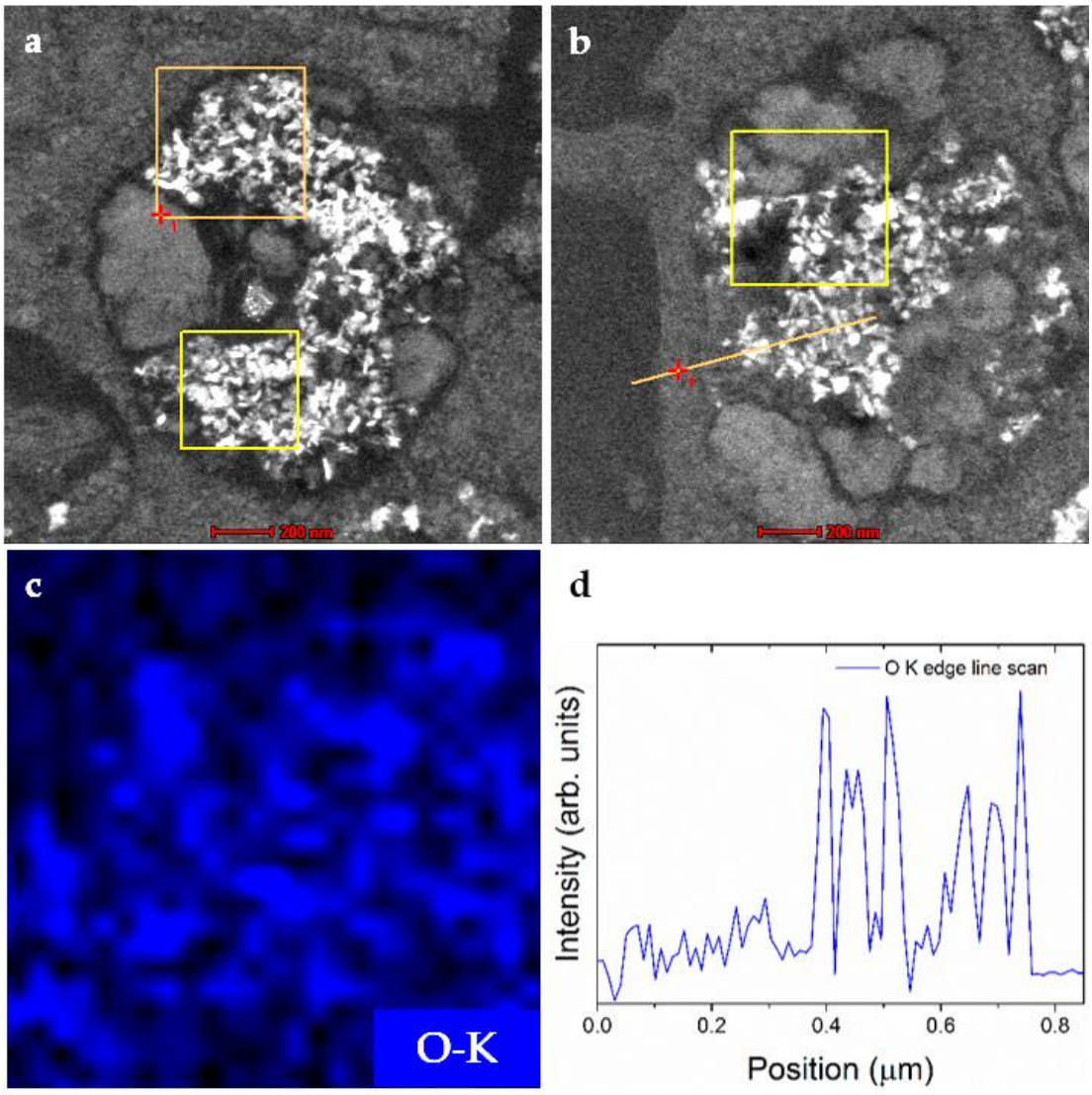

Figure 5.17 STEM-EELS area scans and line scans of LDH in A549 cell environments. Panel (c) depicts O K edge map of orange square region in (a). Correspondingly, panel (d) shows O K edge line scan taken from orange line in (b) with position from left to right in the STEM image.

This can also be observed using STEM-EELS methods, where the acquired EELS spectra in the regions of speculated LDH nanoparticles shows an oxygen peak at approximately 540 eV, representing the delayed oxygen K-edge. These EFTEM and EELS findings further suggest that the LDH materials retain their oxygen content when transfected into the cells at this time point. It can be deduced from this that the LDH structures remain intact after their time spent in the cytosol of the A549 cells.

It was often the case that sample resin sections were susceptible to electron beam damage due to the instantaneous doses in the electron STEM probe (see Appendix). This often leaded to contamination build up and eventual destruction when there is a requisite of longer dwell times to achieve sufficient EDX x-ray counts and well as electron loss events for core loss EELS analysis. However, if the resin section was resilient to the incident electron dose, and significant signal to noise ratios were achievable. It was then possible to conduct EDX and EELS maps in certain samples. Figure 5.17 (a) and (c) present a STEM-EELS map and line scans of the oxygen K-edge in various cellular vesicles. In comparison to the EFTEM mapping, the greater map intensities and hence the greater oxygen K-edge signals appear to correlate with the locations of the up-taken LDH nanomaterials in the cytosol of the cell.

Our findings somewhat present controversial findings with the literature. Previous studies share the opinion that the LDH particles are broken down in the endosomal pathways due to the acidic pH environments of these vesicles (4.5 to 6.5) however, little structural proof exists in this case. Moreover, this also conflicts our own findings where the particles morphological and spectroscopic signatures appear to be retained (Figure 5.10 and Figure 5.17). It could be perhaps that this degradation, believed to be due to the protonation of the nanomaterials may occur over longer timescales. This may also be considered promising from a delivery perspective as certain NSAIDs or genes which may require such life times in the cells.[74]

One of the unfortunate limitations of acquiring analytical data using EFTEM or STEM-EELS methodologies for the resin embedded samples is that in order to achieve a sufficient number of counts for the EDX and EELS spectrometers, a prolonged dwell

time or increased beam intensity is required. For many of the prepared resin sections containing the biological cells, this required dosage would often lead to destruction of the sample and resin as a whole. In addition, there were many samples that had tears and knife marks through the sections which was caused by ultramicrotome sample preparation. This also contributed to the decreased stability of the resin sections under the electron beam, making the task of acquiring microanalytical data all the more challenging.

5.6 Conclusions

The goal of this chapter was to illustrate the nanoscale properties of Mg-Al LDH nanomaterials as they are employed as drug delivery vectors in mesenchymal stem cells and A549 cancer cell lines. The application of transmission electron microscopy techniques disclosed an understanding of the chemical and physical properties of LDH materials in MSC environments. The novel applications of STEM-EDS and SAED methods allow for an extensive characterization of the behaviours of LDH materials as gene-delivery vectors. The associated pDNA and siRNA therapeutics were found to suitably interact with the Mg-Al LDH nanomaterials. This was shown by the presence of Phosphorous in the related spectra. The former was found to cause aggregates of the LDH particles by 'wrapping' onto the layered surfaces. Although the LDH-siRNA nanocomposites showed aggregations as well, this was believed to derive from the LDH particles themselves, with a similar presence of Phosphorous indicating an intercalation into the lamellar framework interlayers. The Mg-Al LDHs were found to be quite versatile in their application to our various cell studies. Our TEM approaches evidenced that these smaller LDH based nanohybrid vectors can be successfully up-taken by MSC cells *in vitro*. Furthermore, SAED analysis showed that the LDH gene delivery vectors retained their layered structure and well-defined crystallographic in MSC environments.

These successes were also mirrored in the case of the A549 cells. The LDHs were also shown to be effectively transfected across the cell membranes and into the cytoplasmic regions. More precisely, the uptake mechanisms were identified as endocytic pathways across the cell membranes of A549 cells. This was evidenced as part of the time study

where uptake processes were directly captured TEM analysis. The LDH particles were then found to aggregate in endosomal bodies within the cell. EFTEM and STEM EELS mapping methods revealed that the aggregates exhibited a presence of oxygen, due to the abundance of LDH particles within these vesicles.

To our knowledge, the time study of the Mg-Al is a first attempt to comprehensively track the LDH particles intracellular fate with such precision using EM methods. It was found that LDH particles were efficiently transfected after only 1 hour and localised in endosomal bodies after 72 hours. Although similar findings were already shown in the literature, they mainly relied on confocal microscopy methods and ultrastructural features were eluded to. More importantly, these results add to the growing body of drug delivery research in relation to LDH nanoparticle life times in the intracellular regions. They may also impact the future design and application of these types of non-viral biocompatible layered materials for the efficient delivery of associated therapeutics that require such time scales. A significant result to emerge from this study LDH structural integrity remained intact in the cellular environments up to 72 hours. The studies of the O K edge using EFTEM and STEM-EELS highlighted that the LDH structure was resilient to the cell culture surroundings as well as within intracellular endosomal regions. This was found to conflict previous studies, raising further characterization requirements to fully understand such behaviours. This data also suggests that there are significant strides to be taken to completely understand the LDH behaviours at the nano and even atomic scales during such processes.

Our results also impact the existing artillery of characterizations available to this research area. Although standard TEM imaging is all in all a routine method of characterization in this subject, the application of advanced EM techniques may be of interest to numerous future studies. STEM, EFTEM, electron diffraction and EELS embellish not only our experimental data sets from these samples but also our overall understandings of these nanoscale processes.

Although there have been significant findings related to LDH behaviours in these cellular delivery applications, there are many paths of research that can be pursued to further these studies. Firstly, the main body of our results in this chapter was restricted

to a 72 hour time frame. It would be interesting to investigate the intracellular fate of the LDH particles over longer time scales, which may elucidate the controversies surrounding our results and previous literature.

Further studies could pursue the application of low dose EFTEM or EEL spectroscopic studies or multi-frame acquisition imaging to the resin-based samples. This would greatly assist the cases where the resin samples were prone to electron beam induced damage.

It was also noted that an improvement in sample preparation such as or more electron beam resilient resins or less ultramicrotome knife artefacts in sections would have been of much needed assistance. An overcoming of these would have increased the range of samples and diversified the possible EELS analyses that could have been performed. For example, multiple EFTEM maps or more statistically significant core loss EELS spectra could be achieved. Moreover, the ability to effectively map or acquire statistically significant images and spectra on a limited number of cells hindered our interpretations and restricted elemental distribution studies. On the other hand, it was previously acknowledged that the protocols of TEM sample preparation of the cell culture samples may influence the LDH behaviours in the cell environments. These undesirable and potentially drastic effects may be overcome by analysing samples that avoid the standard TEM preparations. For example, looking at whole hydrated cells or samples that do not have to be embedded and suitably sectioned. The application of developing technologies such as in-situ liquid cell TEM and helium ion microscopy may assist in understanding the uptake processes of a more native sample. Further details of these methods of characterization will be explored further in the next chapter.

5.7 Bibliography

1. Faraji, A. H. & Wipf, P. Nanoparticles in cellular drug delivery. *Bioorg. Med. Chem.* **17,** 2950–2962 (2009).

2. Xie, J. *et al.* Ultrasmall c (RGDyK)-Coated Fe 3O4 Nanoparticles and Their Specific Targeting to Integrin Rich Tumor Cells. *J. Am. Chem. Soc.* **130,** 7542–7543 (2008).

3. Movia, D. *et al.* A safe-by-design approach to the development of gold nanoboxes as carriers for internalization into cancer cells. *Biomaterials* **35,** 2543–2557 (2014).

4. Curtin, C. M. *et al.* Innovative collagen nano-hydroxyapatite scaffolds offer a highly efficient non-viral gene delivery platform for stem cell-mediated bone formation. *Adv. Mater.* **24,** 749–754 (2012).

5. Gonzalez-fernandez, T. *et al.* Mesenchymal stem cell fate following non-viral gene transfection strongly depends on the choice of delivery vector. *Acta Biomater.* **55,** 226–238 (2017).

6. Choy, J., Philippot, K., Choi, S., Oh, J. & Choy, J. Human-related application and nanotoxicology of inorganic particles : complementary aspects. *J. Mater. Chem.* **18,** 605–712 (2008).

7. Yin, F. *et al.* Functionalized 2D nanomaterials for gene delivery applications. *Coord. Chem. Rev.* **347,** 77–97 (2017).

8. Monopoli, M. P., Åberg, C., Salvati, A. & Dawson, K. A. Biomolecular coronas provide biological identity of nanosized materials. *Nat. Nanotechnol.* **7,** 779–786 (2012).

9. Raftery, R. M. *et al.* Delivering Nucleic-Acid Based Nanomedicines on Biomaterial Scaffolds for Orthopedic Tissue Repair: Challenges, Progress and Future Perspectives. *Adv. Mater.* **28,** 5447–5469 (2016).

10. Guan, S. *et al.* A layered drug nanovehicle toward targeted cancer imaging and therapy †. *J. Mater. Chem. B* **4,** 1331–1336 (2016).

11. Wong, Y. *et al.* Efficient delivery of siRNA to cortical neurons using layered double hydroxide nanoparticles. *Biomaterials* **31,** 8770–8779 (2010).

12. Li, S. *et al.* Cellular uptake and gene delivery using layered double hydroxide

nanoparticles. *J. Mater. Chem. B* **1,** 61–68 (2013).

13. Rives, V., del Arco, M. & Martín, C. Intercalation of drugs in layered double hydroxides and their controlled release: A review. *Appl. Clay Sci.* **88–89,** 239–269 (2014).

14. Bi, X., Zhang, H. & Dou, L. Layered double hydroxide-based nanocarriers for drug delivery. *Pharmaceutics* **6,** 298–332 (2014).

15. Li, D. *et al.* Cancer therapy and fluorescence imaging using the active release of doxorubicin from MSPs / Ni-LDH folate targeting nanoparticles. *Biomaterials* **34,** 7913–7922 (2013).

16. Senapati, S. *et al.* Layered double hydroxides as effective carrier for anticancer drugs and tailoring of release rate through interlayer anions. *J. Control. Release* **224,** 186–198 (2016).

17. Zhang, K. *et al.* Potential for Layered Double Hydroxides-Based , Innovative Drug Delivery Systems. *Int. J. Mol. Sci.* 7409–7428 (2014). doi:10.3390/ijms15057409

18. Choy, J., Choi, S., Oh, J. & Park, T. Clay minerals and layered double hydroxides for novel biological applications. *Appl. Clay Sci.* **36,** 122–132 (2007).

19. Desigaux, L. *et al.* Self-Assembly and Characterization of Layered Double Hydroxide / DNA Hybrids. *Nano Lett.* **6,** 199–204 (2006).

20. Yang, J. *et al.* New Inorganic-Based Drug Delivery System of Indole-3-Acetic Acid-Layered Metal Hydroxide Nanohybrids with Controlled Release Rate. *Chem. Mater.* 2679–2685 (2007).

21. Kang, H. *et al.* Intracrystalline structure and release pattern of ferulic acid intercalated into layered double hydroxide through various synthesis routes. *Appl. Clay Sci.* **112–113,** 32–39 (2015).

22. Chakraborty, J., Roychowdhury, S., Sengupta, S. & Ghosh, S. Mg-Al layered double hydroxide-methotrexate nanohybrid drug delivery system: Evaluation of efficacy. *Mater. Sci. Eng. C* **33,** 2168–2174 (2013).

23. Ladewig, K., Niebert, M., Xu, Z. P., Gray, P. P. & Lu, G. Q. M. Efficient siRNA delivery to mammalian cells using layered double hydroxide nanoparticles. *Biomaterials* **31,** 1821–1829 (2010).

24. Xu, Z. P. & Lu, G. Q. M. Layered double hydroxide nanomaterials as potential cellular drug delivery agents*. *Pure Appl. Chem.* **78,** 1771–1779 (2006).

25. Saha, S., Ray, S., Acharya, R., Kumar, T. & Chakraborty, J. Magnesium , zinc and calcium aluminium layered double hydroxide-drug nanohybrids : A comprehensive study. *Appl. Clay Sci.* **135,** 493–509 (2016).

26. Ladewig, K., Niebert, M., Xu, Z. P., Gray, P. P. & Lu, G. Q. (Max). Controlled preparation of layered double hydroxide nanoparticles and their application as gene delivery vehicles. *Appl. Clay Sci.* **48,** 280–289 (2010).

27. Li, L., Gu, W., Chen, J., Chen, W. & Xu, Z. P. Co-delivery of siRNAs and anti-cancer drugs using layered double hydroxide nanoparticles. *Biomaterials* **35,** 3331–3339 (2014).

28. Tyner, K. M. *et al.* Intercalation, delivery, and expression of the gene encoding green fluorescence protein utilizing nanobiohybrids. *J. Control. Release* **100,** 399–409 (2004).

29. Masarudin, M. J., Yusoff, K., Rahim, R. A. & Hussein, M. Z. Successful transfer of plasmid DNA into in vitro cells transfected with an inorganic plasmid – Mg / Al-LDH nanobiocomposite material as a vector for gene expression. *Nanotechnology* **20,** 045602(11pp) (2009).

30. Rives, V., Arco, M. & Martín, C. Layered double hydroxides as drug carriers and for controlled release of non-steroidal antiinflammatory drugs (NSAIDs): A review. *J. Control. Release* **169,** 28–39 (2013).

31. Lu, M. *et al.* Chemisorption Mechanism of DNA on Mg/Fe Layered Double Hydroxide Nanoparticles: Insights into Engineering Effective SiRNA Delivery Systems. *Langmuir* **32,** 2659–2667 (2016).

32. Choy, J., Kwak, S., Park, J. & May, R. V. Intercalative Nanohybrids of Nucleoside Monophosphates and DNA in Layered Metal Hydroxide. *J. Am. Chem. Soc.* **121,** 1399–1400 (1999).

33. Choy, J. *et al.* Layered double hydroxide as an efficient drug reservoir for folate derivatives. *Biomaterials* **25,** 3059–3064 (2004).

34. Dai, C., Tian, D., Li, S. & Li, X. Methotrexate intercalated layered double hydroxides with the mediation of surfactants : Mechanism exploration and bioassay study. *Mater. Sci. Eng. C* **57,** 272–278 (2015).

35. Bao, W., Wang, J., Wang, Q., Hare, D. O. & Wan, Y. Layered Double Hydroxide Nanotransporter for Molecule Delivery to Intact Plant Cells. *Nat. Publ. Gr.* 1–9 (2016). doi:10.1038/srep26738

36. Choi, S., Oh, J. & Choy, J. Anticancer drug-layered hydroxide nanohybrids as potent cancer chemotherapy agents. *J. Phys. Chem. Solids* **69,** 1528–1532 (2008).

37. Choi, S. & Choy, J. Layered double hydroxide nanoparticles as target-specific delivery carriers : uptake mechanism and toxicity. *Nanomedicine* **6,** 803–814 (2011).

38. Xu, Z. P. *et al.* Subcellular compartment targeting of layered double hydroxide nanoparticles. *J. Control. Release* **130,** 86–94 (2008).

39. Chen, M., Cooper, H. M., Zhi, J., Bartlett, P. F. & Ping, Z. Reduction in the size of layered double hydroxide nanoparticles enhances the efficiency of siRNA delivery. *J. Colloid Interface Sci.* **390,** 275–281 (2013).

40. Ping, Z., Hua, Q., Qing, G. & Bing, A. Inorganic nanoparticles as carriers for efficient cellular delivery. *Chem. Eng. Sci.* **61,** 1027–1040 (2006).

41. Chung, H. E., Park, D. H., Choy, J. H. & Choi, S. J. Intracellular trafficking pathway of layered double hydroxide nanoparticles in human cells: Size-dependent cellular delivery. *Appl. Clay Sci.* **65–66,** 24–30 (2012).

42. Alloyeau, D. *et al.* Direct imaging and chemical analysis of unstained DNA origami performed with a transmission electron microscope. *Chem. Commun.* **47,** 9375–9377 (2011).

43. Nevsten, P., Evilevitch, A. & Wallenberg, R. Chemical mapping of DNA and counter-ion content inside phage by energy-filtered TEM. *J Biol Phys* **38,** 229–240 (2012).

44. Sousa, A. A. & Leapman, R. D. Development and application of STEM for the biological sciences. *Ultramicroscopy* **123,** 38–49 (2012).

45. Andrews, S. B., Pivovarova, N. B. & Leapman, R. D. Quantitative imaging and analysis of biological specimens in the field-emission scanning transmission electron microscope : capabilities and limitations. *Scanning Microsc.* **13,** 147–157 (1999).

46. Leapman, R. D. Detecting single atoms of calcium and iron in biological structures by electron energy-loss spectrum-imaging. *J. Microsc.* **210,** 5–15 (2003).

47. Aronova, M. A., Kim, Y. C., Pivovarova, N. B., Andrews, S. B. & Leapman, R. D. Quantitative EFTEM mapping of near physiological calcium concentrations in biological specimens. *Ultramicroscopy* **109,** 201–212 (2009).

48. Blissett, A. R. *et al.* Sub-cellular In-situ Characterization of Ferritin(iron) in a Rodent Model of Spinal Cord Injury. *Sci. Rep.* **8,** 1–10 (2018).

49. Goping, G., Pollard, H. B., Srivastava, M. & Leapman, R. Mapping protein expression in mouse pancreatic islets by immunolabeling and electron energy loss spectrum-imaging. *Microsc. Res. Tech.* **61,** 448–456 (2003).

50. Bordat, C. *et al.* Distribution of iron oxide nanoparticles in rat lymph nodes studied using electron energy loss spectroscopy (EELS) and electron spectroscopic imaging (ESI). *J. Magn. Reson. Imaging* **12,** 505–509 (2000).

51. Rothen-Rutishauser, B. M., Schürch, S., Haenni, B., Kapp, N. & Gehr, P. Interaction of fine particles and nanoparticles with red blood cells visualized with advanced microscopic techniques. *Environ. Sci. Technol.* **40,** 4353–4359 (2006).

52. Hondow, N. *et al.* Quantifying the cellular uptake of semiconductor quantum dot nanoparticles by analytical electron microscopy. *J. Microsc.* **261,** 167–176 (2016).

53. Leapman, R. D. & Brian Andrews, S. Biological electron energy loss spectroscopy: the present and the future. *Microsc. Microanal. Microstruct.* **2,** 387–394 (1991).

54. Wu, Y. *et al.* Size-dependent effects of layered double hydroxide nanoparticles on cellular functions of mouse embryonic stem cells. *Nanomedicine (Lond.)* **10,** 3469–3482 (2015).

55. Oh, J., Park, C. & Choy, J. Intracellular Drug Delivery of Layered Double Hydroxide Nanoparticles. *J. Nanosci. Nanotechnol.* **11,** 1632–1635 (2011).

56. Qin, L. *et al.* The in vitro and in vivo anti-tumor effect of layered double hydroxides nanoparticles as delivery for podophyllotoxin. *Int. J. Pharm.* **388,** 223–230 (2010).

57. Pietruska, J. R. *et al.* Bioavailability, intracellular mobilization of nickel, and HIF-1α activation in human lung epithelial cells exposed to metallic nickel and nickel oxide nanoparticles. *Toxicol. Sci.* **124,** 138–148 (2011).

58. Zhang, S. *et al.* Size Dependent Endocytosis of Nanoparticles. *Adv. Mater.* **21,** 419–424 (2009).

59. Canton, I. & Battaglia, G. Endocytosis at the Nanoscale. *Chem. Soc. Rev.* **41,** 2718–2739 (2012).

60. Jiang, W. E. N., Kim, B. Y. S., Rutka, J. T. & Chan, W. C. W. Nanoparticle-mediated cellular response is size-dependent. *Nat. Nanotechnol.* **3,** 145–150 (2008).

61. Liu, Z. *et al.* Synthesis,Anion Exchange, and Delamination of Co-Al Layered Double Hydroxide : Assembly of the Exfoliated Nanosheet / Polyanion Composite Films and Magneto-Optical Studies. *J. Am. Chem. Soc.* **128,** 4872–4880 (2006).

62. Choi, G., Kwon, O., Oh, Y., Yun, C. & Choy, J. Inorganic Nanovehicle Targets Tumor in an Orthotopic Breast Cancer Model. *Sci. Rep.* **4,** 29–31 (2014).

63. Xu, Z. P. *et al.* Layered double hydroxide nanoparticles as cellular delivery vectors of supercoiled plasmid DNA. *Int. J. Nanomedicine* **2,** 163–174 (2007).

64. Pannier, A. K. & Shea, L. D. Controlled Release Systems for DNA Delivery. *Mol. Ther.* **10,** 19–26 (2004).

65. Schütz, I. *et al.* Lysosomal dysfunction caused by cellular accumulation of silica nanoparticles. *J. Biol. Chem.* **291,** 14170–14184 (2016).

66. Gunduz, N., Ceylan, H., Guler, M. O. & Tekinay, A. B. Intracellular Accumulation of Gold Nanoparticles Leads to Inhibition of Macropinocytosis to Reduce the Endoplasmic Reticulum Stress. *Sci. Rep.* **7,** 1–10 (2017).

67. Brož, A., Bačáková, L., Štenclová, P., Kromka, A. & Potocký, Š. Uptake and intracellular accumulation of diamond nanoparticles - A metabolic and cytotoxic study. *Beilstein J. Nanotechnol.* **8,** 1649–1657 (2017).

68. Yan, M. *et al.* Systemic toxicity induced by aggregated layered double hydroxide nanoparticles. *Int. J. Nanomedicine* **12,** 7183–7195 (2017).

69. Egerton, R. F., Li, P. & Malac, M. Radiation damage in the TEM and SEM. *Micron* **35,** 399–409 (2004).

70. Zhao, X. F., Wang, W. Y., Li, X. D., Li, S. P. & Song, F. G. Core-shell structure of Fe3O4@MTX-LDH/Au NPs for cancer therapy. *Mater. Sci. Eng. C* **89,** 422–428 (2018).

71. Oh, J. M., Choi, S. J., Lee, G. E., Kim, J. E. & Choy, J. H. Inorganic metal hydroxide nanoparticles for targeted cellular uptake through clathrin-mediated endocytosis. *Chem. - An Asian J.* **4,** 67–73 (2009).

72. Uygur, B., Craig, G., Mason, M. D. & Ng, A. K. Cytotoxicity and genotoxicity of silver nanomaterials. *Tech. Proc. 2009 NSTI Nanotechnol. Conf. Expo, NSTI-Nanotech 2009* **2,** 383–386 (2009).

73. Ahn, C. C. & Krivanek, O. . *EELS Atlas: a reference collection of electron energy loss spectra covering all stable elements*. (Warrendale : Gatan, 1983).

74. Hakeem, A. *et al.* Facile Synthesis of pH-Responsive Doxorubicin-Loaded Layered Doubled Hydroxide for Efficient Cancer Therapy. *J. Mater. Chem. B* (2018). doi:10.1039/C8TB01572D

Chapter 6: Conclusions & Future Work

The overall objective of this thesis set out to fully characterize the properties of Mg-Al and Ni-Fe layered double hydroxide nanomaterials. These obtained findings were effectively realised using the high-end techniques of transmission electron microscopy, such as aberration corrected STEM, in-situ TEM and electron energy loss spectroscopy. With the help of these state-of-the-art EM methodologies, our aim was to assess how the LDH materials behaved in a variety of conditions such as those related to thermal and biomedical cases.

Chapter 3 characterized the intrinsic chemical and physical properties of both micron sized LDH materials of Mg-Al and Ni-Fe compositions. Our synthesized material exhibited well-defined hexagonal structural morphologies with highly crystalline features in both compositions. This section of the thesis studies presented a number of striking properties of the LDH structure. Firstly, dark field TEM analysis showed that the LDH platelets are made up of crystalline domains as opposed to an isotropic single orientation. This was also observed using aberration corrected STEM imaging, where although the materials are made up of a single crystal, the randomly orientated crystallites could be directly visualised at the atomic level. The advanced methods of EFTEM thickness maps of the material shows gradual increase in platelet heights from the edge to central regions. In our opinion, there is an inadequate number of studies involving the atomic scale nature of LDH nanomaterials. Our atomic level characterizations of the Ni-Fe LDH material may impact future designs of LDH related materials across a range of applications such as catalysis or energy storage where edge sites and boundaries effect such performances.

The investigations of the role of the electron beam on the nature of the LDH materials greatly evolved the research of these 2-D nanomaterials. To our knowledge, this is first study applied to these materials documenting how the electron beam can influence the LDHs structural properties. It was found that the electron beam was capable of introducing lattice disruptions. This was highlighted by the broadening and intensity attenuation of electron diffraction reciprocal lattice points. Moreover, the incident

beam also had a significant on the alteration of the chemical environments of the Ni-Fe LDHs.

This was depicted by EELS studies of the Oxygen K edge, where the generation of new peaks represented the formation of transition metal oxides. These TEM and EELS observations strengthen our understanding of the effects of imaging of this samples with electron microscopy. These findings also increase the awareness of the electron beam irradiation has on the LDHs structural integrity, influencing interpretations of future experimental data involved in related assessments. The current study has only examined two of the numerous possible combinations and ratios of the LDH material family. A natural progression of this research could characterize the properties of alternative compositions such as Co-Al, Zn-Al or even tertiary structures which involve a third species in the cationic layers using our established TEM approaches. Ultimately, the results found from LDH material characterizations provided a substantial framework to investigate their behaviours in related scientific applications.

Chapter 4 probed the calcination behaviours of both Mg-Al and Ni-Fe LDH materials using in-situ TEM. Both compositions shared thermal decomposition trends but also exhibited their own unique signatures. In the case of Mg-Al LDHs, a porous material with the formation of oxide and spinel materials was revealed by our in-situ heating experiments. These nanoscale results may assist the prospective designs of future flame retardant based polymers incorporating these LDH materials. More interestingly, the calcination behaviours of Ni-Fe LDHs demonstrated a nucleation and evolution of spherical particles and spinel arrays confined to the original platelet dimensions. A complimentary EELS study showed that the thermal decompositions also affected the O K edge, where signatures of nickel oxides were identified after thermal treatment. These current findings add to a growing body of literature studying EELS features of transition metal particle species. More importantly this work also reveals the thermal evolution of the EELS behaviours in these layered materials for the first time. More broadly, research is needed to understand if the bulk properties are reflected by our nanoscale observations. This could be achieved by calling upon alternative more suitable characterization techniques such as X-ray spectroscopy to determine bonding information of the Oxygen at the bulk level. This chapter also

elucidated crucial information on the effect of heating environments on the morphologies after different calcination procedures. In contrast to in-situ investigations, calcining the Ni-Fe LDHs ex-situ results in the formation of a faceted morphology with highly crystalline features. Similar segregations of the metallic sites in the ex-situ calcined materials was observed using STEM-EELS mapping techniques. Indeed, the present study contributes to existing knowledge on the calcination of these Ni-Fe LDHs at the atomic level. A greater focus on the interfacial regions using aberration corrected STEM could produce some interesting discoveries on the role of these sites in catalytic or oxygen evolution processes. More widely speaking, further research might explore further practical applications using these calcined materials. The acquired data may influence the design and implementation of these structures into innovative energy storage and oxygen evolution devices.

Chapter 5 set out to determine the structural behaviour of Mg-Al LDHs in a range of biomedical applications. The goal was to characterize the chemical and physical properties in cellular environments as well as providing essential information on the cellular mechanisms involved in transfection and ultimate intracellular fate of these biocompatible low cytotoxic layered materials. The investigation of Mg-Al LDH with biomolecules showed a favourable interaction with pDNA and the smaller stranded siRNA in relation to the formation of suitable delivery vectors. An issue that was not addressed by our studies was the investigation of LDH-siRNA complex behaviours with mesenchymal stem cells. However, future work plans to establish the uptake capabilities of MSCs with the LDH-siRNA vectors. In doing so, investigating the role the LDHs play in the delivery of RNA based therapeutics.

LDH based materials were found to be routinely transfected into both MSCs and lung cancer A549 cell lines in vitro. EM characterizations also provided a plethora of significant results regarding the structural properties of the LDH particles in these environments. Firstly, electron diffraction indicated that transfected particles retained their crystalline nature. This to our knowledge, is a first nanoscale characterization discovery of such behaviours, vitally confirming associated delivery mechanisms involved with LDH nanomaterials. The scope of this study was limited to samples

exposed to the particles after 72 hours. It would be interesting to determine how these crystallographic features behave over longer time durations in the cellular regions. This approach could also reveal novel insights into how LDHs are removed, i.e. exocytosis, from these particular cell lines. A second major finding was that the LDHs retained their elemental features when they were in the cell cytosol. It is believed that this is a first time where the advanced in-situ techniques of STEM-EDX, EFTEM and EELS were utilised to extend our knowledge of these processes of LDH nanoparticle delivery. These experiments also contribute additional evidence that suggest the LDHs are resilient to intracellular structural breakdowns. Having said that, the scope of the EELS studies was limited by the nature of the resin embedded samples. Firstly, the thickness of the sections produced too much plural scattering which did not allow significant signals for the Mg and Al $L_{2,3}$ edges to be identified above background. Also in this regard, the sample stabilities under electron beam irradiation limited prolonged dwell times to produced suitable signal to noise ratios for such edges to be resolved.

Although there have been many profound results throughout this thesis, it has also postulated many further questionings of LDH research. The next section of this chapter details potential future avenues of study that could be based on the findings of this thesis. Each prospective study is discussed in a separate manner, including preliminary findings, future impacts and relations to the already established findings from this work and the already published literature. It is noted that although these findings are not entirely conclusive, they give an indication of the potential imaging conditions and material behaviours for future experimentation.

6.1 Characterizing Ni-Fe LDH in liquid environments

The physical and dynamical phenomena of materials in liquid environments at the nanometre scale has been of great interest across nanotechnology in recent times. The observation of processes occurring in liquids at near atomic resolutions can provide vital information in the study of many nanomaterials. Luckily, this has become possible with the development of in-situ TEM instrumentation. These next generation

of TEM sample holders has realised TEM characterizations of nanoscale processes in liquids at higher spatial resolutions compared to that of light microscopy. This has led to an extensive body of research in areas such as catalytic reactions,[1] nanoparticle growth,[2,3] electrochemical processes[4] and nanomaterial dynamics.[5,6] The microfabrication designs have established various types of experiment set-ups to permit these 'liquid cell' studies. In our case, the design of such holders involves two SiN thin films on Si chips. These electron transparent films provide a viewing window through which electrons can transmit through the windows and encapsulated liquids. The thickness of the liquids is governed by the choice of fabricated Si microchips.

Furthermore, the study of dispersions, particle stability and applications of nanoparticles in solution is indeed a primary concern across numerous fields of nanotechnology. The analysis of nanomaterials in various 'wet' environments has sparked significant interest in recent times.[7,8] A broad scope of studies have been published with this experimental approach such as the study of electrochemical systems in batteries and the behaviour of biological cells.[9,10] Moreover, with this field still in its scientific infancy, hurdles remain when it comes to interpreting experimental data from such in-situ experiments.

Along with these exciting imaging capabilities, there is also a mandate for a meticulous approach when interpreting such data from these experiments. In any EM experiment, the effect of the electron beam on the observed results must be taken into account. This was previously seen with our own TEM experiments of the Ni-Fe LDH materials in Chapter 3. This is also crucial in the case of studying liquid based samples in the TEM. There are many possible interactions involving the electron beam and the liquid samples. For example, the beam may induce thermal effects to the liquid sample which may alter diffusion and reaction rates of particles in the encapsulated liquid.[11] The interaction of electrons with the liquid may also result in the formation of H and OH radical species from water ionizations. These products then have the capabilities to interact with the solution in the liquid cell, and must be considered when interpreting liquid cell experimental observations.[12]

Moreover, imaging liquid specimens with electrons also presents hurdles to overcome in acquiring and interpreting experimental data from the electron microscope. The nature of the electron-liquid interaction can lead to further drawbacks from an imaging perspective.

From an experimental standpoint, sustaining the specimen in a 'wet' environment also presents its own experimental difficulties. This was achieved by establishing a continuous flow of water through the liquid channel during TEM and STEM imaging. Using liquid *in-situ* TEM methods, we studied the Ni-Fe LDH nanomaterials in solution, i.e. in water dispersions. This composition was favoured over their Mg-Al counterparts due to the relatively higher Z atomic number, hence providing greater HAADF STEM Z-contrast for an easier visualisation of the platelets and their behaviours in liquid environments. The aqueous dispersions of LDH samples were characterised using a liquid in-situ TEM sample holder (Hummingbird Scientific, USA). Approximately 3µl of the LDH dispersion was encapsulated by two Silicon chips, each with a 50nm electron transparent SiN viewing window. One of the chips consisted of a 100nm spacer, to allow a microfluidic channel to be set up across chips viewing window. Subsequently, a constant flow of H_2O was established by flowing water through the channel to ensure the LDH samples remained in an aqueous environment during imaging in the electron microscope. Figure 6.1 displays representative TEM and STEM images of the Ni-Fe LDHs encapsulated in the liquid cell. On first glance, the LDH particles are easily resolved in the cell, with both fully and partially formed/broken platelets exhibited. The broken platelets could be due to the sonication during sample preparation to disperse the particles or perhaps some platelets were not fully formed during the synthesis procedures. Particles were also found to exist in aggregates in liquid environments, similar to what was observed in dry state TEM analysis.

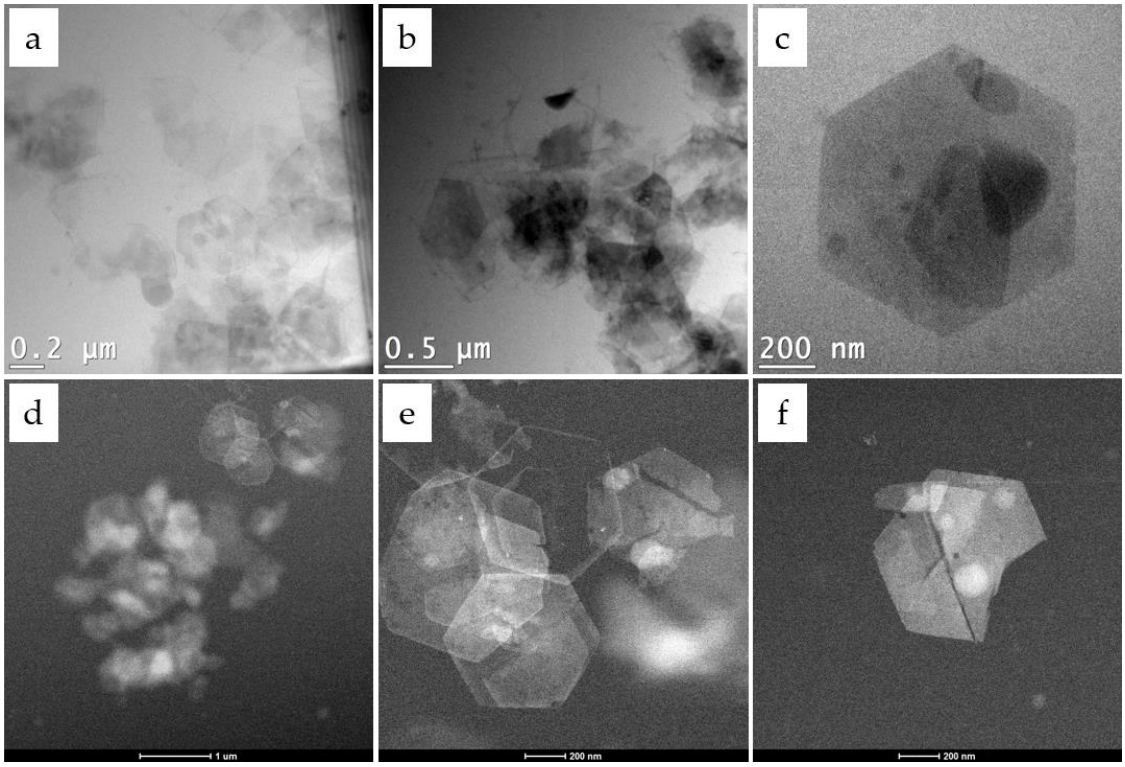

Figure 6.1 (a) - (c) TEM and (d) – (f) STEM images of Ni-Fe LDHs in liquid environments.

Figure 6.1 (e) presents an obscure unexpected contrast of the LDH platelets in the liquid environments. The intensity of the platelets at the edge in comparison to the central regions suggests that the platelet boundaries are less susceptible to electron beam damage in STEM. This 'hollow' platelet also further suggests that the edges of the materials may be more resilient to the incident electron beam or induced beam effects. In addition, Figure 6.1 (d) depicts LDH aggregates with varying planes of focus. This may be due to the adhesion of the platelets on either of the SiN windows or the particles suspended in the H_2O liquid itself.

6.1.1 Beam induced effects in liquid environments

It was initially observed that the LDH particles undergo a drastic change when imaged with the electron beam in liquid environments in both TEM and STEM. As per previous experiments, the influence of the electron beam on the Ni-Fe LDH particles was investigated.

The Ni-Fe LDH nanomaterials were subject to significant damage and etching due to electron beam irradiation in the water environments. It was seen that this was much

more pronounced in comparison to imaging the material under standard TEM vacuum conditions. As the assembled cell is exposed to the beam, not only is the sample subject to incident electrons, the liquid is equally subject to electron irradiation. In the case of water in these experiments, this interaction produces H and OH free radicals into the liquid cell encapsulation. These free radicals are capable of producing further free radicals which are all capable of interacting with the LDH platelets in the liquid environment. This effect is undesirable in this case of imaging as these water ionization species can unfortunately degrade the LDH materials in the liquid. Even though this is a rather interesting behaviour, it can largely hinder the imaging capabilities of the LDH specimens.

Hence, it is suggested that the radiolysis by-products of the H_2O radiolysis has a role to play in the breakdown and dissolution of the LDH platelets. It is has been previously established that the interaction of the electron beam with water results in the production of H^+ ions, which potentially creates an environment for the LDHs to stably exist, considering they are prone to degradation in acidic environments.[13] Moreover, the influence of direct electron beam damage to the sample via heating and 'knock-on' effects cannot be overlooked.
As such, the same LDH material was subject to similar imaging conditions in STEM in dry state vacuum environments, where the LDH particle structural stability was examined over time.

We also considered obtaining chemical information about the sample in liquid via EDX and EELS analysis. However, the application of these analytical techniques during in-situ liquid cell experiments was found to have its own experimental challenges. The limitations of such experiments has already been described by Dr. Edmund Long, a former member of the Nicolosi research group. The main concern with EDX analysis is the attainability of sufficient signal from the samples in the liquid environments. There is a significant generation of x-rays from the set-up of the in-situ liquid cell. The production of x-rays from the titanium metallic over-plate and also from the SiN windows encapsulating the liquid leads to the collection of unwanted x-rays in the

detector. As such, we chose to focus are pilot study on the imaging capabilities of the LDHs in the water.

Figure 6.2 presents sequential STEM images of the same Ni-Fe platelet, visualising the processes of the degradation of the material. A formation of large holes right across the platelets was almost instantaneously observed. This continuation of damage led to the complete destruction of the material on the order of minutes in the liquid cell experimental set up. When the Ni-Fe LDH samples were exposed to the electron beam, this appeared to induce the generation of small spherical nanoparticles distributed across the platelets surfaces.

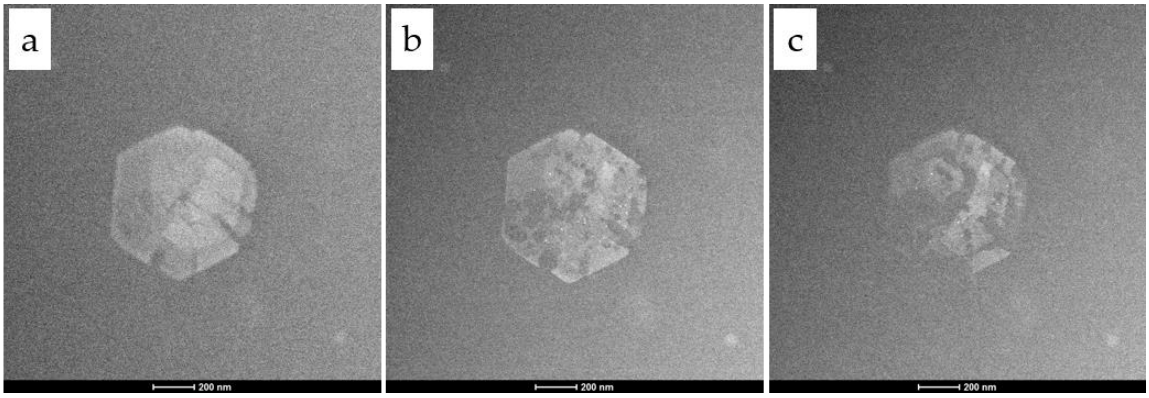

Figure 6.2 STEM image series of the Ni-Fe LDH as it is being irradiated by the rastering STEM probe.

The effect of the beam was significantly more pronounced in liquid environments. In fact, almost instantaneous destruction of the platelets occurred in the encapsulated liquid. We also readily observed drilling of holes through the platelets when the STEM probe was parked on the sample. This damage was found to occur much quicker in the liquid environments relative to the conventional vacuum analyses, suggesting perhaps a different damage mechanism. The production of free radicals due to electron beam interactions with aqueous has been well studied to date, and the production of free radicals may lead to the generation of acidic environments, where the LDHs stability would be affected and further prone to degradation by the reduced pH in the liquid cell.

The findings provide insights for future research of the associated formation and growth mechanisms of the Ni-Fe LDH structures. A possible study would be to conduct LDH synthesis procedures in-situ, where the co-precipitated solution would be thermally treated as it is encapsulated in the liquid cell. Once again, the induced effects of the electron-sample interactions could play a significant role in this case.

6.2 LDH-nanoparticle composites

6.2.1 Ni-Fe LDH and MXene heterostructures

A relatively new family of the 2-D nanomaterial world are titanium carbides, known as MXenes. These are layered based carbides and carbonnitrides compounds derived from etching of the Aluminium from MAX compounds. The MAX materials are ternary early transition metal carbides, carbonitrides and nitrides with a hexagonal structure. The general formula is $M_{n+1}AX_n$ where M is an early transition metal, A in an 'A-group element' and X represents is a carbon or nitrogen.[14,15] There has been an overwhelming number of publications related to the MXene materials with excellent performance properties with excellent applications in battery designs, photonics and energy storage.[16–18]

A more recent development of these materials is their combination with LDH nanomaterials, leading to the synthesis and preparation of novel heterostructures, again with superior properties in electrocatalysis and oxygen evolution.[19,20] However, these studies utilised small LDH based materials adhered to larger MXene sheets. We chose to combine our Ni-Fe LDH nanomaterials with Ti_3C_2 MXene that were both previously synthesized in our labs. Conversely to the previous work, we intended to use the large Ni-Fe LDHs as supports onto which the relatively smaller MXene sheets would be deposited. A TEM characterization of the MXene material can be found in the Appendix. The nanocomposite materials were formed by simply mixing the two dispersions under gentle sonication, where an electrostatic interaction would be favoured between the oppositely charged sheets of the respective materials.[21] Both TEM and SEM were used to initially characterize the LDH-MXene composite material. Figure 6.3 presents preliminary characterizations of these composites using STEM imaging.

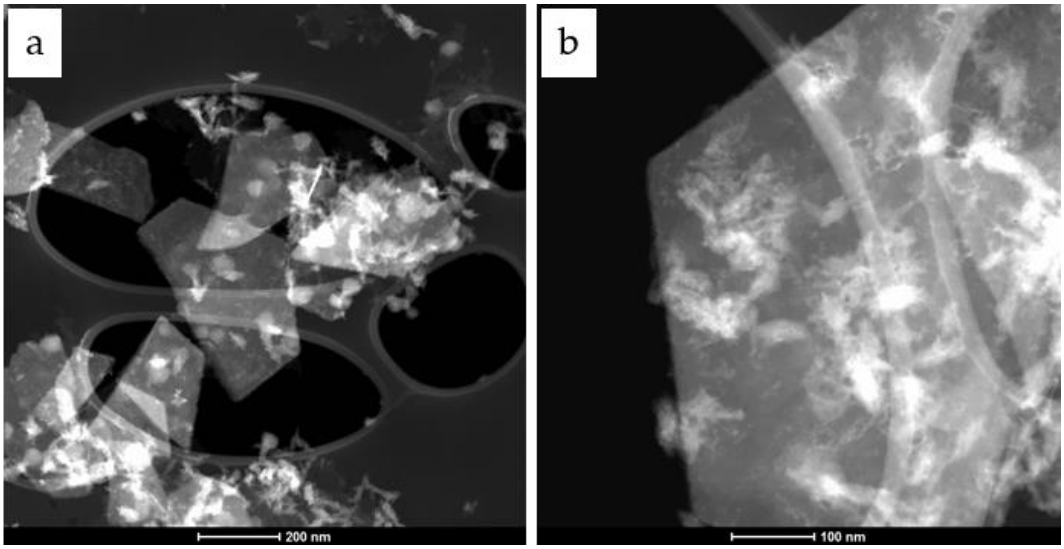

Figure 6.3 STEM imaging of LDH-MXene nanocomposite.

The smaller particle aggregations, shown by the brighter contrast regions, are believed to the adherence of MXenes onto the Ni-Fe LDH nanoplatelets.

Moreover, the associated SEM EDX map highlights the elemental distribution of the LDH-MXene nanocomposite. Figure 6.4 shows SEM-EDX maps of the Ni, Fe, O and Ti from the composite LDH-MXene sample.

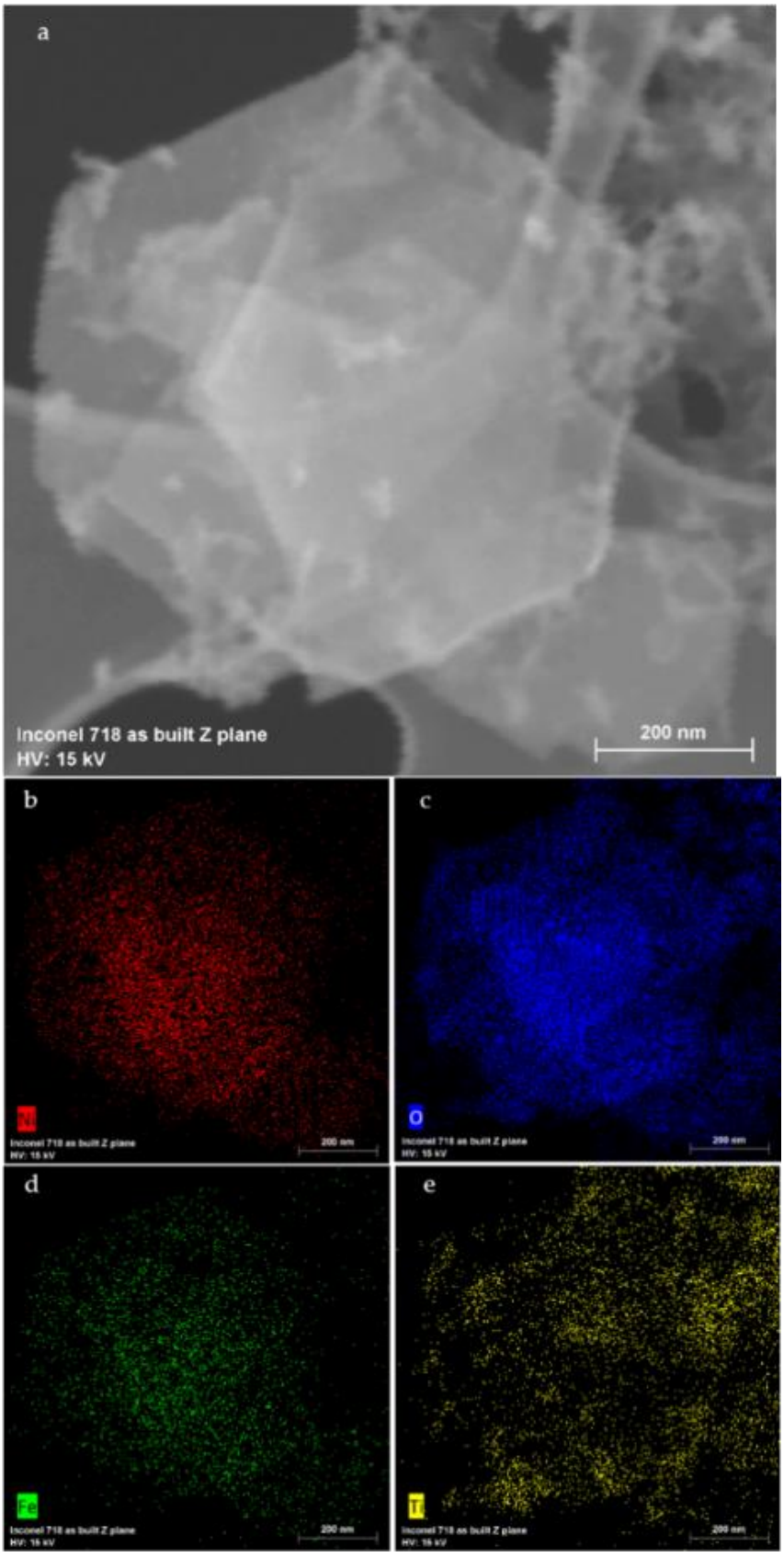

Figure 6.4 SEM-EDX maps of the LDH-MXene composite sample.

The Titanium signals shown in the SEM-EDX map originating from the Mxene layered material. This along with the Ni and Fe LDH confirms the adherence of the MXene layers onto the supporting Ni-Fe LDH platelets. This was also corroborated with STEM-EELS analysis of the composite material. Figure 6.5 shows a STEM-EELS area scans of the core loss regions showing the (a) Carbon K edge, Nitrogen K edge and Titanium $L_{2,3}$ edge and (b) the O K edge, Iron $L_{2,3}$ edge and Nickel $L_{2,3}$ edge.

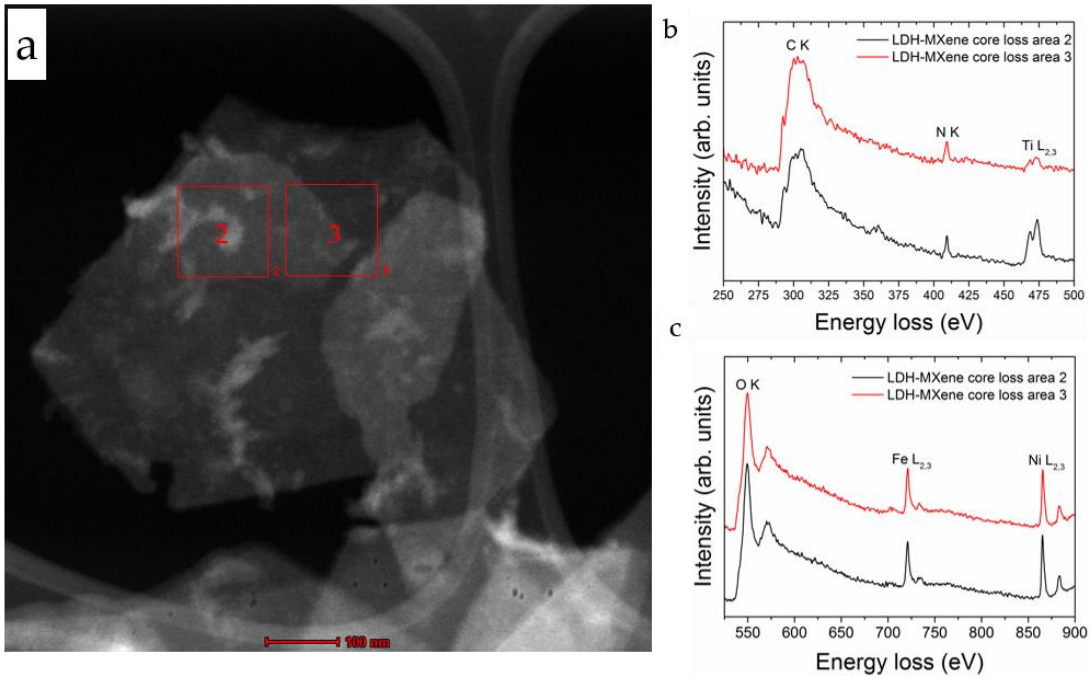

Figure 6.5 STEM-EELS area scans of core loss regions of the LDH-MXene composites. (a) STEM image highlighting area acquisitions. Scale bar is 100nm. (b) Core loss EELS spectra of the C K, N K and Ti $L_{2,3}$ edges. (c) Core loss spectra showing the O K, Fe $L_{2,3}$ and Ni $L_{2,3}$ edges.

In particular, the presence of these transition metal peaks identifies an interaction of the MXene with the Ni and Fe in the LDHs. The peaks deriving from the lighter elements such as Carbon, Nitrogen are also believed to originate from the MXene material. It is also possible that the Oxygen could ambiguously derive from the hydroxyls in the LDH layers or from the MXenes themselves. The nature of the Titanium in the sample was also probed using a STEM-EELS line scan, as shown in Figure 6.6.

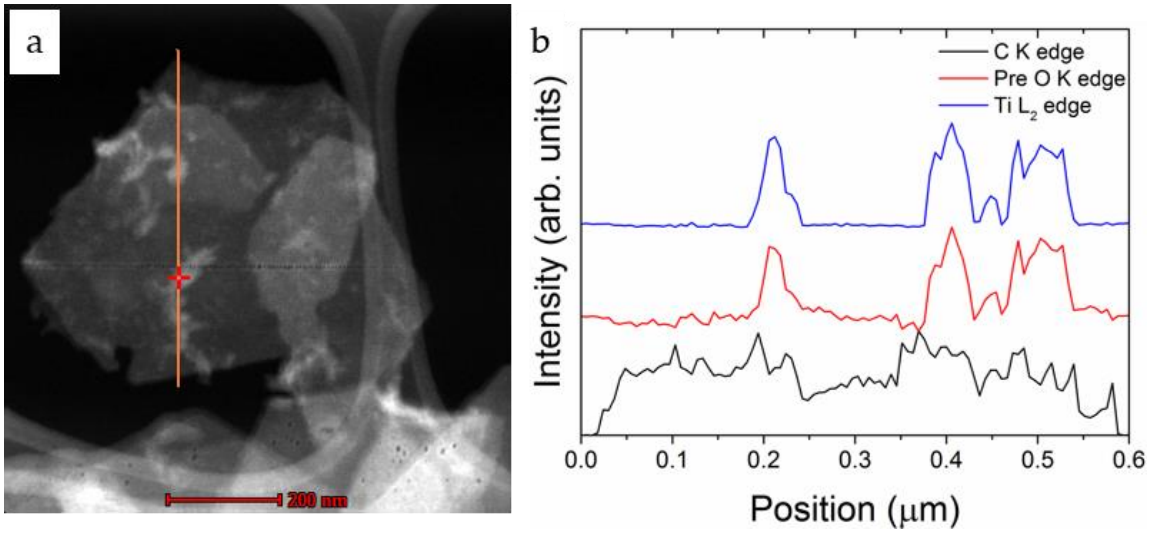

Figure 6.6 STEM-EELS line scan of the LDH-MXene composite. (b) depicts the C K edge, the Titanium L2 edge. The line scans in (b) shows the edge intensity related to the position from top to bottom.

This line scan illustrates the distribution of the EELS signals across the LDH-MXene material. In this case, the Titanium L_2 edge intensities highlight the localisation of MXene. This correlates well to the speculated particles adhered to the Ni-Fe LDH layers (Figure 6.3) and SEM EDX maps (Figure 6.4)

Perhaps the behaviour of the pre peak in the O K edge is of more interest. The coincidence of the Ti L_2 peaks and peak prior to the O K edge (red and blue line scans in Figure 6.6 respectively) possibly indicate that the MXene particulates on the LDH materials have become oxidized. Similar peaks were also observed in our O K edge EELS studies of beam induced effects and calcinations of NI-Fe LDH materials. Further analysis where various area scans of the core loss regions using STEM-EELS methods can be found in the Appendix. However in this experiment, these oxidations of the MXenes may be due to the interaction of the OH hydroxyl groups on the LDH layers. On the contrary, it is probably more likely to be a cause of exposures to aqueous solvents during nanocomposite synthesis as well as using aged samples to begin with. Future work is recommended to refine such procedures by using a 'fresher' sample of MXene sheets, as well as exploring potential electrochemical studies using such composite nanomaterials. In addition, further EM characterizations could be conducted such as electron diffraction to probe the crystal properties or using EELS to understand oxidation states of the transition metals synthesized with fresh Ti_3C_2

materials or alternative MXene/LDH structures. Future studies could also investigate the effect on the synthesis route on the morphological and crystallographic features of the LDH-MXene hybrid materials. Our preliminary characterizations only exploited a straight forward route to synthesize these composites.

We further pursued the properties of these composites by exposing them to thermal environments using our in-situ heating TEM holder. This was conducted to see if the role of the introduced MXene structures influenced the calcination behaviours of the Ni-Fe LDH, a process which was extensively studied in Chapter 4. Figure 6.7 presents BFTEM images of the LDH-MXene composite at various elevated temperatures. Additional images at different elevated temperatures can be found in the Appendix.

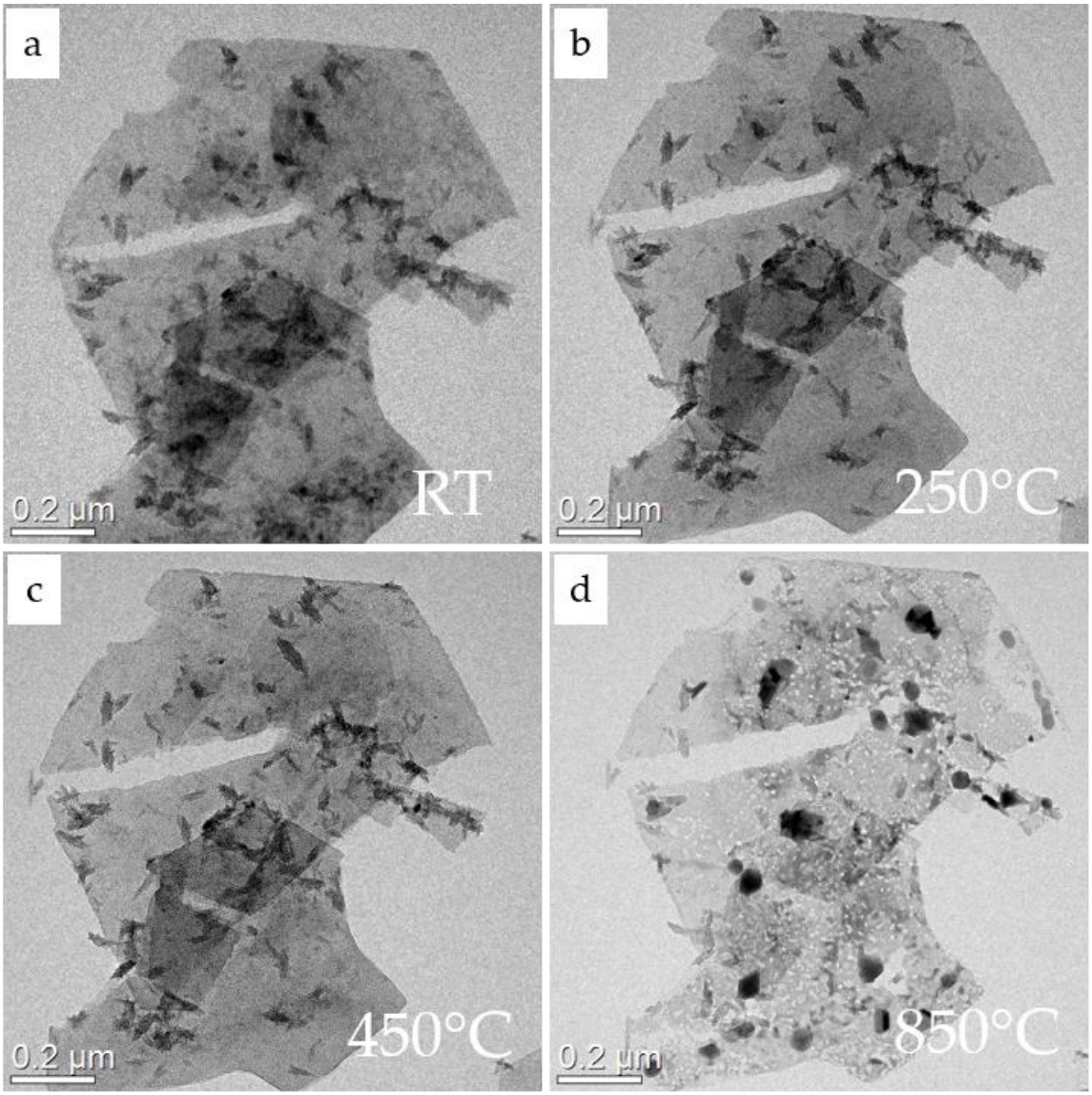

Figure 6.7 In-situ heating TEM experiments of LDH-MXene composites. (a) – (d) presents BFTEM images at room temperature (RT), 250°C, 450°C and 850°C respectively.

The evolution of the spherical particles were also seen to nucleate at the elevated temperatures at 850°C. The growth of such particles was also consistent with the previous Ni-Fe LDH calcinations at temperatures up to 850°C. This suggests that the inclusion of the MXenes onto the LDH hexagonal sheets does not play a significant role in the calcination behaviours. These findings also yield potential impacts for the fields of catalysis research which rely of calcinations to produce catalytically active structures. Electrochemical studies would provide further insight into the effect of

calcinations has on the performance of these composites in energy storage applications.

6.2.2 Mg-Al LDH – Quantum Dot composite material

The combination of LDH nanomaterials with alternative is not just limited to applications in materials science. In fact, the development of nanocomposites involving LDH and other nanomaterials has recently attracted interest from a biomedical aspect. These novel composites have shown successful preparations and application in the areas of therapeutic and diagnostic applications. For example, the synthesis of hybrid structures with polyethylene glycol (PEG), Au nanoparticles, silica nanoparticles and quantum dots have resulted in successes in these related fields of research.[22–24] A common inconsistency in these fields, which we have seen previously in the study of nanoparticle – cell interaction characterizations, is the lack of EM characterizations to truly elucidate the structure and behaviours of these nanocomposites. We decided to investigate the potential combination of Mg-Al LDH with CdSe quantum dots (QD-LDH). The latter has already been previously established as an effective drug carrier as well as image contrast agents for diagnostic evaluations. The potential combination of these materials with structures with alternative drug loading capabilities, such as LDH nanomaterials, could potentially lead to more beneficial ways of nanoparticle treatment of cells. In order to realise such potentials, there is a requirement of establishing characterization methodologies to assess the properties of such materials. We chose to employ TEM and STEM imaging techniques to assess the properties of potential composite materials involving CdSe quantum dots with Mg-Al LDHs (QD-LDH). Similar to the case of the LDH-MXene materials, separate dispersions of Mg-Al LDHs and QDs were mixed and subjected to gentle sonication for approximately 1 hour. Samples were prepared for TEM analysis using our previous drop cast methods. Figure 6.8 presents TEM and STEM of the QD-LDH nanocomposites. The aggregating nature of the Mg-Al LDH material is still observed, as was previously seen with the Mg-Al LDHs used as drug delivery agents.

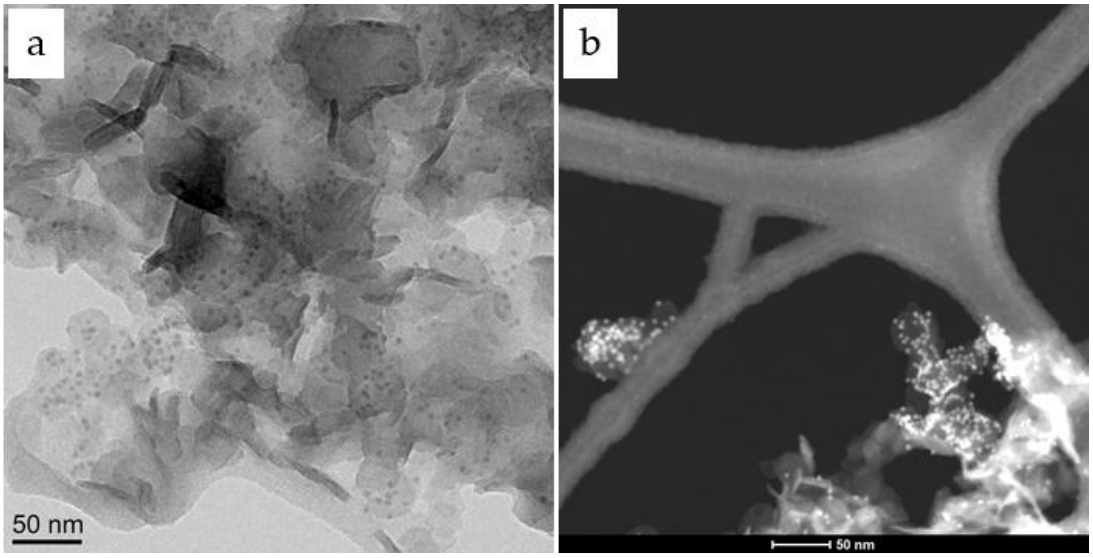

Figure 6.8 (a) TEM and (b) STEM images of Mg-Al LDH combined with CdSe quantum dots.

However, the spherical CdSe QDs are seen to attach to the surface of the LDH materials, which is a promising feature of potential material where its purpose is to combine their features for therapeutic and diagnostic applications. Moreover, the use of HAADF STEM Z-contrast of the QD-LDH effectively highlights the location of the QDs on the LDH surfaces. The relatively high Z-number of the heavy metal Cadmium and Selenium of the QDs relative to the Mg, Al and O of the LDH provides excellent contrast for their localisation to be highlighted in STEM imaging. These QD particles are approximately about 10nm in diameter and are decorated across the 50nm diameter LDH surfaces. This may also have implications in the delivery of drugs or extent of potential diagnostics in cellular applications due to their accessibility on the LDH surfaces. Moreover, the aggregation of the QDs may be prolonged by being adhered to the positively charged LDH sheets, which may be beneficial for achieving significant signals in optical microscopy applications in cells. The nature of the combination of these two therapeutic materials may also be effective in the enhancement of uptake by cell membranes, again due to the cationic nature of the LDH surfaces.

6.2.3 Mg-Al LDH incorporated into collagen based scaffolds

Collagen-based scaffolds studies, some of which published by our collaborators in RCSI Dublin, has led to a diverse active field of bioengineering research.[25–27] This has explored the development of collagen based materials for the successful delivery of a range of nanoparticle delivery vectors and promotion of osteogenic and chondrogenic features.[28–30] The interaction of the nanoparticle based delivery vectors and the delivery platforms play an important role in the full understanding of these processes, particularly at the nanoscale. In light of this, we employed EM characterizations to study the interaction of Mg-Al LDHs, of similar size to the ones employed as delivery vectors in the previous chapter, with collagen scaffold biomaterials. Initial experiments used SEM methods to study the ultrastructure of the collagen materials. This however resulted in significant imaging complications at first. The insulating nature of the collagen materials led to undesirable charging effects during SEM characterizations. This could be reduced by applying a conductive coating to the material. However in doing so this sample preparation method introduced potential artefacts from coating and more importantly, it greatly hindered any high-end characterizations in the SEM such as back-scatter Z-contrast imaging or EDX mapping methods. Fortunately, helium ion microscopy (HIM) provides manners to overcome charging hindrances of these samples. The insulating nature of the collagen materials, this time imaged with helium ions, could be compensated by the introduction of electrons into the specimen. This permitted a protocol of imaging these types of materials without charging effects and also uncoated, making imaging of a more 'native' sample possible. Figure 6.9 presents HIM images of the LDHs incorporated into the collagen scaffolds. A porous nature of the collagen scaffold was observed, with the adhesions of particles of various sizes and morphology on their regions (Figure 6.9 (b)). Unfortunately, these features did not resemble that of LDHs or even LDH aggregates and were deemed not to be those of the doped LDHs into the scaffold. In our case, these discrepancies arise from the complex procedures of collagen syntheses resulting in salt depositions from saline solutions as well as other remnant artefacts from scaffold production.

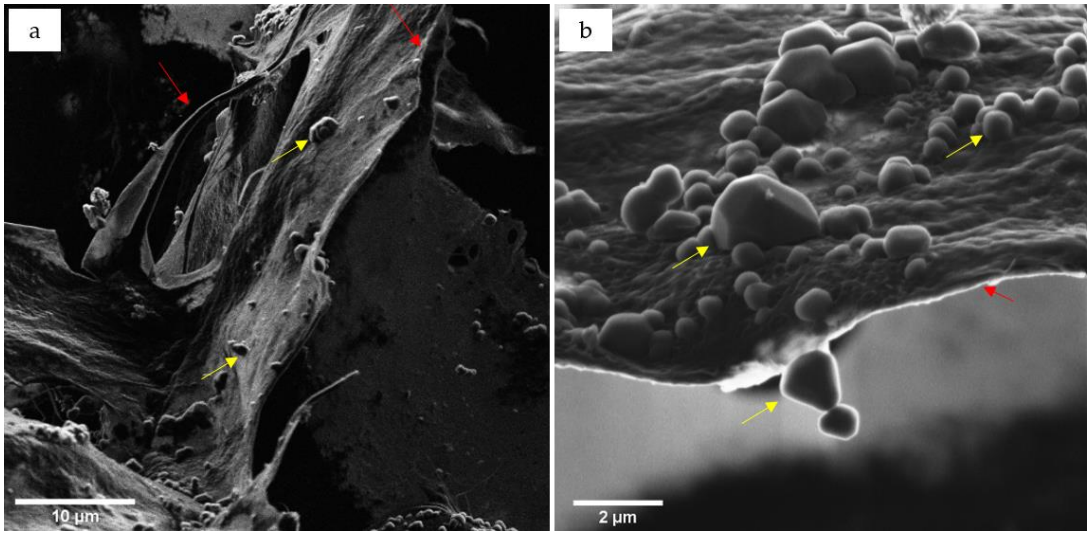

Figure 6.9 HIM imaging of LDH-collagen hybrid materials. Collagen scaffold regions and sample artifacts are denoted by red arrows and yellow arrows respectively.

However, an unfortunate result from these preliminary studies was the failure to identify significant regions of LDH nanomaterials within the scaffolds. This could be reasoned from the cases that the Mg-Al LDH concentration was simply too low to find regions within the relatively large scaffold areas. In addition, the nature of collagen synthesis in acetic acids may also have dissolved the LDHs in the syntheses of these types of materials. A suggested alternative would be to use larger platelets as a first protocol to investigate whether the Mg-Al platelets could be resolved in the scaffolds using such HIM imaging capabilities. These results show that further work on the imaging optimization and understanding of LDH-collagen scaffold interaction would be of widespread interest from both a microscopy and bioengineering aspect.

Another limitation related to the charging nature of these collagen based samples, coating them with a conductive metal and their HIM characterizations is the incapability to conduct reliable EDX analysis of the LDH-collagen composites. In the case of the insulating samples, the generation of x-rays requires that the incident voltage be relatively greater than the studied x-rays of the studied elements. This is not feasible for samples of insulating nature as the charge build-up makes imaging with suitable contrast almost impossible. For the coated scaffolds, the EDX detector collects a significant amount of shadowing and introduces unwanted EDX artefacts from the heavy metal x-rays from the conductive coat, making it difficult to discern which x-

rays derive from the sample itself. The identification of the elemental composition of collagen-nanomaterial hybrids is hugely beneficial for their characterization, as it removes any speculations in identifying nanoparticles, as we have already seen with our own samples (Figure 6.9). In addition, the attainable resolutions of these samples using scanning microscopy techniques could not reveal single LDH or single collagen fibril features. In view of this, we chose to utilise TEM methods to study such materials to obtain this much sought after information. Firstly, we needed to fabricate suitable electron transparent TEM samples. This was achieved by placing the freeze-dried LDH-collagen samples in H_2O and extensively ultrasonicated for up to 8 hours. The supernatant dispersions were then dropcast onto lacey carbon TEM grids. Excess water was wicked away with filter paper and the grids were allowed to air dry. Figure 6.10 presents STEM imaging and corresponding EDX analysis of the unstained TEM samples. Heavy metal staining was avoided to prevent spectra artefacts in high-end STEM-EDX studies. Particles are observed to adhere to the individual collagen fibrils, as shown in Figure 6.10 (a). The brighter intensity of the particles is believed to be due to the STEM Z-contrast of the Mg and Al in the LDH layered materials relative to the lighter elements of the collagen (e.g. hydrogen, carbon and oxygen). These fibril structures also compare well to previous studies of similar materials.[31–33] Moreover, the distribution of the LDHs suggest that these collagen materials could potentially be implemented as a delivery platform of LDHs, LDH-pDNA and LDH-siRNA vectors. A suitable progressive study would be to investigate if the associated LDH materials could transfect into cells such as MSCs when they are seeded onto bulk LDH-collagen materials. In the long term, these studies could be of crucial importance to employ these delivery vectors in *in vivo* and clinical trials. Also, these pilot studies provide precursory information on the ultrastructure on these novel composite materials. Further EM studies could be conducted to further understand the behaviour of LDH and collagen interaction using techniques such as STEM-EDX or STEM-EELS mapping. However, sample thicknesses may restrict the latter in achieving credible signal to background ratios. An example of the STEM-EDX mapping of similar collagen hybrids (collagen-nanohydroxyapatite-silver) is shown in the Appendix.

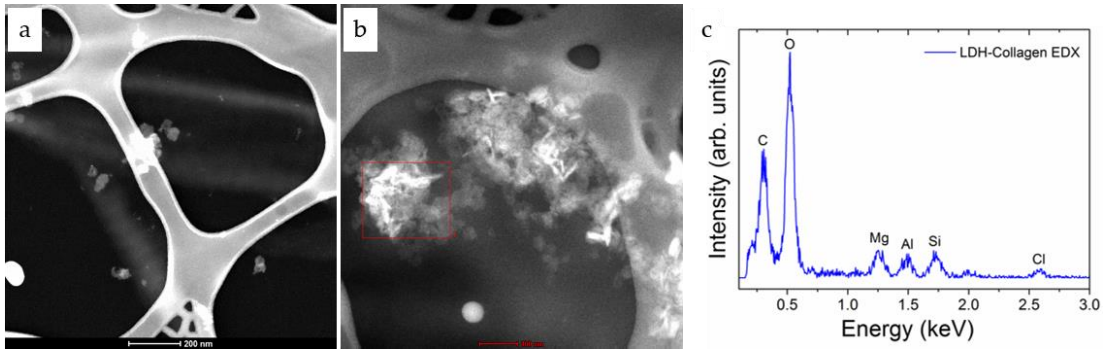

Figure 6.10 STEM imaging and STEM - EDX analysis of Collagen-LDH materials. The EDX peaks assigned to Mg, Al and O correspond to the presence of the LDHs within the collagen based scaffolds.

6.3 HIM of LDH interactions with A549 cells

Although it lacks techniques such as elemental analysis and diffraction studies, helium ion microscopy opens up a large domain of studies where biomaterials and bioengineered samples exhibit charging complications in EM characterizations. In the context of the results of this thesis, there is an abundant room for determining the behaviour of LDHs are they are exposed to cells for biomedical applications. As previously established in Chapter 5, the LDH materials were found to be successfully delivered to A549 cells in plentiful amounts. However, the technique of TEM requires the need for a complex sample preparation as well as imaging of a sub 100nm thin section of a typical sample. Further research should be done to investigate the nanoscale procedures of cellular interactions with the LDH particles on the whole cell level, i.e. in 3-D and in a more native state. In light of this, we performed preliminary experiments of untreated A549 cells. Samples were fixed in glutaraldehyde, washed in phosphate buffer saline, dehydrated through ethanol gradients and critical point dried before SEM and HIM analysis. SEM characterizations were conducted at 1 kV to prevent sample charging. Similarly, the electron flood gun was employed during HIM experiments to compensate for such charge build ups. Figure 6.11 and Figure 6.12 present HIM and SEM images of the untreated A549 cells respectively. The ultrastructure of the whole cells is observed, with varying morphologies across the

sample. The membranes and nuclei of the cells could be easily identified, as shown by the red and yellow arrows respectively.

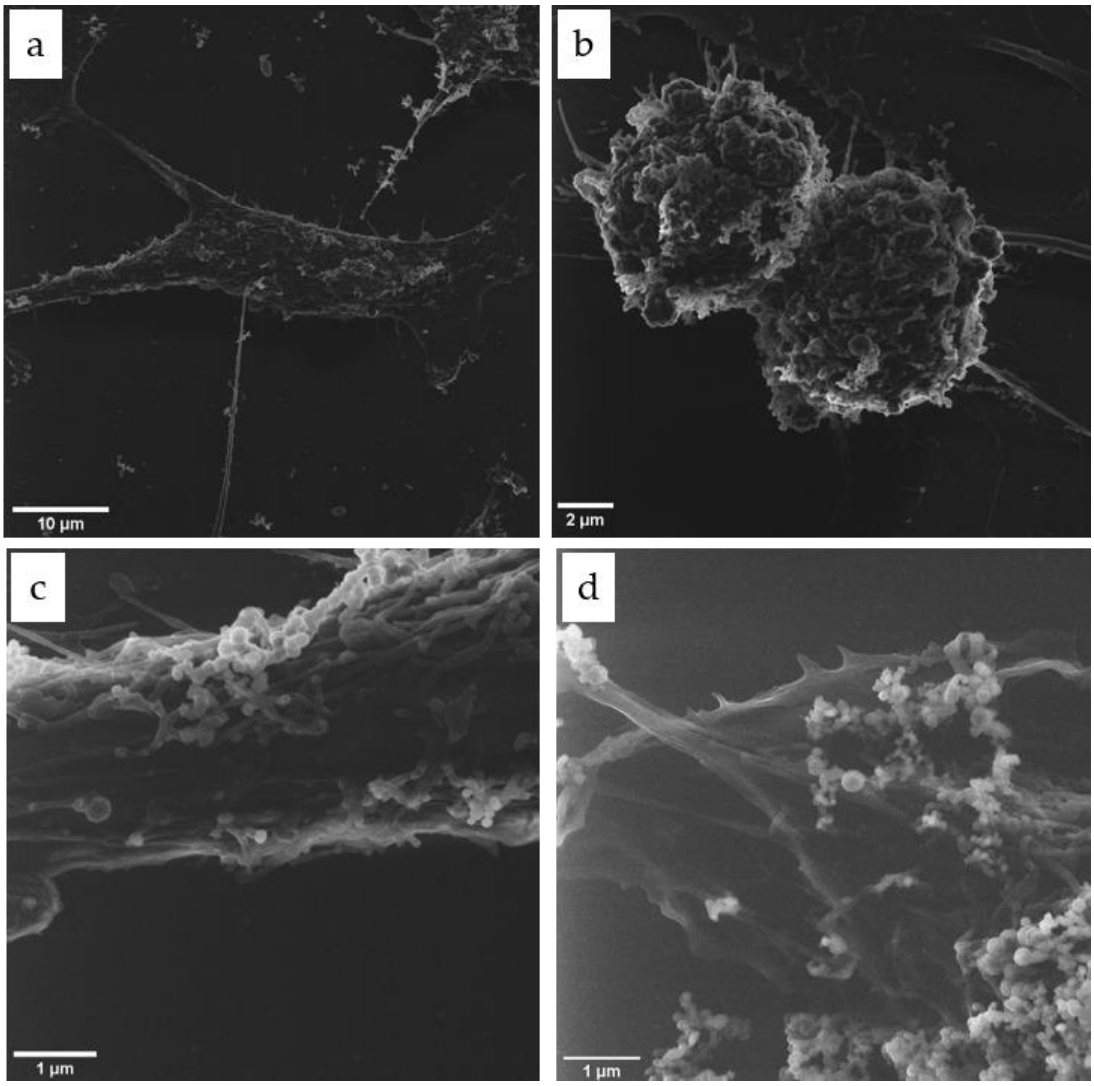

Figure 6.11 HIM imaging of critical point dried A549 cells. (a) and (b) show lower magnifications depicting whole cell morphologies. (c) and (d) present higher magnifications of cell membrane features.

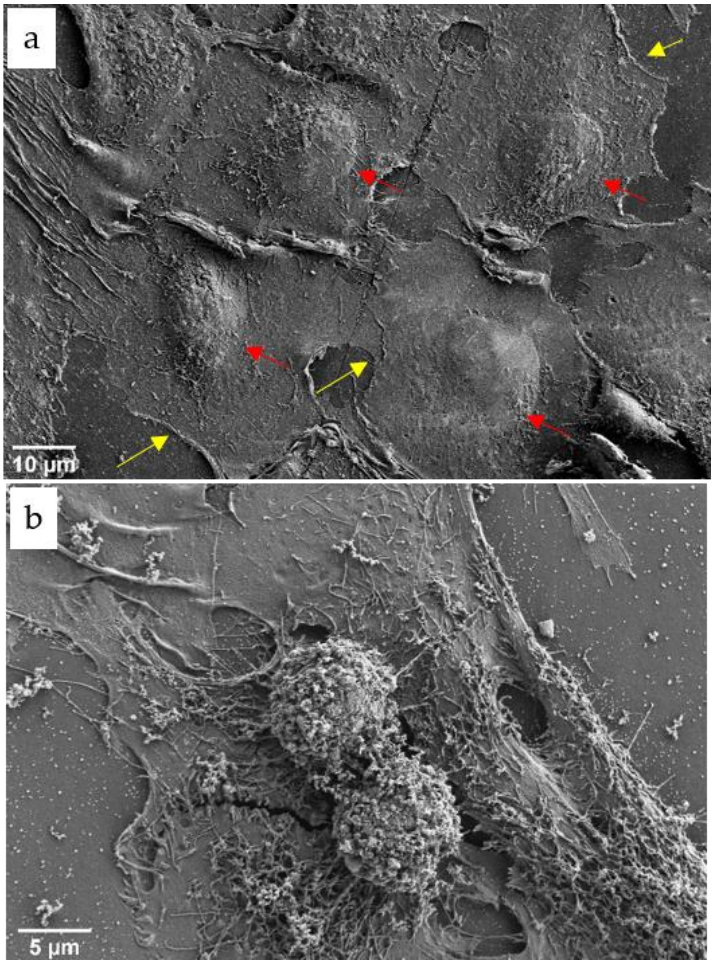

Figure 6.12 SEM imaging of critical point dried untreated A549 cells. Varying morphology of cells shown in (a) and (b) separately. Red arrows and yellow arrows highlight cellular nuclei and cell membranes respectively in (a)

6.4 In-situ liquid cell TEM analysis of whole cells

Although SEM and HIM can provide great depths of information from 'whole' cells, the sample preparation also requires extensive processing such as fixation and dehydration involved in critical point drying methods. As such, methodologies to study cellular behaviours in drug delivery processes of hydrated more native systems is of crucial importance for a fuller understanding at high spatial resolutions.

Liquid cell TEM could provide such answers. More recently, the application of this complex in-situ technique has expanded beyond the world of materials science. There have in fact been numerous developments in the study of biological specimens using liquid in-situ TEM and STEM. Imaging of whole cells in liquid states has been studied

in previous works. Topics such as the structure of Escherichia coli cells, the behaviour of bacteria and individual protein distributions in whole mammalian cells have been studied in recent times.[34–36] There lies in-depth potential investigations of how the Mg-Al LDHs are transfected in whole hydrated cells. A fascinating study would be the intracellular localization of the Mg-Al nanomaterials in whole hydrated A549 cells. One obvious concern with the STEM/TEM imaging of these samples is the achievable contrast of the Mg-Al nanoplatelets in up to micron thick liquid cell set-ups. Previous studies have utilised heavy metals tagged to epidermal growth factors to provide sufficient STEM Z-contrast to be identified in whole cells. This could be applied in the case of the LDHs exposed to the A549 cells. By exposing the previously established QD-LDH composites, the heavy Cd and Se metals in the QDs should provide suitable Z-contrasts relative to the lower lighter materials in the cells and cell media. However, this could also raise other questions such as the cytotoxic effect of the heavy metal QDs that could be induced in the cells.

In conclusion, we have shown that there are a wide variety of avenues into which LDH research can be directed. Firstly, our initial in-situ liquid TEM experiments of the Ni-Fe LDH provided promising platforms for future studies. The established behaviours and particle features in liquids will assist in impending works of the yet to be revealed growth mechanisms of the Ni-Fe LDHs using these techniques. This indeed is a particular avenue of interest of our own research within our microscopy research group. More broadly, both Mg-Al and Ni-Fe LDH compositions were found to interact with a range of other nanomaterials such as MXene and QDs, as well as biomaterials such as collagen. This once again highlights the diversity of the LDH material as it opens up a large number of potential applications. Moreover, preliminary EM characterizations have shown how they can be applied to probe the properties of these novel materials. Thus, the development of EM methodologies, can also be considered as an interesting path of study to take involving these materials. Undoubtedly, there is an obvious demand for the progression and application of these high-end EM techniques to understand future properties and diverse applications of these novel LDH materials.

6.5 Bibliography

1. Gai, P. L. Development of Wet Environmental TEM (Wet - ETEM) for In Situ Studies of Liquid - Catalyst Reactions on the Nanoscale. *Microsc. Microanal.* **8,** 21–28 (2002).

2. Zheng, H. *et al.* Observation of single colloidal platinum nanocrystal growth trajectories. *Science (80-.).* **324,** 1309–1312 (2009).

3. Liao, H.-G., Niu, K. & Zheng, H. Observation of growth of metal nanoparticles. *Chem. Commun.* **49,** 11720 (2013).

4. Zeng, Z., Liang, W. I., Chu, Y. H. & Zheng, H. In situ TEM study of the Li-Au reaction in an electrochemical liquid cell. *Faraday Discuss.* **176,** 95–107 (2014).

5. Yan, F. *et al.* Controlled synthesis of highly-branched plasmonic gold nanoparticles through peptoid engineering. *Nat. Commun.* **9,** 1–8 (2018).

6. Niu, K.-Y., Liao, H.-G. & Zheng, H. Revealing Dynamic Processes of Materials in Liquids Using Liquid Cell Transmission Electron Microscopy. *J. Vis. Exp.* 5–9 (2012). doi:10.3791/50122

7. de Jonge, N., Peckys, D. B., Kremers, G. J. & Piston, D. W. Electron microscopy of whole cells in liquid with nanometer resolution. *Proc Natl Acad Sci U S A* **106,** 2159–2164 (2009).

8. Liao, H.-G. & Zheng, H. Liquid Cell Transmission Electron Microscopy. *Annu. Rev. Phys. Chem.* **67,** 719–747 (2016).

9. Peckys, D. B. & De Jonge, N. Visualizing gold nanoparticle uptake in live cells with liquid scanning transmission electron microscopy. *Nano Lett.* **11,** 1733–1738 (2011).

10. Tan, S. F. *et al.* In situ Kinetic and Thermodynamic Growth Control of Au-Pd Core-Shell Nanoparticles. *J. Am. Chem. Soc.* **140,** jacs.8b05217 (2018).

11. De Jonge, N. & Ross, F. M. Electron microscopy of specimens in liquid. *Nat. Nanotechnol.* **6,** 695–704 (2011).

12. Garrett, B. C. *et al.* Role of water in electron-initiated processes and radical chemistry: Issues and scientific advances. *Chem. Rev.* **105,** 355–389 (2005).

13. Parello, M. L., Rojas, R. & Giacomelli, C. E. Dissolution kinetics and mechanism of Mg – Al layered double hydroxides : A simple approach to describe drug release in acid media. *J. Colloid Interface Sci.* **351,** 134–139 (2010).

14. Barsoum, M. W. The Mn+1AXn Phases : A New Class of Solids. *Prog. Solid State Chem.* **28,** 201–281 (2000).

15. Alhabeb, M. *et al.* Selective Etching of Silicon from Ti3SiC2 (MAX) Produces 2D Titanium Carbide (MXene). *Angew. Chemie Int. Ed.* **19104,** 5444–5448 (2018).

16. Zhou, Z. *et al.* Layer-by-layer assembly of MXene and carbon nanotubes on electrospun polymer films for flexible energy storage. *Nanoscale* **10,** 6005–6013 (2018).

17. Dong, Y. *et al.* Saturable Absorption in 2D Ti3C2MXene Thin Films for Passive Photonic Diodes. *Adv. Mater.* **30,** 1–8 (2018).

18. Zhang, C. J. *et al.* Stamping of Flexible, Coplanar Micro-Supercapacitors Using MXene Inks. *Adv. Funct. Mater.* **28,** 1–10 (2018).

19. Yu, M., Zhou, S., Wang, Z., Zhao, J. & Qiu, J. Boosting electrocatalytic oxygen evolution by synergistically coupling layered double hydroxide with MXene. *Nano Energy* **44,** 181–190 (2018).

20. Wang, Y. *et al.* Three-dimensional porous MXene/layered double hydroxide composite for high performance supercapacitors. *J. Power Sources* **327,** 221–228 (2016).

21. Ren, C. E. *et al.* Charge- and Size-Selective Ion Sieving Through Ti 3C2T MXene Membranes. *J. Phys. Chem. Lett.* **6,** 4026–4031 (2015).

22. Cao, Z. *et al.* Enhanced colloidal stability and protein resistance of layered double hydroxide nanoparticles with phosphonic acid-terminated PEG coating for drug delivery. *J. Colloid Interface Sci.* **521,** 242–251 (2018).

23. Usman, M. S., Hussein, M. Z. & Fakurazi, S. Gadolinium-Doped Gallic Acid-Zinc / Aluminium-Layered Double Hydroxide / Gold Theranostic Nanoparticles for a Bimodal Magnetic Resonance Imaging and Drug Delivery System. *Nanomaterials* **7,** 244 (2017).

24. Dong, S., Guan, W. & Lu, C. Quantum dots in organo-modified layered double hydroxide framework-improved peroxynitrous acid chemiluminescence for nitrite sensing. *Sensors Actuators, B Chem.* **188,** 597–602 (2013).

25. Glowacki, J. & Mizuno, S. Collagen scaffolds for tissue engineering. *Biopolymers* **89,** 338–344 (2008).

26. Curtin, C. M. *et al.* Innovative collagen nano-hydroxyapatite scaffolds offer a highly efficient non-viral gene delivery platform for stem cell-mediated bone formation. *Adv. Mater.* **24,** 749–754 (2012).

27. Al-Munajjed, A. A. & O'Brien, F. J. Influence of a novel calcium-phosphate coating on the mechanical properties of highly porous collagen scaffolds for bone repair. *J. Mech. Behav. Biomed. Mater.* **2,** 138–146 (2009).

28. Menciá Castanõ, I., Curtin, C. M., Duffy, G. P. & O'Brien, F. J. Next generation bone tissue engineering: Non-viral miR-133a inhibition using collagen-nanohydroxyapatite scaffolds rapidly enhances osteogenesis. *Sci. Rep.* **6,** 1–10 (2016).

29. Matsiko, A., Levingstone, T. J., O'Brien, F. J. & Gleeson, J. P. Addition of hyaluronic acid improves cellular infiltration and promotes early-stage chondrogenesis in a collagen-based scaffold for cartilage tissue engineering. *J. Mech. Behav. Biomed. Mater.* **11,** 41–52 (2012).

30. Cunniffe, G. M., Dickson, G. R., Partap, S., Stanton, K. T. & O'Brien, F. J. Development and characterisation of a collagen nano-hydroxyapatite composite scaffold for bone tissue engineering. *J. Mater. Sci. Mater. Med.* **21,** 2293–2298 (2010).

31. Cic, M. O., Consolider, G. & Science, M. Elemental distribution analysis of type I collagen fibrils in tilapia fish scale with energy- filtered transmission electron ... (2009). doi:10.1016/j.micron.2009.04.001

32. Asgari, M., Latifi, N., Heris, H. K., Vali, H. & Mongeau, L. In vitro fibrillogenesis of tropocollagen type III in collagen type i affects its relative fibrillar topology and mechanics. *Sci. Rep.* **7,** 1–10 (2017).

33. Jee, S. S., Thula, T. T. & Gower, L. B. Development of bone-like composites via the polymer-induced liquid-precursor (PILP) process. Part 1: Influence of polymer molecular weight. *Acta Biomater.* **6,** 3676–3686 (2010).

34. Peckys, D. B., Veith, G. M., Joy, D. C. & de Jonge, N. Nanoscale imaging of whole cells using a liquid enclosure and a scanning transmission electron microscope. *PLoS One* **4,** 1–7 (2009).

35. Woehl, T. J. *et al.* Correlative Electron and Fluorescence Microscopy of Magnetotactic Bacteria in Liquid : Toward In Vivo Imaging. *Sci. Rep.* **4,** 22–29 (2014).

36. Wang, Y. *et al.* A structural study of escherichia coli cells using an in situ liquid chamber TEM technology. *J. Anal. Methods Chem.* **2015,** (2015).

Chapter 7: Appendix

7.1 Experimental Chapter 1

7.1.1 Physical characterizations of Mg-Al and Ni-Fe LDHs

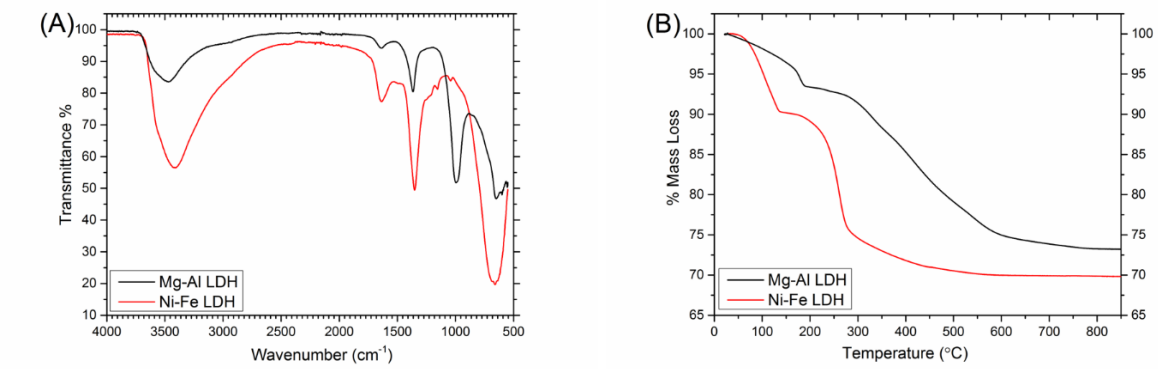

Figure 7.1 Standard FTIR and TGA analysis of Mg-Al (black) and Ni-Fe (red) LDHs.

7.1.2 Electron Diffraction spot intensity analysis

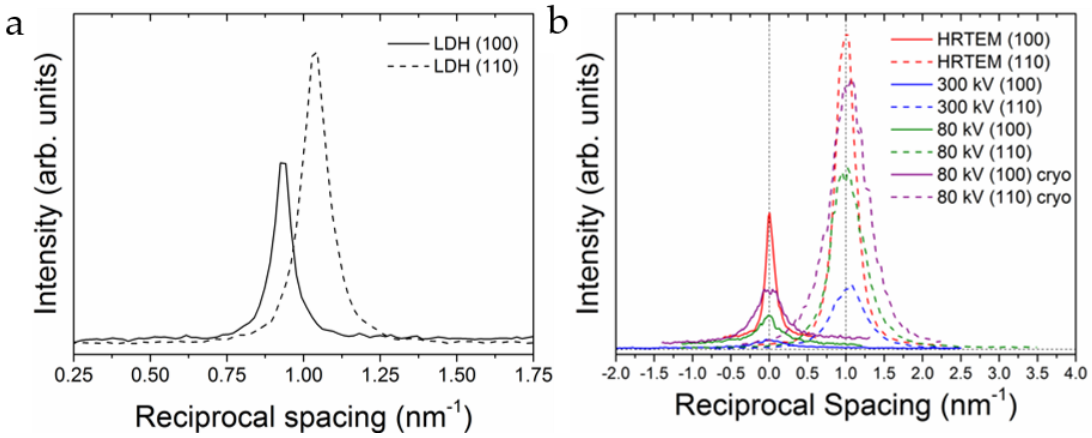

Figure 7.2 Diffraction spot intensity profiles taken from the (100) and (110) planes of the Ni-Fe LDH. Graph (a) shows the initial intensity profiles of imaged Ni-Fe LDH at 300 kV. In contrast, graph (b) shows the profiles after beam exposures to the electron beam under different conditions as follows: post HRTEM (red), 300 kV (blue), 80 kV (green) and 80 kV at cryogenic temperatures (purple). Peak positions of the (100) and (110) profiles were shifted for peak intensity ratio comparisons.

7.1.3 Localized STEM-EELS studies of Ni-Fe LDH platelets

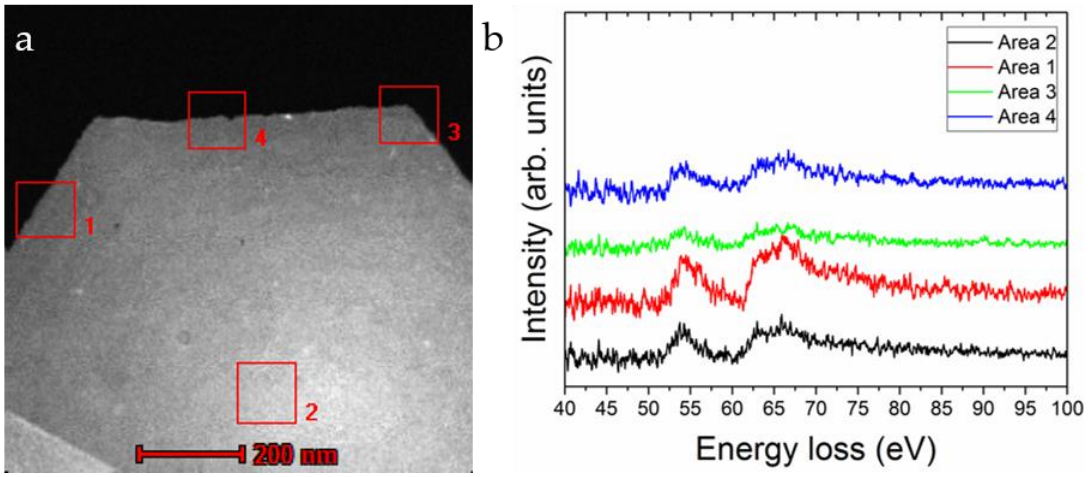

Figure 7.3 (a) STEM image of Ni-Fe LDH platelets with regions of acquisition of low loss EELS spectra. (b) Ni and Fe M-edge EELS spectra of Areas 1-4 as indicated in (a).

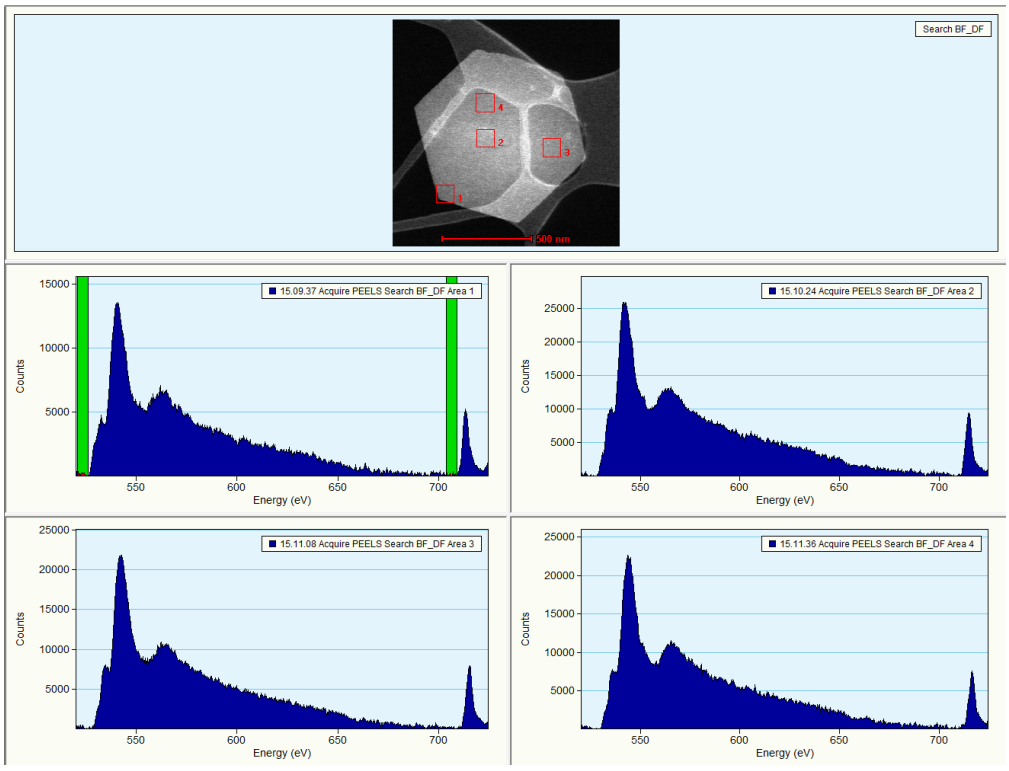

Figure 7.4 Oxygen K edge features at various locations of the Ni-Fe LDH platelet.

7.1.4 Aberration corrected STEM imaging of Ni-Fe LDH platelets

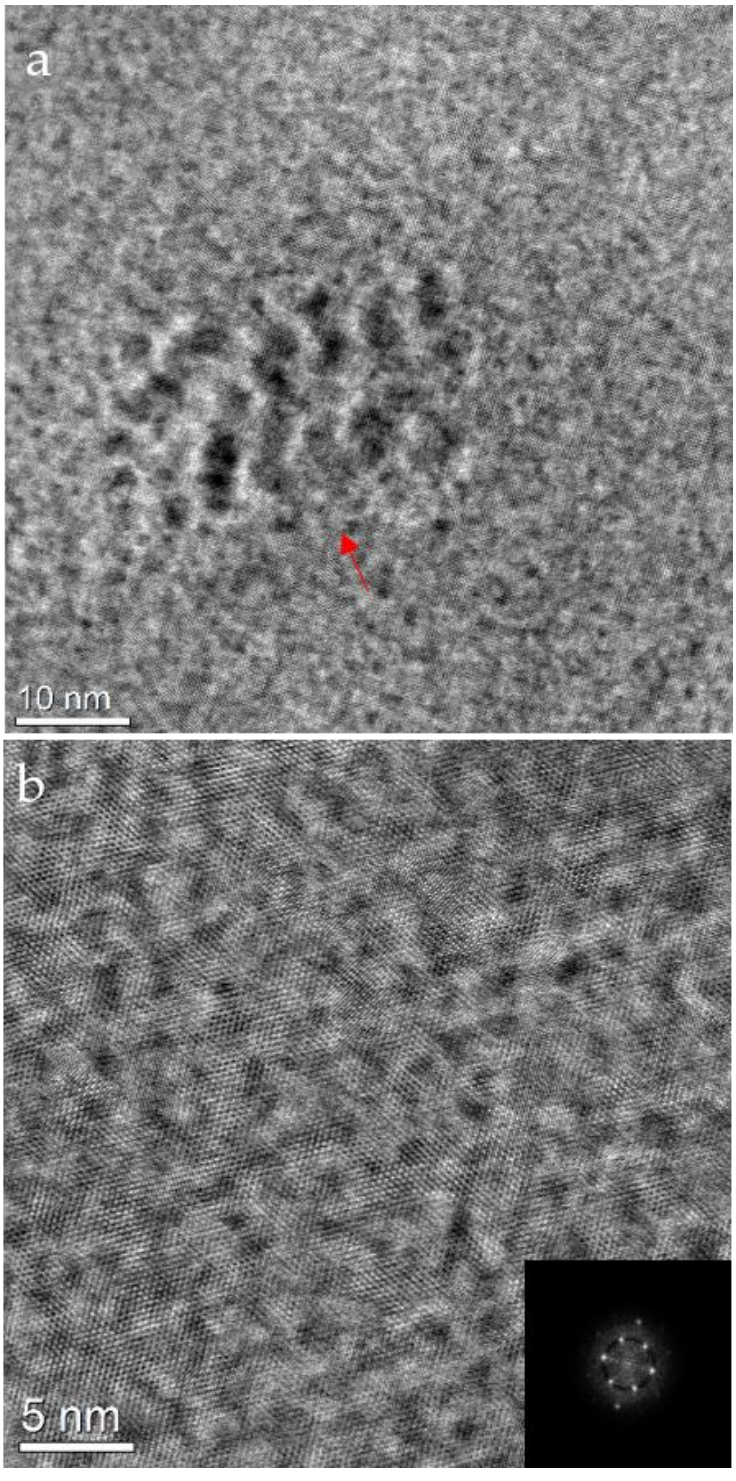

Figure 7.5 AC-STEM imaging of Ni-Fe LDHs. (a) Lower magnification showing damaged regions of the LDH platelet (indicated by red arrow). (b) Higher magnification image. FFT pattern of whole image region inset in (b). Images have been enlarged for clarity.

7.2 Experimental Chapter 2

7.2.1 In-situ heating experiments of Ni-Fe LDH nanomaterials

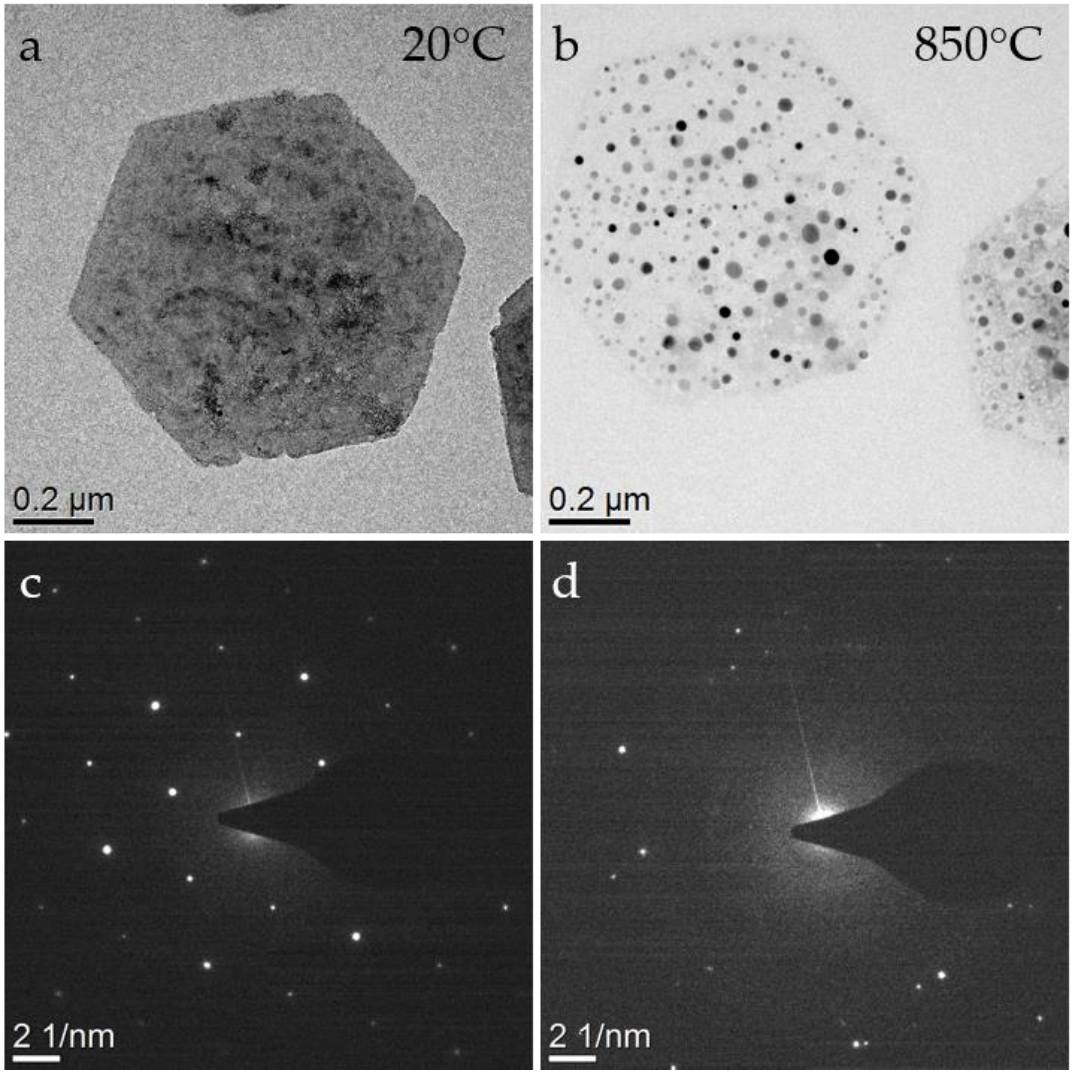

Figure 7.6 Additional Ni-Fe LDH platelets subject to in-situ TEM heating experiments as conducted in Chapter 4. (a) and (b) present BFTEM images at the beginning (20°C) and end (850°C) of our applied in-situ heating protocols. The corresponding SAED patterns are presented in (c) and (d) respectively.

7.2.2 TEM characterization of single particle calcined Ni-Fe LDH nanomaterials

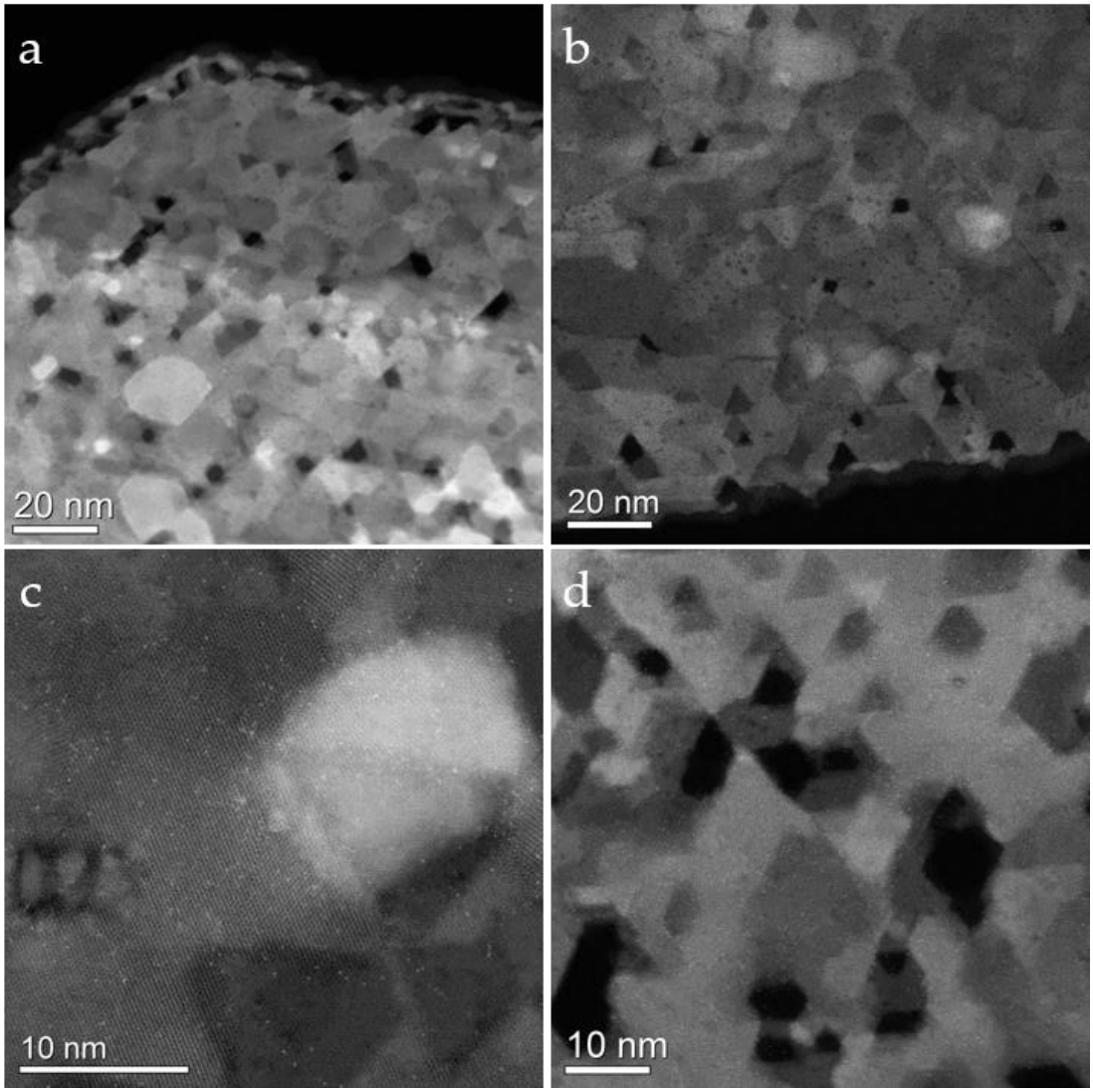

Figure 7.7 AC-STEM images of calcined Ni-Fe LDH nanomaterials. Sample grids were calcined at 850°C for 6 hours in a standard laboratory oven.

7.3 Experimental Chapter 3

7.3.1 Experimental details of LDH and plasmid DNA complex formation.

Plasmid DNA (pDNA) encoding green fluorescent protein (pGFP; Amaxa, Lonza, Cologne AG, Germany) under the control of the cytomegalovirus promoter was used as the reporter gene. The pDNA was amplified by first transforming chemically competent DH5α *E. coli* cells (Biosciences, Ireland) according to the manufacturer's protocol. Transformed cells were then expanded in Lysogeny broth (LB) plates containing 100 μg/mL of ampicillin as the selective antibiotic. After 24 h at 37°C, bacterial colonies were harvested and further expanded in LB broth containing ampicillin and cultured overnight in a shaker incubator at 37°C. Plasmid purification was performed using a QIAGEN® EndoFree®Plasmid Maxi kit (Qiagen, Sussex, United Kingdom) and final nucleic acid concentration was determined using NanoDrop 1000 spectroscopy. Plasmids were further diluted in TE buffer to obtain a working concentration of 0.5 μg/μl and stored at -20°C until use.

LDH-pGFP synthesis: LDH at concentrations of 0.1, 0.25, 0.5 and 1μg/μL were tested. At each concentration, the LDH was mixed with pGFP in decarbonated water at ratios of 0:1, 1:0 (controls) and 1:1, 2:1, 1:2, 5:1, 1:5, 10:1 and 1:10. The components were allowed to complex for 5 minutes in an air-tight container before exposure to cells.

7.3.2 Experimental details of MSCs and LDH exposures

MSC isolation, expansion and transfection with LDH-pGFP nanohybrids: Mesenchymal stem cells (MSCs) were isolated from 8 week old male Sprague Dawley rats with the approval of the Research Ethics Committee of the Royal College of Surgeons in Ireland (REC Approval No. 237) as described previously (114). The MSCs were cultured in growth media which contained Dulbecco's Modified Eagles Medium supplemented with 2% penicillin/streptomycin, 1% L-glutamine, 10% FBS (Labtech, UK), 1% glutamax (Biosciences, Ireland) and 1% non-essential amino acids

(Biosciences, Ireland). Cells were passaged at 70-90% confluency and expanded to passage 5 for all experiments. MSCs were seeded at a density of $5X10^4$ cells per well in 6 well adherent plates (Corning, Costar, Ireland) 24h prior to transfection. At 1h prior to transfection, media was removed and the cells were washed in PBS before 1 mL of OptiMEM (Gibco, Ireland) was added to each well. LDH-pGFP nanohybrids were made as described in preceding sections and, following complexation, media was added in a 1:1 ratio to the nanoparticle mixture to produce the transfection medium of which 500 μL was added to each well. After 4 h, transfection media was removed, cells were washed twice in PBS and growth media was replenished.

7.3.3 TEM/STEM of Mg-Al LDH and LDH-pDNA complexes

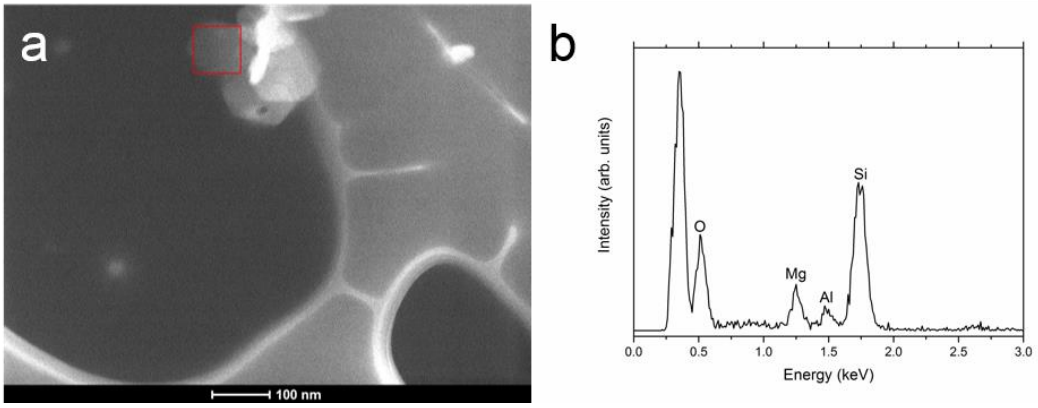

Figure 7.8 (a) STEM image and (b) associated STEM-EDX spectra of pristine Mg-Al LDHs used for delivery applications. EDX spectra is acquired from the red square region in the STEM image.

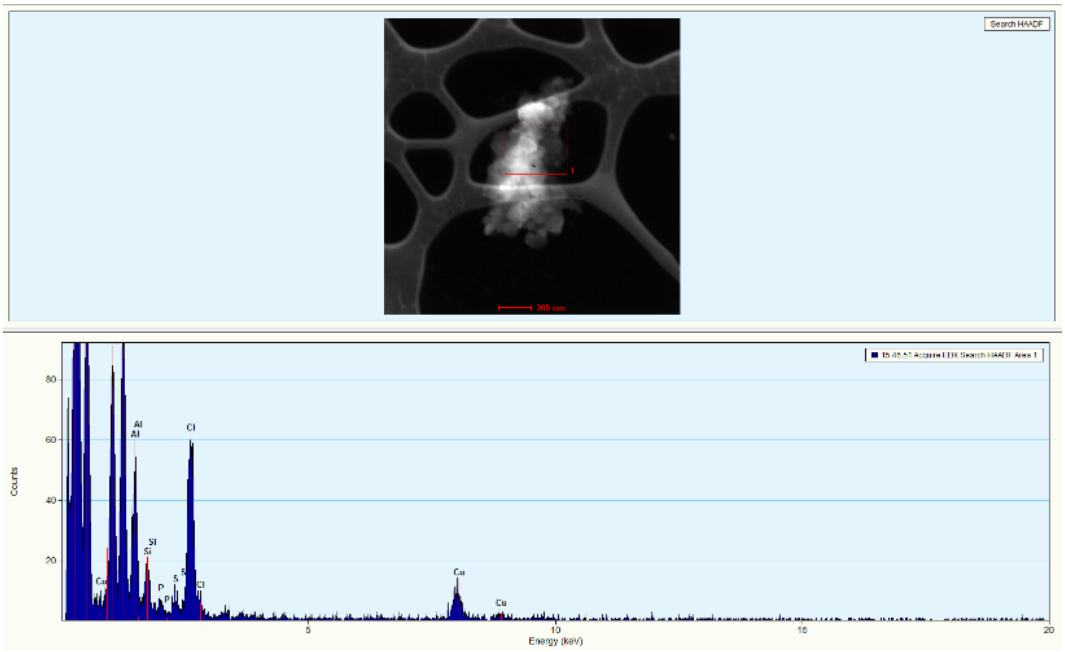

Figure 7.9 Additional STEM-EDX analysis of LDH-pDNA vectors. EDX spectra is acquired from the red square region in the STEM image.

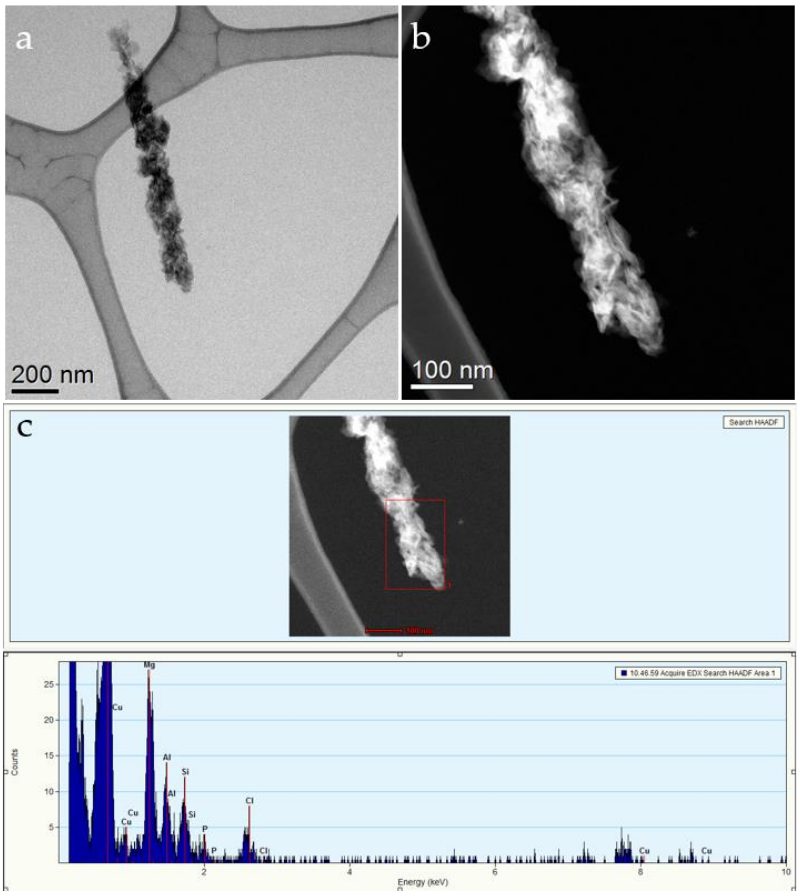

Table 7.1 Additional TEM, STEM and STEM-EDX analysis of LDH-pDNA vectors. EDX spectra is acquired from the red square region in the STEM image.

7.3.4 Additional Images of Mg-Al LDHs exposed to MSCs

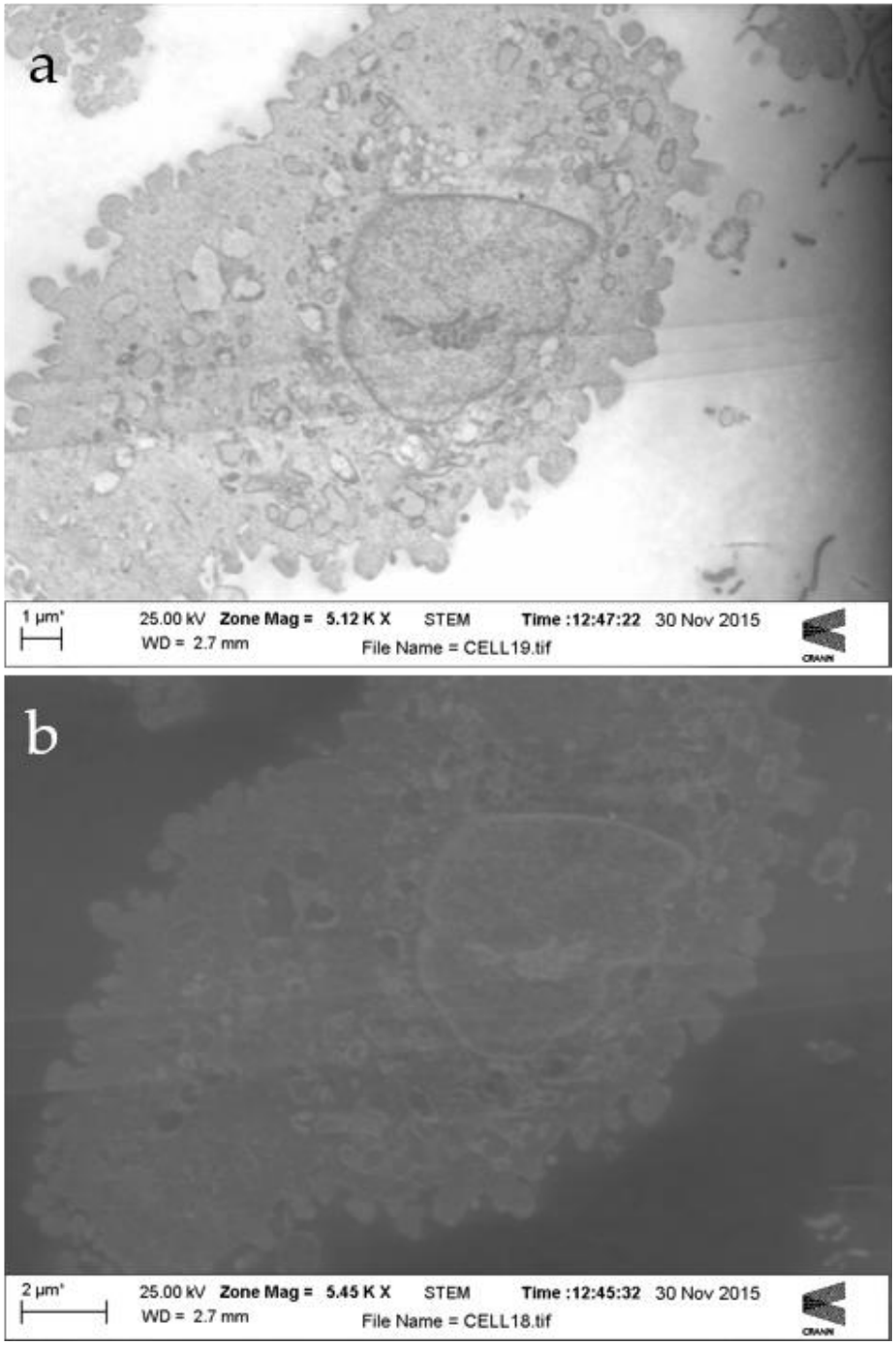

Figure 7.10 SEM images of MSCs embedded in plastic resin section. Image were acquired at 25 kV using the (a) bright field and (b) dark field transmitted electron detector in a Carl Zeiss Ultra SEM.

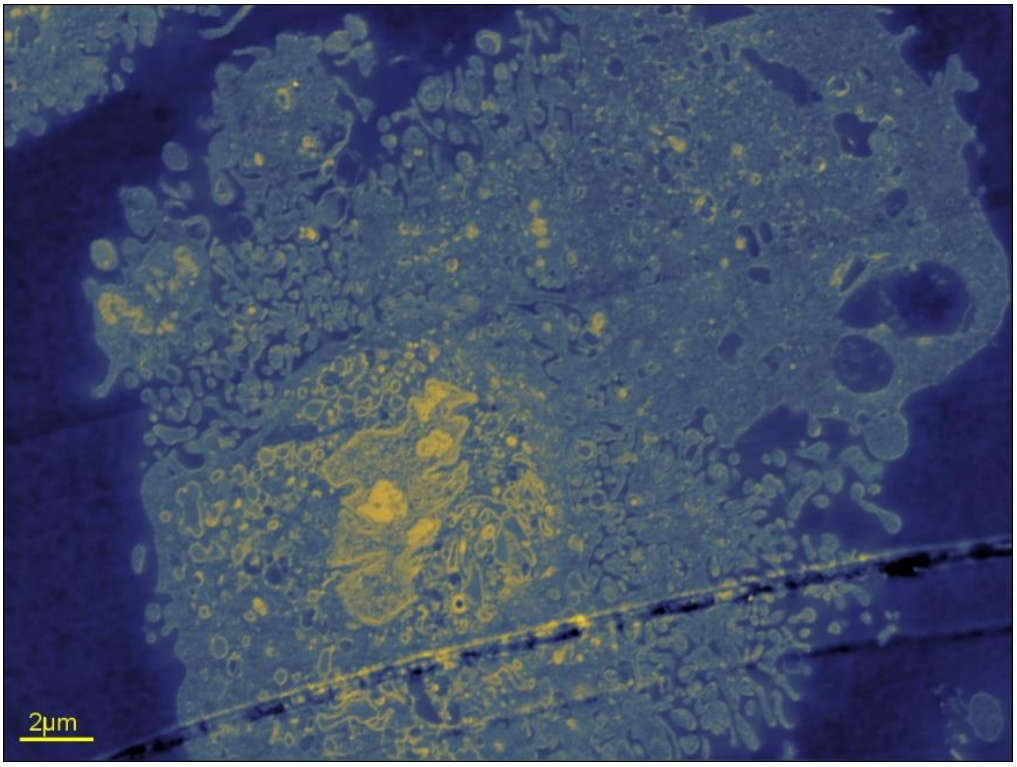

Figure 7.11 False coloured SEM image of the MSC cell exposed to Mg-Al LDH in an acrylic resin section.

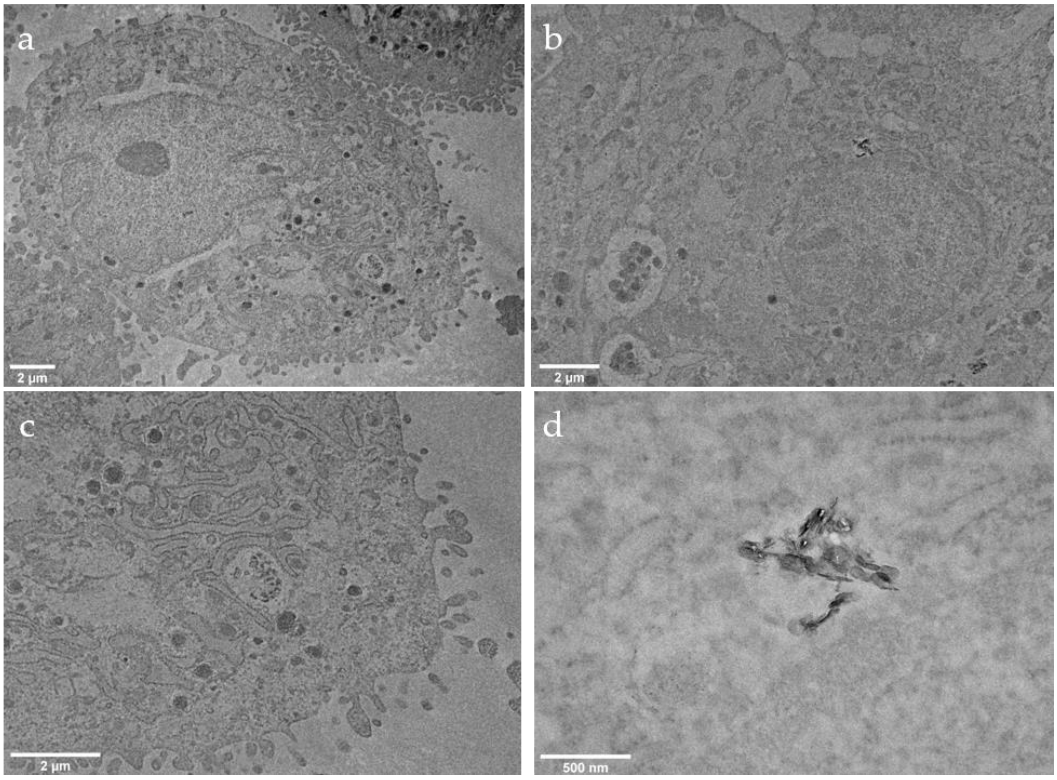

Figure 7.12 TEM images of MSCs in plastic embedded sections from LDH exposure experiments. TEM images were acquired at 200 kV using a JEOL 2100 TEM.

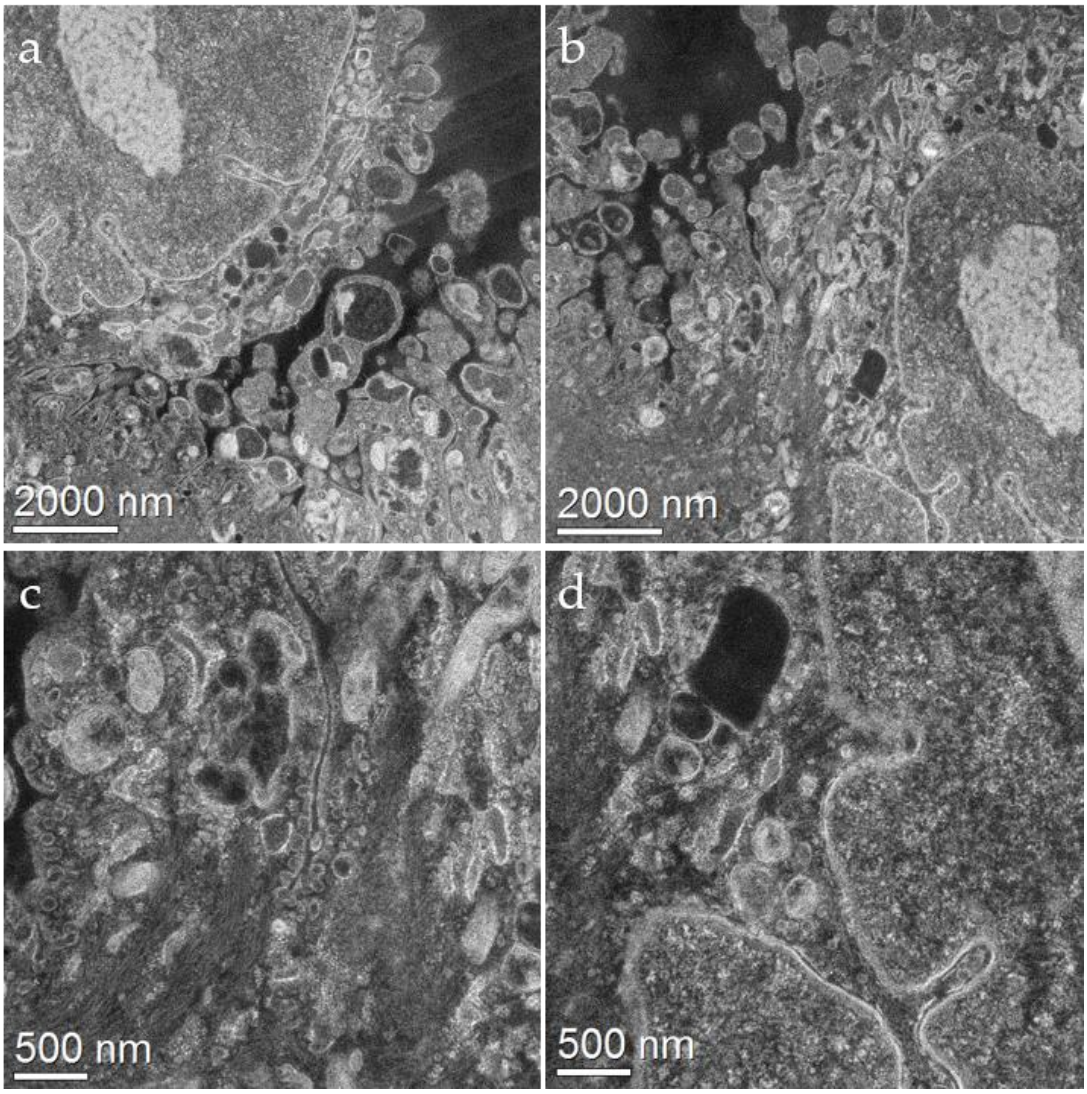

Figure 7.13 Additional STEM images of MSC ultrastructure from LDH exposure experiments at various magnifications.

7.3.5 Electron Beam damages to resin sections

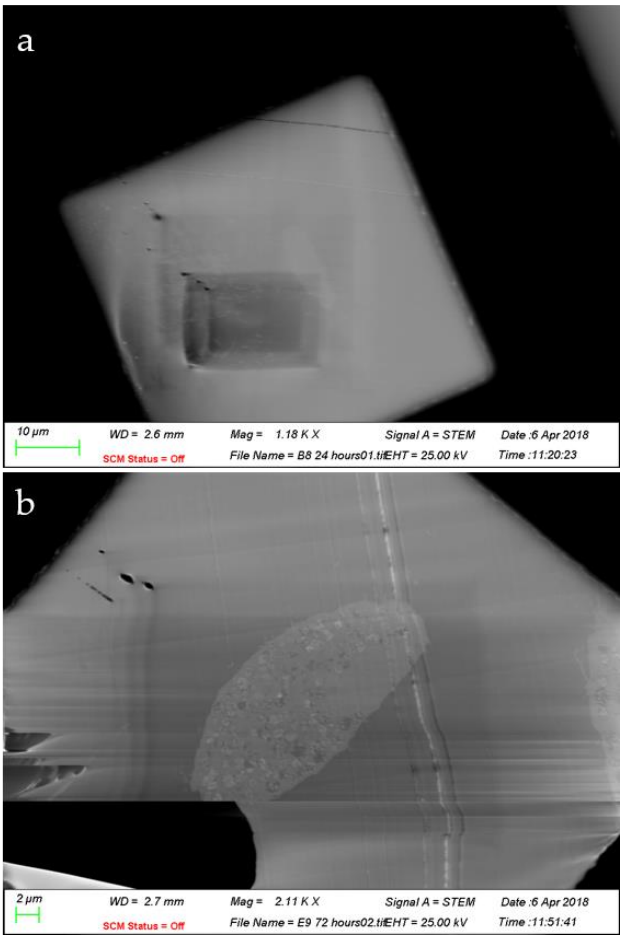

Figure 7.14 Thinning and sample tearing damages to epoxy resin sections during SEM imaging.

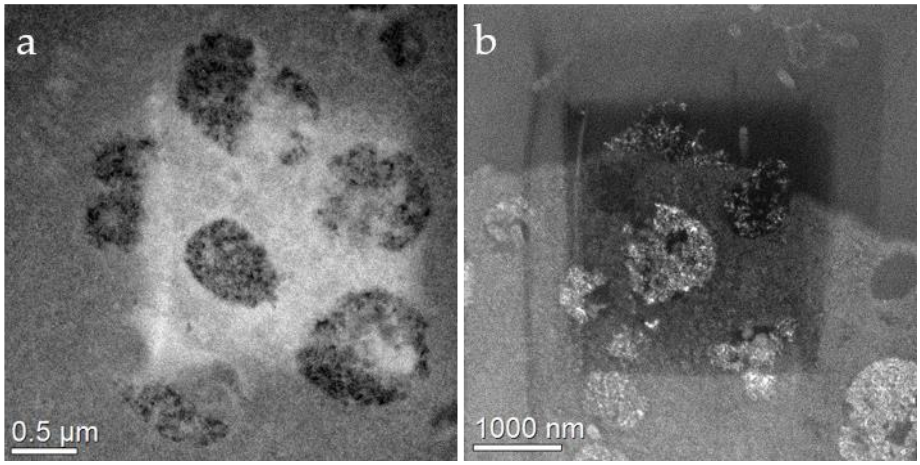

Figure 7.15 STEM damages to epoxy resin sections containing A549 cells involved in the LDH exposures, observed in TEM post STEM experiments.

7.3.6 Additional LDH A549 cell images.

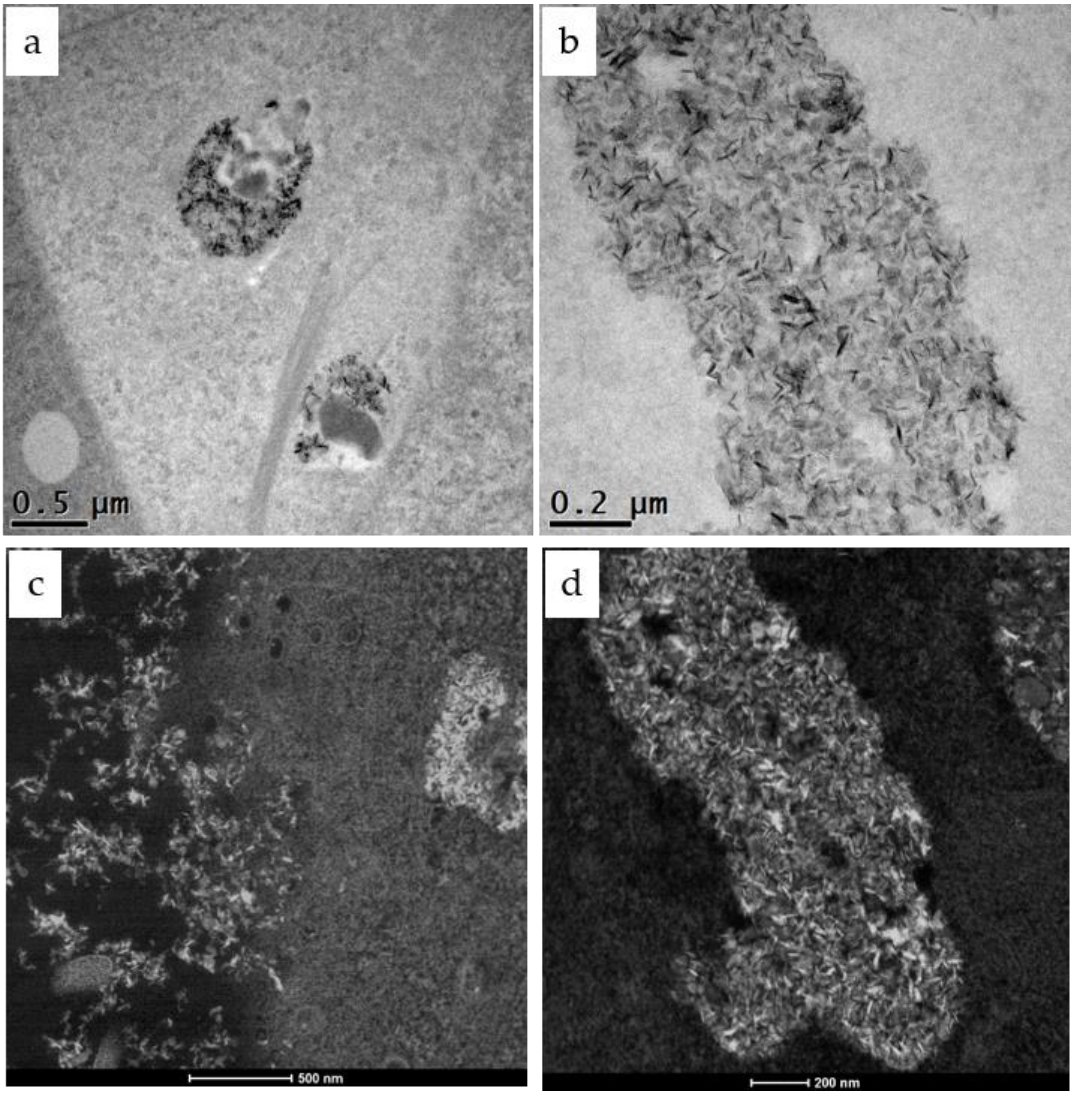

Figure 7.16 Additional TEM and STEM images of initial exposures of Mg-Al LDHs to A549 cells, where the samples were fixed after 14 hours.

7.3.7 Time study of LDHs exposed to A549 cells

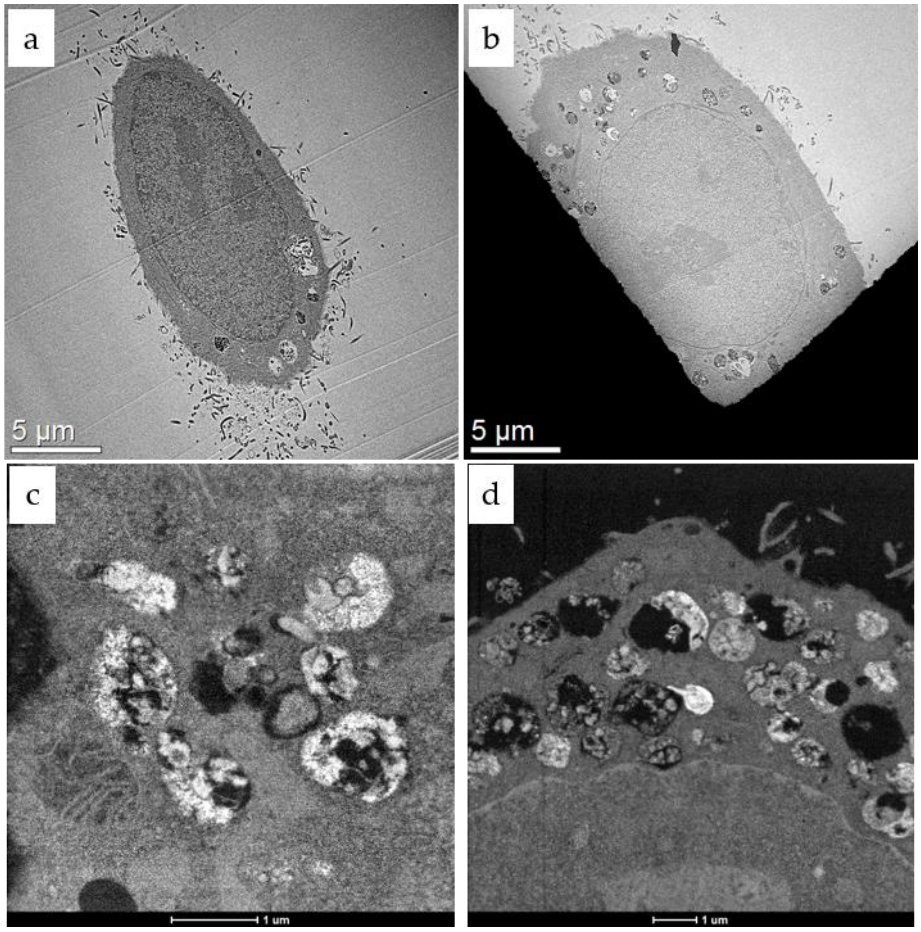

Figure 7.17 Low magnification (a) and (b) TEM and (c) and (d) STEM images of LDHs exposed to A549 cells fixated after 24 hours.

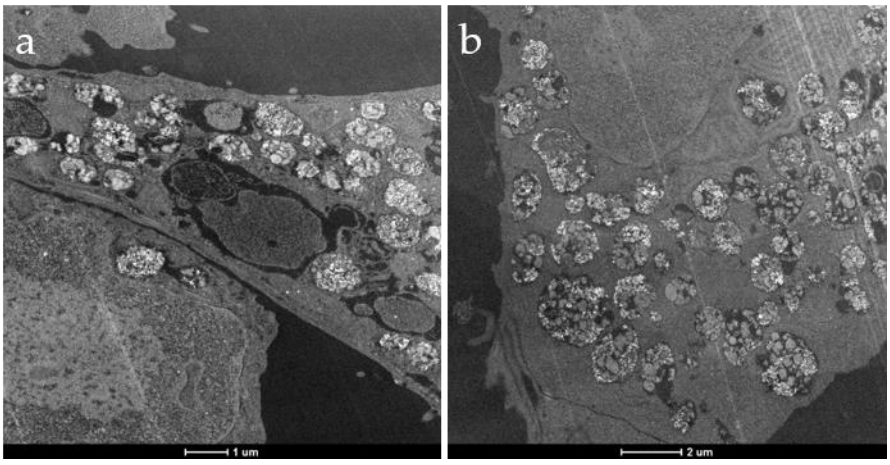

Figure 7.18 STEM images of Mg-Al LDHs exposed to A549 cells after 72 hours.

7.4 Conclusions and Future Work

7.4.1 In-situ liquid cell TEM characterization of Ni-Fe LDHs

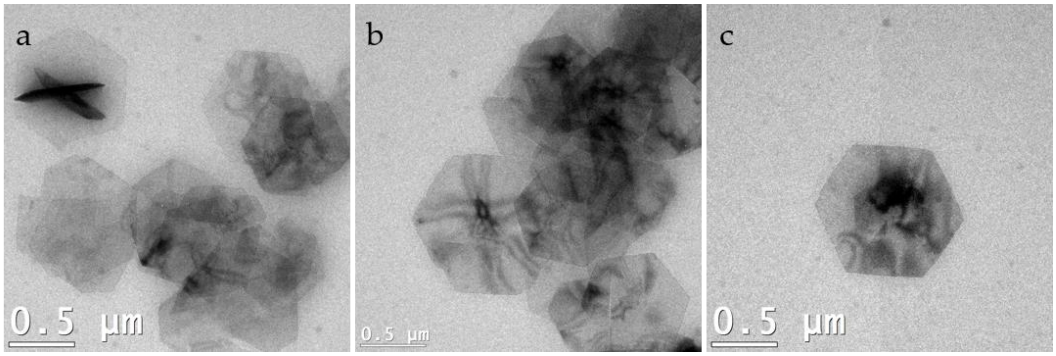

Figure 7.19 TEM images of Ni-Fe LDHs in liquid cell TEM characterizations.

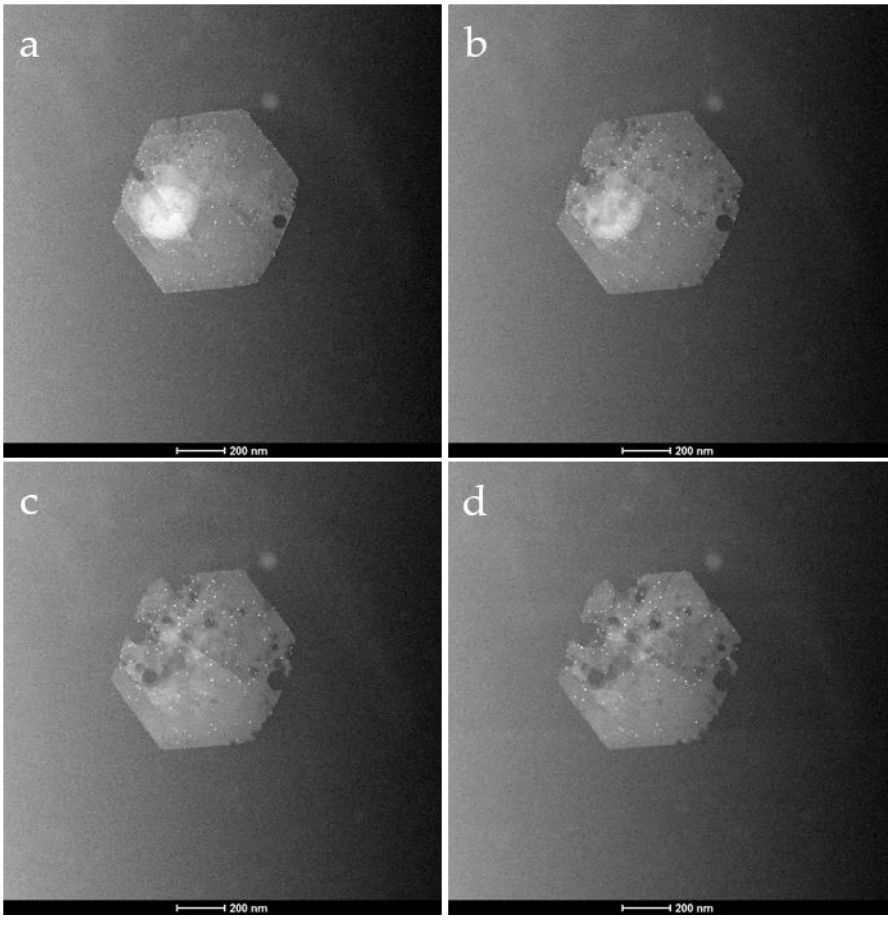

Figure 7.20 STEM images highlighting beam induced degradations of Ni-Fe LDH nanomaterials in liquid environments.

7.4.2 LDH-MXene composites

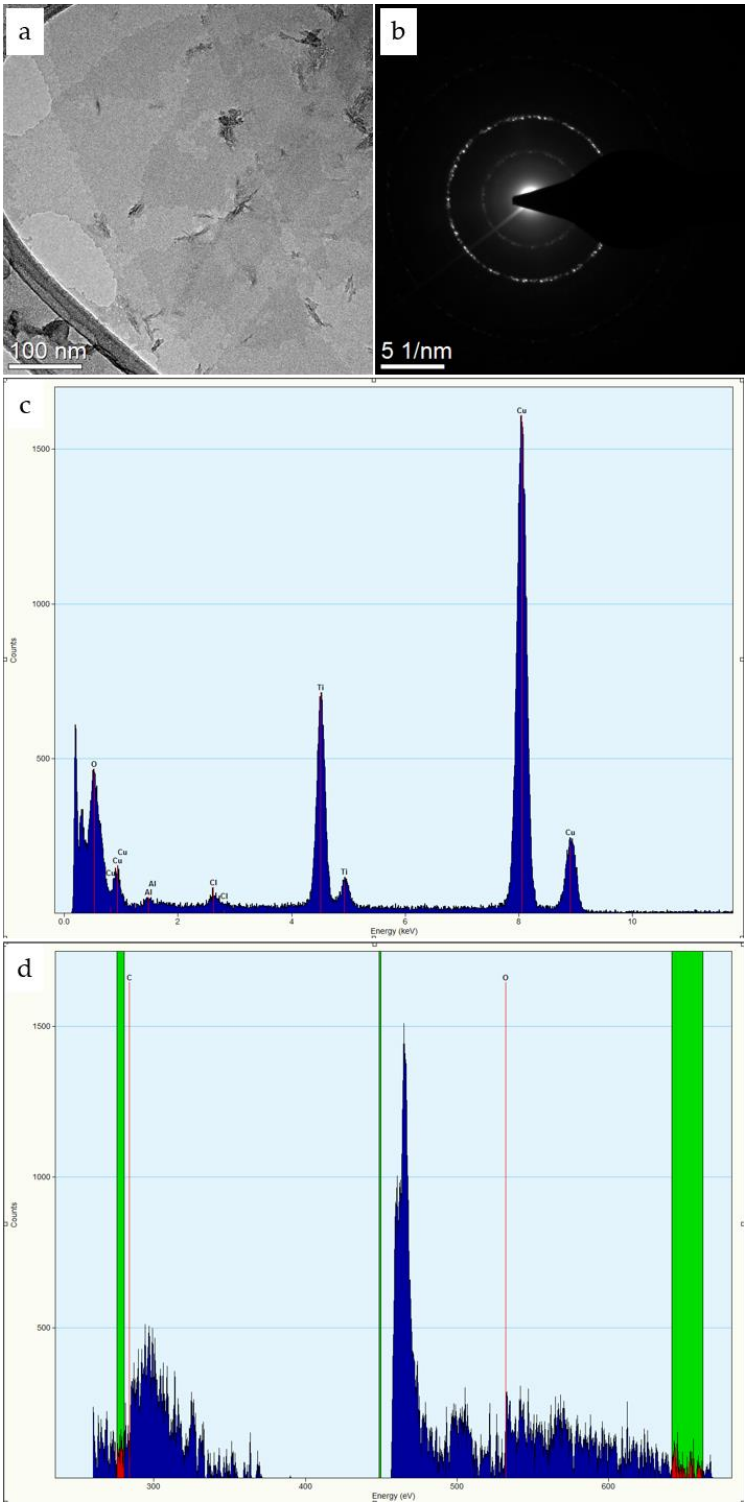

Figure 7.21 (a) TEM (b) SAED, (c) TEM-EDX and (d) TEM-EELS of the C K edge and Ti $L_{2,3}$ edge of the MXene material used in the synthesis of LDH-MXene nanocomposites.

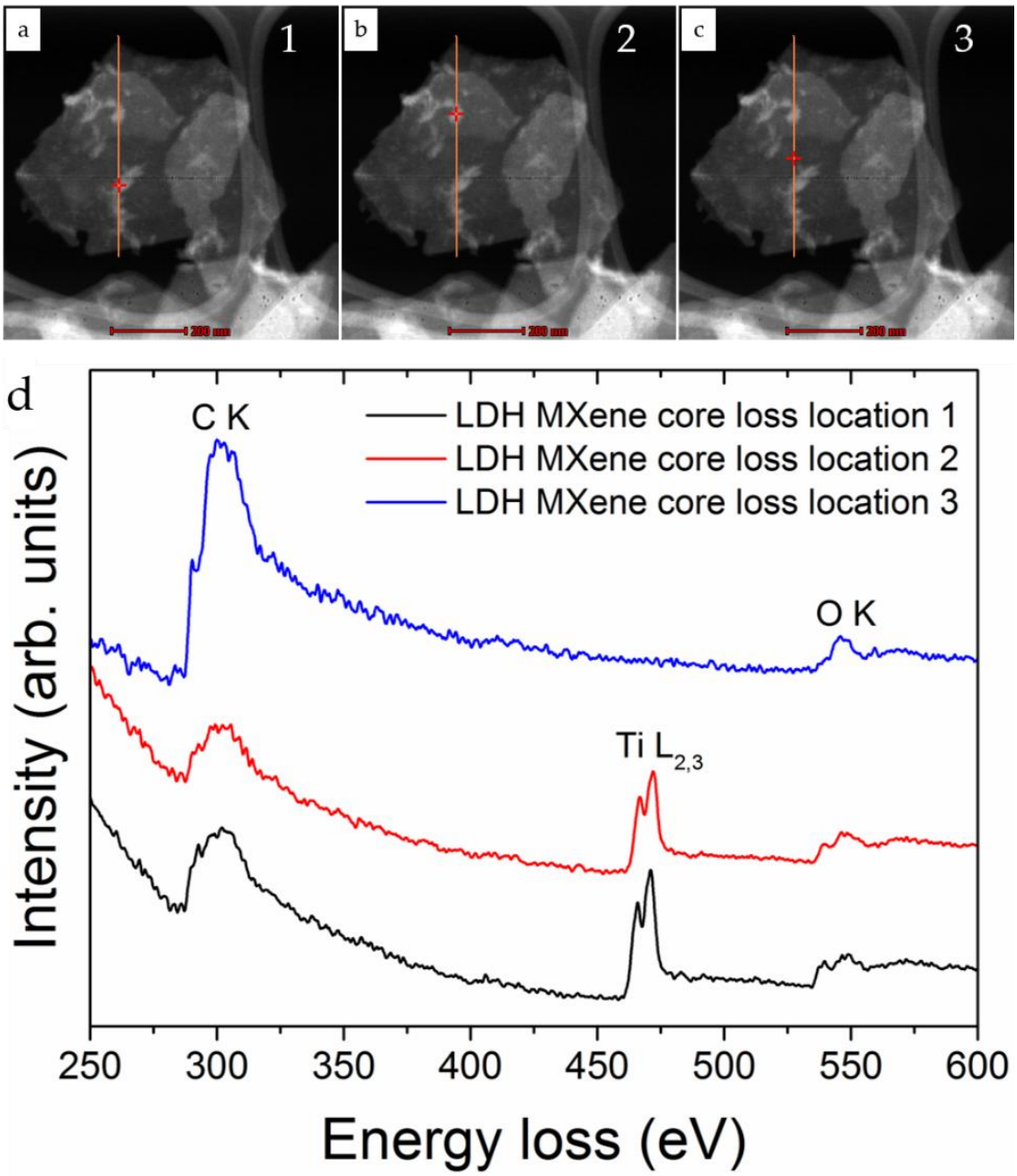

Figure 7.22 STEM-EELS core loss spectra from various point locations during line scan acquisitions of LDH-MXene composites. Locations 1 and 3 highlighting Ti $L_{2,3}$ edge, denoting presence of surface adhered MXenes on the Ni-Fe LDH.

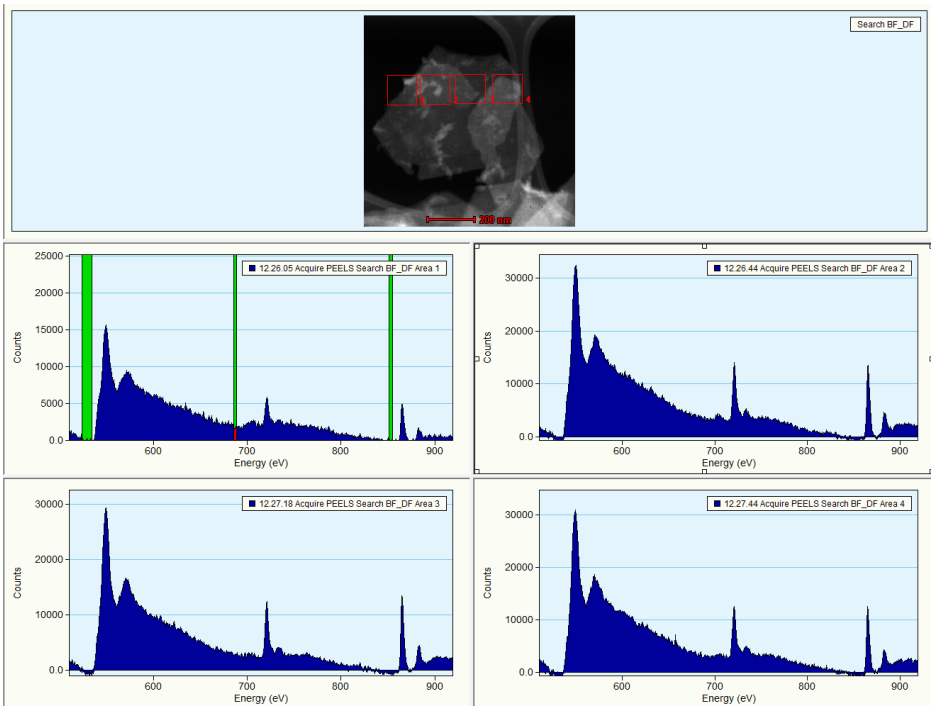

Figure 7.23 STEM- EELS area scan Ni and Fe L edge core loss regions of the Ni-Fe LDH-MXene nanocomposite.

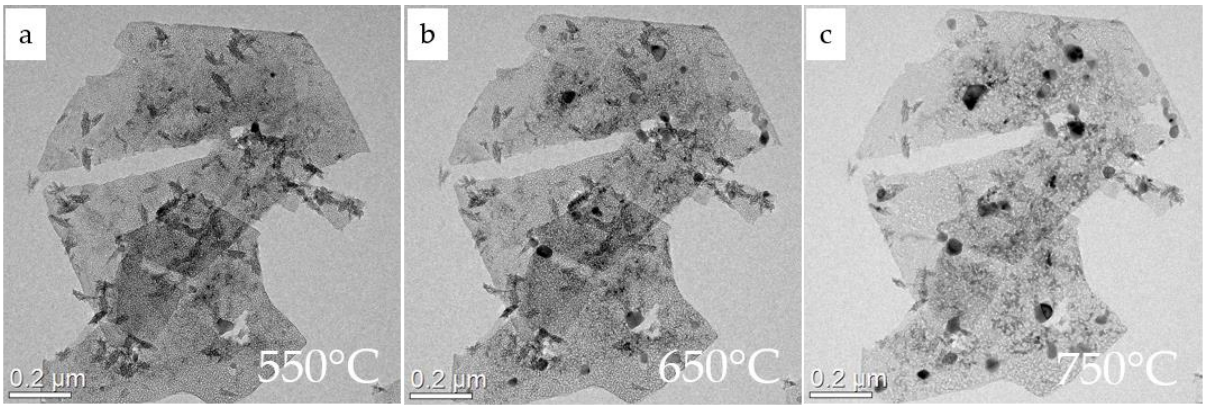

Figure 7.24 BFTEM images at additional temperatures of the LDH-MXene in-situ heating experiments at (a) 550°C, (b) 650°C and (c) 750°C.

7.4.3 STEM imaging STEM-EDX mapping of collagen based scaffolds

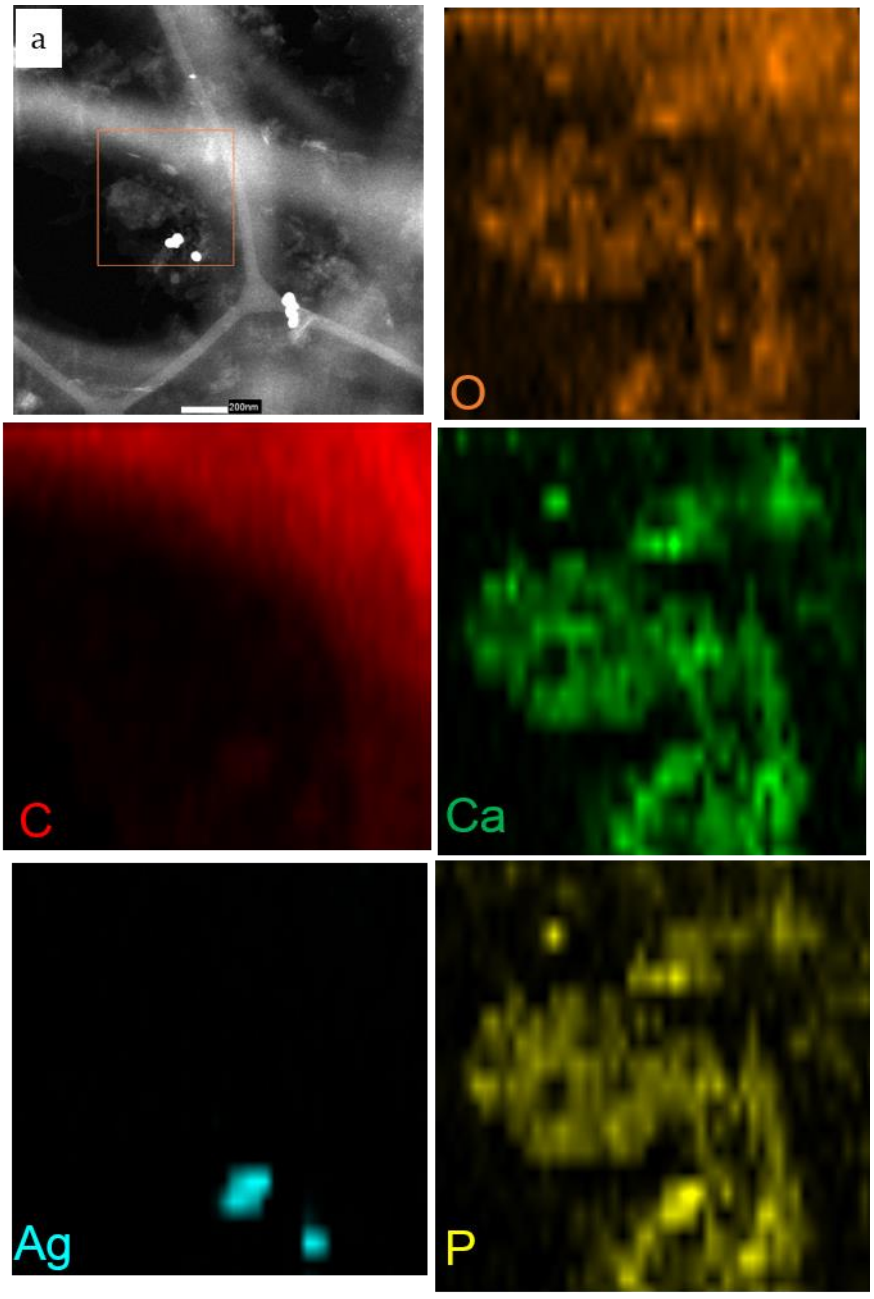

Figure 7.25 STEM - EDX of Collagen-nanohydroxyapatite-silver composite. STEM image of region, with map area shown by orange square in (a). Panels represent EDX maps of elements in the sample.